An Investigation into Deformation and Failure in Thin Sheet Electrical Steels Using a Non-Local Modelling Approach

Luke Michael Jones

Supervisors: Hassan Ghadbeigi, Christophe Pinna

A report submitted in partial fulfilment of the requirements
for the degree of Doctor of Philosophy in Mechanical Engineering

in the

Department of Mechanical Engineering

December 18, 2023

Declaration

All sentences or passages quoted in this document from other people's work have been specifically acknowledged by clear cross-referencing to author, work and page(s). Any illustrations that are not the work of the author of this report have been used with the explicit permission of the originator and are specifically acknowledged. I understand that failure to do this amounts to plagiarism and will be considered grounds for failure.

Name: ______________________________

Signature: ______________________________

Date: ______________________________

“Let me not think of my work only as a stepping stone to something else, and if it is, let me become fascinated with the shape of the stone.”
- Hosea Jan Frank

Acknowledgements

I would like to express my deepest gratitude to my supervisors Dr. Hassan Ghadbeigi and Dr. Christophe Pinna, whose excellent guidance through challenging times has supported the successful completion of this project. The incredibly fine balance of mentoring and self-education afforded by their supervision has allowed me to grow both on a personal and professional level. The knowledge shared and discovered with me through a process of constant yet considerate antagonism has prepared me in a way that I feel has given me the skills and confidence to achieve my future work, and I am fortunate to have been shaped by this masterful process.

During my time working on this project I have formed deep friendships with the people around me, I would like to thank in particular Dr. Emiliano Ximenes and Dr. Tianwei Zhang who I spent my first year sharing an office with and who both provided endless humour and advice. I would also like to thank the many members of *The Farm* and my research group for their friendship and advice, especially Dr. Alex Perez, Fathi Alhussadi, Dr. Hamid Jamshidi, Dr. Jundi He, Lucas Biazon, Ludo Fossà, Dr. Marco Galindo Fernandez, Maria Clara Coimbra Goncalves, Dr. Marius Monoranu, Dr. Matthew Falcone, Steve Jackson and Dr. Kenneth Chinembiri.

I have had the pleasure of working with many other academic and technical staff at the university who have been of great help throughout the project and their support is greatly appreciated. I would like to thank in particular Chris Todd, Dr. Ria Mitchell and especially Richard Kay, with whom I have enjoyed many long conversations. I am grateful to Dr. Matteo Benedetti, Jonathan Wood, and Dr. Rachel Tomlinson for their role in developing my teaching skills and I would like to acknowledge how personally fulfilling my time working with them has been.

Finally, I could not have completed this project without the endless love and support of my friends, family, and partner. Shay, thank you for always being there, listening, and sharing this time in my life. To my immediate family - my little sister Summer and my parents Julie and David - words cannot express my gratitude. Your support has been fundamental to my completion of this project, and indeed to every success I have been fortunate enough to experience in my life.

Abstract

Electrical machines are typically manufactured using stacked thin laminations of ferromagnetic material as a core in order to guide and amplify magnetic flux. Silicon steel, also known as electrical steel, is one of the most commercially successful materials for this role. This is due to its high magnetic permeability, low coercivity, and high resistivity, as a result of the alloying elements and large grained microstructure. The required geometries for rotors and stators are manufactured using the blanking process, which introduces edge damage and degrades the magnetic properties causing increased energy loss. Understanding the effects of the various parameters on edge damage is vitally important to guide and improve the blanking process.

In this work, a novel non-local damage model is developed to predict edge damage resulting from this process. The model is an extension of the Bao-Wierzbicki type fracture model, which performs well due to its sensitivity to stress state. The difficulties in calibrating a damage model, such as the high variance of the fracture dynamics due to the size effect, have been addressed. It was found that calibrating the model based only on the limited geometries manufacture from sheet stock was possible through highly localised strain measurements from digital image correlation (DIC). To investigate low triaxiality samples, a device compatible with DIC for preventing out of plane deformation due to buckling is demonstrated. A new method for in-situ damage detection is presented using hall effect sensors to detect the change in magnetic flux flowing through a sample. The model is validated using a number of geometries and load conditions and found to reproduce fracture mechanics accurately.

Contents

List of Figures

List of Tables

Nomenclature

J	Third deviatoric stress invariant
$\bar{\theta}$	Normalised lode Angle
$\boldsymbol{S}$	Deviatoric stress
η	Stress triaxiality
η_{avg}	Average stress triaxiality
$\overline{\sigma}$	von Mises equivalent stress
σ	Cauchy stress
σ^D	Damage softened stress
σ^g	Stress in single grain
σ_{Hyd}	Hydrostatic stress
σ_i	Principal stress
σ_{new}	Stress calculated in current increment
σ_{old}	Stress calculated from previous increment
σ_{trial}	Trial stress (used for elastic predictor)
σ_y	Yield stress
τ	Critical resolved shear stress
θ	Lode Angle
q	von Mises equivalent stress
$\bar{\varepsilon}^{pl}$	Equivalent plastic strain
$\dot{\bar{\varepsilon}}^{pl}$	Equivalent plastic strain rate
$\dot{\gamma}$	Shear strain rate
$\dot{\varepsilon}^g$	Strain rate of a single grain

$\dot{\varepsilon}_f^{pl}$	Equivalent plastic strain at fracture
$\dot{\varepsilon}_{ref}$	Reference strain rate
ε	Johnson Cook normalised strain rate
γ	Material viscosity parameter (Perzyna model)
$\boldsymbol{F}$	Deformation gradient tensor
$\boldsymbol{I}$	Identity tensor
$\boldsymbol{m}$	Schmid tensor
λ	Stretch
$\mathcal{E}$	Induced electromotive force
ν	Poisson's ratio
ρ	Density or Resistivity
B	Magnetic Flux
B_p	Peak magnetic flux
C_d	Stable time increment
d	Thickness of lamination
E	Young's Modulus
F	Force
f	Frequency
F_{max}	Maximum force
G	Shear Modulus
H	Nanohardness
k	Bulk Modulus
L	Characteristic element length
P	Power
p	Pressure
T	Temperature
t	Time
T^*	Johnson Cook normalised temperature

T_m	Melt temperature
T_{ref}	Reference temperature
α^{Σ}	Sum of non-local weights in interaction radius
α_i	Non-local weight of element i
$\bar{D}$	Damage softening variable
η_i^{α}	Non-local triaxiality contribution of element i
Γ	Non-local penalty term
$\hat{\theta}$	Johnson Cook fracture model temperature parameter
ε_d	Strain at damage onset
ε_f	Strain at fracture
ε_i^{α}	Non-local strain contribution of element i
ξ	Non-local target element position
A, B	Calibration constants for asymptotic section of loci
C_n	Calibration constants for damage and fracture loci
D	Damage driving variable
d_n	Johnson Cook fracture model fitting parameters
G_f	Energy required to open a unit crack
N	Total number of elements in interaction radius
R	Interaction Radius
x	Non-local source element position
Φ	GTN model yield function
f	Void volume fraction (GTN model)
f_c	Critical void volume fraction (GTN model)
f_f	Void volume fraction at fracture (GTN model)
f	Void state (GTN model)
q_n	GTN model fitting parameters
Z	Coalescence rate of micro voids (GTN model)
C_{CC}	Cross correlation criteria

C_{LS}	Least Squares correlation criteria
$f(x,y)$	Pixel intensity at position (x,y) in reference configuration
f_m	Average pixel intensity in subset in deformed configuration
f_m	Average pixel intensity in subset in reference configuration
$g(x,y)$	Pixel intensity at position (x,y) in deformed configuration
H	Subset Entropy
I_i	Pixel intensity of neighbouring pixel i
I_p	Pixel intensity
S, M, N	Subset dimensions
$\mathscr{E}$	Landau-Lifshitz total free energy
$\mathscr{E}_\lambda$	Magnetoelastic anisotropy energy
$\mathscr{E}_D$	Magnetostatic energy
$\mathscr{E}_H$	Zeeman energy
$\mathscr{E}_k$	Magnetocrystalline anisotropy energy
$\mathscr{E}_{ex}$	Exchange energy
A, B, n	Johnson Cook plasticity model quasi static constants
C	Johnson Cook plasticity model strain rate constants
m	Johnson Cook plasticity model temperature constant

Chapter 1

Introduction

Due to the increasing focus on the reduction of fossil fuel emissions a renewed focus on the development of the electric automobile and electrical machines is underway. Electric motor cores are composed of stacks of thin laminations of silicon steel in order to reduce energy loss. Improving and understanding the manufacturing process of such a critical material is of paramount importance to increasing efficiencies. Blanking is the commercially dominant method to manufacture high volumes of rotors and stators, producing the complex geometries required in a short time. For efficient and high performance electrical machines a material with high magnetic permeability and high resistivity is required, these key properties ensure high torque and low power loss (known as core loss).

Though the addition of silicon reduces core losses, it causes the material to become brittle and consequently difficult to manufacture via rolling. The highest silicon content used is approximately 3.2 weight percent due to these disadvantages. Core losses arise from several mechanisms: magnetic hysteresis, induced eddy currents, and anomalous losses due to movement of magnetic domain boundaries. The addition of silicon increases the relative magnetic permeability therefore decreasing hysteresis effects, while also increasing electrical resistivity thereby reducing the induction of eddy currents. Other alloying elements such as aluminium and manganese are also added in order to improve magnetic and mechanical qualities [1]. Blanking introduces deformation at the cut edge, which negatively impacts the magnetic performance. Additionally various parameters -such as the clearance or radius of the tool as wear increases - can alter the quality of the cut edge mechanically. These defects may induce the formation of large burrs, which in the extreme can penetrate neighbouring lamination's coatings, thereby removing the insulative effect and producing much greater eddy currents.

Modelling of the fracture and damage is complicated by the geometry of the final product; the large grain size of on average 150 µm in comparison to the final sheet thickness of 200 µm means established calibration techniques and macroscale models are difficult to use. This research therefore focuses on developing a new calibration and modelling strategy that can more directly be used for this class of sheet materials.

1.1 Background

Although the blanking of laminations allows mass production it potentially causes defects at the blanked edge due to the introduction of plastic deformation, damage in the form of micro-voids, micro-cracks, residual stresses, and burrs. The introduction of these defects cause sub-optimal properties both mechanically and magnetically, and much effort is dedicated to the reduction of defects, primarily in the design of the die. The complex effects of die geometry, particularly when considering wear, is critical to increasing efficiency in industry and is still being researched. Commercially, the material may be supplied to the customer in a *semi-processed* (unannealed) or *fully-processed* (annealed) state. In the *semi-processed* state, the material is blanked and then annealed; this allows some of the defects, particularly magnetic property degradation due to residual stress, to be ameliorated. In the *fully-processed* state the annealed material is blanked, which introduces the aforementioned damage and degrades magnetic performance of the material. The stress state of materials has been shown to significantly impact the fracture mechanics, and during the blanking process severe changes in stress state are present in the vicinity of the edge. The ability to understand and model the blanking process for such material, specifically to ensure minimum degradation of the material, is highly desirable. As complex stress states arising in at the work-tool interface require high fidelity models with extremely small elements, any model must be sufficiently computationally performant to allow large scale modelling, be sensitive to stress state, and be compatible with complex contact conditions caused by the interaction of the tool, die, and work.

Low stress triaxialities cannot be investigated using established methods due to buckling, and high variability in fracture dynamics requires careful consideration of a fracture criterion on which to calibrate a model. In order to understand the effects of the various aforementioned blanking parameters, a model which can predict the damage and fracture mechanics is required. Several such models are available, of particular relevance is the Bao-Wierzbicki fracture model - which is highly sensitive to stress state and performs well in compression, shear, and tension. Close to fracture the load carrying capacity of the material is decreased due to microvoids increasing the effective stress experienced by the material. Modelling fracture only cannot accurately reproduce this behaviour. By the addition of progressive damage and softening sub element phenomena such as the micro-voids observed in [2] is possible. Most damage/material models are implemented locally - the calculation of the material response at the integration point depends solely of information at that point. Conversely, non-local models use information from neighbouring integration points, and are required if strain based damage calibration is to be used to avoid mesh dependence. A Wierzbicki type damage model may also be eventually coupled directly with a measure of magnetic degradation/loss increase. Magnetic performance has been shown to vary from different preparation methods as reported in [3, 4]; changes have been observed to the mechanical properties with the addition of copper, such as significant precipitation hardening [5]. In light of this, various processing methods have been trialled to ensure that the sample preparation method did not affect the results, this has provided evidence that it is extremely important to consider even the edge effects due to sample preparation.

1.2 Research Objectives and Novelty

The main objective of this research is to further the understanding of various blanking parameters - for example: tool wear, clearance, punch speeds - on silicon steel. This is achieved through developing a predictive tool, which can ultimately be applied to solve the industry-relevant challenge of decreasing core loss and in order to do this a novel experimental methodology is required for calibration on the final product thickness of 0.2 mm (as opposed to bulk product), allowing for coupling to the magnetic performance. A novel non-local model based on an extension and modification of the Bao-Wierzbicki type fracture model allowed calibration using strain without the typical pathological mesh sensitivity observed in local models. In order to aid the calibration of such model using the developed methodology, a number of aspects of digital image correlation (DIC) validity are explored; a 2 dimensional entropy metric is introduced for the first time in the context of DIC image quality.

A lab scale blanking rig was used for verification of the finite element results, this simplified model accurately replicates several key aspects of the real blanking process while allowing in situ strain measurement. As the frequency of tool replacement/reconditioning is the major driving factor in the cost of the blanking operation, understanding the effect of wearing parts will help inform design and maintenance decisions throughout the life-cycle of the part; two tools were compared in this manner for further verification of the model.

A variety of concerns are addressed with regards to strain measurement via digital image correlation acquired in sub-optimal conditions, such as when paired with the novel restraining system, by using a multifaceted approach considering various quantitative measures such as shear strain angle and divergence to judge potential error. Furthermore, the application of a two dimensional entropy measure has been applied for the first time to assess the quality of speckle patterns, harmonising existing methods based on gradient analysis and one dimensional entropy.

1.3 Thesis Layout

The research is presented in the following chapters:

Introduction This chapter introduces the scope of the research, its objectives and novelty.

Literature Review A holistic review of the state of the art in modelling, experimental methodologies, and material specific properties is presented. Silicon steel and its properties are first discussed, followed by a review of the manufacturing route and its effects on the final application qualities; in particular the final step, blanking, is reviewed. Experimental methods for the quantification of sheet products and calibration of further models are displayed. The effect of the grain size on the mechanical properties and the implications on experimental methodologies are discussed.

Methodology The experimental methodology of the project is described, various established technologies are used alongside the novel methodologies developed in order to calibrate the model as described in later chapters.

Experimental Results The results of the experiments are displayed and discussed, including statistical analysis. The effect of sample preparation method is first addressed in order to set a baseline for further experimentation. Standard tensile tests are performed at various strain rates and temperatures giving data for calibration of the Johnson Cook model. An investigation of all assumptions about the material is first made and it is shown that localised DIC measurement is the only suitable method to generate data for calibration of the numerical model with this material. Several geometries are used to gather fracture and damage data, with a restraining system used in low triaxiality samples.

Modelling The implementation of the model is described, starting with a brief description of the implementation of the established elastoviscoplastic Johnson Cook model and adding the novel non-local extended and modified Bao-Wierzbicki type damage model. The novel damage model is then activated and used to simulate the calibration samples and a comparison is made between the experimental and simulated results. The blanking rig is then simulated in two and three dimensions for verification. Tool wear is investigated with progressively a worn tool simulated with large edge radius punch showing the effect on final fracture. All aspects of the models are detailed e.g. boundary conditions, physical element size, etc. and assumptions are discussed.

Conclusion A conclusion on the main evidence presented in the thesis is drawn and a framework for further investigations laid out.

Chapter 2

Literature Review

2.1 Silicon Steel

Electrical steel (also known as silicon steel) is a ferromagnetic alloy of iron and interstitial silicon. The electrons in these materials spontaneously align into domains, due to their intrinsic magnetic moments seeking to minimise their energy state. In the unmagnetised state, the domains are randomly aligned with respect to one another, thus causing an overall cancellation of the magnetic field; if many of the domains are aligned the material acts as a magnet. The resistance of a magnetic material to changes in its magnetisation is known as coercivity, and is measured with the magnetic field intensity required to demagnetise the material from a magnetised state. Silicon steel is a soft magnetic material, meaning it is easy to magnetise and demagnetise with a coercivity of less than $80\,\mathrm{A\,m^{-1}}$ [6, 7].

In recent years the increased focus on sustainability has led to the rapid development of battery (BEV) and hybrid (HEV) electric vehicles. Silicon steel is a key material in the motors of such vehicles as both the rotors and stators are manufactured from laminations of such material . By improving the understanding of these materials, a number of key performance indicators such as power to weight ratio, and efficiency may be improved. Although some alternatives exist, such as Fe-Co, Fe-Ni, or Fe composites [8], no material to date can match the performance-to-price ratio silicon steel provides in most applications.

2.1.1 The metallurgical properties of silicon steel

The alloying element composition of silicon steel is selected to minimise energy loss in the magnetic performance of the material. The major alloying element, silicon, is used to increase the resistivity, ρ. A higher resistivity reduces eddy current induction, explained further in Section 2.1.4. Silicon content of up to 6.5% by weight is possible [9], with the ideal characteristic that at this high percentage almost no magnetostriction is observed [10]. Unfortunately the manufacturability becomes poor, and above around 3wt% the material is so brittle it becomes extremely difficult to cold roll [11, 12]. Very high percentage silicon steels therefore require various alternative methods of manufacture such as vapour deposition or spray forming [13] which are not commercially viable at large scale and as such the highest content commercially available is typically around 3.2wt%. Figure 2.1(a) shows the effect of various alloying elements on the resistivity, it is notable that silicon is the element with the greatest effect on resistivity. The effect of silicon content on the magnetic properties is shown in

Figure 2.1(b), notably increasing silicon content does negatively affect some parameters, for example decreasing the saturation induction. The major alloying element, silicon, is interstitial and does not alter the phase at 3.2wt%, as shown in Figure 2.2 [14] wherein αFe, the body centred cubic phase is shown below approximately 10% silicon content.

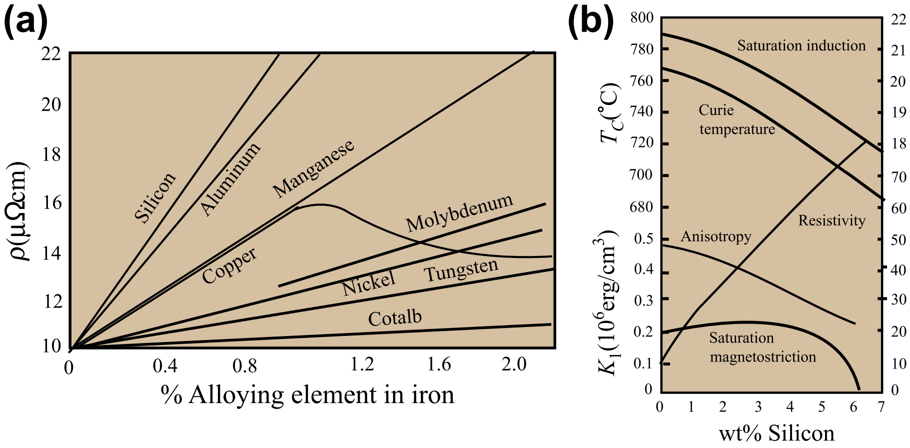

Figure 2.1: *(a) The effect of addition of various alloying elements to iron on the resistivity. (b) The effect of silicon content on the magnetic properties. Figure reprinted from [15] with permission from Elsevier*

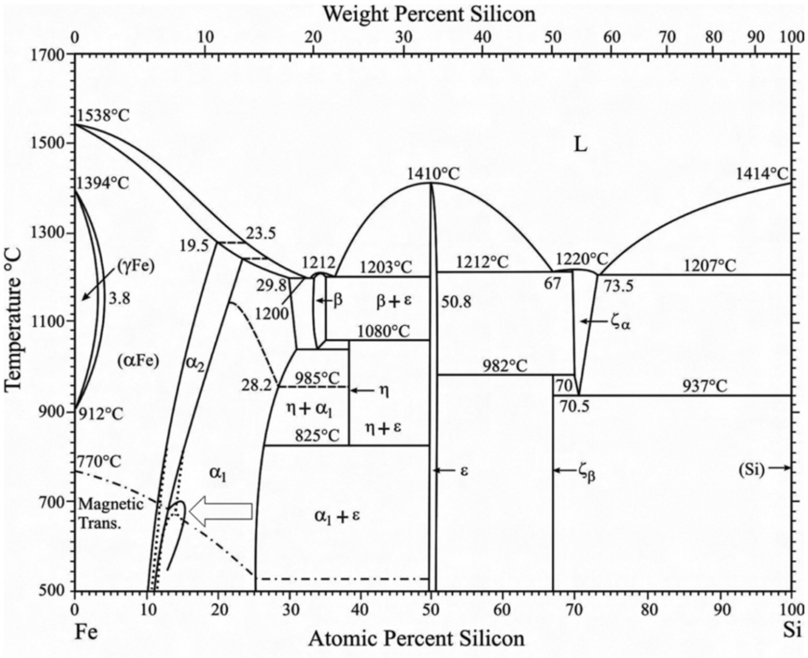

Figure 2.2: *A phase diagram for silicon in iron. Reprinted from [14].*

The components in an electrical machine may *age* causing an increase in core loss. Such ageing is caused by the precipitation of impurities [11]. Domain pinning was directly observed in a $LiTaO_3$ crystal with defects [16], demonstrating the mechanism by which such ageing degrades magnetic performance. In ultra low sulphur (less than 10ppm) silicon steels, nitride formation was reported to be accelerated with a decrease in sulphur during annealing [17]. This inhibited ferrite grain growth, the smaller grains and AlN present at the surface increased hysteresis loss. Copper rich precipitates were observed during ageing of material produced by strip casting [18], harming the magnetic properties but, due to precipitation hardening, improving the yield and tensile strengths as high as 630 MPa and 716 MPa respectively. Graphite formation is strongly promoted by high silicon content [19], therefore very low carbon content is required to maintain good magnetic properties and prevent significant ageing.

2.1.2 Crystallographic Texture

The atoms in many materials are arranged such that a highly ordered large scale repeating pattern is formed. In most circumstances the bulk material is a polycrystal, i.e. made of several crystals, also known as grains. Silicon steel is an example of such a polycrystalline material, arranged in a body centred cubic (BCC) structure. The orientation of the crystallographic lattice may have important implications on the properties of the material due to anisotropies arising quantum scale effects, explained further in Section 2.1.3.

A *crystallographic texture* arises when many grains are oriented in the same direction. Both Grain Oriented Electrical Steels (GOES) and Non-Grain Oriented Electrical Steels (NOES) are available, with the former exhibiting strong anisotropy due to the formation of Goss grains with preferred orientation $\{110\}\langle 001\rangle$, and the latter being isotropic in the plane of the sheet. The strip casting process has recently been developed as a rolling practice to manufacture thin sheets [20, 21, 22, 23]. This process of strip casting is particularly useful for GOES, as the initial casting and subsequent shearing due to the rollers helps nucleate the preferential (for GOES) texture known as the Goss texture immediately [20, 21]. The benefits of strip casting are also present when processing NOES, as the product is closer to its final dimension (and therefore requires less processing) than when using traditional rolling methods as described by Roberts [24] or Beckley [11], wherein discrete slabs are rolled. As Song et al. [20] notes this does increase the number of Goss nuclei; consequently care must be taken to ensure the magnetic properties of non-oriented product are indeed isotropic.

The cube texture is optimal for NOES steels [25] as opposed to the Goss texture in GOES. This is because in radial flux machines, the commercially dominant type, the flux will rotate about the sheet during the operation of the machine in which the lamination of electrical steel is placed.

Texture is typically measured using the *Texture Factor (TF)*, which provides a quantitative measure of the quality of the sheet in terms of the ratio of grains with the optimal alignment. The texture defined as follows [26] (as cited in [27]):

$$\mathrm{TF} = \frac{\text{volume fraction of } \{100\} \text{ planes}}{\text{volume fraction of } \{111\} \text{ planes}} \text{ on the sheet surface} \tag{2.1}$$

Some error is associated with this simplification though, and as such a different metric, the *Magnetic Texture Factor (MTF)* was developed to better capture the aggregate effect of crystals with some misorientation [28]. The MTF is defined as:

$$\mathrm{MTF} = \frac{\text{volume fraction of } \langle 100\rangle \text{ directions}}{\text{volume fraction of } \langle 111\rangle \text{ directions}} \text{ along the magnetisation vector} \tag{2.2}$$

The difference between the two equations highlights the fact that some misorientation from the ideal texture is acceptable, the magnetisation strength is simply decreased slightly. This distinction is relevant as it illustrates that the degradation of magnetic properties is gradual. The following sections will explore the magnetic properties in greater detail, and explain the causes of energy loss in electrical machines.

2.1.3 The magnetic characteristics of silicon steel

In the field of crystallography, directions and planes in relation to a crystal/lattice structure are typically denoted using Miller indices: in this notation planes are represented using brackets, (hkl); families of equivalent planes by $\{hkl\}$; directions by $[hkl]$; and families of directions by $\langle hkl \rangle$. The integer indices contained within the brackets are the reciprocals of the intercept that the plane makes with the lattice.

In ferromagnetic materials there exist directions which are easier and harder to magnetise. This *magnetocrystalline anisotropy* arises from quantum mechanical effects, primarily the spin-orbit interaction [29]. For example, the easy magnetism direction for iron is $\langle 100 \rangle$, and the hard direction $\langle 111 \rangle$ [30]. Figure 2.3 displays the planes which lay in these directions for a cubic crystal. The processing route of the material can affect the orientation of the crystallographic lattice across many grains, and if a preferred orientation is apparent (i.e. many crystals are aligned in the same direction) this is known as a texture. For rotating electrical machines the direction of the magnetic field will rotate, as such isotropic magnetic properties are desirable in the plane of rotation. Alternatively for non rotating electrical machines such as transformers, a texture can be purposely introduced in order to cause anisotropy - thereby reducing energy loss in the orientation that the material will encounter magnetic fields.

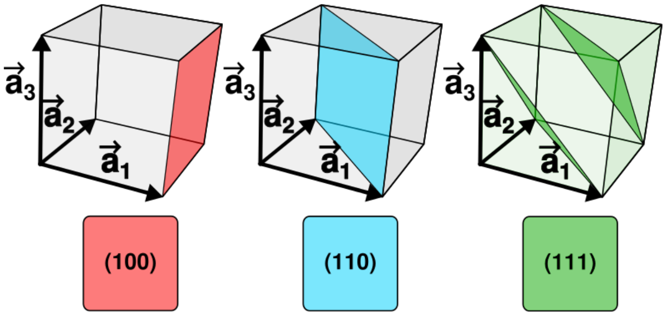

Figure 2.3: *Planes with varying Miller indices for a cubic crystal. Adapted from [31]*

Magnetic domains

Converse to most materials wherein the intrinsic magnetic moment of one electron is cancelled by another electron, ferromagnetic materials have unpaired electrons which are the principle source of magnetism. As outlined in the introductory paragraph, magnetic domains are spontaneously produced in ferromagnetic materials and are randomly aligned - consequently, the bulk material does not have a magnetic field. If all electrons were aligned into a single domain the magnetic field would extend outside the material, which is a higher energy state than that of a material with randomly aligned domains. The formation and size of domains is controlled by minimisation of energy according to the free energy equation [32]:

$$\mathscr{E} = \mathscr{E}_{ex} + \mathscr{E}_D + \mathscr{E}_\lambda + \mathscr{E}_k + \mathscr{E}_H \tag{2.3}$$

Where $\mathscr{E}_{\text{ex}}$ is the exchange energy, that is the energy due to the interaction between the spin of the electron and magnetic moment of the nucleus; $\mathscr{E}_D$, the magnetostatic interaction energy, associated with long range dipole interactions; $\mathscr{E}_\lambda$ magnetoelastic energy, the property which may be associated with magnetostriction; $\mathscr{E}_{\text{k}}$ is the magnetocrystalline anisotropy energy, due to the fact some directions of the crystal lattice are easier to magnetise than others; and finally $\mathscr{E}_{\text{H}}$ is the Zeeman energy, the energy due to the externally applied magnetic field. Understanding the physics of the domain formation can guide the search for optimal parameters for the magnetic performance in electrical machines; for example, controlling grain size or alloying elements will affect the overall energy balance. Figure 2.4 demonstrates the effect of forming domains on the magnetostatic energy, 2.4 (a) shows a material without domains, a large field must flow out of the block. In 2.4 (b) the material has split into two domains, this reduces the amount of flux that must flow outside of the material, finally 2.4 (c) shows a material with four domains, in which no flux must exit the block. It is important to consider that while $\mathscr{E}_{\text{m}}$ will decrease, the other energies may well increase to accommodate this, but the net energy will be lower.

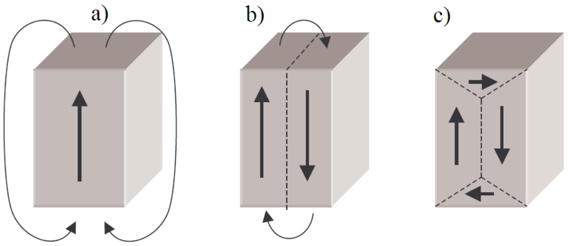

Figure 2.4: *A magnetic material divided into domains means the field does not have to flow out of the material as severely, thus decreasing the magnetostatic energy.*

Domains walls are the transition region between two well aligned domains, and as shown in Figure 2.5 may be of either the Bloch or Néel type. A Bloch wall is a transition of magnetisation in plane, whereas a Néel wall is a transition out of plane. Bloch walls are the typical domain wall in bulk ferromagnetic materials, and are where the majority of changes in magnetisation occur [33]. In silicon steel the domain wall size is 179 nm or less, dependent on the relative orientation of the two domains [34]. In an applied magnetic field the domain walls move to minimise their energy with respect to the field; the walls may be pinned by defects in the crystal such as inclusions, dislocations, surface defects (i.e. roughness) [35]. This domain wall movement is the key feature for soft magnetic materials, with lower energy wall movement causing lower coercivity. Once the applied magnetic field has aligned the majority of the available spins the material becomes saturated; when saturated, the application of a stronger magnetic field to the material will hardly increase the induced magnetic field.

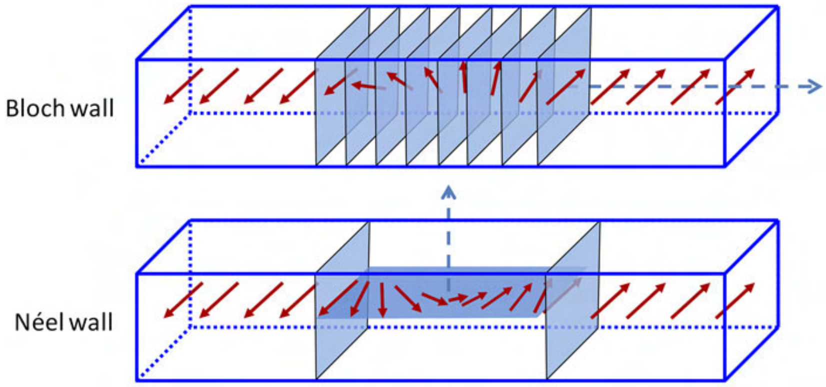

Figure 2.5: *The transition between two domains by Bloch and Néel domain walls. The dashed line indicates the axis of rotation of magnetisation. Figure courtesy of Bhatia et al. [36]*

2.1.4 Energy loss in electrical machines

Many factors effect the magnetic properties of the material, and consequently the energy loss which is dissipated as heat and noise. Energy loss can largely be divided into hysteresis loss and eddy current loss, with so called excess loss accounting for all other minor energy loss. Hysteresis loss is that caused by the doing work on the magnetic domains to physically realign them. Eddy loss is caused by resistive heating in the conductive material due to induced eddy currents. Grain size, residual stress [27, 26, 37], and even external mechanical stresses [38] can have great impact. It is widely accepted that the optimal grain size is around 150 µm [39, 40], larger grain sizes in essence mean a more perfect crystal is formed, meaning fewer accommodation domains (at boundaries) [40]. However, above the optimum grain size other losses occur due to the increasing formation of eddy-currents in larger diameter grains [37] which is proportional to the square of the wall velocity. Optimum grain size is application dependent, at higher frequencies (e.g. 1000 Hz) smaller grains provide equal performance to larger ones [41] because the proportion of excess loss to hysteresis loss changes. Figure 2.6 shows the variation of length scales over which the magnetic force acts - it is shown that domains do not traverse grain boundaries, but a grain may contain multiple domains. Consequently, for certain applications where the frequency is high, the size of the crystal is less important due to the effect of domain wall movement in the crystal increasing the formation of eddy currents.

As a conductor moves through a magnetic field a current is induced in it, this current induces its own magnetic field that acts to oppose the original field. This phenomena is known as Lenz's law, and can be described by Faraday's law of induction, Equation 2.4:

$$\mathcal{E} = -\frac{dB}{dt} \tag{2.4}$$

Where dB is the rate of change of magnetic flux, dt is the change in time, and $\mathcal{E}$ is the induced electromotive force. Note that due to Lenz's law ${}^{d\Phi_B}/_{dt}$ is preceded by a negative sign. In order to further improve motor cores, instead of simply machining or casting a solid block, many thin laminations are used in order to reduce eddy currents. Thinner laminations reduce eddy currents due to the smaller area over which the magnetic field acts, as described

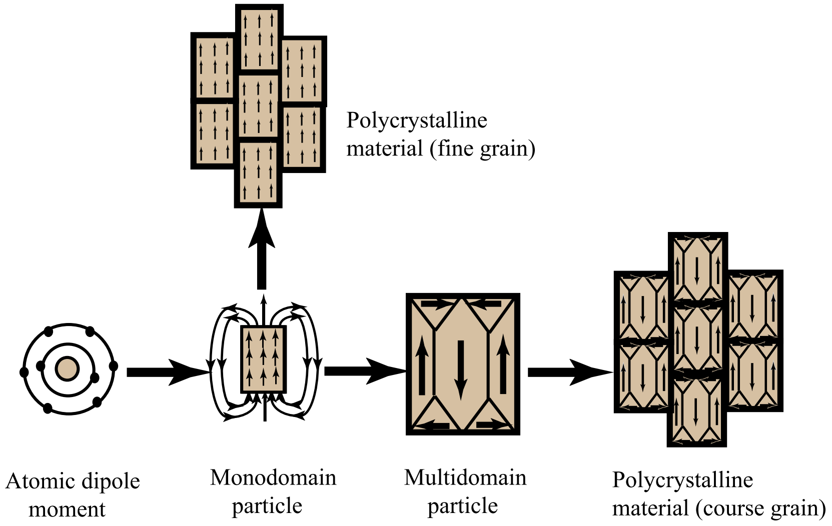

Figure 2.6: *The hierarchy of magnetic length scales, silicon steel is a coarse grain polycrystalline multi-domain material. Figure reprinted from [15] with permission from Elsevier*

by Equation 2.5 [42, 43].

$$P = \frac{\pi^2 B_p^2 d^2 f^2}{6\delta\rho} \tag{2.5}$$

Where ρ is the resistivity, δ the density, d the thickness of the lamination, B_p the peak magnetic flux density, and f the frequency of the driving AC cycle. The thickness of the lamination makes a significant difference in eddy current formation and consequent losses, for the same material and magnetic induction, and is the one factor which can be controlled.

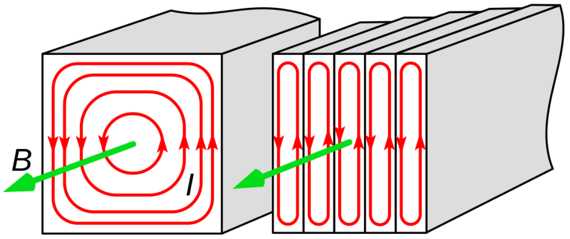

Figure 2.7: *An illustration of the induced eddy currents, I in a solid material in comparison to a laminated stack. The applied magnetic field, B, is displayed as a green arrow. The laminations are electrically insulated from each other so each eddy current must flow independently.*

This section has described the energy losses in electrical machines, and explained the reason for these losses. The microstructure has been shown to have a large influence on the loss, but it has also been noted that the formation of eddy currents - a major loss component - can also be reduced by the decrease of thickness of the lamination. The manufacturing processes to achieve such thin laminations and the influences of these processes are explored further in the next section.

2.2 The manufacture of electrical machine components

Electrical machine components are manufactured from stacked laminations, for the reasons discussed in Section 2.1.4. Thin sheets are produced by continuous casting - the molten material is poured into a water jacketed mould which solidifies a thin shell around a molten core. This semi solid material is immediately fed into another mould comprised of several roller elements. The thickness of the material is reduced in bulk by hot rolling, i.e. rolling above the recrystallization temperature. Upon approaching the final thickness the material is cold rolled (below the recrystallization temperature), which allows better control of surface finish and final dimension [11, 24]. The result of these combined processes is a thin, uniform strip of electrical steel with a thickness on the order of tenths of millimetres and width of a few meters [11]. The laminations are then cut into the potentially quite complex geometries required; for example, in the case of synchronous reluctance motors with thin bridges retaining permanent magnets, the demand is high on the magnetic and mechanical properties - requiring a material with both low loss and high strength. Several methods to cut these geometries are available; waterjet cutting, electrical discharge machining (EDM) and blanking among them. Commercially, blanking is the preferred method due to its high throughput. Blanking introduces damage to the material at the cut edge, which reduces the magnetic performance of the material. This concept is explored further in the following section, and is critical to the reduction of iron loss in electrical machines

2.2.1 Rolling and strip casting

Though grain size differs between surface an mid layers, the difference reduces as the sheet thickness is reduced [44]. At the same temperature, grain growth is inhibited by smaller thicknesses [41]. Strip casting has been shown to be commercially viable for production of non-oriented silicon steel with balanced magnetic and mechanical properties, (with/and) products with high magnetic saturation values of up to 1.709 T being achievable in 0.2 mm thick sheet [18]. This high induction was possible due to optimisation between grain size and thickness, with grains of 190 µm being produced in this process. A high induction is desirable in this application because a greater torque can be generated in motors using higher induction values. By tuning the ageing process and growing copper rich precipitates an increase in yield strength of greater than 100 MPa was achieved. Nozawa et al. [35] showed that chemically polishing silicon steel laminations can decrease losses by removing the forsterite (Mg_2SiO_4) on the sheet surface, as this removes the domain pinning effect caused by the interface of the materials. Surface loss was further decreased by laser etching the surface, thereby increasing the number of effective domain walls.

Mo et al. [45] reported improved plasticity with a *warm* rolling process at 500 °C in 6.5wt% Fe-Si, and hot compression at temperatures of 650-950°C allowed optimum reductions of 0.7 (true strain) [46]. Despite these advances, lower silicon contents are preferred in industrial application to allow cold rolling.

2.2.2 Blanking

Blanking is the commercially preferred method for cutting the laminations into the required geometry for use in electrical machines. A punch and die of the required shape are manufactured from high strength steels. Parts may be blanked in one step, or in several incremental steps. Four distinct stages are present in blanking, upon contact with the work the punch begins to induce plastic deformation into the part, leading to the rollover or indentation zone seen in the final product. As the punch continues the material shears, producing a high quality edge known as the shear or burnish zone. After a certain penetration the material becomes very thin and cracks form leading to fracture, producing a rough area known as the fracture zone. For best surface finish cracks formed at the top and bottom of the work must meet, typically this occurs at an angle of between 7° and 11° [47]. A burr may be produced on the bottom face of the part as material is plastically deformed further by the punch continuing its movement. The zones are shown diagrammatically in Figure 2.8.

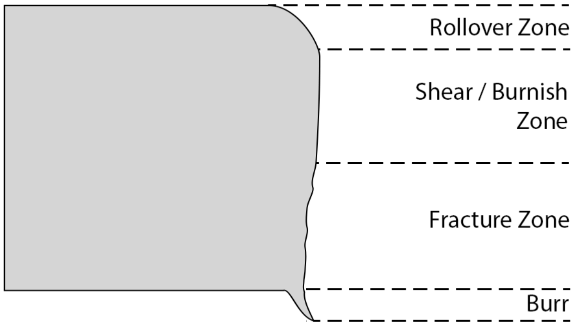

Figure 2.8: *A diagram showing the different zones of the edge of a blanked part.*

Clearance

A large factor in the quality of the cut edge is the clearance between the punch and die. In conventional blanking a typical clearance is between 2-10% of the thickness of the sheet [48, 47]. A 2% Si content electrical steel used nanoindentation to measure the residual stress due to the punching process, additionally observing the magnetic domains at the punched edge, noting wider domains at the edge (3-8µm) which decreased upon annealing (1-3µm) [49]. Varying the punch-die clearance not only affects the final product, but as demonstrated by Subramonian et al. [50] has significant effects on the life of the tool itself, because non uniform punch stress can cause non uniform wear. Accounting for this non uniformity the authors were able to produce a variable clearance tool which improved tool life. It is also found that the stress on the punch decreases exponentially with an increased punch radius, and that the optimal combination of variables is dependent on both the material and the thickness; however doing so increases the size of the rollover and fracture zones. Hambli [51] recommended that in order to minimise the blanking force clearance should be set to 10% of the sheet thickness, but minimising fracture angle required a clearance of 5%. Additionally variable clearance was found to produce more uniform wear leading to significantly longer tool life [50], and vibrations of the stripper plate apply lateral forces to the punch, possibly influencing tool life [52].

Weiss et al. [53] showed that as the ultimate tensile strength of the material increases its sensitivity to blanking parameters in terms of magnetic performance increases, and that specific loss could be reduced by minimising residual stresses by reducing cutting clearance. A further study demonstrated increased specific loss as a result of increased cutting line length, and increased tool wear [4]. Ghadbeigi et al. [2] showed cut edge deformation was highly influenced by individual grains, namely hardness increased toward the cut edge and was highly correlated with geometrically necessary dislocations. Other studies [54, 55] similarly found increased hardness toward the cut edge in electrical steels, with the magnetic deterioration dependent on the area of increased hardness.

Blanking is considered a shear dominated process, so literature on similar shear cutting processes is also of interest. A study of shear slitting on ET122-30 showed many parameters were important, with variables such as the rake angle of the knives, clearance, cutting speed, etc. affected the burnished and plastically deformed areas, residual stresses and consequently magnetic properties [56]. Ultimately this process shares many of the same parameters - particularly clearance - which have the same effect in both cases.

Blanking speed

Another important factor in the manufacture of blanked parts is the speed at which the punch penetrates the part. This is significant not just economically - where a faster cycle time increases the throughput of parts - but also in terms of the quality of the part and the influence on the wear of the tools.

Zakariya and Mahardika [57] reported increased shear zone area with increased punch velocity in copper. Kurniawan et al. [58] reported the same effect in titanium, additionally noting that the blanking force increased with increased punch velocity, but with a decreasing trend. Other studies have simulated high speed blanking, the authors highlighting the importance of including temperature dependence [52, 59].

Demmel et al. [60] introduced a method to measure the heat generated during blanking at the cut edge by using the punch and work as components of a thermocouple.This technique demonstrates that maximum temperature increases when punch velocity is increased; for example, the peak temperature rose to over 3 times (as high as 275 °C) when punch velocity was increased by 9.4 times. As clearance increased the effect of the velocity of the temperature was decreased, but still present. Higher temperatures are known to reduce yield stress by promoting dislocation motion. This effect was reported in the fine blanking of complex geometry in Q235B steel where the increase in temperature decreased flow stress, thus improving cut edge quality and reducing punch force without inducing a phase change. The punch force has been shown to be significantly affected by the punch velocity in electrical steels [2]. Contrary to potential expectations, high punch forces are found at lower punch velocities, which may be caused by the low number of grains through the thickness of the material where most deformation occurs in one grain only.

Effect of blanking on the material properties

Gürbüz et al. [61] showed some losses introduced by residual stresses in blanked electrical steel parts were somewhat offset by an applied tensile stress, and made worse by an applied compressive stress. The importance of this effect becomes relevant when considering that motors may be manufactured in such a way that subjects laminations to compressive stress; additionally, the rotor will experience tensile stress due to centrifugal force when in service. Compressive stress of less than $-50\,\mathrm{MPa}$ was shown to significantly increase both hysteresis and eddy current losses and furthermore even in non-oriented steel there exists anisotropy in the degree of these losses [62]. Some reduction of losses can be achieved by applying a small tensile stress of less than 50 MPa [63]. Additional induced anisotropy is an important factor to consider with any motor design, to ensure even torque throughout the travel of the rotor.

Ultra high strength steels (UHSS) have limited ductility, much like silicon steels; a study of JSC1190Y UHSS found a small radius improved the quality of the punched part by preventing cracks forming and increasing the burnished area [64]. The quality of the blanked part can be measured in situ to assess tool wear; Lorenz et al. [65] developed an online optical monitoring system capable of measuring the burnish height of material of 0.5-1mm at a production speed of 250 strokes per minute (SPM), opening the possibility of more data driven models. Kubik et al. [66] presented a method for the analysis of tool wear in industrial settings at 300 SPM using a variety of sensors, particularly piezoelectric transducers, which are used in conjunction with artificial intelligence techniques such as a multi-class state vector machine. This technique did however show sensitivity to the location of the sensors, and the authors note that the model is inherently enriched with information about the press upon which it was trained, possibly limiting the larger applicability.

The orientation of the sheet in the blanking apparatus was shown to have negligible impact on the texture evolution [67], as the formation of shear bands was the primary deformation mechanism resulting in formation of 110 fibres.

Teng et al. [68] investigated the effect of concave punch geometry in micro blanking of 0.1 mm stainless steel. In comparison to a flat punch geometry, the maximum punch force was reduced and the burnished area was greater, however the blanked part did experience some plastic deformation causing a bowing out of the normal direction plane.

In comparison with conventional blanking, *fine blanking* uses reduced clearances (as low is 0.5-1.2% of the thickness of the sheet) and counter forces in order to improve cut quality [69]. Liu et al. [70] presented a fine blanking process with the addition of ultrasonic vibration on the punch, which significantly reduced roll-over. In copper foil, the addition of ultrasonic vibration of frequency 36.1 kHz and amplitude 1.66 µm resulted in an increase in the size of the burnished area for both small (7.3 µm) and large (48.4 µm) grained samples [71]. The authors attributed the reduced surface roughness and delayed crack onset to the polishing effect of the punch due to the vibration.

2.3 Strain measurement using DIC

Digital image correlation is a full-field non-contact strain measurement technique. A reference image is compared to several deformed images, and the displacements are calculated. After the displacements have been obtained derived quantities of interest are available, such as strain. To achieve the comparison between reference and deformed images, division into small areas known as subsets is required. Each subset is then compared, and a correlation coefficient is assigned between an initial guess for the subset in the reference and deformed conditions which is iteratively refined to maximise the correlation.

Typical correlation criteria include [73, 74, 75]:

$$C_{cc} = \frac{\sum_{(i,j)\in S}\left(f\left(\tilde{x}_{ref_i}\widetilde{y}_{ref_j}\right)-f_m\right)\left(g\left(\tilde{x}_{cur_i},\widetilde{y}_{cur_j}\right)-g_m\right)}{\sqrt{\sum_{(i,j)\in S}\left[f\left(\tilde{x}_{ref_i},\widetilde{y}_{ref_j}\right)-f_m\right]^2\sum_{(i,j)\in S}\left[g\left(\tilde{x}_{cur_i},\widetilde{y}_{cur_j}\right)-g_m\right]^2}} \tag{2.6}$$

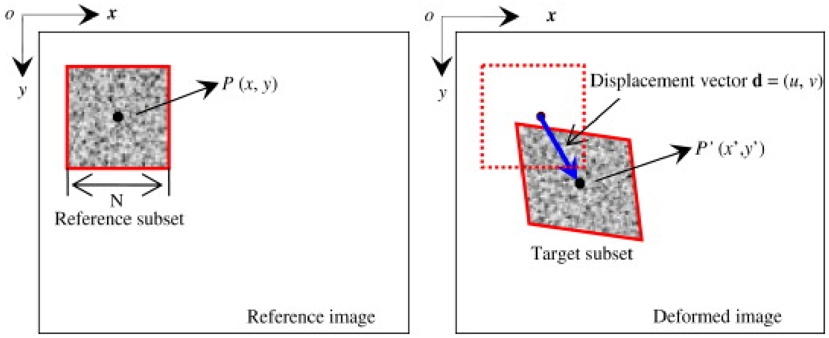

Figure 2.9: *A square reference subset is deformed to match the defomration of the image in the deformed configuration. The displacement vector is directly obtained from the difference of the centroids of the two subset configurations. Figure reprinted from [72] with permission from Elsevier*

Where f and g are the grayscale intensity in the reference and current configurations. And f_m and g_m are defined as:

$$f_m = \frac{\sum_{(i,j)\in S} f\left(\widetilde{x}_{ref_i}, \widetilde{y}_{ref_j}\right)}{n(S)} \qquad (2.7) \qquad\qquad g_m = \frac{\sum_{(i,j)\in S} g\left(\widetilde{x}_{cur_i}, \widetilde{y}_{cur_j}\right)}{n(S)} \qquad (2.8)$$

Where $n(S)$ is the number of points in the subset. After the initial guess the least squares criteria is then minimised [73, 74, 75, 76]

$$C_{LS} = \sum_{(i,j)\in S} \left[\frac{f\left(\widetilde{x}_{ref_i}\widetilde{y}_{ref_j}\right) - f_m}{\sqrt{\sum_{(i,j)\in S}\left[g\left(\widetilde{x}_{ref_i}, \tilde{y}_{ref_j}\right) - f_m\right]^2}} - \frac{g\left(\widetilde{x}_{cur_i}, \widetilde{y}_{cur_j}\right) - g_m}{\sqrt{\sum_{(i,j)\in S}\left[g\left(\widetilde{x}_{cur_i}, \widetilde{y}_{cur_j}\right) - g_m\right]^2}} \right]^2 . \tag{2.9}$$

The exact implementation is of course application specific; in this thesis DaVis 10.2 was used which applies the algorithms found in [75]. The correlation criteria is essentially a measure of how similar two subsets are, and the goal may be to maximise or minimise depending on the exact criteria, for the aforementioned examples C_{CC} is maximised while C_{LS} is minimised.

There are several sources of error in DIC measurements, random and systematic. Random (variance) errors result from image sensor noise and correlation error, whereas systematic (bias) errors arise from various sources such as lens distortions or out of plane motion in 2D DIC [77]. Because the strain is calculated by differentiation of the displacement field it is much more sensitive to noise [73], and as such a trade-off is present between noise and the bias introduced by smoothing of the strain field due to large subset size (or other parameters similarly acting as a low pass filter).

Some systemic errors are possible and simple to correct, for example radial distortion, for which a variety of models are available to assist - such as that presented by Pan et al. [78].

An alternative full-field non-contact optical method to DIC was introduced by Hartmann et al. [79], where a spatio-temporal optical flow technique was developed. This work allowed further derivatives of the strain to be easily obtained, these derivatives contain information on, for example, shear band geometry and internal lengths arising from grain size. In recent years artificial neural networks have been introduced for strain measurement [80, 81]. Yang et al. [81] introduced the *DeepDIC* approach consisting of two independent networks calculating displacement and strain separately - as the strain was calculated directly from the image and was not a derived quantity, the strain predictions were robust and outperformed commercial DIC software in terms of average error. Furthermore the full field data is obtained in milliseconds per frame, and being significantly computationally cheaper in inference than traditional DIC algorithms, there is a very real possibility that this technology will become the industry standard in the coming years.

2.3.1 Speckle quality analysis

User defined parameters such as subset size are critical to result quality and are strongly linked to the surface pattern. A number of metrics have been developed for quantitatively assessing surface patterns in recent years, including the Shannon entropy; sum of square of subset intensity gradient (SSSIG); mean intensity gradient; and various other methods that are more self-evident such as speckle size, distribution, and number. Various studies have also addressed the use of DIC with non optimal patterns when investigating materials under difficult circumstances - e.g. very high magnification - in these cases the natural surface of the material is often used.

An early quality assessment method was introduced by Lecompte et al. [82] in which the mean speckle size is considered, the binarised image is used to detect speckles, and a histogram of the speckle sizes is produced. A tight distribution (high and narrow peak) on the histogram was indicative of a better quality pattern.

Speckle quality has been measured using entropy in various forms, Yaofeng and Pang [83] investigated the coupled relation between subset size and speckle quality by introducing subset entropy, defined in Equation 2.10.

$$H = \frac{\sum_{P \in S} \sum_{i=1}^{8} \mid I_P - I_i \mid}{2^{\beta} M N} \tag{2.10}$$

Where H is subset entropy, P is a pixel in the subset S, M and N are the dimensions of the subset, I_P is the intensity of pixel P, I_i is the intensity of a neighbouring pixel, and β is the bit depth of the image. By comparing the pixel intensity of the eight neighbours at each pixel the measure has an increased geometric 'awareness', arguably being more valid in the two dimension case than the simple application of Shannon entropy by flattening the image to one dimension. This metric still lacks larger scale geometric information.

In an attempt to overcome issues in other criteria Su et al. [84] proposed a measure based upon the root mean square error of DIC, considering both systematic and random error. In this work the authors noted the choice of optimal correlation criterion is dependent upon the image quality - cross correlation (CC) was found to be preferable in noisy images due to its elimination of noise induced bias, whereas in ideal images the sum of squared differences (SSD) could perform better.

The sum of the square of subset intensity gradients (SSSIG) was introduced by Pan et al. [85], as this is a measure is based upon the SSD but also related to the subset entropy measure. A higher SSSIG parameter indicates a better speckle pattern, this measure is influenced by the size of the subset, and as such the authors presented an iterative algorithm to automatically select subset size based on a threshold of the SSSIG parameter. Similarly, the mean intensity gradient is a metric based on the same principles, but for use in estimating the pattern quality globally rather than on a per-subset basis. There are other gradient/difference-based parameters available, such as the mean subset fluctuation [86]; derived from other methods, this parameter global quality essentially by averaging the quality values over every subset.

Crammond et al. [87] compared several of the aforementioned measures, noting that global measures were not sufficient to judge speckle quality by themselves. The authors also discussed the use of Laplacian of Gaussian edge detection, which is able to overcome some issues with more basic edge detection in threshold images for the more simple metrics such as speckle size and number.

2.4 Finite element modelling

Finite element modelling can be applied to the blanking process to predict important factors in both machine design and final product quality, such as the punch force or burr formation respectively. There are many constitutive models available to predict the flow, damage and fracture of various metallic materials under various conditions. In this section a brief background on the relevant concepts from continuum mechanics forming the basis of many models are discussed, followed by a review of a number of relevant models to the blanking process.

2.4.1 Solid mechanics

To understand the various models discussed in this section, let us first discuss some important concepts common to any model. Plastic flow in metals at room temperature is primarily realised though dislocation motion in the crystal lattice - this motion occurs along slip planes, with the slip direction in the closed packed crystallographic planes. This slip is shear deformation, thus neither the crystallographic structure or volume of the crystal are changed. Consequently the hydrostatic stress has no effect on plastic flow, as it is the average of the normal stress components of the stress tensor. The hydrostatic stress is defined as:

$$\sigma_{\mathrm{Hyd}} = \frac{\sigma_{11} + \sigma_{22} + \sigma_{33}}{3} \tag{2.11}$$

Where σ_{ij} is the direction of the stress. Stress which does cause plastic deformation is known as the deviatoric stress and is defined as:

$$\boldsymbol{S} = \sigma - \sigma_{\mathrm{Hyd}} \tag{2.12}$$

The ratio between the hydrostatic and deviatoric stresses is known as the stress triaxiality, η, and is defined as:

$$\eta = \frac{-\sigma_{\mathrm{Hyd}}}{\boldsymbol{S}} = \frac{-p}{q} \tag{2.13}$$

Another commonly referenced quantity in the literature is the Lode angle, θ, which is related to the third deviatoric stress invariant, J, by [88]:

$$J = \left(\frac{r}{q}\right)^3 = \cos(3\theta) \tag{2.14}$$

Which may be normalised to the range of $-1 \leq \bar{\theta} \leq 1$ via:

$$\bar{\theta} = 1 - \frac{6\theta}{\pi} = 1 - \frac{2}{\pi}\arccos\xi \tag{2.15}$$

Figure 2.10 shows a representation of the stress state of a material element in the Haigh-Westergaard space, in which the principal stresses are the axes. In this figure it is clear that the hydrostatic axis is where all principal stresses are equal, $\sigma_1 = \sigma_2 = \sigma_3$, the angle between the projection to a principal stress and the stress state is the lode angle, θ. The Cauchy stress tensor is not shown, but would be represented in this visualisation by a vector from the origin to the point P.

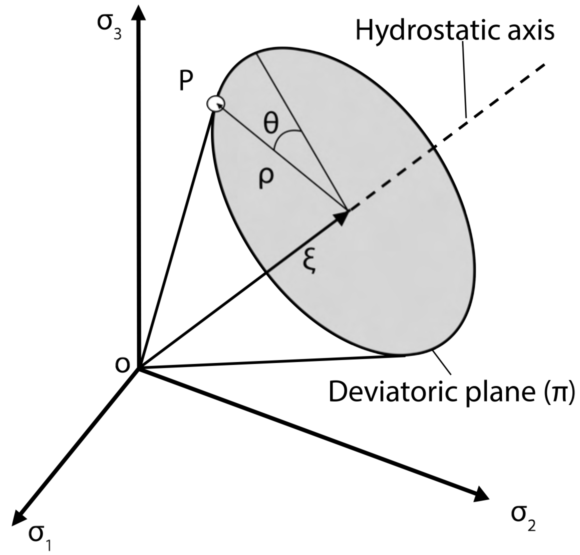

Figure 2.10: *The visualisation of stress state in the Haigh-Westergaard space. P is the stress state of a material element, ξ is the hydrostatic stress, ρ is the deviatoric stress, θ is the Lode angle. Figure reproduced from [89] with permission from Elsevier*

2.4.2 Plasticity modelling

Johnson-Cook Plasticity

The phenomenological Johnson-Cook model is relatively simple and requires few experiments for calibration, leading to its popularity. The flow stress is defined as:

$$\sigma_y\left(\varepsilon_{\mathrm{p}}, \dot{\varepsilon}_{\mathrm{p}}, T\right) = \left[A + B\left(\varepsilon_{\mathrm{p}}\right)^n\right]\left[1 + C\ln\left(\dot{\varepsilon}_{\mathrm{p}}^*\right)\right]\left[1 - \left(T^*\right)^m\right] \tag{2.16}$$

Where the flow stress is a function of the equivalent plastic strain ε_{p}, plastic strain rate ($\dot{\varepsilon}_{\mathrm{p}}$ and five material parameters that can easily be experimentally fit, A, B, C, n, m. These parameters can be found easily as they are not interdependent - one can find the first, A, B, and n in one experiment via simple tensile tests. The following, C, can be found in another experiment that modifies only the strain rate, and the last m by modifying only the temperature.

In this equation the asterisk indicates the strain rate and temperature are normalised, this is achieved in the following way:

$$\dot{\varepsilon}^{*} = \frac{\dot{\varepsilon}}{\dot{\varepsilon}_{\text{ref}}} \tag{2.17}$$

Where $\dot{\varepsilon}_{\text{ref}}$ is the strain rate of a quasi static tensile test, used as a reference strain rate and which is the strain rate of the test which determined the constants of the first term of the equation (i.e. A, B, n).

$$T^{*} = \frac{(T - T_0)}{(T_m - T_{\text{ref}})} \tag{2.18}$$

Where T_m is the melting temperature and T_{ref} is a reference temperature, the temperature of the test which determined the constants of the first term.

The Johnson-Cook model is applicable to high strain rate applications.

An implementation using an implicit radial return algorithm as opposed to the more common forward Euler implementation is described by Ming et al. [90]. This implementation improved the precision of results in comparison to implementations wherein the plastic strain rate is directly obtained.

A modified form of the Johnson-Cook model was developed to increase strain rate sensitivity [91], which allowed better experimental agreement over a wider range of strain rates for a number of materials. This modified model was used to investigate cold drawing of SWRH82B steel, and again the model was able to more closely the flow curves from split hopkinson bar tests.

Other plasticity models

The Sellars-Tegart model was used to predict flow and defect evolution in hot rolling of 3wt% Si electrical steel [92], finding buckling of defect side walls and consequent surface defects were dependent on reduction and the aspect ratio of the defect. This study did not include damage softening effects and used a relatively simple frictional model (Coulomb and stick-slip friction) - nevertheless good experimental agreement was achieved. As noted in the paper and in work by Brown and Kn [93] 90% of frictional work in Si steels is assumed to be converted to heat. As such, the friction between work and die in the blanking process can be justified to use the same frictional model.

Another model which is dependent upon the strain, temperature and strain rate is the Perzyna equation [94]:

$$\sigma_y = \left[1 + \left(\frac{\dot{\bar{\varepsilon}}^{\text{pl}}}{\gamma(\text{T})}\right)^{m(\text{T})}\right] \sigma_0\left(\varepsilon^{\text{pl}}, \text{T}\right) \tag{2.19}$$

Where $\dot{\bar{\varepsilon}}^{\text{pl}}$ is the equivalent plastic strain rate, γ is the material viscosity parameter, m the strain rate hardening constant, and σ_0 the static subsequent yield stress. Again this model is suited to blanking due to the large range of strain, strain rate and temperature experienced by the material during the blanking process [94]. It is however unstable and tends to have convergence problems at very low m values [95]. An alternative to this formulation is the

Peirce equation in which the power term is moved; though this mitigates the issue somewhat, it does not eliminate it at very low values [95].

Bai and Wierzbicki [96] showed that the effect of stress state was highly influential on plasticity in Al 2024-T351. A model including the effects of the stress triaxiality and lode angle was developed, with the large difference between uncorrected and (stress state) corrected results in flat grooved specimens being of particular interest. Without correction for stress state effects an over prediction of force of almost 20 kN was observed, which was eliminated with the applied corrections. It is important to note not every material is sensitive to stress state, the authors give two examples of 1045 and DH36 steels which are independent of hydrostatic stress and lode angle respectively.

The plastic incompressibility assumption is neglected in the Bai-Wierzbicki model, Dong and Jia [97] proposed an adjusted model with Lode angle dependence for structural steel - particularly under shear dominated loading, where significant effect on yield stress was observed. The model addresses the complex calibration and high number of parameters required in alternative models, and the post necking behaviour issues. The high number of parameters required for calibration lead to complexities that the Dong and Jia model simplified by neglecting the hydrostatic stress, on the basis that it has relatively small impact on the yield. This simplification also restores the assumption of plastic incompressibility. The post necking behaviour was also addressed by noting that the conventional logarithmic stress and strain values are not applicable due to the complex triaxial stress state present upon necking. As such, a post-necking modification was applied to the calibration values.

Microstructural Evolution

Yield begins when the shear stress on a slip system reaches what is known as the *critical resolved shear stress* (CRSS). Kheradmand et al. [98] used micropillars in 3% Si electrical steel to show crystallographic orientation dependency of critical resolved shear stress, noting non-glide stress components are also required to accurately describe the deformation. A similar method coupled with nanoindentation and orientation methods was demonstrated to allow rapid identification of slip systems [99].

Hill and Hutchinson [100] found texture development as a result of plastic deformation changes the shape of yield loci, meaning that material hardening is not isotropic. Eyckens et al. [101] states that even for proportional loading isotropic models are at best an approximation, further stating that the Bauschinger effect (where the yield locus is translated, meaning following tension for example, the compressive yield point will be lower than the same material that has not been under tension) is not captured by isotropic hardening models.

The Viscoplastic Self-Consistent (VPSC) model treats individual grains in a polycrystal as ellipsoidal inclusions in an otherwise *homogeneous effective medium* (HEM) [102]. The model's constitutive equation for a single grain is given by:

$$\dot{\varepsilon}^{g} = \sum_{s=1}^{N} \mathbf{m}^{s} \dot{\gamma}^{s,g} = \dot{\gamma}_0^{g} \sum_{s=1}^{N} \mathbf{m}^{s} \left(\frac{|\mathbf{m}^{s} : \boldsymbol{\sigma}^{g}|}{\tau^{s}} \right)^{n} \operatorname{sgn}\left(\mathbf{m}^{s} : \boldsymbol{\sigma}^{g}\right) \tag{2.20}$$

where $\mathbf{m}$ is the Schmid tensor (essentially describing the slip systems of the crystal), $\dot{\gamma}$ the shear rate, $\dot{\gamma}_0$ a normalisation factor, τ is the critical resolved shear stress, g the grain, s

the slip system, N the total number of slip systems, and n the flow rule exponent.

Takajo et al. [102] used a VPSC model to predict the texture evolution of an ultra low carbon steel at various reductions, finding that plastic stiffness between grains became more uniform with high deformations (as in the Taylor model), but intermediate deformations required a variable inclusion-medium interaction model to precisely predict texture. Furthermore neighbouring grains were found to influence each other by modifying the texture evolution [102] meaning slower texture development and a more spread texture - which agreed better with experiments than other models (e.g. Taylor).

Dong and Shin [103] used a dislocation based constitutive model which employed probabilistic cellular automata to predict microstructural evolution in the rolling process [103]. This approach produced predictions that agreed well under tensile loading and multi-pass cold rolling. Dong and Shin'smodel was used in multiphase steel, and was used to predict evolution in the phases, as is non oriented electrical steel. Similar to other works mentioned later, the grain orientation is random at the beginning of the simulation - though appropriate for the modelling of a single pass, it obviously cannot accurately model the evolution of a texture in multiple passes. This effect cannot be effectively "cancelled" by annealing, as work by Song et al. [21] has shown secondary recrystallisation produces large Goss grains (and a strong Goss texture) due to the lower surface energy of $\{110\}$ planes [104] and the formation of dense shear bands after cold rolling (which is not seen in hot rolling) [21]. Takajo et al. notes texture evolution can be accurately predicted in some cases without the use of CPFE [105, 102].

Research on artificial neural networks has allowed fantastic progress in many fields which is now beginning to be applied to the field of computational mechanics. Unterberg et al. [106] introduced a convolutional neural network to analyse the material properties in the blanking process, using data from Magnetic Barkhausen Noise (MBN). It illustrated the possibility to identify blanked parts as being from the beginning, middle, or end of a coil via the MBN signal. Such complex signal processing may allow insights into the magnetic performance by being coupled with further models in the near future, and demonstrates the effect of subtle microstructural changes on the magnetic properties.

Size effect

The *size effect* is a well known complication in the modelling and manufacturing of various materials. When the grain size is a significant proportion of the overall size of the part the mechanical behaviour may be significantly impacted; the grain size, orientation and shape all have effects on the flow stress and morphological evolution [107]. The flow state decreases as the proportion of the surface grains increase - this is due to dislocation pile up at the grain boundaries, which is not possible at the surface. The size effect has been shown to be important in blanking; Xu et al. [108] investigated brass foils of 100 µm with grains of either 8.2 µm or 55.6 µm and found that the coarse grained specimen showed a much greater variation in maximum blanking force. Additionally, the ratio between clearance and grain size was shown to be a main factor in determining the deformation behaviour, and that when this ratio is equal to 1 the ultimate shearing strength reaches a maximum.

Voronoi tessellation has been applied to model both microstructure and size effects. The hierarchical structure of a martensitic steel was investigated, prior austenite grains were generated as Voronoi cells allowing verification of a modified Hall-Petch relation due to sub grain features [109]. Han et al. [110] used a 3D Voronoi model and CPFE to simulate micro-tensile tests of copper; it was shown that the flow stress was significantly affected by the grain size for the same diameter sample, decreasing with larger grain size. The diameter of the samples tested ranged between 0.2 mm and 1.5 mm, and it was found that increasing the diameter of the sample increased the flow stress. This result can be explained by proportionally fewer surface grains and more internal grains, as surface grains may more readily deform. Earlier work by Zhang et al. [111] used a similar technique, showing that macroscopic flow was possible through the collective basal-slip only. The authors also note the highly non-linear morphological evolution due to the size effect. Gai et al. [112] used a two scale technique to model damage in composites; in essence upon damage the macroscopic model's elements were subdivided using Voronoi cells. This approach allowed simulation of complex cracking behaviour in a computationally efficient manner, and by using Voronoi cells, inclusions were modelled in a more realistic manner.

Clearly, the influence of the size effect may be important in the simulation of blanking for silicon steel, due to its large average grain diameter of 150 µm in relation to the thickness of 0.2 mm. Voronoi tessellation is a good candidate for the generation of grain geometry, and has been widely applied in the literature already using CPFE models.

2.4.3 Damage and fracture models

Failure in ductile materials can generally be divided into void initialisation, growth and coalescence, and shear band localisation [113], with many models separating the two mechanisms [114]. Damage initiation can be modelled in ABAQUS either via the ductile criterion or the Johnson-Cook criterion (these are simply two different inbuilt and simple models).

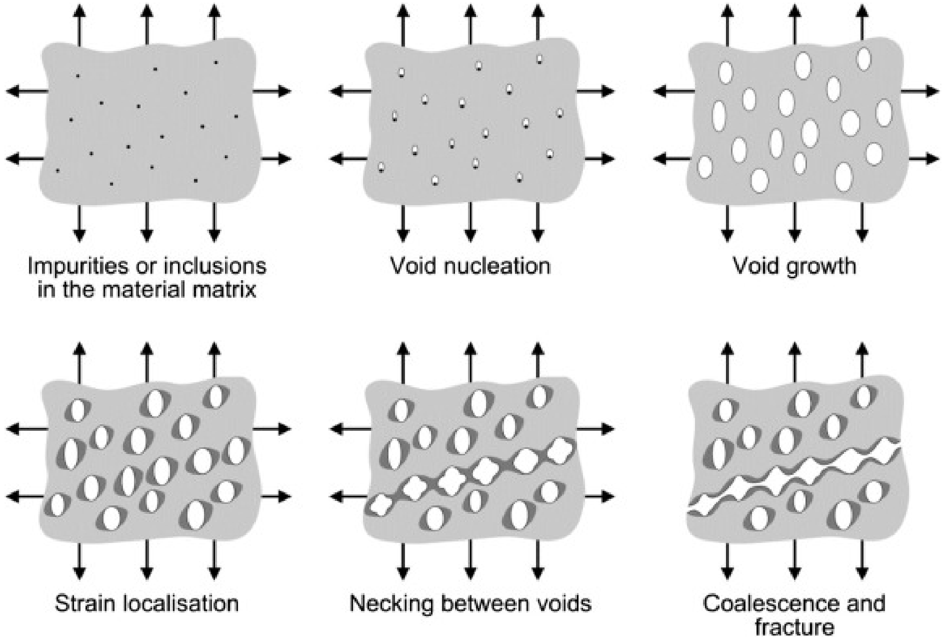

Figure 2.11: *The mechanism of ductile fracture, voids nucleate, grow and coalesce. Reprinted from [115] under CC-BY-4.0*

In the ductile initiation model damage is initiated when:

$$\omega_{\mathrm{D}} = \int \frac{\mathrm{d}\dot{\bar{\varepsilon}}^{pl}}{\dot{\bar{\varepsilon}}^{pl}_{\mathrm{D}}\left(\eta, \dot{\bar{\varepsilon}}^{pl}\right)} = 1 \tag{2.21}$$

Where η is the stress triaxiality, p is the pressure stress, q is the von Mises equivalent stress and $\dot{\bar{\varepsilon}}^{pl}$ is the equivalent plastic strain rate.

The Johnson-Cook damage model is similar to the plastic flow model of the same authors.

$$\bar{\varepsilon}^{pl}_{\mathrm{f}} = \left[d_1 + d_2 \exp\left(-d_3\eta\right)\right]\left[1 + d_4 \ln\left(\frac{\dot{\bar{\varepsilon}}^{pl}}{\dot{\varepsilon}_0}\right)\right]\left(1 + d_5\hat{\theta}\right) \tag{2.22}$$

In this case d_{1-5} are damage parameters and $\hat{\theta}$ is a temperature dependence modelling parameter. Such a damage model is typically suited to high strain rate applications [113] so may be a well suited to blanking wherein strain rates in the cut edge region may be high.

The Gurson-Tvergaard-Needleman (GTN) damage model was extended from the Gurson model is defined by [116]:

$$\Phi\left(\Sigma_{ij}, \sigma_y, f*\right) = \left(\frac{\Sigma_{eq}}{\sigma_y}\right)^2 + 2f*q_1 \cosh\left(\frac{q_2\sigma_{kk}}{2\sigma_e}\right) - 1 - q_1^2 f*^2 = 0 \tag{2.23}$$

Where $f*$ is the void state, defined as:

$$f* = \begin{cases} f, & f \leq f_c \\ f_c + Z\left(f - f_c\right), & f > f_c \end{cases} \tag{2.24}$$

and q_1, q_2 are fitting parameters, $\sum_{eq} = \sqrt{3s_{ij}s_{ij}/2}$ is the von Mises equivalent stress with s_{ij} is the stress deviator, σ_y is the undamaged yield stress, f is the volume fraction of voids, f_c is the critical void volume fraction, and Z the coalescence rate of micro-voids [116, 117].

Z the coalescence rate of micro-voids is defined as:

$$Z = \frac{f_u - f_c}{f_{\mathrm{F}} - f_c} \tag{2.25}$$

Where f_F is the void volume fraction at failure and f_u is the reciprocal of q_1.

Void evolution is omitted here but available in [117]'s paper on the matter, governed by a further four equations. Clearly the GTN damage model is complex, and although its parameters can be found from tensile tests and scanning electron microscopy with relative ease, simpler models such as the Johnson-Cook damage may be preferable for extension and further coupling, e.g. to magnetic property degradation. The fitting parameters q_1 and q_2 act to amplify the hydrostatic stress [116, 117] and are involved with void coalescence alongside a number of other parameters in [117]. The technique to find these parameters is also more complex than *only* tensile tests, and requires tests to be stopped upon necking for imaging (typically via electron microscopy), and further imaging post fracture. The GTN model also cannot accurately simulate ductile fracture under low stress triaxialities [118], critical in shear cutting processes such as blanking. It has also been reported that the volume fraction of inclusions cannot directly be used for calibration of the GTN model as not all inclusions nucleate voids [119, 120]. Chhibber et al. [120] also notes that the determination of stress state is difficult in notched samples due to large stress and strain gradients through the sample. Peng et al. [121] used optical microscopy in combination with digital image correlation to calibrate the GTN model for 316L stainless steel, finding agreement between void location in experiment and prediction. The authors note the changing failure initiation site with different notch radii, driven by the changing stress state.

He et al. [118] proposed an improved shear modified GTN model which used two independent damage mechanisms to predict fracture under low stress triaxiality; the model was verified in aluminium alloy 6061, showing better experimental agreement than the unmodified GTN model.

Yan et al. [117] predicted edge cracking from rolling in 2% Si electrical steel using the GTN model. Several reductions and tensions were simulated to find the optimal parameters to reduce crack formation, additionally a larger work roll was found to reduce edge crack growth. In order to calibrate the GTN model a number of tensile tests are required, with scanning electron microscopy undertaken at necking and fracture to calibrate void content parameters f_c and f_F. Additionally, the authors extrapolated from a Holloman-type equation obtain plasticity and elasticity constants without damage.

Li et al. [122] noted that coarser grains lead to fewer voids on the fracture surface but accelerated void coalescence, relevant to silicon steel due to the large grain size as noted in Section 2.1.3. To account for this effect, an extension to the GTN model was introduced considering the normalised third invariant and stress triaxiality which accounted for the size effect by improving the response of the model to void shear coalescence. Grain diameters of approximately 14 µm to 64 µm were investigated in micro-scale copper specimens. This coarse grain void suppression effect is extremely relevant to silicon steel due to its large grain size, approximately triple that of the largest grain in Li et al.'s study, and helps inform both damage modelling and experimental approaches.

Damage in anisotropic sheet metals was investigated by Kami et al. [123]; when combined with the Hill48 model good experimental agreement in aluminium alloy AA6016-T4 was found. Furthermore the forming limit curves were found via simulation and agreed with those found experimentally.

Lemaitre [124] introduced an isotropic damage model based upon the concept of effective stress. The model is defined as:

$$D = D_C \left(\frac{p[\frac{2}{3}(1+v) + 3(1-2v)(\frac{\sigma_H}{\sigma_{eq}})^2 - \epsilon_D}{\varepsilon_f - \varepsilon_d} \right) \tag{2.26}$$

Where v is the Poission ratio, $\frac{\sigma_H}{\sigma_{eq}}$ is the ratio of hydrostatic to deviatoric stress, p The material constants ε_f, ε_d, and D_C are therefore to be found, which were suggested to be obtained by several interruptions of a tensile test and observing the changing Young's Modulus as damage accumulates. A 'Teacher-Learner based optimisation' algorithm was used by Verma and Saxena [125] in order to obtain the constants for the Lemaitre model for a dual phase steel. Upon successfully obtaining the constants, good experimental agreement with the dog-bone specimen was achieved. Good agreement to experimentation is also shown in shearing processes [126, 127], in comparison to the Gurson model and its derivatives. SEM was used by Kumar and Tandon [128] in order to study the incremental sheet forming in A11050 H14, where the damage was defined as the ratio between the damaged (voids) and undamaged areas. The authors used a simplified coupled version of the model, only considering isotropic hardening - nevertheless, fracture location was well predicted. The Lemaitre model does not consider compressive stress states to affect the damage response, which may lead to non realistic predictions unless damage is deactivated under such circumstances [126]. A modified Lemaitre model which included the effect of Lode angle found excellent agreement experimentally in dual phase steel [129]. The model's prediction of ductile fracture was considerably improved over the Lemaitre model.

Lian et al. [130] presented a coupled model which used the dissipation-energy evolution law:

$$\dot{D} = \frac{\sigma_y L}{2G_f}\dot{\epsilon} \tag{2.27}$$

Combined with an advanced plasticity model taking the Lode angle into account good overall agreement was achieved with experiment, however the authors note some overestimation in plane strain conditions. This is due to the simple damage evolution law only considering the equivalent plastic strain, instead of also including the effect of stress state. An important aspect is highlighted here: that the damage model can be relatively simple as long as plasticity is correctly predicted.

Another phenomenological approach was introduced by Bao and Wierzbicki [131], wherein a fracture locus was developed based upon the stress state and the total equivalent plastic strain. The authors noted that a discontinuity may be present in the locus, as the deformation mode changes from ductile void based fracture to shear dominated fracture. Stress state is of great importance in this model due to its direct contribution to the calibration; vast changes in stress state throughout the deformation are common in many sample types and as such an averaging procedure is required. Equation 2.28 shows the average triaxiality as defined in [131]

$$\eta_{avg} = \frac{1}{\bar{\varepsilon}_f}\int_0^{\varepsilon_f} \frac{\sigma_H}{\bar{\sigma}} d\bar{\varepsilon} \tag{2.28}$$

Where $\bar{\varepsilon}$ is the equivalent strain, $\bar{\varepsilon}_f$ is the equivalent strain at fracture, and $\frac{\sigma_H}{\bar{\sigma}}$ is the ratio of hydrostatic to Mises equivalent stress. The fracture model's driving variable was based upon this same integral reaching a critical value. Calibration of the model was performed using a variety of sample geometries, including cylinders of varying diameter to height ratios, round tensile samples based on the ASTM-E8 standard, notched samples, and a butterfly shear sample with a reduced section. The requirement to produce a large number of different geometries for testing may make the model less attractive for certain applications - indeed in the present thesis a methodology was required to overcome the limitation testing on thin sheet stock.

The model proposed by Bao and Wierzbicki was further extended by Wu et al. [132] to include damage softening by the introduction of an initiation locus. Damage evolution is driven by energy-dissipation increments allowing stress softening behaviour, and under complex loading conditions this extension performed significantly better than the case without softening. In shear the softening was under-predicted, likely due to the energy increment based formulation, which required a single value to be chosen as the dissipative value. Additionally, due to the calibration method *(direct current potential drop)*, shear dissipation may be under-predicted due to less void formation and greater shear band localisation. The calibration method is a further limiting factor in some cases, in silicon steels the principle action of the silicon content is to increase resistivity - in combination with small cross sectional areas ohmic heating may become a dominant factor. The same model was used by Wu et al. [133] to predict chip formation in a medium carbon steel.

The MBW model was also applied to predict ductile fracture in pipelines by Keim et al. [134], with the lowest crack propagation speed in comparison to other models (GTN and Cohesive Zone) being observed in the MBW model. This was due to the formation of shear lips being most accurately predicted in the latter model by increased ductility absorbing crack driving energy. Such a comparison indicated that in this case the model basis, be that micro-mechanical, surface-based or phenomenological provide similar results, but the dynamics of the simulation are improved by the increased sensitivity the MBW model can provide due to its phenomenological nature. The authors additionally note the mesh sensitivity observed in the damage evolution portion of the loading, admitting that a non-local formulation would allow mesh resizing without the requirement of recalibration. Such mesh sensitivity is interesting because the evolution equation is energy based, but still dependent on strain increments, as shown in Equation 2.29 [134].

$$\Delta D_n = \frac{\sigma_y}{G_f} \int_{\bar{\varepsilon}}^{\bar{\varepsilon}} d\bar{\varepsilon} \quad \text{for } D_i = 1 \wedge \eta > \eta_c \tag{2.29}$$

Consequently such a shortcoming highlights the desire to eliminate strain increments or harness strain directly (in the form of another locus) as a highly desirable outcome. The former possibly allowing mesh independence in a local model and the latter allowing much simpler calibration and the various benefits of non-local models as discussed in Section 2.4.3.

The plasticity model discussed in Section 2.4.2 by Bai and Wierzbicki [96] was in fact coupled with the fracture model based upon [131], a damage evolution law was introduced to allow damage softening based upon the equivalent plastic strain, as defined by:

$$D\left(\bar{\varepsilon}_{\mathrm{p}}\right) = \int_{0}^{\bar{\varepsilon}_{\mathrm{p}}} \frac{\mathrm{d}\bar{\varepsilon}_{\mathrm{p}}}{f(\eta, \bar{\theta})} \tag{2.30}$$

The Lode angle dependence included in the model was averaged in a similar matter to Equation 2.28. The authors found that the linear damage evolution law was shown to be appropriate for monotonic loading, but under more complex loading nonlinear evolution laws are required.

In a study by de Geus et al. [135], a soft ductile phase and brittle hard phase was simulated by assigning different models to individual elements of a mesh; the soft phase was simulated using the Johnson-Cook damage model and the hard phase via the Rankine model. In utilising an ensemble model, a significant change in total response was reproduced as the 'hard' volume fraction increased. This study shows that assigning different models or properties on a per element basis can produce valid results of complex conditions with low computational cost. In 304 stainless steel Seo et al. [136], found that fracture strain was highly dependent upon the strain rate, with a marked decrease in the transition from quasi-static conditions of $\dot{\varepsilon} < 0.1$ to high rates of $\dot{\varepsilon} > 1$. While the authors found the Johnson-Cook models (plasticity and fracture) could predict fracture strain within 20% in the worst case, the Wierzbicki type models do not take strain rate into account. This may lead to errors if applied to a highly dynamic situation such as blanking; the sensitivity of a material's fracture strain to the strain rate is naturally material dependent.

Non-Local models

Unlike local models which use only contained within the material point under consideration, non-local models use information from other material points. Non-locality may be implemented for both plasticity and damage models, in this thesis non-local damage is of interest. Jirásek [137] describes the many implementation possibilities; generally speaking any variable can be chosen as the non-local variable. Integration over a volume or their differential counterparts, gradient based formulations, are used to realise the non-locality. Integral type models are defined as:

$$\bar{f}(x) = \int_v \alpha(x, \xi) f(\xi) d\xi \tag{2.31}$$

Where $\alpha(x, \xi)$ is a non-local weight function, x is the target point and ξ is the source point. This non local formulation was applied in the present study with the non local variable chosen to be equivalent plastic strain. The non-local weight function is defined as:

$$\alpha(x, \xi) = \frac{\alpha_0(||x - \xi||)}{\int_V a_0(||x - \xi||) d\xi} \tag{2.32}$$

Where $\alpha_0(||x - \xi||)$ is a monotonically decreasing non negative function of the distance between the target and source point. This definition in required to ensure the non-local operator does not introduce spurious strain to a uniform strain field in the vicinity of a boundary. α_0 is implemented as:

$$\alpha_0(||x - \xi||) = \left(1 - \frac{(||x - \xi||)^2}{R^2}\right)^2 \tag{2.33}$$

Where R is the interaction radius for the non-local operator.

Felder et al. [138] demonstrated a gradient enhanced non local thermo-mechanically coupled extension to an isothermal model. Mesh dependence was eliminated and convergence quickly achieved. The model neglected strain rate dependence, but did predict differing responses due to thermal softening caused by adiabatic heat generation. A modified non-local GTN model was presented by Aldakheel et al. [139] wherein a phase field evolution equation predicted experimentally observed results - such as cup and cone fracture - with low computational cost due to a novel *explicit-implicit* algorithm.

Computational aspects of non-local models

Any model must be performant enough to ensure reasonable run times, introducing non-locality requires a method of tracking *target* elements in the vicinity of the *source* element which introduces a potentially significant additional computational workload. In computer science the so-called *Big O* notation is a measure of the worst case run time, for an algorithm which has a run time proportional to the number of elements upon which the algorithm acts the time complexity is said to be $O(n)$. Similarly, should a nested loop be required over every element the time complexity is $O(n^2)$. A similar concept applies to the amount of memory used by an algorithm, typically there is a trade-off between increased time or memory complexity.

The Octree is a data structure in which three dimensional space is subdivided recursively into eight cubes [140]. The time complexity of a search in an octree is $O(\log(N))$. Octrees are commonly used for finding the neighbouring elements in the interaction radius of non-local models [137], although other methods are possible such as binary space partitioning or kd-trees.

Such data structures can also be used for meshing, Ankit et al. [141] presented an integral type non-local damage model using an octree mesh and a scaled boundary finite element solver, allowing massively parallel computation on approximately 12,000 cores by mesh partitioning retaining a parallel efficiency of greater than 90% in most cases. Use of an octree mesh allowed a much lower number of elements (125.2 million) in comparison to a voxel based approach (1.07 billion).

2.5 Calibration and validation of models

2.5.1 Damage calibration

The introduction of damage into the finite element literature has allowed sub-element modelling responsible for the softening behaviour seen in many materials, however the concept of damage must be understood to be a mathematical tool. Although based upon very real concepts such as the void volume fracture, for instance, depending on the calibration method there are vastly different results for damage onset. In this section, a number of techniques for identifying damage are reviewed. Tasan et al. [142] compared several methods for the identification of damage in metallic samples, and it was noted among all methods reviewed slow damage accumulation followed by rapid accumulation was observed. Mechanical methodologies such as indentation hardness, indentation modulus, and elastic compression modulus agreed within experimental uncertainty while density showed higher damage values than void area and volume fraction methods. Figure 2.12 shows the results of the methods investigated by Tasan et al..

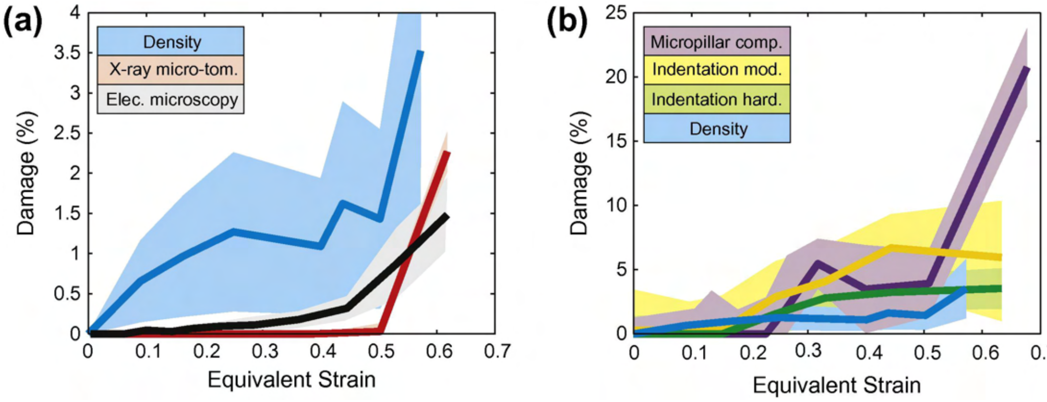

Figure 2.12: *The several damage identification methods investigated by Tasan et al. [142] which are theoretically equivalent. Reprinted from [142] with permission from Elsevier.*

As such the authors suggest that indentation and compression based methods are the most accurate for damage measurement, noting that such methodologies do not provide information on the type of damage occurring and therefore should be coupled with SEM or tomography. Hardness-based techniques are not to be used without caution, however, as other work suggested a heat treatment to remove deformation history induced effects was required. Damage would be unaffected by this heat treatment, thus improving the results of the indentation based methodology [143, 144]. This was recommended because a number of microstructural mechanisms simultaneously affect the hardness alongside damage, the authors reported that hardness did not decrease in four tested metals while damage was present as verified via other methods.

The resistivity of a material increases as it accumulates damage, with the resistivity measured though the method of direct current potential drop (DCDP). Vecchiato et al. [145] used DCDP to investigate crack growth in single-edge-crack round bars, as the author notes the output voltages are on the order of 1 mV for currents of up to 50 A. DCDP is also applicable to uncracked tensile specimens, but is strongly influenced by necking - additionally, the change in voltage due to void initiation and coalescence is on the order of 1-10µV [146]. A damage model for advanced high strength steel was also calibrated this way [130]. Although the technique is very sensitive, with a minimum crack resolution of tens of microns, in optimal conditions such a high current draw has the potential to cause significant ohmic heating.

Computed Tomography (CT) uses X-ray photons to penetrate a sample and obtain an image on a phosphor screen, the sample is rotated relative to the source and detector (or vice versa) to obtain projections (images) from many angles through the sample. Tomographic reconstruction is then used to convert the many projections to a three dimensional volume. Kumar et al. [147] used CT to assess damage in WB36 ferritic steel in compact tension and single edge notched tensile samples (SENT). A voxel size of 1.26 μm^3 limited the detection of some voids which were linked to secondary nucleation of voids on carbide inclusions, particularly for the SENT samples Nevertheless, substantial void growth was detectable in the compact tensile samples. Scott et al. [148] removed coupons of 0.8x0.8x12.5mm from interrupted tensile tests of hole tensile specimens of a high strength steel and scanned them with a voxel size of 1.15 µm. Peak void volume fraction was observed 600 µm from the edge of the hole, and coalescence at an equivalent plastic strain of approximately 60%. X-ray Diffraction Contrast Tomography (DCT) is a method of determining crystallographic orientation in three dimensional polycrystals. Thibault et al. [149] used DCT to map an austenitic stainless steel, intergranular stress corrosion cracking was observed. The intergranular cracking could be sensitised by carbide precipitation at the grain boundary, or more resistant if the adjacent grains were low angle and low Σ coincident site lattice, as well as low index planes. Although applied in a corrosion setting, this study highlighted the importance of and provided insights into grain boundaries, and gave insights into the effect of grain boundary structure on the damage and fracture. Herbig et al. [150] similarly used DCT to investigate fatigue fracture, concluding that the grain orientation has an effect on the crack path, and also tentatively reported a lack of clear correlation between slip plane orientation and fracture surface but noting the limited resolution of the DCT method may be responsible for this. Another fatigue study with DCT found predominantly trans-granular cracking associated with crystallographic slip planes, but noted that crack propagation was retarded by certain orientations and at certain grain boundaries [151].

Electron back-scatter diffraction (EBSD) is an alternative and more mature method for gathering information on the crystallographic orientation. EBSD has been widely applied to study the crystallographic orientation and texture evolution in silicon steels [152, 153, 154], but due to its ex-situ destructive nature it is significantly more difficult to couple with damage studies, as seen with DCT. Nevertheless, low cycle fatigue damage was studied in a 3% Si steel by Schayes et al. [155], demonstrating transgranular crack initiation at $\varepsilon = 0.5\%$ and intergranular crack initiation at $\varepsilon = 1\%$. The authors noted the difficulty in applying techniques such as TEM and X-ray diffraction in this material due to the large grain size, thus meaning the dislocation density is hard to determine.

Klocke et al. [156] developed an inverse parameter identification method to calibrate the constants required for some of the JC plasticity model and the Cockcroft-Lantham damage model. This inverse approach avoids expensive and difficult testing such as the split-Hopkinson bar test at high temperatures, strains, and strain rates. As the technique was applied to the simulation of machining, the authors note that good results are dependent on high-quality friction models. Conversely, simplistic friction models would harm the inverse procedure by creating an error that cannot be calibrated out through adjusting the plasticity and damage model parameters. Clearly then, such a procedure is highly attractive in situations where parameters such chip morphology and cutting force are easily obtainable; when applied to blanking there may be more complications due to the limited information about the process, e.g. typically the work is fully enclosed and only force data of the entire punch can be measured. Despite this extra difficulty, the Lemaitre model was partially calibrated using an inverse in blanking by Cai and Chen [157] for DP1000 and Al6082

Silva et al. [158] used a method for studying damage using flux leakage from the magnetic circuit formed by a sample and hall effect sensors known as low-field magnetic analysis (LFMA). This method was validated against hardness and x-ray diffraction results, and it was found the magnetic flux density was proportional to the strain. This method shows great promise, specifically when considering both the concerns around magnetic property degradation at the blanked edge of electrical steels and the difficulties of measurement associated with other techniques. Using the same concept of magnetic flux leakage detection non-destructive testing of wire ropes has been developed [159, 160]. Tian et al. [160] demonstrated a concentrator to improve the magnetic circuit and improve the signal to noise ratio. The principle of magnetic flux leakage is shown graphically in Figure 2.13.

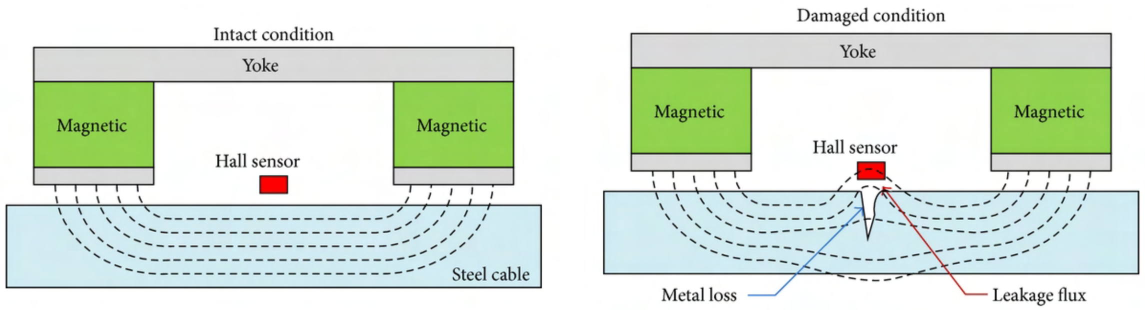

Figure 2.13: *The principle of magnetic flux leakage damage detection based techniques. Figure reproduced from [159] under CC BY 3.0*

2.5.2 Damage under changing stress state

Kong et al. [161] studied damage under varying stress states in a 2198 T8 aluminium alloy using a cross-shaped specimen, noting a marked reduction in strain to fracture if a sample was first sheared before the tensile mode loading was applied. Flat cracks were observed in the microstructure as a result of the shear loading path, leading the authors to conclude that void based damage accumulation was significantly less important due to the low intermetallic particle and void content of the virgin material. Laminography was utilised to detect damage nucleation at the end of the shear load path. Wu et al. [132] verified the extension to the modified Bai Wierzbicki model discussed in 2.4.3 by notching a prestrained round bar specimen. This allowed the stress state to be significantly modified, increasing from $\eta = \frac{1}{3}$ to approximately $\eta = 1.2$. While the Lode angle is essentially constant in the application of blanking [162], the triaxiality is variable - many models thereby justify the use of triaxiality through this distinction.

2.5.3 Low stress states in thin samples

It has been shown that stress state has a large influence on fracture [131, 163]. Pham et al. [164] developed an anti-buckling method for testing of ultra-thin (0.15mm) sheet metals under planar shear tests, testing both austenitic stainless steel and copper. This method allowed shear strain measurement of up to 0.5 without buckling, where otherwise only up to 0.25 was possible. Stiebert et al. [165] demonstrated a method for obtaining measurement of ultra thin grade material using a multi-layer in plane torsion test, though this technique is limited by the requirement to transmit the torsion through the stack. As adhesive alone is insufficient, the use of penetration of the first layer and forming of the middle layers with an pyramidal indenter is required. Although this procedure has negligible implications on the stress state around the area of the and some difficulty due to small clamping area, it allows flow curves to be obtained at much greater strains. Figure 2.14 shows a copper sheet sample tested with and without the restraining system, with wrinkles appearing at a much lower strain without it.

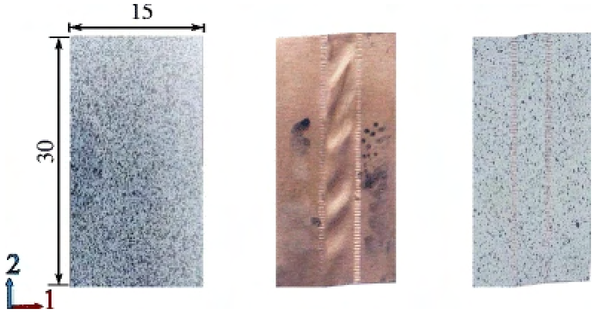

Figure 2.14: *A copper shear sample tested with (DIC speckled) and without (bare copper) the restraining system developed by Pham et al. [164]. Wrinkles appear at a significantly lower strain when the restraining system is not used. Reprinted by permission from Springer from [164]*

Zistl et al. [166] used a pneumatic hold down system to partially restrain a H shaped biaxial sample, preventing buckling and allowing a significant proportion of the negative triaxiality stress state to be investigated experimentally. The authors report a maximum out of plane displacement of 0.3mm; although suitable for the samples demonstrated, this is clearly unsuited for materials such as the 0.2mm laminations in the present study.

2.6 Summary

The demand for electrical machines is increasing, and a major constituent of nearly all high power motors is silicon steel in the form of stacked laminations. Blanking is the most widespread and industrially applicable manufacturing technique for the production of motor components from laminations of silicon steel. Despite the many advantages of blanking it does have a number of drawbacks that will negatively affect the magnetic properties, including the production of burrs and residual stress. Due to the complex interaction between the many process parameters such as punch speed, clearance, tool geometry, etc. the investigation of the blanking process is challenging. Many studies have characterised the effect of changing various parameters individually, but the complexities involved with tool (and motor) design mean high quality damage and fracture modelling of the process is required.

A number of damage and fracture models have been developed over the years, many producing satisfactory results across a broad range of conditions, the unique complexity associated with the rapidly changing and highly variable stress states found in blanking present particularly challenging conditions for many models. Calibration of any model is made more challenging by the influence of the material geometry on the type of testing that can be performed. In silicon steel laminations, the effect of a large grain size relative to the thin final product may impact the realisation of representative results - therefore, testing with final product dimensions is necessary for accurate experimentation. However, some experimental techniques are difficult to employ with final product dimensions, as they may (for example) result in buckling from elastic instability in thin samples at low stress triaxiality.

The review undertaken reveals several important parameters in researching NO20, the material of main interest: the impact of geometry and sample preparation; the difficulties in applying current methodologies and compatibility with NO20; the effect of grain size on modelling applications, the relevancy of stress states in relation to fracture; and the acknowledgement of downstream work compatibility. In existing work many assumptions are made, such as an isotropic mechanical response. Furthermore, complications due the sheet geometry of the final product require careful consideration of preparation and test methodology - it is as yet unclear whether the manufacturing method of samples will influence the results, and if so, how best to negate this. The sample geometries and test methodologies utilised in existing research are largely incompatible with NO20, due to due to its high resistivity, sheet geometry, and large grain size. As a consequence of this, many existing models are difficult or impossible to calibrate. Furthermore, the large grain size effects the modelling assumptions, requiring a novel approach to overcome their limitations. Previous work has shown that fracture is highly dependent on stress state; thus generating a calibration across a wide range of stress states is important, and new methodologies will be required to achieve this in sheet geometries. Finally, any damage and fracture model should be designed to be compatible with downstream work, namely prediction of function performance by means of coupling with magnetic loss.

Chapter 3

Methodology

In this chapter, the experimental methodology developed for calibration of the damage model is detailed, alongside methods for verification of the calibration procedure itself and the modelling results. Sample design and preparation is discussed. The main calibration strategy is developed under the constraints of using final product material of thickness 0.2mm. Alternate methods for in-situ damage onset identification are explored, principally direct current potential drop and low flux Hall Effect sensing. μ-Computed Tomography is used to further explore the size effect by employing digital volume correlation. An in-situ DIC instrumented blanking rig developed and presented in [2] is improved upon, in order to both ensure plane strain conditions and verify numerical results. A novel *semi-biaxial* sample geometry is presented for further verification of the model. Nanoindentation is used with electron backscatter diffraction, attempting to correlate small changes in hardness with grain orientation for further modelling possibilities at the meso scale. Optical profilometry is used to explore the *orange peel* effect identified in interrupted tensile tests. The aforementioned techniques are used to investigate the fracture mechanics of the material at various points along the processing route.

3.1 Material Selection

Non-grain-oriented silicon steel (NOES/NGO) manufactured by *Cogent Power - TATA Steel* was used in this study - fully processed variants of grades NO20-1200 (0.2mm) and NO35 (0.35mm), and unfinished forms of thicknesses 0.5mm and 2mm. These variants are chosen to demonstrate the difference in calibration strategy required, due to the size effect caused by the relatively large average grain diameter of 150µm in comparison to the 200µm nominal thickness of the product. Additionally, the final annealed product was compared with cold rolled product. The normalised chemical composition of the material at the 2mm stage is shown in Table 3.1.

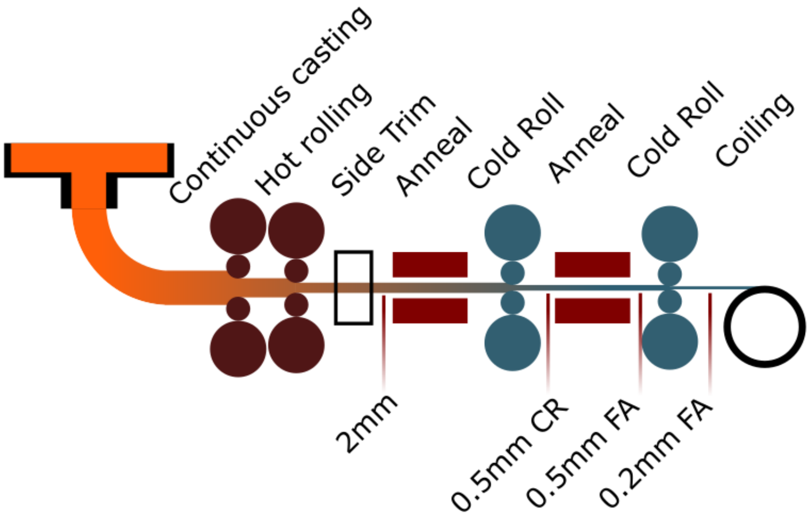

Figure 3.1: *A simplified diagram of the processing route for electrical steel. Samples were manufactured from material as indicated by the bottom labels. Intermediate coiling steps are not included.*

Element	Content (wt%)	Element	Content (wt%)
C	0.00245	Cu	0.023
Si	3.23	Mo	0.001
Mn	0.17	Al	1.06
P	0.019	Nb	0.002
S	0.001	Ti	0.008
N	0.0017	V	0.004
Cr	0.025	Ni	0.01

Table 3.1: *Normalised composition of material*

3.2 Strain measurement using Digital Image Correlation

Digital Image Correlation *(DIC)* is a full field non contact strain measurement technique. A reference image is compared to a deformed image, and the relative deformation is then used to derive strain. The images are divided into subsets, and the subset fitted to the deformed image using the cross correlation metric. Subsets must be unique in order to overcome the correspondence problem and provide a high correlation metric [75], and as such a speckle pattern is typically applied to the sample. Several methods are available to produce a speckle pattern on a sample, depending on the physical size of the region of interest.

Strain measurement using DIC is sensitive to the processing parameters chosen, principally the subset and step size, therefore for each experiment a sensitivity study for these parameters was undertaken to ensure the strain converged. Specific values are detailed in each experimental section. Generally, it is accepted that the ideal speckle pattern contains at least 3 features per subset, that the step size is approximately $\frac{1}{3}$ subset size, and that each feature be 3-5 pixels [167]. Furthermore, the density of black to white should be 50% [168], all features should be of approximately the same size, and features should be randomly distributed [77].

The speckle application method depends upon the size of the region of interest, with a larger ROI requiring larger speckles as to obtain the ideal features as previously described. For larger ROIs a spray can application method was used: a thin white coat of spray paint was applied and allowed to become tacky before application of black speckles. For this reason Rust-Oleum Painter's touch was used for room temperature tests, and Plastikote Industrial High Heat for heated tests, as the former is faster drying but the latter is heat resistant. Black speckles were then applied by holding the spray can at a distance from the sample.

Samples with a smaller region of interest (such as that used in the in-situ blanking rig as described later in Section 3.9) require smaller speckles than is practical to achieve using a spray can. An atomiser was used to apply laser toner to the sample immediately after applying the white base coat, followed by the application of a thin layer of Kenro Kenair Anti-Reflect to set the small toner particles. The small toner particles allow higher magnification into the region of interest while maintaining a small subset size - a comparison of the results of the two methods is displayed in Figure 3.2. A sufficiently high magnification into the ROI is important to achieve convergence of strain, as later discussed.

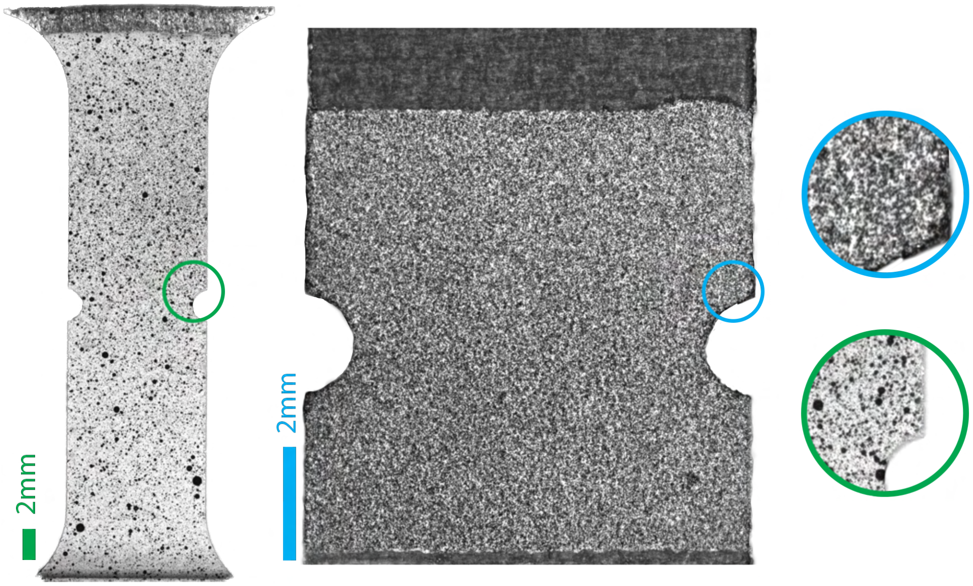

Figure 3.2: *A comparison of the physical speckle size and consequent acceptable field of view achievable with a spray can and an atomiser*

In each case a range of processing parameters were trailed, and upon convergence of the results the final parameters were chosen as they achieved the highest strain resolution with an acceptable noise floor.

It is also obviously important to ensure the painted speckle layer acts as a strain witness, as if the sample is coated it may respond differently to base material. In this study it was found the Suralac 7000 & 9000 coatings did not interfere with the strain measurement.

3.2.1 Speckle quality validation using a gradient entropy measure

Many methods exist to quantify the quality of an image in regards to its suitability for use with DIC. A method combining the gradient intensity and entropy measures was developed based on a preprint paper in the field of image compression [169], with the Shannon Entropy taken for the histogram of the derivatives of the image. This approach provides a geometrically informed interpretation to existing gradient methods, ensuring that, for example, repeating patterns or simple gradients score low. Image gradients are calculated by convolution with a kernel, many are available in the image processing literature, but the most common are listed in Table 3.2.

Name	X-kernel	Y-kernel
Sobel	$\begin{bmatrix} 1 & 0 & -1 \\ 2 & 0 & -2 \\ 1 & 0 & -1 \end{bmatrix}$	$\begin{bmatrix} -1 & 2 & -1 \\ 0 & 0 & 0 \\ 1 & 2 & 1 \end{bmatrix}$
Roberts	$\begin{bmatrix} 1 & 0 \\ 0 & -1 \end{bmatrix}$	$\begin{bmatrix} 0 & 1 \\ -1 & 0 \end{bmatrix}$
Prewitt	$\begin{bmatrix} 1 & 0 & 1 \\ 1 & 0 & 1 \\ 1 & 0 & 1 \end{bmatrix}$	$\begin{bmatrix} 1 & 1 & 1 \\ 0 & 0 & 0 \\ 1 & 1 & 1 \end{bmatrix}$

Table 3.2: *Common kernels used in image processing*

When both the X and Y derivatives are obtained a histogram may be generated, counting the number of occurrences of grey levels at each location. 256 values are represented in an 8 bit image, consequently the maximum change is 0-255 or 255-0 for a range of 512. This histogram can be flattened and used as the input for the Shannon Entropy. A factor of half may be used to map the result to the range 0-8. When using a logarithmic base of 2, this ensures the maximum value of the entropy measurement (unit *bits*) is consistent with the bit depth. This modified equation is shown in Equation 3.1.

$$H(X) = -\frac{1}{2}\sum_{i=1}^{n} P(X_i)\log(P(x_i)) \tag{3.1}$$

Figure 3.3 shows several demonstrative images where the gradient based entropy measure has been used with the Sobel kernel. Figure 3.3 (a)-4 is a real DIC speckle pattern with a threshold filter applied, so only pure black and white are shown to demonstrate the geometric awareness in comparison to Fig. 3.3 (a)-2. Pure Gaussian noise is shown in the third column, which scores lower with the new metric because it is homogeneous and the kernel causes a small amount of averaging.

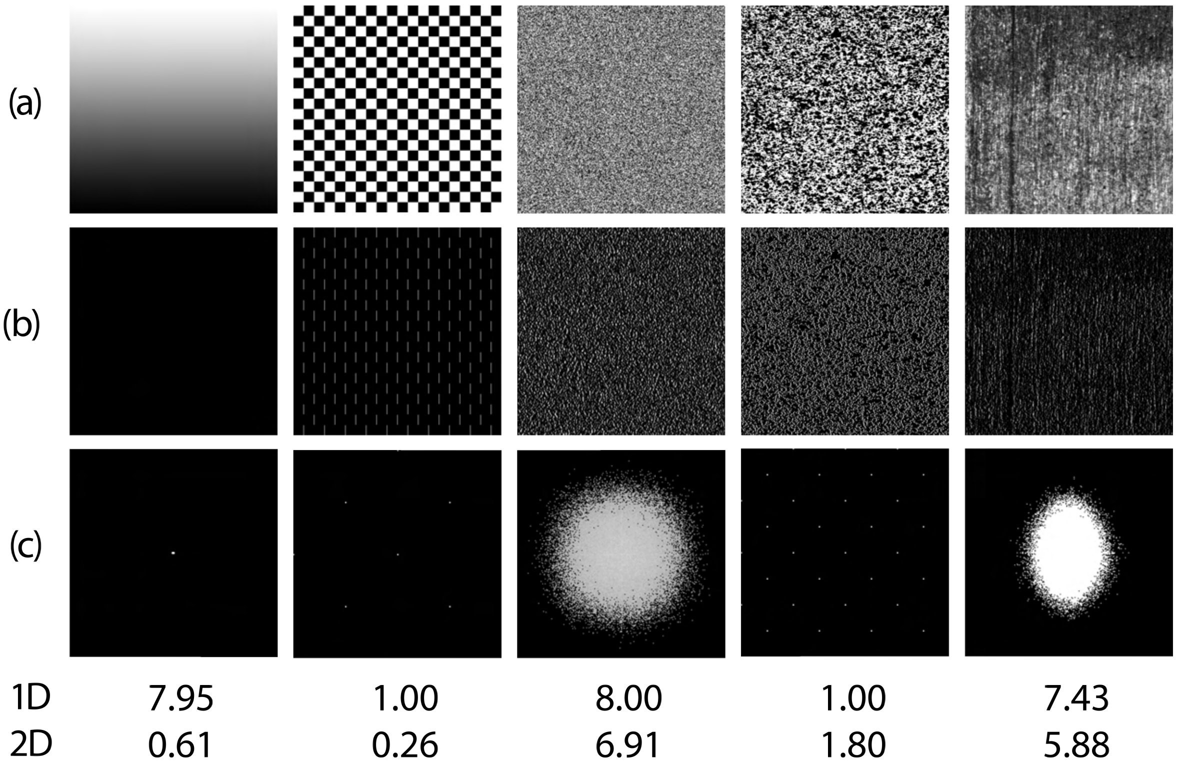

Figure 3.3: *A selection of images showing the gradient based entropy measure. Row (a) shows the test image. Row (b) shows the X derivative. Row (c) shows the histogram of the derivatives. The 1D entropy measure (obtained by flattening the image) is compared to the 2D method.*

3.3 Calibration of Johnson-Cook plasticity model parameters

The Johnson-Cook plasticity model was chosen to model the material due to its applicability under a wide range of conditions, being particularly well suited to high strain rate applications as observed in blanking. The model is of the form:

$$\sigma_y\left(\varepsilon_{\mathrm{p}}, \dot{\varepsilon}_{\mathrm{p}}, T\right) = \left[A + B\left(\varepsilon_{\mathrm{p}}\right)^n\right]\left[1 + C\ln\left(\dot{\varepsilon}_{\mathrm{ref}}\right)\right]\left[1 - \left(T^*\right)^m\right] \tag{3.2}$$

Many methods for calibration of the JC parameters are documented in literature, with Gambirasio and Rizzi outlining various strategies and discussing ease and quality of fit for each [170]. In the present work the lower yield stress method was adopted. Three experimental steps are required, one per square bracket. First, the parameters A, B, and n are identified from quasi static tensile tests. The C parameter is calibrated using tensile tests at various strain rates. Calibration of m is achieved by tensile tests at different temperatures.

3.3.1 Sample preparation

Standard *dog-bone* samples were prepared according to the ASTM-E8 standard for sub-size flat specimens [171]. The sample geometry is shown in Figure 3.4. Samples were prepared using by waterjet cutting using an Omax ProtoMAX machine, a machinability of 50 was found to be an acceptable value with a cut quality of 3 and cut radius of 0.35mm. Sample edges were then sanded using P1000 sandpaper to remove burrs, and painted as described in Section 3.2.

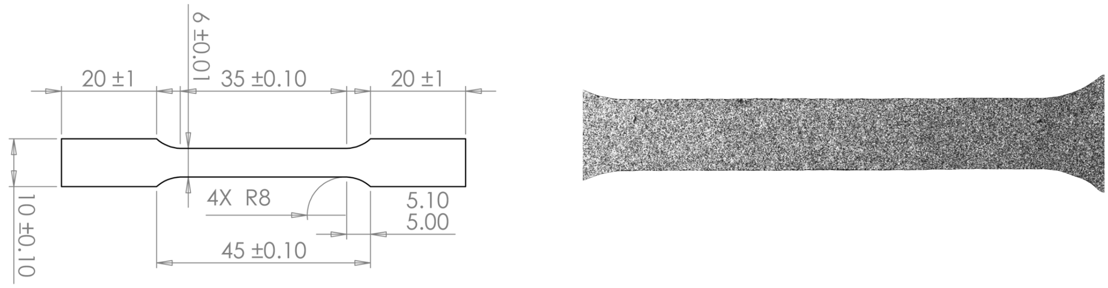

Figure 3.4: *Left: Drawing of sample geometry. Right: Sample with speckles applied for DIC.*

3.3.2 Quasi-static parameters

Parameters A, B, and n were obtained using a series of quasi-static tests at room temperature (20 °C). Samples were manufactured in line with the rolling direction (RD), 45° to it, and in line with the transverse direction (TD). For each sample set (RD, 45°, TD) at least 3 repeat samples were tested. A crosshead rate of $0.5\,\mathrm{mm\,min^{-1}}$ was chosen which gave a strain rate of $0.4\,\mathrm{s^{-1}}$. The first parameter A is the yield stress, with other parameters found using the non linear fitting tool in Origin Pro 2019 with A fixed. Origin Pro implements the Levenberg-Marquardt algorithm to minimise the sum of the square residuals.

3.3.3 Strain rate parameters

In Equation 3.2 $\dot{\varepsilon}_{\mathrm{ref}}$ is defined as the reference strain rate, i.e. the strain rate of the tests at which A, B, and n were determined. This leaves only C remaining which is found by nonlinear fitting in Origin Pro as in section 3.3.2.

A crosshead rate of $100\,\mathrm{mm\,min^{-1}}$ was used giving a strain rate of $40\,\mathrm{s^{-1}}$ and extends the investigation from low strain rates as presented in [172]. This strain rate was directly measured by calculating the gradient of strain from DIC.

3.3.4 Temperature parameters

In Equation 3.2 T^* is defined as:

$$T^* = \frac{(T - T_0)}{(T_m - T_{ref})} \tag{3.3}$$

Where T_m is the melting temperature and T_{ref} is a reference temperature, the temperature at which the first parameters A, B and n were determined. The melt temperature is available in literature, 1490 °C [173], leaving only the m parameter in Equation 3.2 remaining. A *Severn Thermal Solutions* high temperature furnace with an observation window in combination with a *Nene Testing Systems* 12kN servo-hydraulic tensile testing machine was used to measure heated samples at 100-400°C in 100°C increments. The experimental equipment is displayed in Figure 3.5.

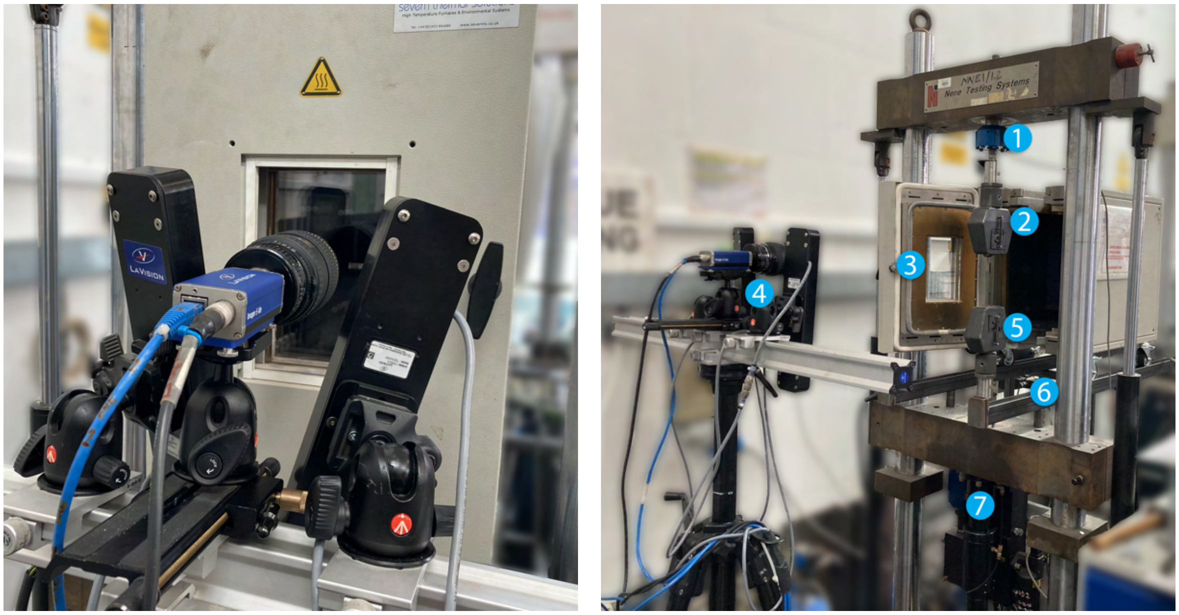

Figure 3.5: *An image of the environmental heating chamber and DIC equipment. 1: Force transducer, 2: Fixed jaw, 3: Heating chamber, 4 :DIC camera and lights, 5: Moving jaw, 6: Trolley to move chamber, 7: Hydraulic ram.*

3.4 Sample preparation for microscopy and indentation

In order to investigate the material using optical microscopy, electron microscopy, and nano-indentation, a flat and smooth surface is required. To produce such a surface, samples are first mounted in either Bakelite using a hot mounting process, or in resin using a cold mounting process. Silicon steel is extremely sensitive to water and oxidises quickly, therefore samples were prepared a day prior to, or on the day of investigation. Additionally this sensitivity was noted to degrade the surface during preparation, as such water was not used as a lubricant in any steps after initial grinding.

Many samples were investigated in the RD-TD plane, meaning the amount of material available to remove was extremely low as the sheet thickness was at minimum 0.2mm; the minimum amount of material was removed by starting polishing with high grit grinding papers. Such samples were manufactured with small tabs which were bent at a 90 degree angle to ensure the sample was properly set into the plastic.

As oil based diamond suspensions and pastes were used, each step was followed by 1-3 minutes in an ultrasonic bath. Samples were quickly removed and dried to minimise oxidation and then inspected under a microscope to ensure the abrasive from the previous step was removed. The typical polishing procedure is detailed in Table 3.3

Step	Abrasive carrier	Abrasive	Time	Platen RPM	Head RPM
1	SiC paper (water lubricated)	P800	1:00	160	61
2	SiC paper (water lubricated)	P1200	1:00	160	61
3	Cashmire cloth (oil suspension)	9 µm	6:00	130	61
4	Cashmire cloth (oil suspension)	6 µm	6:00	130	61
5	Trounoire cloth (oil suspension)	1 µm	8:00	130	61
6	Trounoire cloth (colloidal alumina)	0.05 µm	10:00	100	61
7	Trounoire cloth (no suspension)	NA	1:00	100	61

Table 3.3: *Details of polishing schedule to produce samples with a mirror finish. Steps 6 and 7 may be omitted for samples only requiring optical microscopy.*

Figure 3.6: *Samples mounted and polished for further characterisation. Left: Two notched samples from an interrupted tensile test. Right: A 0.2mm thick circle mounted for nanoindentation. The samples on the left have a fluorescent dye in the cracks and voids.*

3.5 Nano-indentation

Nanoscale indentation tests were performed to investigate the mechanical properties in highly localised regions. Confirmation of the change in mechanical properties due to the sample preparation method at the cut edge is possible by performing many indentations from this edge to the bulk material. Additionally, nano-indentation was used in conjunction with EBSD (electron back-scatter diffraction) to investigate the effect of crystallographic orientation and grain boundaries on local material properties, forming the basis for mesoscale simulations. A Hysitron TI Premier with a Berkovich tip was used to apply 1000µN peak force with a 15 second dwell time, the load profile and typical load displacement graph is shown in Figure 3.7. The Berkovich indenter tip is a three sided pyramidal with a half angle of 65.35° and a total included angle of 142.35°.

As the indenter is pushed into the sample both elastic and plastic deformations occur, the load is measured continuously and the hardness value extracted from the unloading portion of the load-displacement curve. Because the geometry of the indenter tip is well known, the following equations are used to calculate the hardness, H, and the Young's Modulus, E:

$$H = \frac{F_{max}}{A} \tag{3.4}$$

$$E = \frac{S\sqrt{\pi}}{2\sqrt{A_{max}}} \tag{3.5}$$

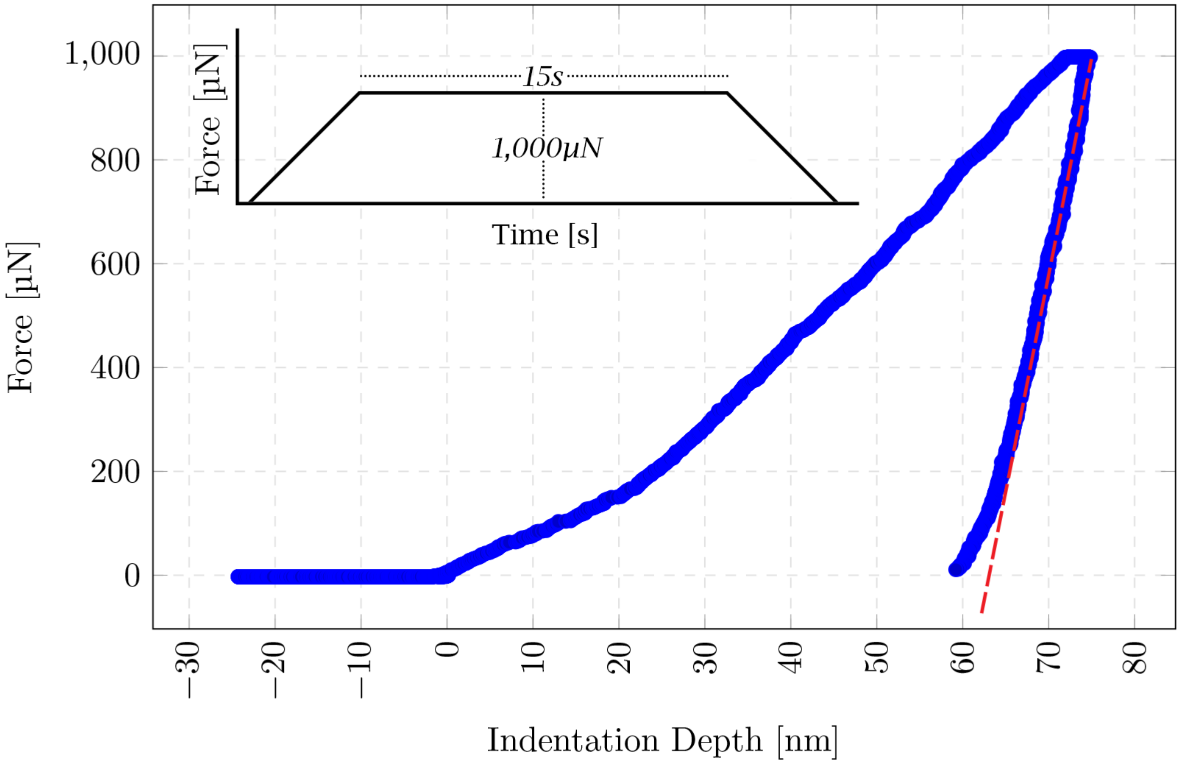

Figure 3.7: *A typical load displacement curve, inset is the trapezoidal loading profile with a dwell time of 15s. The red dashed line indicates the fitted portion of the curve.*

Where P_{max} is the maximum load, A is the contact area, and S is the gradient of the unloading portion of the curve.

3.6 Progressive Damage and Fracture identification

Testing and measuring fracture and damage directly on final products is highly desirable, however testing extremely thin sheets of 0.5 mm and less is challenging. Although similar microstructures may be developed via a heat treatment regime of bulk material, allowing traditional samples and testing methodologies to be utilised, this presents several disadvantages upon further examination. Due to the large average grain size (150 µm) relative to final thickness (0.2 mm) the so-called size effect may become significant, changing the results between bulk and thin materials. Furthermore, it is prudent to envisage the material testing holistically - the very reason for such thin products is to improve the magnetic qualities of the material. For this reason developing a methodology in which one may in future work link the magnetic testing regime with the mechanical is required, and the magnetic performance cannot be tested on bulk materials.

3.6.1 Damage Parameters

Piecewise cubic polynomials were chosen to fit the data, with the constraint that each section is G^1 continuous, i.e. that the zeroth and first derivatives are continuous. Once the fracture/onset strain is found at all triaxiality ratios measured, an interpolating function is fit using the Modified Akima piecewise cubic Hermite interpolation. Because the triaxiality at and below $-\frac{1}{3}$ is asymptotic, the portion of the loci between the lowest measured triaxiality and this $-\frac{1}{3}$ cutoff value is modelled using the asymptotic function as presented in [131]. Such a strategy was chosen because the fracture and damage loci are significantly different than that presented in the original paper, the measured points should be represented as exactly as possible as there is not an underlying physical explanation for the shape of the fitted curve, instead being purely phenomenological.

Geometries were chosen to provide a range of stress states; the ASTM sample in section 3.2 was used to provide data at a triaxiality of 0.3. A shear sample developed in [174] was used for triaxiality of approximately 0 and is displayed in Figure 3.8. Notched samples of various notch diameters were used for other stress states. Compressive samples of stress state $\eta = -0.3$ were tested but failure was not observed, consistent with justification for the cutoff value.

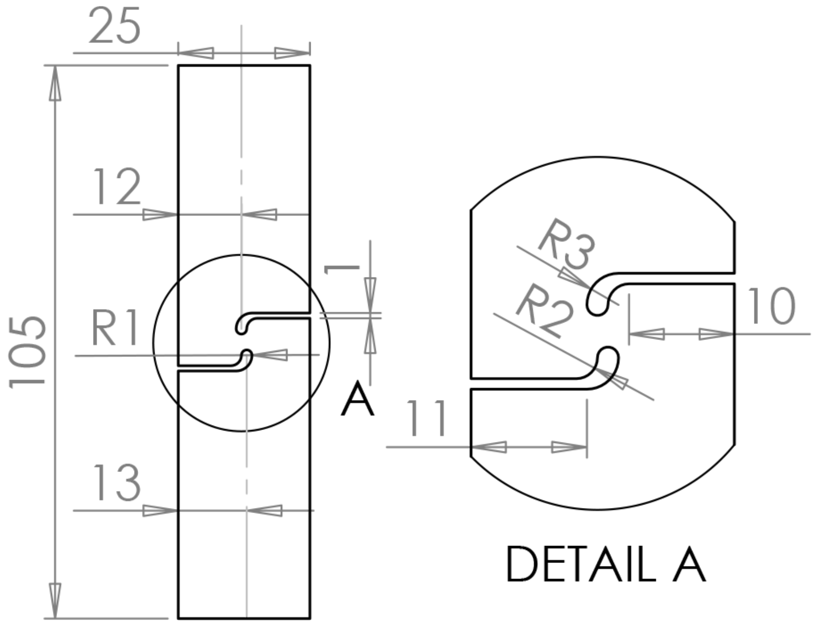

Figure 3.8: *A drawing of the shear sample used to investigate low triaxiality.*

3.6.2 Identification of fracture

The identification of fracture is typically rather simple with optical methods, however it must be remembered that fracture typically occurs subsurface by void coalescence and that the optical measurement technique of DIC requires an additional layer of paint on the surface. Other factors, such as failure modes in which the sample ‘tears’ over a number of frames, can also cast doubt on the results. In order to overcome these difficulties, the identification of the fracture strain has been achieved through the introduction of derivative terms of the strain.

A Virtual Strain Gauge (VSG) was placed at the fracture location, which provides a scalar value which is the averaged strain in the region of the VSG. The first and second derivatives are calculated, and the frame just prior to fracture is identified when the second derivative exceeds a threshold. The fracture is thereby consistently identified, which in obvious cases is consistent with optical fracture identification. The derivatives are consistently calculated with respect for the frame number as the frame number corresponds with an equally spaced image acquisition time. When the crosshead has also been moved at a constant rate the measurement is equivalent to taking the derivative with respect to the crosshead displacement. Alternatively, a strain gauge covering the entire visible sample can be used for the derivation; in Section 6.3 a comparison of the two methods is shown, proving that they are equivalent.

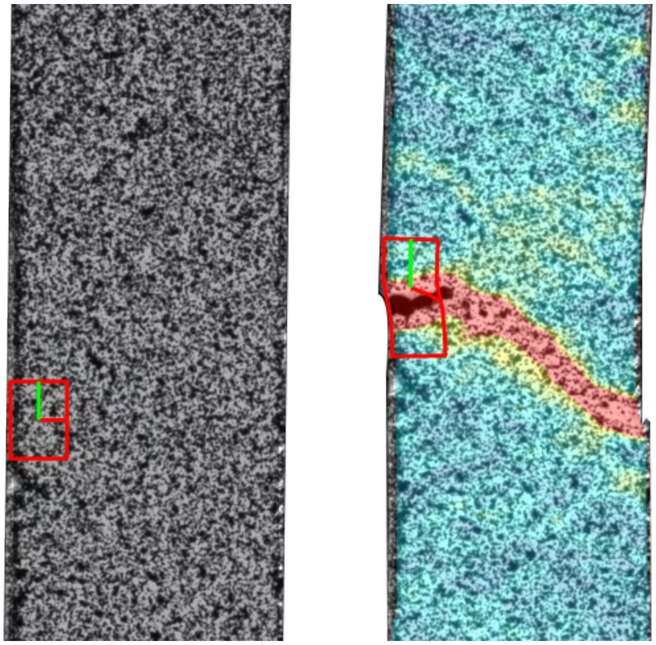

Figure 3.9: *A virtual strain gauge (red box) is applied in the region of the fracture. The VSG is 3.2x2.4*mm. *This generates the values plotted in Figure 3.10.*

3.6.3 Restraining system

Due to the desire to calibrate models on final product material, all mechanical tests must allow investigation on sheet material of thickness as low as 0.2mm. Under low triaxiality samples manufactured from such thin material buckle instead of deforming as expected. This effect is present even under perfect alignment as simulated using FEA. Consequently a requirement arose for a device allowing a variety of geometries to be restrained while also allowing DIC measurement. Figure 3.11 shows the system, wherein two 3D printed PLA sections are clamped around a sample, one section houses a sapphire glass window flush with its back surface. Sapphire glass was chosen due to its high hardness, thus reducing the likelihood of the sample scratching the glass part. The glass is designed to be removable in

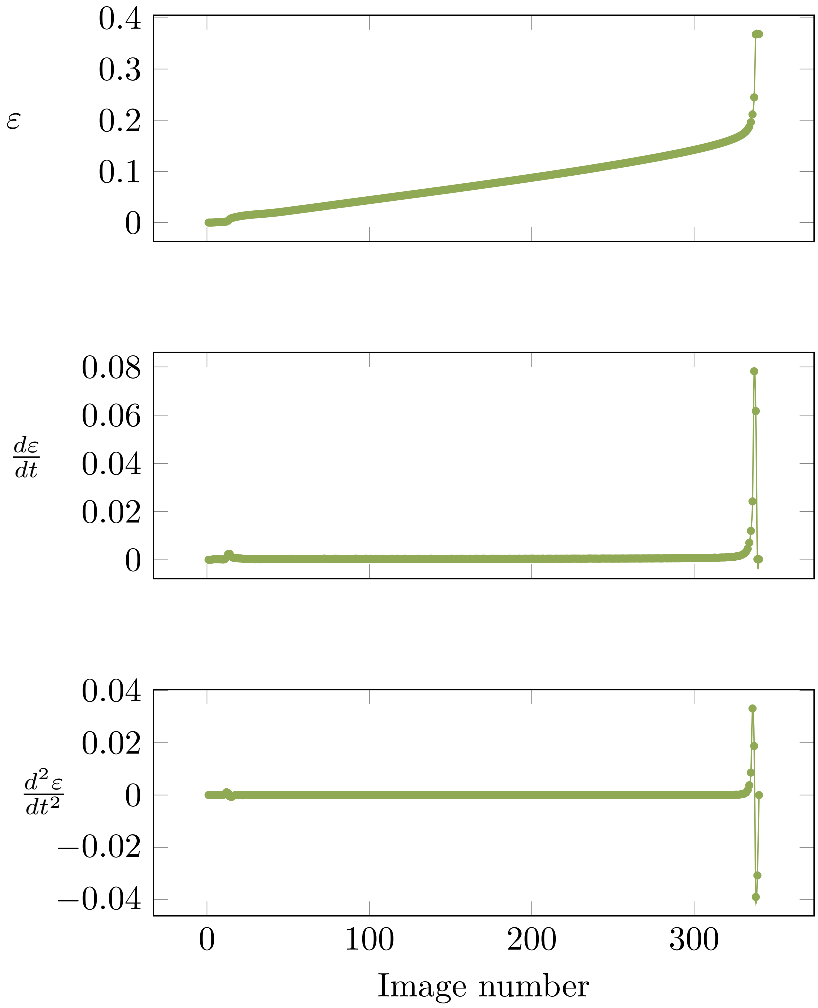

Figure 3.10: *A comparison of strain and it first two derivatives. The large spike produced is an indication of fracture.*

such a circumstance, but no scratches formed over the course of testing.

Not all samples are compatible with the restraint; the butterfly shear sample as demonstrated in [131] fails outside of the region of interest, although the behaviour of the ROI is briefly improved until this failure. It is noted that the butterfly specimen required significantly higher clamping forces to stay planar prior to breaking. This behaviour was demonstrated with both fixed and pinned configurations. A shear sample presented in [174] was however compatible, achieving a similar sized ROI with more supporting material.

The frictional effect on the force due to this restraining system is somewhat difficult to quantify. Two methods are available: as shown in Figure 3.13 the sample can be pushed through the restraint, while the restraint is fixed; alternatively the residual force after sample fracture can be analysed. Friction coefficients of the PLA and sapphire glass could also be used as an input to find the force via reverse analysis using FEA. In any case, the additional load measured does not affect the calibration strategy in this study - as the fracture parameters

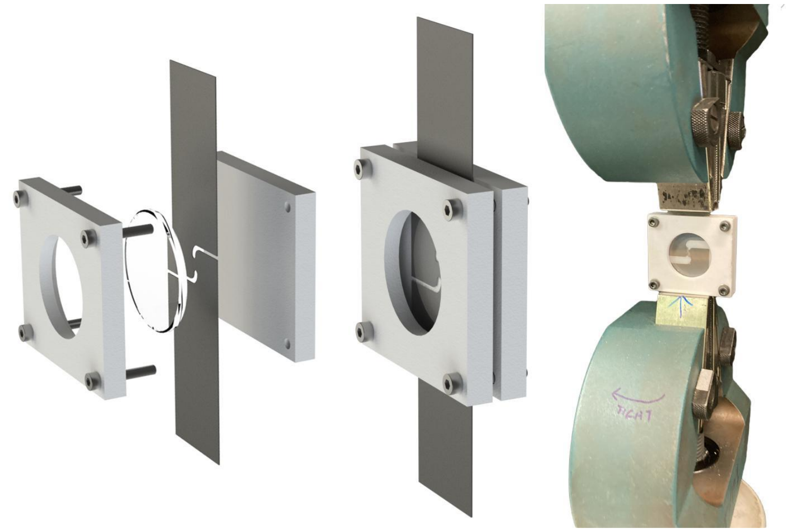

Figure 3.11: *A render of the restraining system used for low triaxiality samples. Two plastic sections, one holding a sapphire glass window, are clamped around the sample. Right: Sample in tensile machine with applied restraint.*

are calibrated using only strain, and the onset parameters require only the identification of peak force and are independent of the magnitude.

Figure 3.12: *A sample which is not compatible with the restraint and fails outside of ROI.*

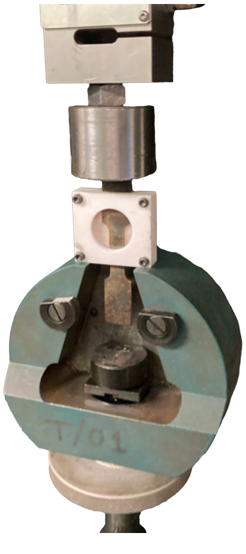

Figure 3.13: *A test of frictional forces due to the restraining system. A sample is pushed through the clamped pieces.*

The restraining system may introduce spurious strain measurements if the paint smears, dirt or oil is present on the window, or a particle of the toner becomes loose. After each test the glass piece was removed and cleaned using isoproyl alcohol. Such effects cause erroneous

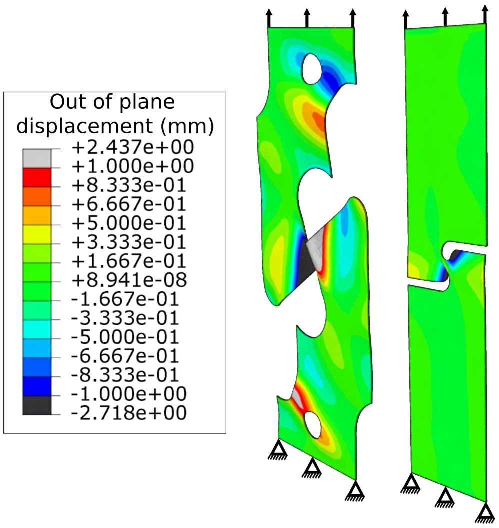

Figure 3.14: *A simulation of two shear geometries with perfect alignment, proving that the restraining system is required.*

DIC measurements, but can be minimised with proper sample preparation (an additional clear coat) and identified and discarded by studying the divergence and shear angle of the DIC vector field. The shear angle in the ROI of shear samples is approximately uniform - as any smearing occurs in the ε_{yy} direction the shear angle is affected and significantly different to the uniform field. Though 2D divergence of the vector field in the x,y plane should be close to zero because the amount of material is not changing, in reality a small amount of divergence is always present due to the Poisson effect - although, values significantly higher than background level also indicate smearing has occurred.

3.6.4 Low magnetic field damage measurement

The thin geometries used in the study meant that the magnetic field from a strong permanent neodymium magnetic was detectable through the sample at low intensity. This property was exploited in an attempt to correlate the field strength with damage onset and fracture. The magnetic permeability of the material is significantly higher than that of the atmosphere, and thus the magnetic flux lines preferentially flow through the sample. Detection of the residual flux was achieved by means of a Hall Effect sensor placed in opposition to the magnet. When the sample is strained the magnetic properties are degraded, giving rise to a lower flux reading, however this reading eventually increases upon fracture, presumably due to a combined effect of void content, crack initiation, and necking.

A *Honeywell SS494B-T2* linear Hall Effect sensor was used in conjunction with a *National Instruments USB 6002* DAQ to acquire flux measurements, and was lightly held against the surface of the sample using clear tape. An *RS PRO* neodymium-iron-boron magnet of dimensions 25 mm x 10 mm x 3 mm was attached to the other side of the sample to provide the magnetic field.

3.7 Two Stage Geometry

Because the edge effect of the sample preparation method was a concern, an alternative to existing two stage post deformation triaxiality shifting samples such as presented in [175] where the sample is cut after the initial deformation was desired. A geometry based upon the ASTM-E8 sample was created, with additional grip sections centrally and perpendicular to the sample. A reduced section was also added to help localise deformation to ensure subsequent shearing was possible. The new geometry is displayed in Figure 3.16. A further benefit to this geometry is that both decreasing and increasing triaxiality steps may be assessed (i.e. shearing to tension, or tension to shearing). The significant deformation in the region of interest does however make the triaxiality calculation more challenging.

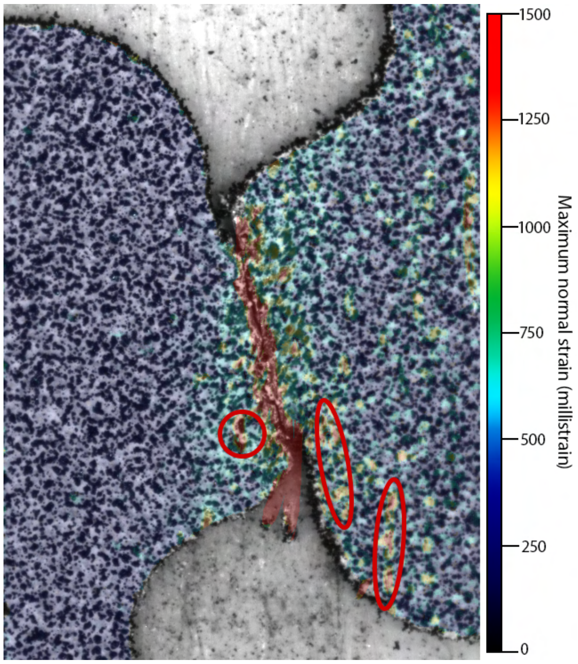

(a) *A restrained shear sample with some spurious strain highlighted with red ellipses*

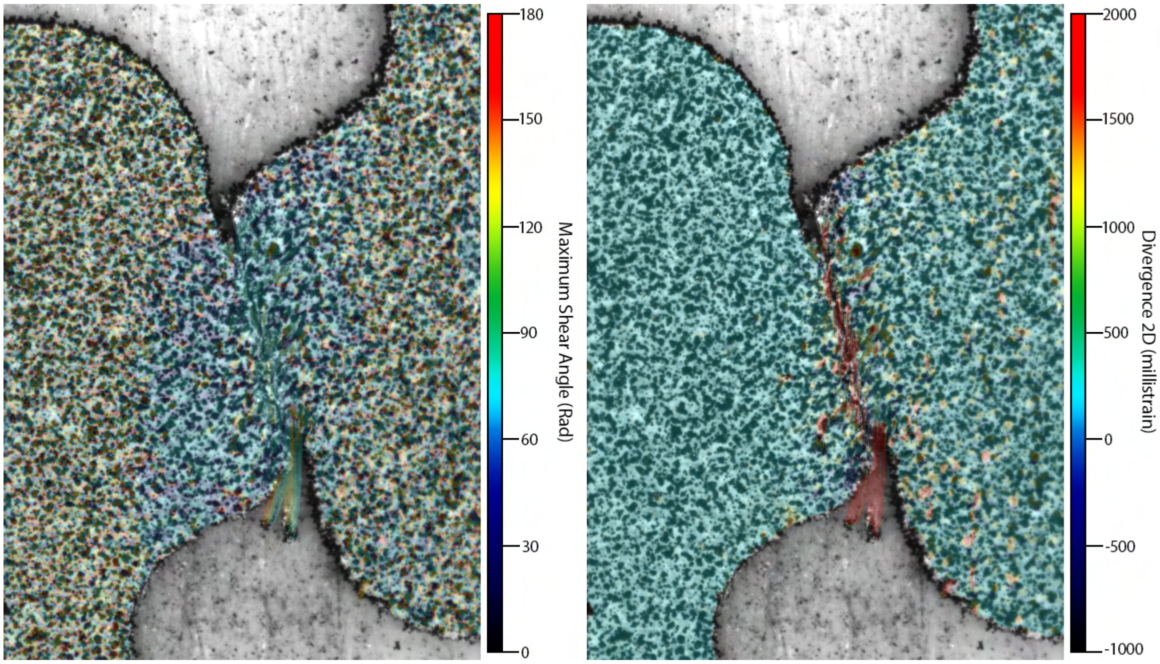

(b) *The maximum shear angle*[a] *field is uniform in the shearing region, but random in non shearing locations and locations of spurious strain*

(c) *Divergence is high in some locations indicating the possibility of spurious strain*

Figure 3.15: *Different scalar field quantities are analysed to ensure strain measurements in restrained samples are correct. The as measured strain is shown in (a), which is compared with (b) and (c) to ensure the strain measurement in the ROI is not erroneously high due to effects from the restraint*

---

[a] The unit of Radians is correct, the shear angle is calculated as $\arctan(\varepsilon_{xy} + \varepsilon_{yx}, \varepsilon_{xx} - \varepsilon_{yy})$, the angle may fall outside the interval $(-\pi/2, \pi/2)$

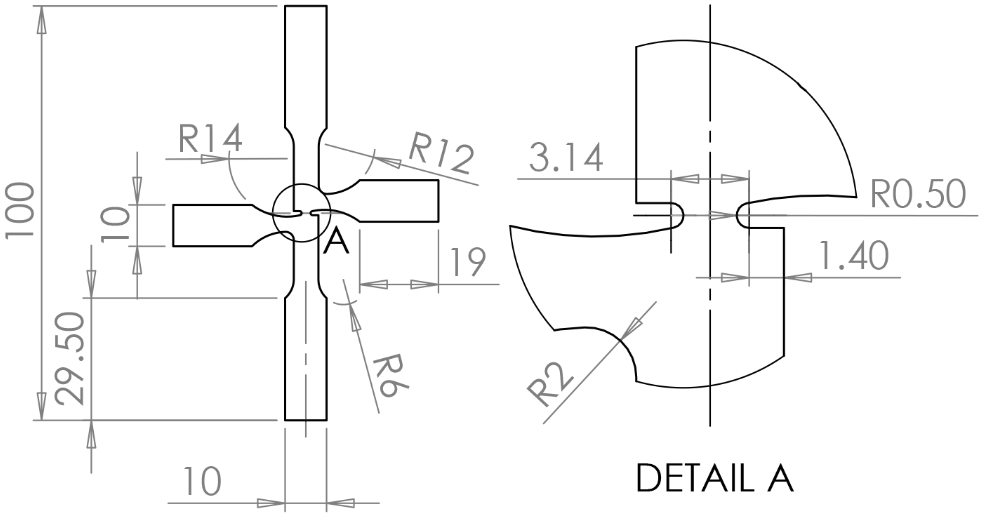

Figure 3.16: *A new two stage sample for introducing triaxiality changes mid deformation.*

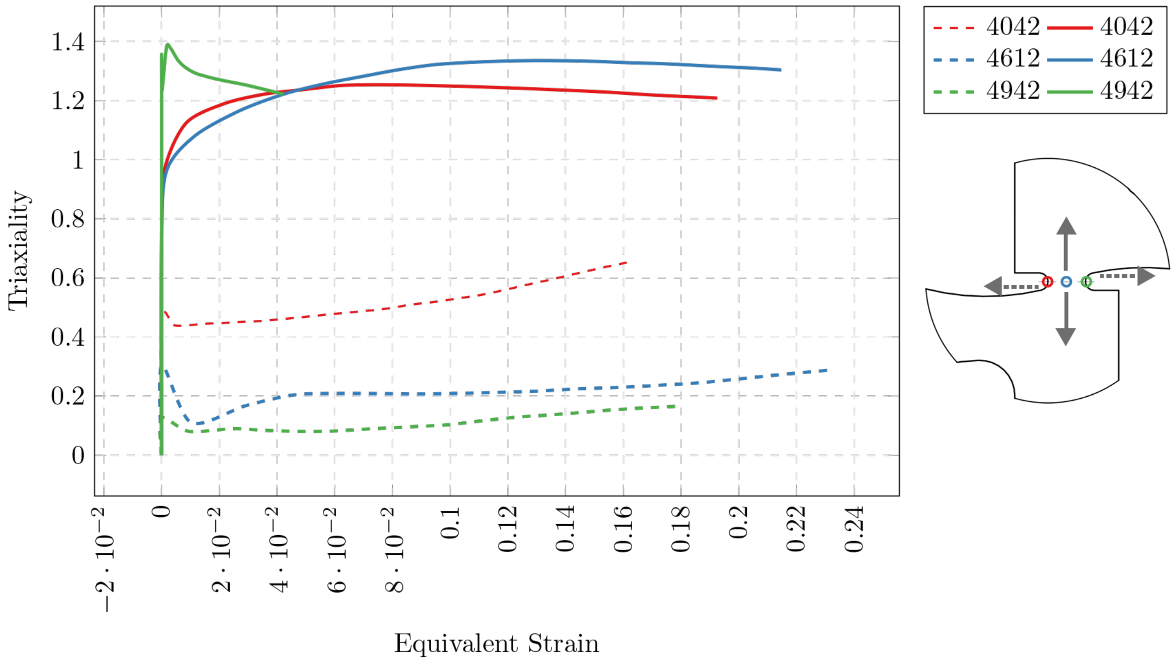

Figure 3.17: *A plot of the triaxiality against equivalent strain at three locations across the region of interest and under different loading modes.*

3.8 X-Ray Microscope Computed Tomography

A Zeiss Xradia 620 Versa X-ray Microscope (XRM) was used in conjunction with an in-situ Deben CT5000N TEC tensile testing rig with 500N load cell to investigate the progression of failure in a 0.5mm wide sample.

Due to the high density of the material X-ray penetration is low; additionally, due to the high aspect ratio inherent in samples manufactured from sheet stock, ascertaining an acceptable exposure for thin and thick faces presents a great challenge. For these reasons an extremely small sample was developed, such that the thickness of the region of interest approximated the thickness of the sheet. Such a small ROI ensured that handling and set-up of the sample would almost certainly destroy or deform it, and therefore additional supporting structures were required. The supporting structures were designed to be cut away once the sample was secured in the rig. Figure 3.18 shows the sample geometry with supports and as scanned, Figure 3.19 shows the sample being set up in the Deben rig, prior to supports being cut away.

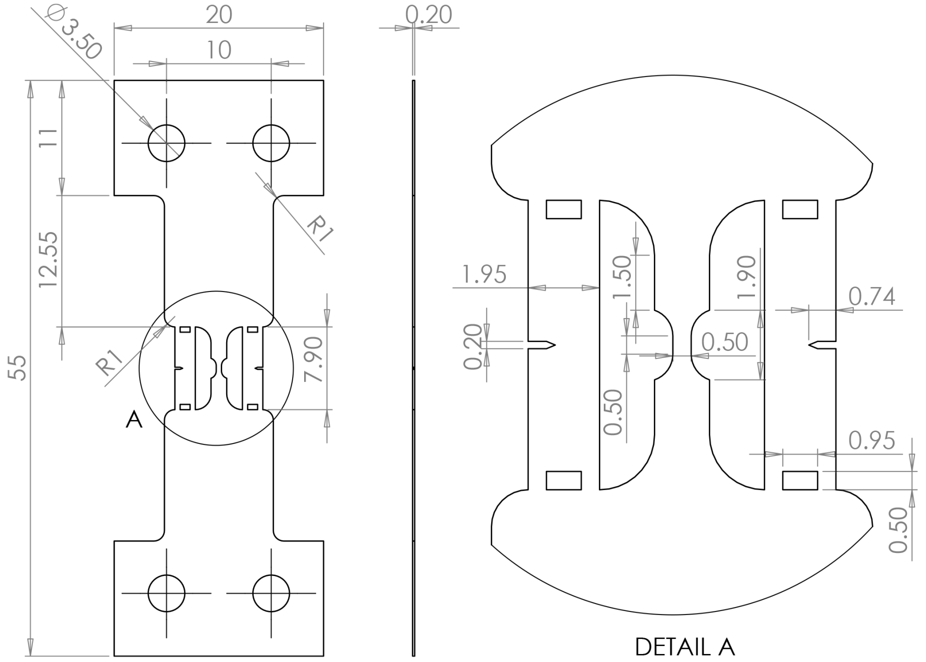

Figure 3.18: *μCT sample with removable support struts.*

The physical size of the rig means the X-ray source is fairly far from the sample, effectively reducing penetration. Due to this constraint, and the already high material density, a 4x objective with binning of 4 was chosen to ensure the exposure time was relatively short. A short exposure time is highly desirable when using the in-situ rig, as many scans are required per sample. A filter was used to remove low energy X-rays. Table 3.4 shows the parameters used.

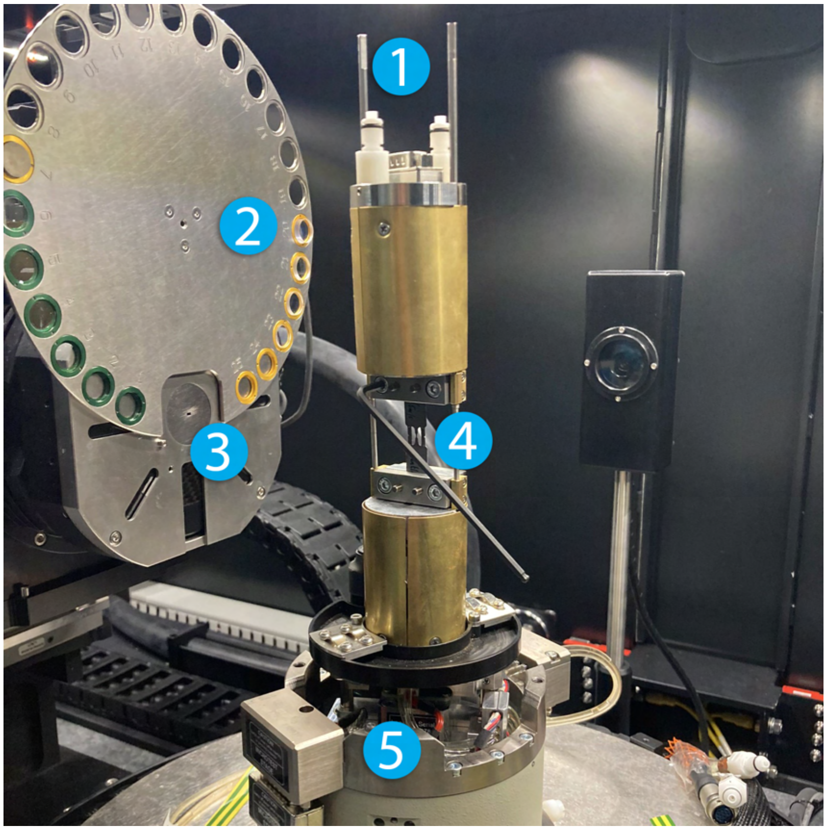

Figure 3.19: *μCT sample being set up in tensile rig. 1: Temporary support struts for setup, 2: Filter wheel, 3: X-Ray source, 4: Sample, 5: Load cell. The top half of the rig is removed for setup.*

Parameter	Value	Parameter	Value
Source Voltage	160kV	Voxel size	2.49μm
Source Power	25W	Exposure	1s
Objective	4x	Projections	1601
Binning	4	Filter	HE6

Table 3.4: *Scan settings used in this study*

3.9 In-situ blanking

An open faced blanking rig developed in [2] was extended to ensure plane strain conditions at the measurement face by the use of a sapphire glass window held parallel and in contact to the open face with a slotted angle piece. As such, the ability to take optical measurements remained while ensuring no out of plane deformation was possible. Due to the very high speed nature of blanking and extremely small working area a high speed camera system was required. A Phantom VEO 410L high speed camera was used to capture images at 5 kHz at a resolution of 1280x608 pixels and 16 bit depth. A Miniconstellation 120C28 5000K LED light was used to light the sample, the frequency and pulse length being equal to the frame rate and exposure time of the camera. A high magnification telecentric lens was used to provide a field of view of approximately 4 mm x 6 mm.

Strips as received of dimension 300 mm x 30 mm were cut into four sections of 75 mm x 30 mm using tin snips. This size allowed the sample to be adequately clamped between the die block and sample holder without protruding from the rig.

A worn punch was compared with a newly ground punch to investigate the influence of the complex stress state arising from wearing tools. The worn punch had a diameter of 0.57 mm and the reground tool had no detectable radius. The two tools are compared in Figure 3.20

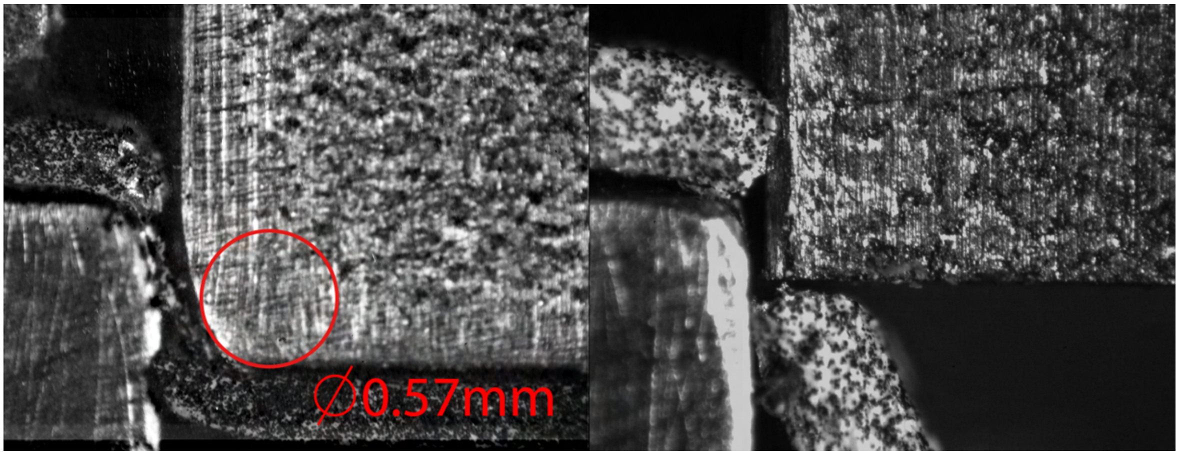

Figure 3.20: *A comparison of the worn and reground tooling.*

3.10 Optical profilometry

Upon deformation sample surfaces become rough, the so-called *orange peel effect*. This roughness post deformation is suggestive of inter-grain movement via deformation at grain boundaries, as a supplemental mechanism to intra-grain deformation by dislocation movement. Additionally, the effect of sample edge surface roughness on the fracture strain was investigated, in order to ensure the fracture was not a result of a stress riser. A Bruker Contour Elite white light interferometer was used to acquire the topography of deformed samples. The deformed topology can be compared between low and high strain regions via coupling to DIC measurements, and the roughness and bulk crystallographic deformation used to infer the relative contribution of the aforementioned deformation modes. Figure 3.23 shows the rough texture developed under deformation in the vicinity of the fracture, although this texture develops throughout the plastically deformed region. To obtain data across the full sample, several measurements were stitched together. In a similar manner, optical profilometry was used to capture the surface roughness at the cut edge, in order to ensure samples did not fracture due to stress risers caused by the manufacturing method. Table 3.5 shows the settings used to obtain the images, because the texture was pronounced, a large backscan and length value were required.

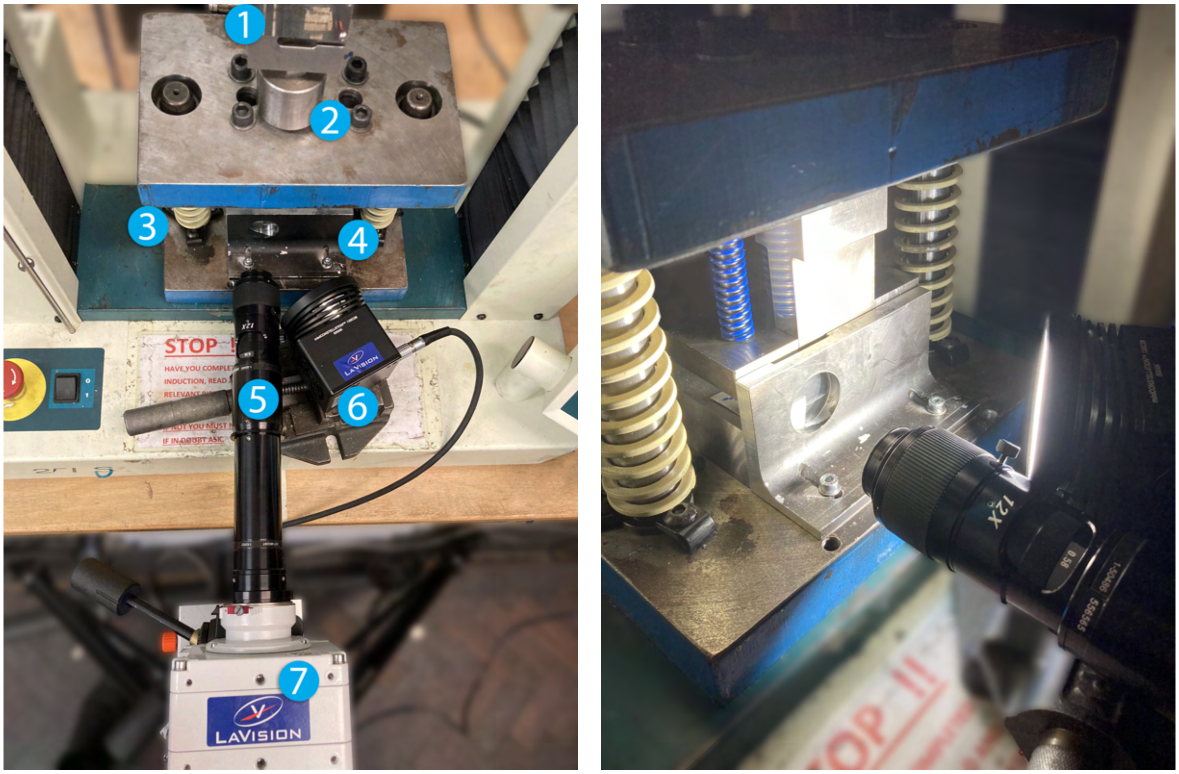

Figure 3.21: *In-situ strain measurement in blanking. 1: Load cell, 2: Compression head, 3: Blanking rig body, 4: Restraining window, 5: High magnification telecentric lens, 6: High speed LED strobe, 7: High speed camera.*

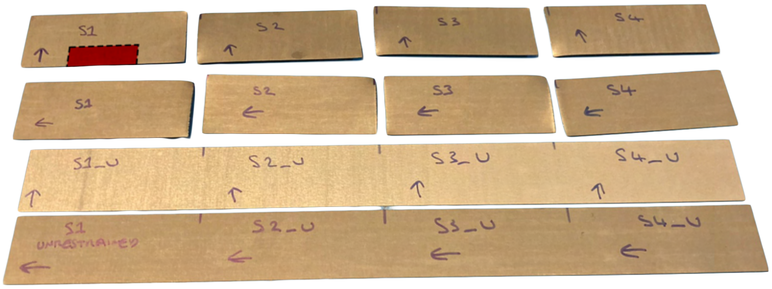

Figure 3.22: *Samples for the blanking rig in strips and once cut. The red overlay in the top left sample indicates the size and location of the blank once cut*

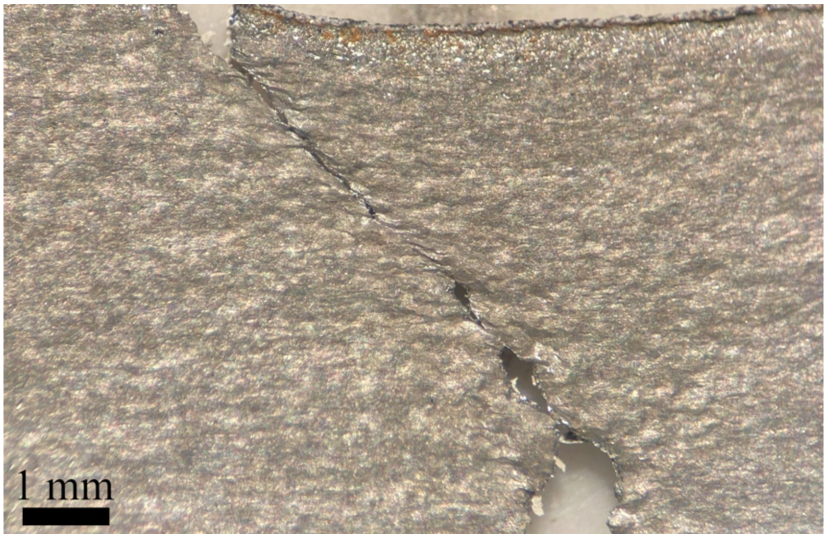

Figure 3.23: *A micrograph of the rough texture developed during deformation.*

Parameter	Value
Processing method	VSI
Backscan	10 µm
Length	30 µm
Threshold	5%
Averaging	Off
Objective	5x

Table 3.5: *The settings used to obtain the interferometer measurements*

Chapter 4

Experimental Results

In this chapter, the experimental results are detailed. The majority of the work stems from the development of a calibration procedure for the finite element model, focusing on the fracture in various sample geometries. By far the most common fracture initiation site was observed to be the edge of the samples, prompting an investigation into the sensitivity of the results to various possible manufacturing methods, each with varying edge roughness and possible heat effects. Similarly, the sensitivity of the sample to small misalignment is reported, to ensure a sound foundation for the fracture results. The results will demonstrate that the edge roughness and sample alignment cannot solely explain the fracture behaviour of the material, and the size effect must be a contributing factor. Aside from the work that forms a calibration for the FEA, the material at several stages prior to the final grade of NO20 (0.2mm) was investigated in a similar manner. Investigation of the influence of the material thickness is an important step in validating size effect presumptions, and may form the basis of further work in modelling the whole manufacturing process chain. The microstructure of semi-finished products is compared with the NO20 grade using EBSD, proving the validity of the mechanical comparisons. The effect of the edge cutting method on the specific loss is also reported for remote laser cut samples. An attempt to observe the fracture initiation mechanics sub surface is reported using a micro-scale sample in an x-ray microscope; although the resolution was too low to observe void initiation and growth, the deformation history is of interest displaying highly similar fracture as macro-scale samples. Digital image correlation was employed heavily in the investigation, and the validation and error estimation is described in detail in this chapter. A metric for speckle quality was adapted from a compression algorithm which provides an entropic criterion with a meaningful two dimensional aspect, and a number of test cases and representative experimental images are presented with this metric alongside other published methods.

4.1 Microstructural characterisation

The microstructure of the sample was investigated using EBSD to measure the grain size, and the assumptions of equiaxed grains, with no preferred orientation was confirmed. In order to do this the coating and first few microns of the surface of the material were removed, and the figures in this section are presented in the RD-TD plane. Figure 4.1 shows a large area scan of NO20 material, an average grain size of 150 µm is found. Figure 4.4 displays the results of the hardness taken of the scanned surface in Figure 4.1. In the background of this figure a reference of the average grain diameter of 150 µm is shown as alternating grey stripes. The indentations were aligned relative to the scratch, although no correlation can be made between the map produced from EBSD and that of hardness values. The hardness values do, however, align roughly with the average grain diameter, indicating some effect may be detectable with further work.

Figure 4.3 shows grains of approximately 150 µm after annealing, the microstructure is the same as the 0.2mm product shown in Figure 4.1. Pitting is visible due to over-etching from the colloidal silica step. This proves the microstructure of the 0.5 mm precursor annealed material is identical to the NO20 product.

The highly distorted microstructure shown in Figure 4.2's EBSD image, grains are elongated along the rolling direction. The index rate is much lower than in other images due to the residual strain in the material.

Tables 4.2 and 4.3 contain information of the scan settings and hit rate for the EBSD results. It is shown that the highly distorted microstructure of the annealed material has a significantly lower hit rate due to internal stresses.

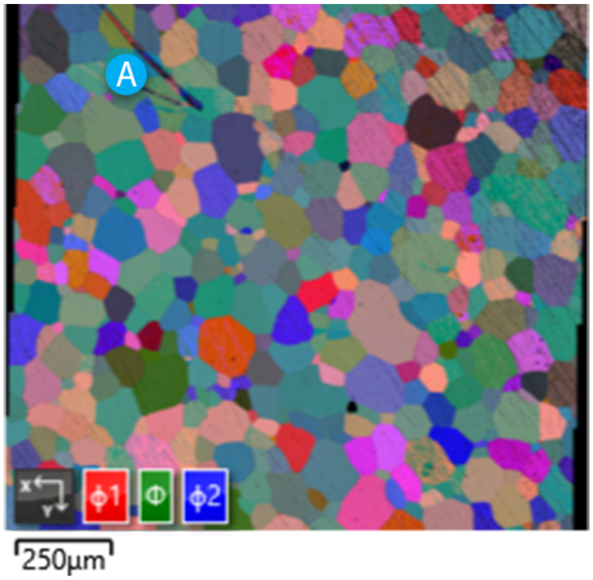

Figure 4.1: *Large area EBSD Euler colour plot for 0.2mm NO20S9000 product, damage from a scratch is visible at (A).*

Using the information gathered in this section, further investigation of the thinnest product, NO20, is undertaken in the rest of the work. This material is of interest because of the

Parameter	Value	Parameter	Value
Source Voltage	20kV	Step Size	1 µm
Acquisition Rate	107 331 Hz	Hit Rate	96.69%

Table 4.1: *EBSD scan setting information for NO20*

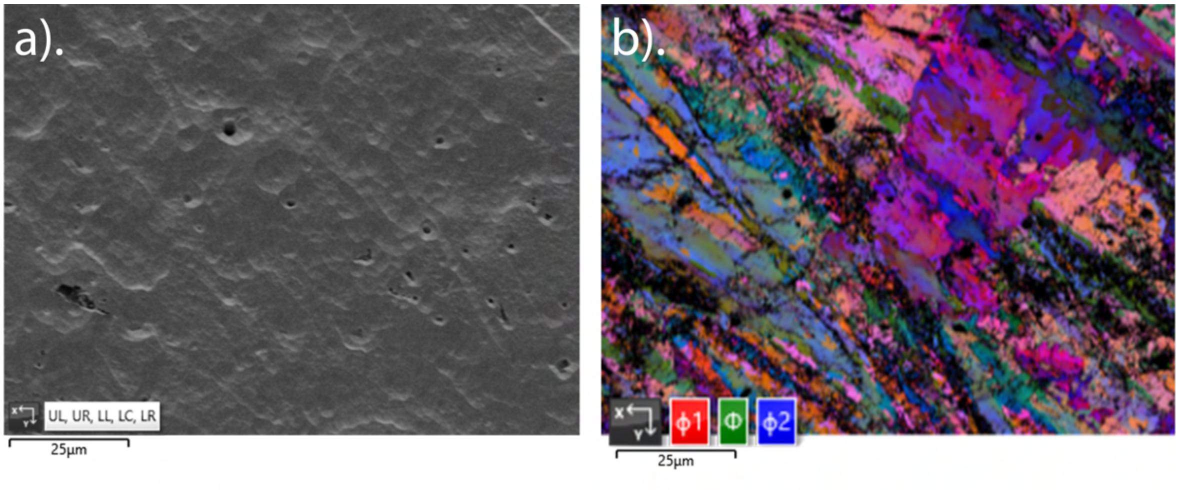

Figure 4.2: *(a) SEM image and (b) EBSD Euler colour plots for 0.5mm cold rolled material*

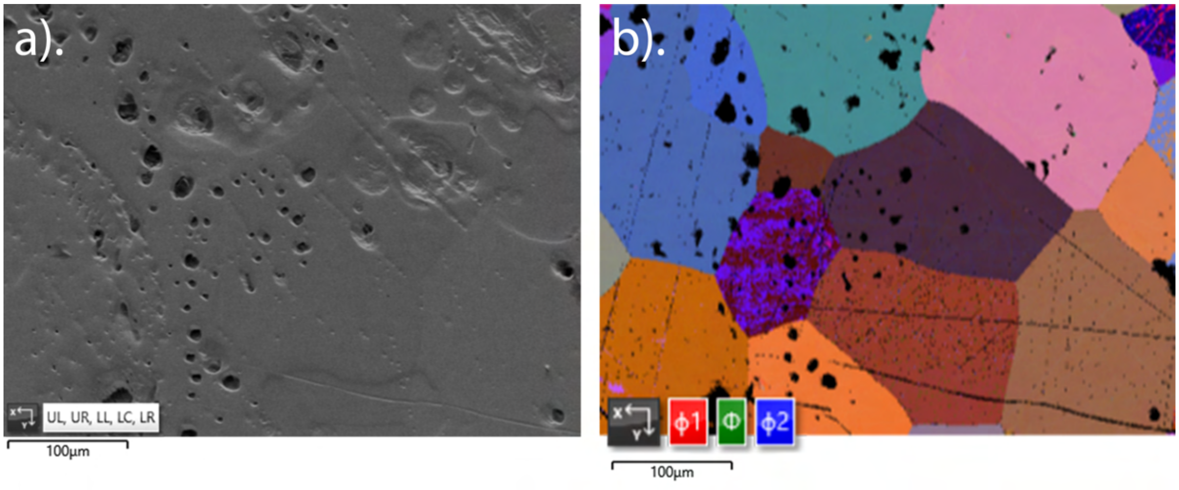

Figure 4.3: *(a) SEM image and (b) EBSD Euler colour plots for 0.5mm final annealed material*

Parameter	Value	Parameter	Value
Source Voltage	20kV	Step Size	1 µm
Acquisition Rate	476.95 Hz	Hit Rate	94.96 %

Table 4.2: *EBSD scan setting information for 0.5mm FA*

Parameter	Value	Parameter	Value
Source Voltage	20kV	Step Size	1 µm
Acquisition Rate	192.80 Hz	Hit Rate	67.03%

Table 4.3: *EBSD scan setting information for 0.5mm CR*

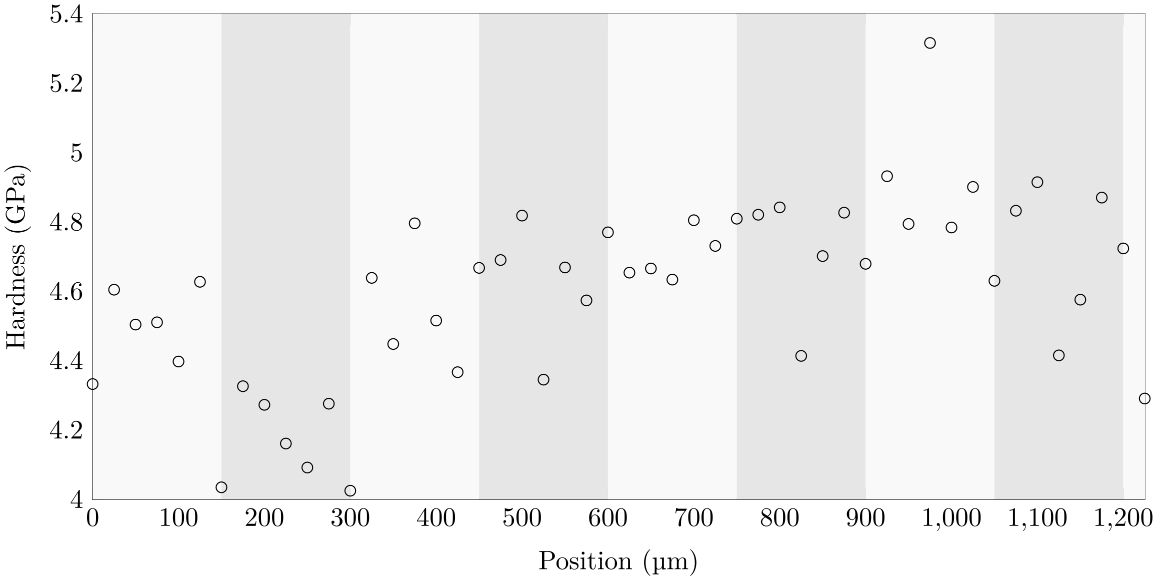

Figure 4.4: *Hardness measurements in the sample shown in Figure 4.1. The striped background indicates the average grain size of* 150 µm.

large grain size of on average 150 µm in comparison to the sheet thickness of 200 µm was hypothesised to produce significant size effects.

4.2 Influence of cut method

Recognising that the microstructure of the material will have an influence on the material properties using the results obtained in Section 4.1, care must be taken in the preparation of all samples to ensure that the cutting method does not introduce bias into the results due to microstructural changes. The influence of the cutting method used to generate the sample geometries is investigated in this section by comparing three cutting methods, waterjet, laser, and wire electrical discharge machining (EDM). It is known that stress risers can cause fracture by stress concentration and thermal processes can locally alter the microstructure or introduce residual stress. Due to the low forces involved in testing the material it is critical that any such influence be identified and eliminated to avoid biasing the damage model calibration.

4.2.1 Force - Displacement comparison

The sensitivity of the preparation method on the force - displacement material response was tested. Due to the low number of grains it was hypothesised that heat generating methods may significantly influence the results by causing microstructural changes at the cut edge. Figure 4.5 shows representative force - displacement curves for each cutting method trialled, it can be seen that there is a large influence on the displacement to fracture depending on the preparation method.

A highly localised strain measurement at the fracture site is then compared for the same sample sets in Figure 4.6. In each case, the physical size of the subset was chosen to be 0.3 mm meaning the results are directly comparable. The speckle quality is comparable across samples, each containing at least 3 features per subset, with random distribution and good contrast, although the quality is lower in the EDM samples due to larger speckles.

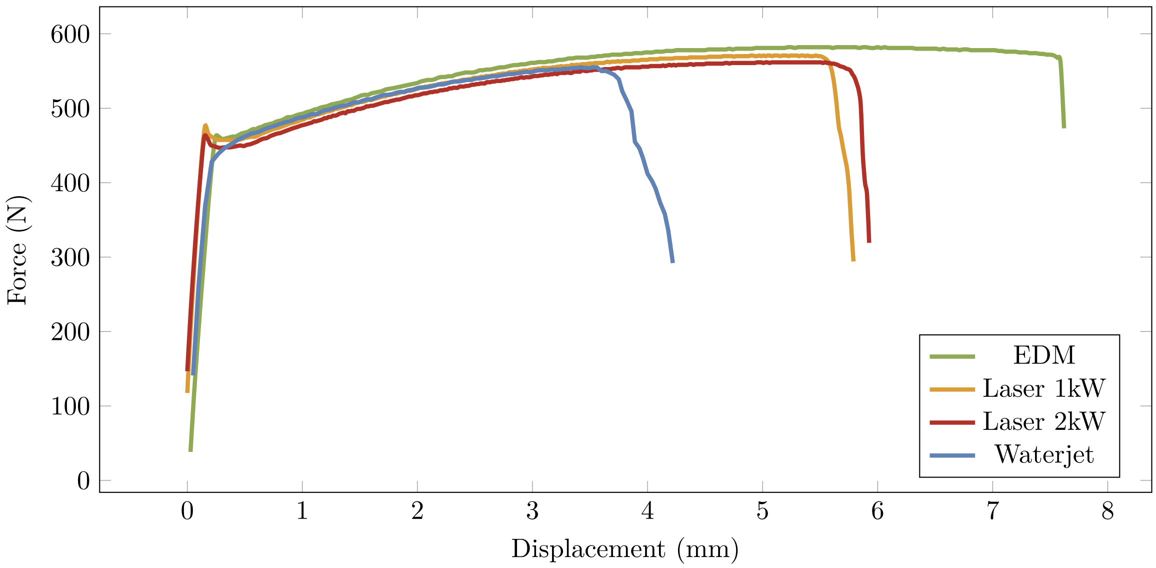

Figure 4.5: *Representative force-displacement results from different preparation methods*

Little difference was observed in yield and hardening behaviours between all sample types, although fracture behaviour was significantly different if observing total displacement at fracture. Waterjet cutting produced the smallest displacement at failure, possibly due to stress risers from a comparatively rough edge.

Digital image correlation was used to observe the strain field for these compared sample types, and it was found that the fracture strain was constant between all sample types, although the overall deformation changed. In samples produced via waterjet cutting, less overall deformation was observed prior to strain localisation, however, the localised strain was equivalent to other preparation methods. Samples prepared using EDM produced greater overall deformation, and the strain gradient at fracture was lower than in other sample types.

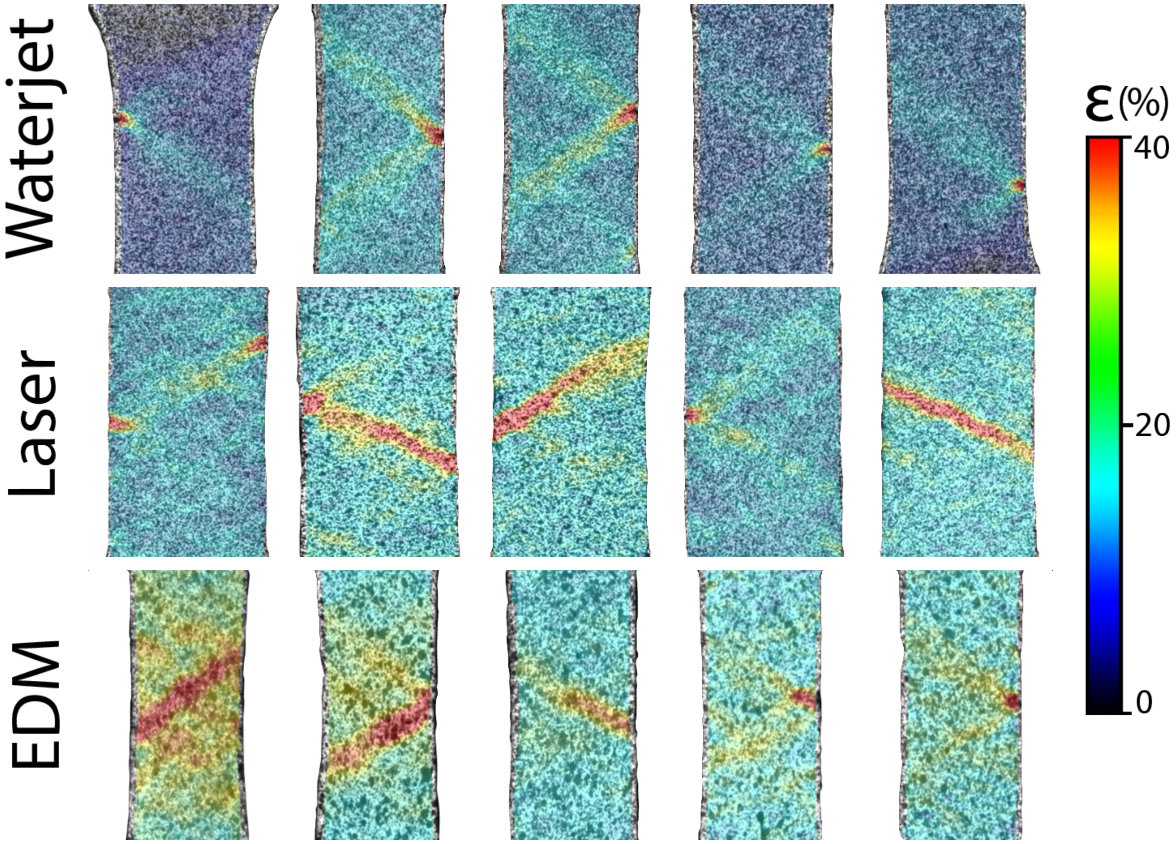

Figure 4.6: *Deformation at fracture for a selection of samples with various preparation methods. Maximum normal strain is overlaid as a colour map.*

4.2.2 Effect of cut method on edge quality

The effect of the cutting process on the edge quality was investigated in this section by comparing the surface roughness. This is justified by the potential for edge roughness features to act as stress risers, which have a significant influence due to the material thickness. Raw waterjet cut samples do have higher roughness than the other methods, which are comparable, but this is minimised by sanding. A con-focal light microscope was used to measure the surface roughness and morphology of samples with varying preparation methods. The best surface quality was observed in the EDM samples and the worst in the waterjet as machined without further preparation. Figure 4.7 shows the difference in surface morphology for these sample types. An important feature to note is the flatness of the edge along the transverse direction (short axis). During the waterjet preparation method, one edge will be preferentially eroded due to the cone of the jet. In the context of premature failure from the generation of a stress rise, this is not a concern; stress risers will occur due to lateral defects across the thickness of the sample, parallel to the loading direction. For this reason, a line profile roughness measurement is a more appropriate measure than a surface roughness measurement. The primary parameter is chosen as opposed to the roughness, as the large features on the surface should be considered in the measurement in the context of stress risers, and these would be filtered away by the high-pass filter if using roughness.

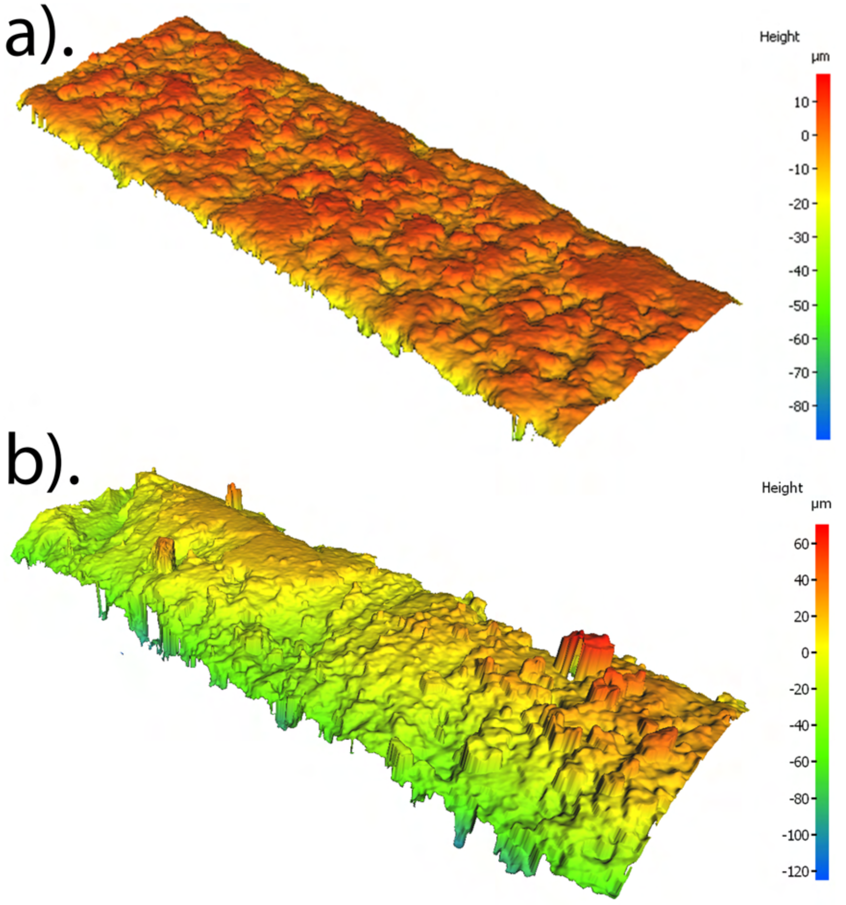

Figure 4.7: *An example of the difference in edge quality for (a) EDM and (b) waterjet samples.*

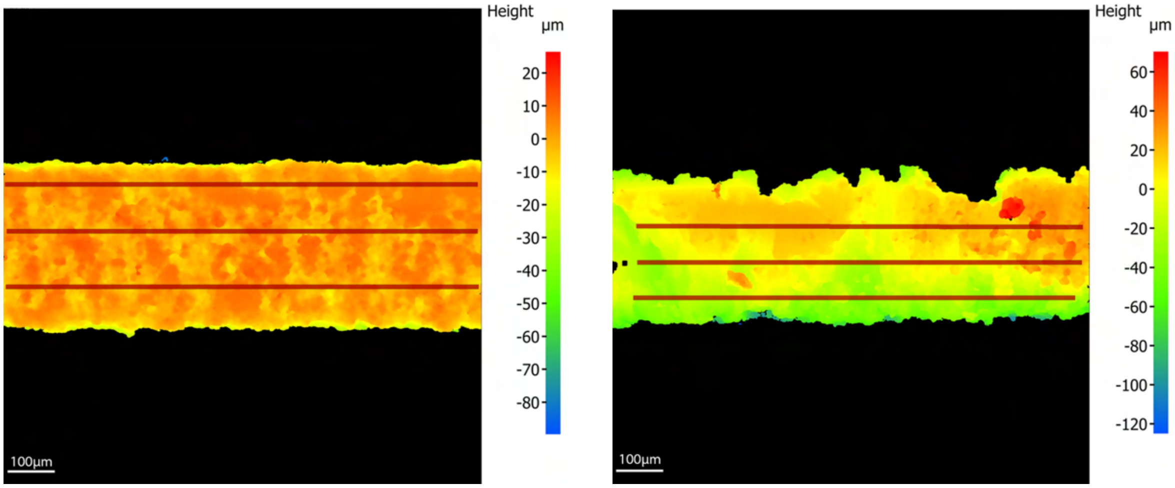

(a) **(b)**

Figure 4.8: *Line profile measurement locations in dark red for the samples shown in Figure 4.7. (a) EDM, (b) Waterjet*

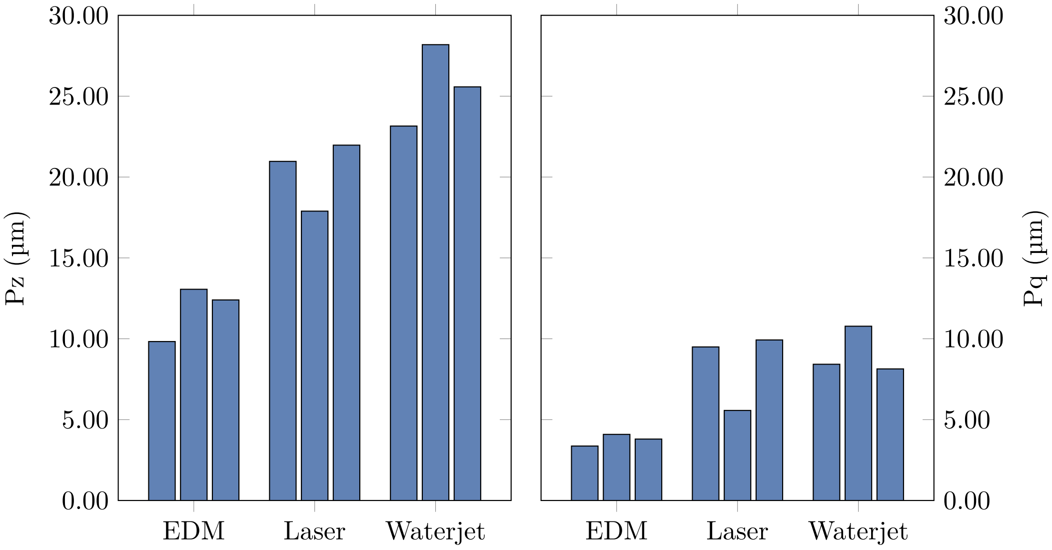

(a) **(b)**

Figure 4.9: *Line profile roughness for different preparation methods. (a) Pz, the mean peak to valley height, (b) Pq, the root mean square height of the profile.*

4.2.3 Inherent variation in mechanical properties

Figure 4.10 shows the variation observed in force - displacement curves for 12 samples manufactured with two laser power parameters, all in the RD. It is shown that a large range of displacement to fracture is measured, which could be due to the low number of grains partaking in the deformation. Similar scatter is found with other preparation methods and in other sample directions. A range of approximately 1 mm is observed wherein the sample may fail; an outlier is also observed at approximately 3.6 mm which is likely due to an edge imperfection causing a stress concentration. Figure 4.11 demonstrates that fracture strain determined by DIC at the fracture site has relatively low variability in comparison and should be preferred for the calibration of a numerical model. Figure 4.12 demonstrates that the fracture strain measured by this method does not vary by preparation method more than 10%, which compares extremely favourably to the large variation demonstrated in Figure 4.5 where the displacement to fracture has just under a 100% difference between the lowest and highest methods. Further effects of laser cutting parameters have been investigated in Appendix D, as this method was required for the manufacture of the samples used in the x-ray microscope.

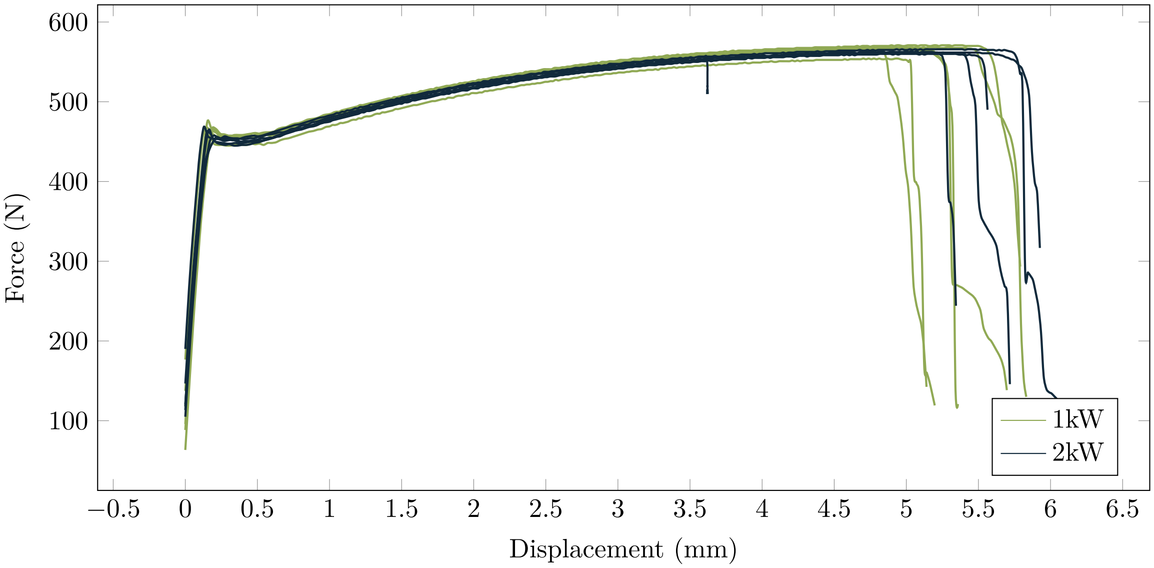

Figure 4.10: *The scatter in fracture displacement for RD samples prepared with two laser parameters.*

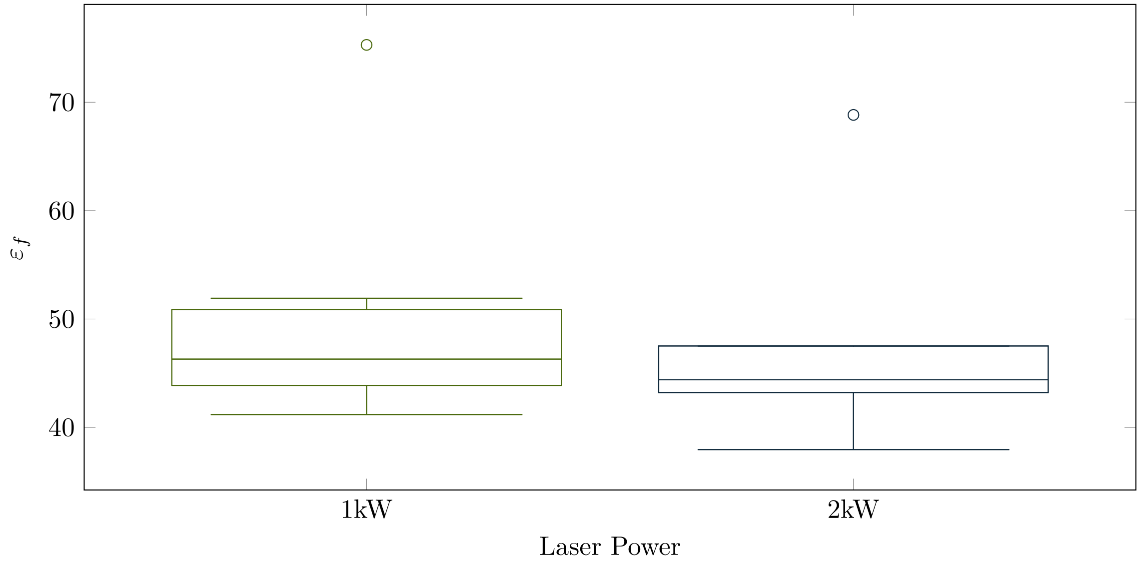

Figure 4.11: *Fracture strain comparison for the same samples displayed in Figure 4.10. ε_f refers to the maximum normal strain using a log strain tensor.*

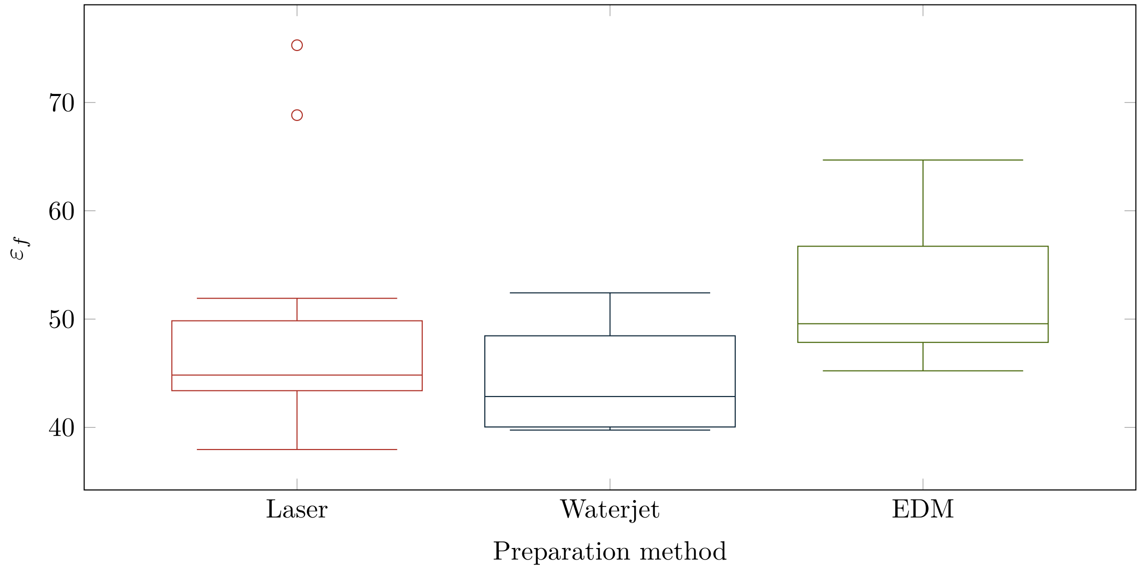

Figure 4.12: *Fracture strain comparison for different sample preparation methods. ε_f refers to the maximum normal strain using a log strain tensor.*

4.2.4 Conclusion

In this section, the influence of the preparation method on edge quality and subsequent fracture values for use in a numerical model has been demonstrated. A very large influence is found in the overall deformation at fracture, and no clear 'best' cutting method for the calibration of a numerical model can be justified. Both laser cutting and EDM may produce thermal effects at the cut edge, which retard crack initiation, and the possibility of fracture due to stress risers in waterjet cut samples is evident by the higher roughness. Moreover, the inherent scatter in sample force and displacement at fracture no matter the preparation method, as determined via typical means such as the use of a load cell and extensometer, has been shown to be so large as to be unreliable. Such variation is likely caused by the size effect, i.e. the large grain size compared to the bulk material size, causing significant anisotropies.

By using the strain at the fracture initiation site as determined by high-resolution DIC measurement, with disambiguation provided by the study of the first and second strain derivatives with respect to time (as outlined in 3.6.2), it is possible to generate a measure of fracture that is consistent with any sample preparation method. Using this method, it is shown that EDM may have an additional effect on the specimen, possibly due to highly localised microstructural changes and residual stress generation at the cut edge, which is shown as a slight increase in fracture strain compared to the other methods. Further evidence for this is provided by the strain distribution, where strain localisation occurs over a larger area and fracture initiation is more frequent away from the edge of the specimen than with other preparation methods.

The influence of laser power on the plastic flow and fracture has been demonstrated to be negligible, and further investigation is included in Appendix D. For the reasons found in this section, it was determined that further samples for calibration of the damage model are to be prepared using waterjet cutting to ensure no thermal edge effects affect the fracture. Only samples that require features smaller than possible with waterjet cutting will use the laser cut method, as this has also been shown to have a comparable distribution of fracture strain.

4.3 Influence of material orientation

Now that the methodology of highly localised strain measurement for obtaining consistent fracture results has been tested and proved to be acceptable for this material, the influence of the sample orientation with respect to the rolling direction of the material should be confirmed. In order to determine if the material orientation was a significant factor in the plastic flow and damage mechanisms, the material was tested in the rolling direction (RD), the transverse direction (TD), and at 45°. Due to the microstructural characterisation presented already, little to no effect is expected; however, such an assumption is confirmed in this section.

For the purposes of this study, the damage-onset strain is considered as the strain at which the ultimate tensile strength occurs, which may be easily identified by the DIC image taken at the moment the peak force is detected. The fracture (ε_f) and damage onset (ε_i) strains are reported using the localised DIC method in Figure 4.13. The results are a combination of laser and waterjet cut sample types; EDM samples were excluded, as justified in Section 4.2.4. No discernible effect on the two strain values due to orientation is observed. In these plots, the outliers are displayed as solid dots, defined as $\varepsilon > Q_3 + 1.5IQR$, where Q_3 is the 3rd quartile and IQR is the inter-quartile range. The reason for these may be due to the painted surface not acting as a strain witness in those samples.

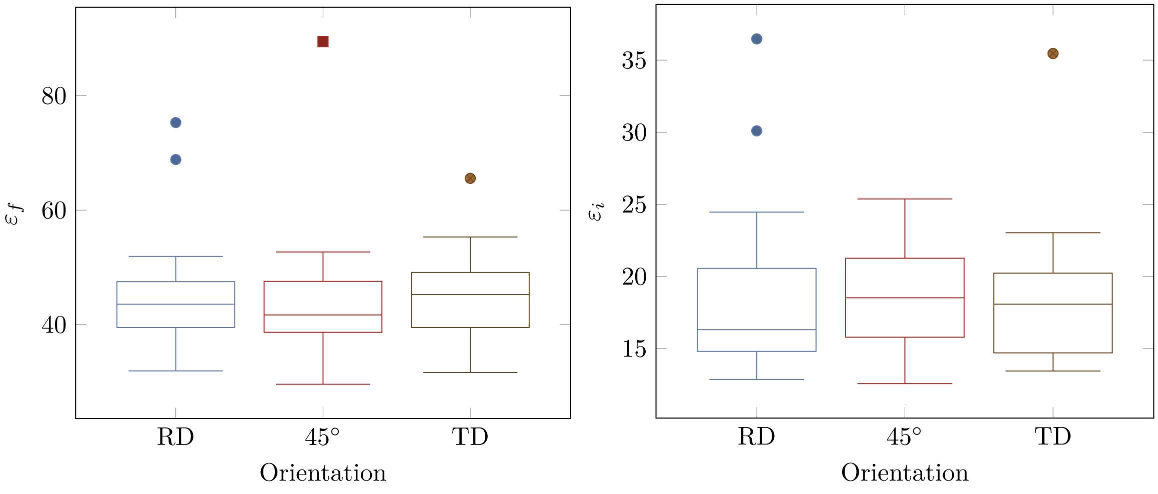

(a) (b)

Figure 4.13: *Boxplots of the (a) fracture strain ε_f and (b) the damage initiation strain, ε_i, with respect to the orientation the sample was manufactured from.*

4.4 Fracture with degraded blanking conditions

In this section, *degraded blanking conditions* refers to the condition of a worn tool and larger than ideal clearances. A variety of degraded blanking conditions were investigated by using a worn tool with a radius of 0.57 mm and two sample thicknesses of 0.2 mm and 0.35 mm to produce clearances of 30 to 60 %. Such conditions allow investigation of the complex stress states that arise in a mixed-mode shear-tensile deformation, which improves the verification potential for numerical modelling. The worn tool was also compared with a new tool; a very poor edge quality is observed with such a worn tool, and a high level of strain is observed in a large region due to the low strain gradient.

Figure 4.16 displays a series of frames for an unpainted sample. The formation of a shear band is visible in Figure 4.16 (a). Frame 4, the sample does not however fracture along this path under the worn tool condition; instead, the weakened material along the shear band promotes rotation of the sample to produce a tension-dominated stress state, which produces fracture as shown in Figure 4.16 (b). This aligns well with the behaviour of the macroscopic shear samples, where shear-dominated stress states display significantly higher fracture strain than tensile-dominant ones. Due to the final fracture after shear band formation occurring over a time of 400 µs the image quality is degraded by motion blur because the camera's exposure time was 199 µs, Figure 4.16 (b) is therefore annotated for clarification using: a red dashed line to indicate the sample outline; yellow lines to bracket the shear band; and a blue line to show the location of fracture.

Figure 4.17 shows the force measured during the stroke of the tool, with 4.17 (a) showing the force due to the springs only. Two distinct jumps are visible as the return springs and stripper plate springs are compressed. Subfigure 4.17 (b) shows the total force in the blanking operation, a peak force of 6900 N is observed.

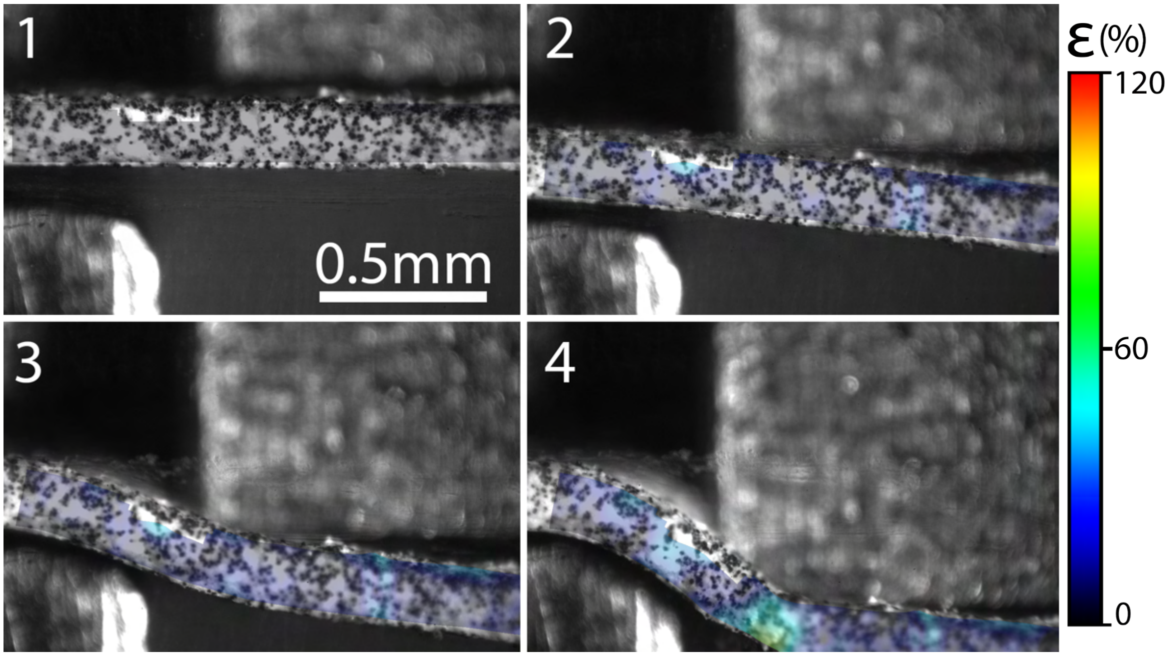

Figure 4.14: *A composite of frames showing the strain distribution in situ in a* 0.2 mm *thickness sample.*

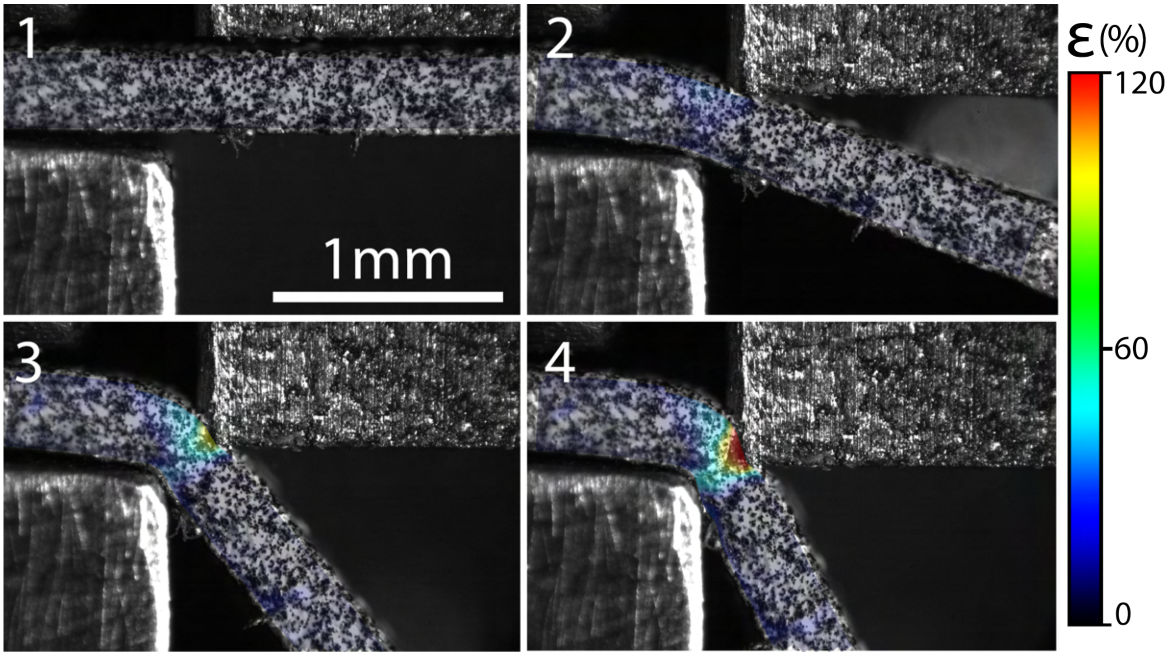

Figure 4.15: *A composite of frames showing the strain distribution in situ in a* 0.35 mm *thickness sample under single edge cutting conditions.*

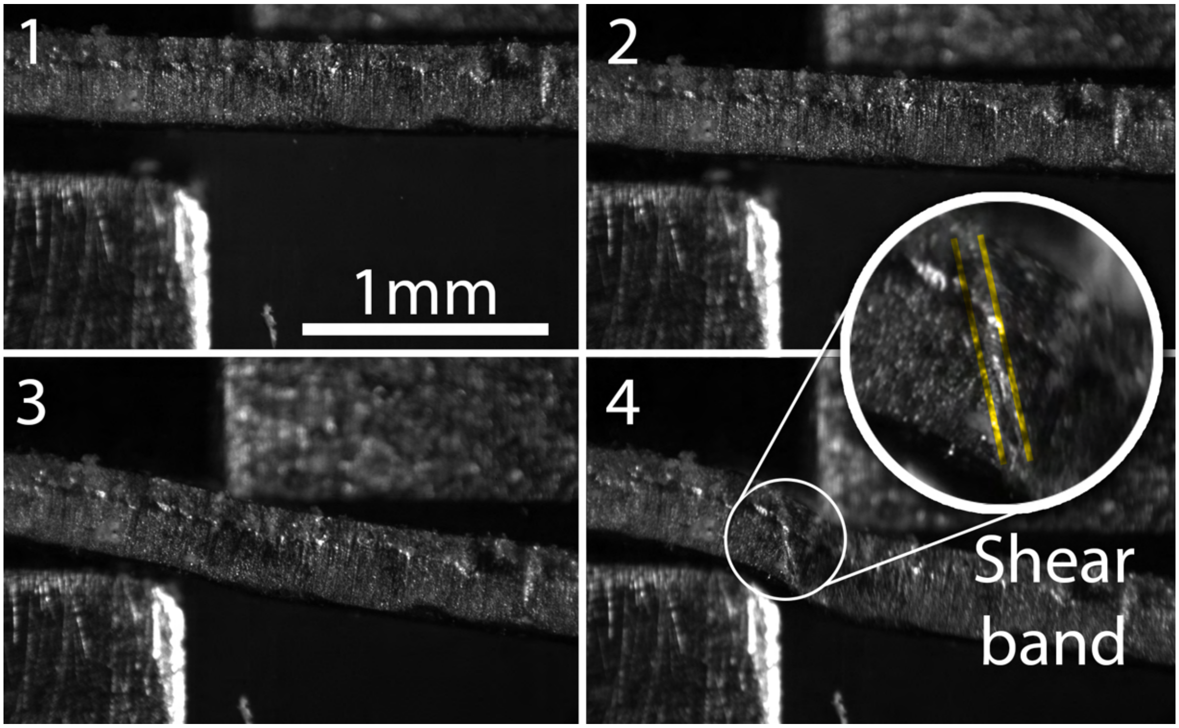

(a) *A composite of frames throughout punch travel. Shear band formation is visible immediately prior to fracture, shown in a pop-out bracketed by yellow lines.*

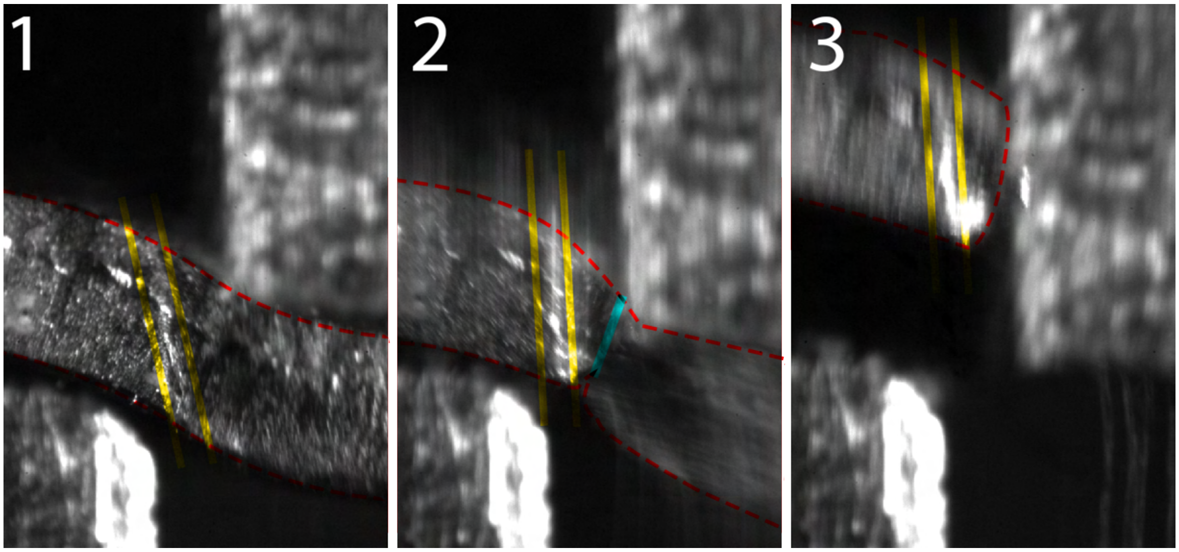

(b) *Fracture does not occur along the shear band. The sample edge rotates, producing a tensile dominated stress state and fracturing at the blue line. The shear band is visible post fracture.*

Figure 4.16: *An in situ analysis of an unpainted sample of* 0.35 mm *thickness.*

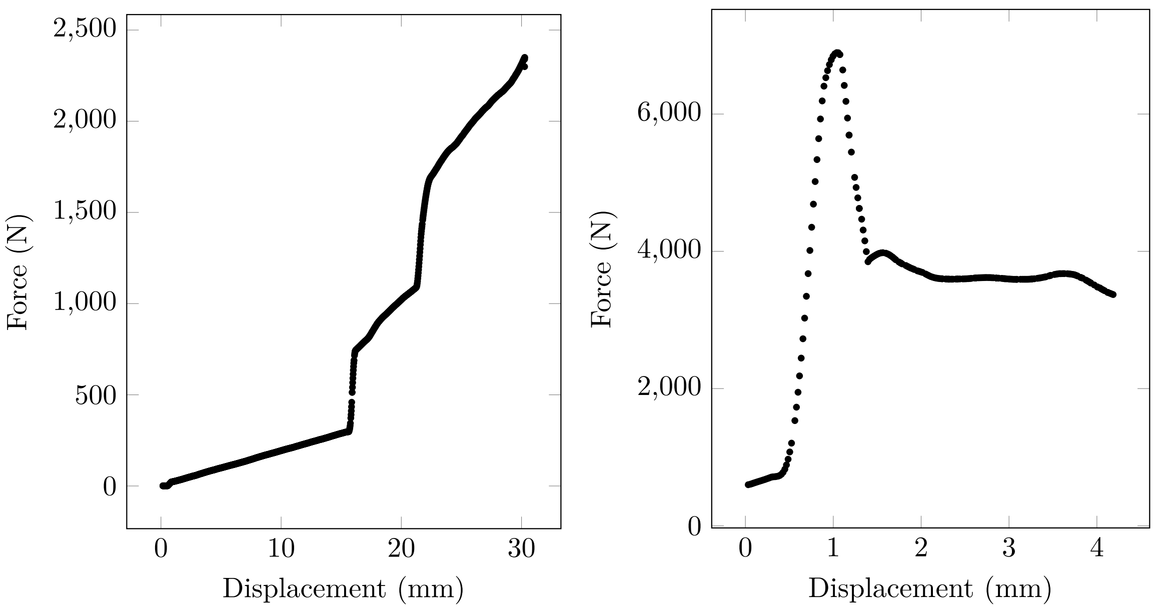

(a) **(b)**

Figure 4.17: *Plots showing the blanking force. Subfigure (a) shows the influence of the springs only, and (b) the total force for a single edge cut.*

4.5 Calibration of damage and plasticity

The Johnson Cook plasticity model was calibrated for NO20 silicon steel; the quasi-static parameters were first calibrated using the tensile test data gathered in Section 4.2. These parameters were then fixed and used to calibrate the remaining variables for strain rate dependence and temperature dependence. The Johnson-Cook plasticity model is found to provide an acceptable fit for the flow stress for quasi-static and high strain rate tests; some divergence from the experimental result is found with high temperature tests.

4.5.1 Quasi static parameters

Raw force displacement data was combined with true strain data from DIC using a virtual extensometer of dimension 25 x 6 mm to produce true stress-strain curves. This dimension corresponds exactly to the gauge section as defined by the ASTM standard. Using this information, the first term of the Johnson-Cook model was calibrated using Orthogonal Distance Regression (ODR). The parameters are reported in Table 4.4. An R^2 value of 0.991 is achieved (between plasticity onset and the ultimate tensile strength).

Parameter	Value
A	395.8 MPa
B	876.0 MPa
n	0.86624

Table 4.4: *Johnson Cook plasticity model calibrated quasi static parameters*

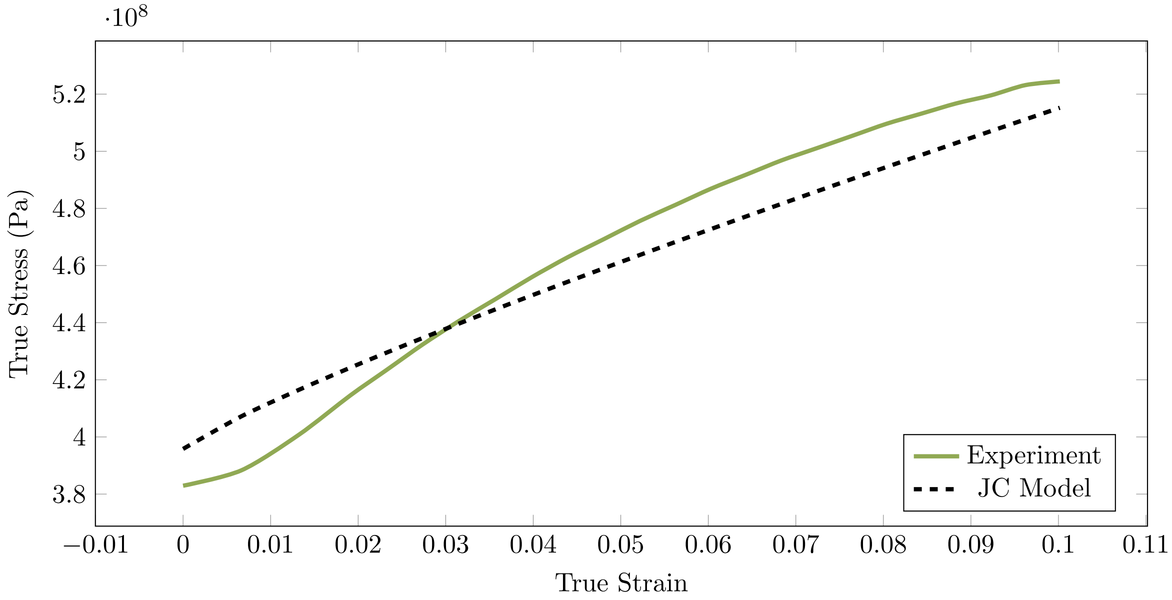

Figure 4.18: *Johnson Cook model compared to experimental curve for quasi static parameters.*

4.5.2 Strain rate dependence

The strain rate parameter C was found using the Levenberg-Marquardt nonlinear regression algorithm, which converged with an R^2 value of 0.94663. ODR was not used in this case because of convergence difficulties of unknown origin. The quasi-static parameters A, B, and n were fixed in this calibration. Table 4.5 shows the reference and high-speed strain rates used for calibration. The crosshead displacement rate of 100 mm min^{-1} was chosen as this rate was also used for punch velocity in the lab scale blanking rig in this work.

Parameter	Value
C	0.09106
$\dot{\varepsilon}_{ref}$	0.0021
$\dot{\varepsilon}$	0.04808

Table 4.5: *Johnson Cook plasticity model calibrated strain rate parameters*

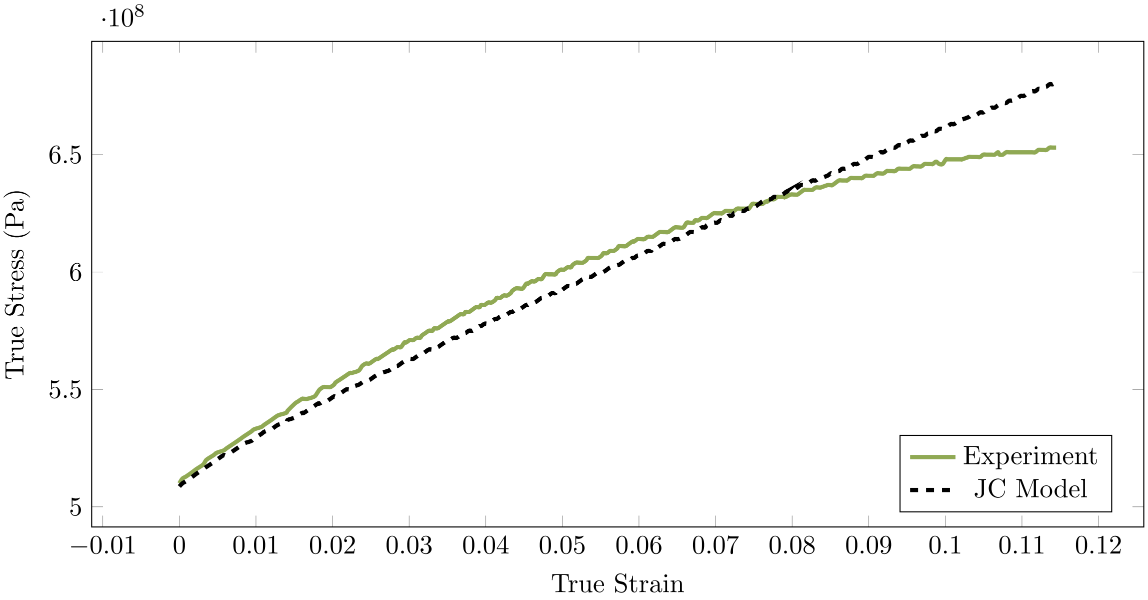

Figure 4.19: *Johnson Cook model compared to experimental curve for strain rate dependence at* 100 mm min^{-1} *crosshead rate.*

4.5.3 Temperature dependence

The temperature dependence of the material was investigated between room temperature (25 °C), 100 °C, 200 °C, 300 °C and 400 °C using the same ASTM-E8 tensile geometry as the prior two sections. The results of the investigation are plotted in Figure 4.20, a scatter plot is chosen to show the additional noise in the high temperature data in comparison to room temperature. Such noise is due to the use of a higher-capacity hydraulic machine with a high-capacity load cell with which the environmental heating chamber is compatible. A poor fit is achieved using the Johnson Cook model in this case, with an R^2 value of 0.65.

Parameter	Value
T	573.15 K
T_m	1773.15 K [176]
T_{ref}	298.15 K
m	$4.63119 * 10^{-4}$

Table 4.6: *Johnson Cook plasticity model calibrated temperature parameters*

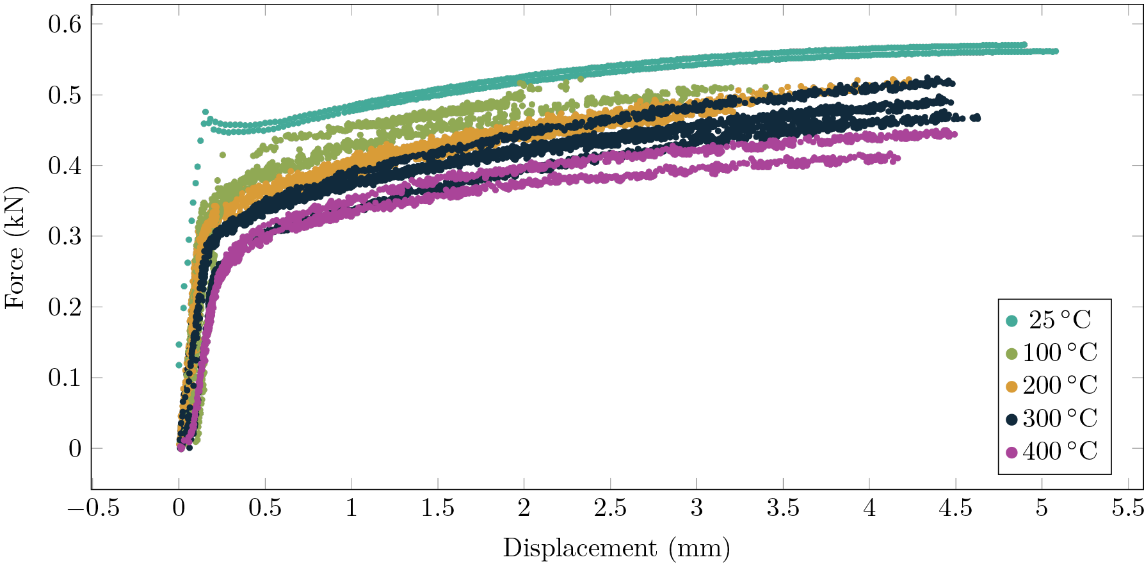

Figure 4.20: *Force-displacement scatter plot for tests.*

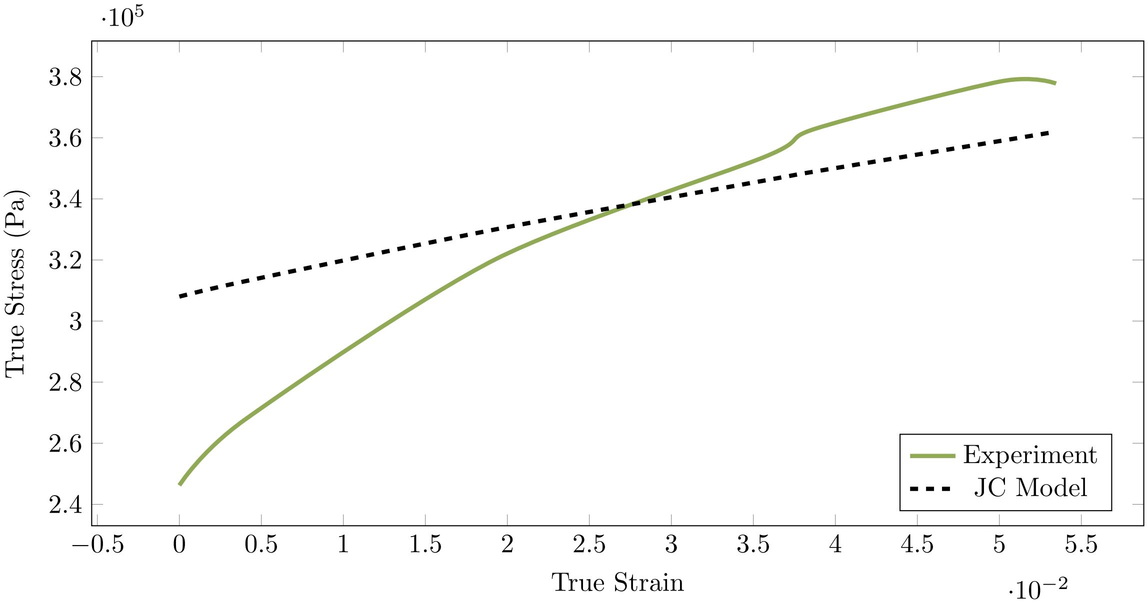

Figure 4.21: *Johnson Cook model compared to experimental curve at 300 °C.*

4.5.4 Damage and fracture strain calibration

A number of geometries were generated from the sheet stock such that, when loaded using a uniaxial tensile testing machine, a variety of stress states were induced. The samples were loaded to fracture in each case, and digital image correlation (DIC) analysis was performed to produce a strain map. The images were processed such that the subset size was the same physical size between each sample type. In each case, samples were manufactured with orientations in line with the RD, TD, and at 45°, no detectable difference between such orientations was detected, in agreement with the findings presented in Section 4.3. Figure 4.22 shows the other sample types used to calibrate the model. A shear sample to study the stress state $\eta = 0$ is shown in (a), two notch samples are shown in (b) and (c) with radii of 2 mm and 4 mm respectively investigate stress states $\eta > \frac{1}{3}$. The ASTM-E8 dogbone sample already presented in Section 4.2 is used for stress state $\eta = \frac{1}{3}$. Finally, Figure 4.23 shows a compressive sample designed to test the stress state $\eta = -\frac{1}{3}$ is shown without DIC overlay, as it did not fracture, in agreement with existing literature. The shear sample showed the highest strain to fracture, and the tensile sample showed the lowest. A boxplot of each sample type is shown in Figure 4.24, a large variation is observed, particularly for shear samples. This increased variance may be explained by the shearing region containing fewer grains due it its small size, therefore promoting the influence of each grain and grain boundary on the fracture dynamics. Table 4.7 contains the average triaxiality values for each sample type. Importantly, these values were obtained at the location of fracture (i.e. the edge of the sample) for more accuracy; in the notch samples, the difference between edge and centre stress states can be significant.

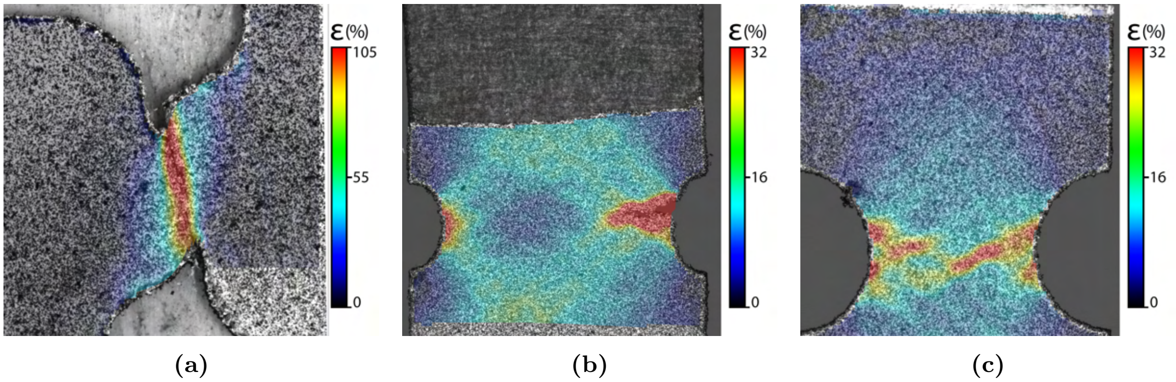

Figure 4.22: *A number of sample geometries with overlaid strain field. The shear geometry fractures at a significantly higher strain than other sample types*

Sample Geometry	Triaxiality η
Shear	0.00
ASTM-E8	0.3235
Notch 2mm	0.34
Notch 4mm	0.445

Table 4.7: *Average stress state at the fracture initiation site for each sample geometry*

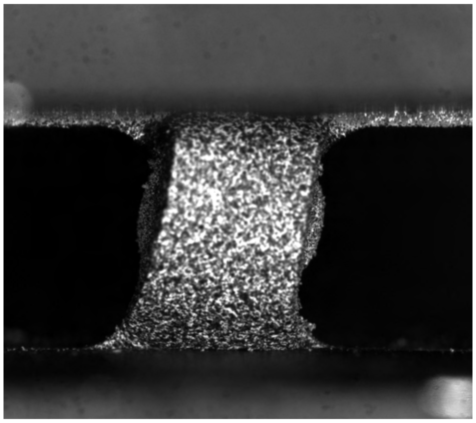

Figure 4.23: *A compressive sample which did not fracture*

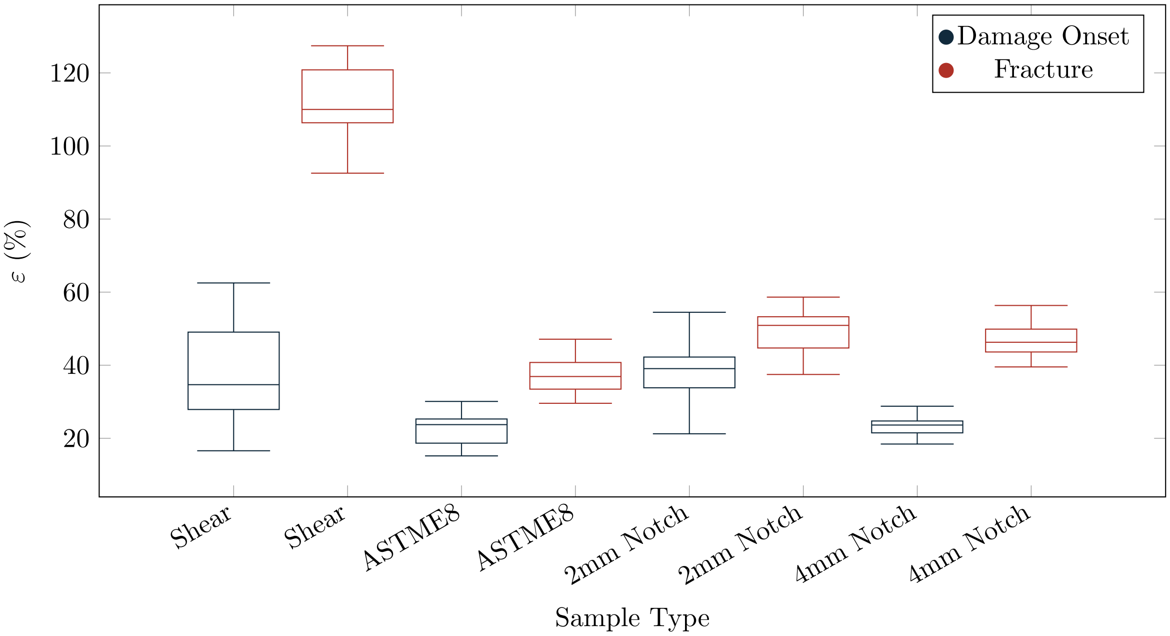

Figure 4.24: *A boxplot of the damage onset and fracture strain from all sample geometries.*

The average triaxiality, η, reported in Table 4.7 is defined by the equation:

$$\eta = \frac{1}{\varepsilon_f}\int_0^{\varepsilon_f} \eta d\varepsilon$$

For each strain measurement, the physical size of the subset was constant; this was considered important as each sample required a different field of view (FOV) to ensure the crack was captured. Additionally, the values reported are not smoothed or interpolated because this would introduce a non-linear bias, which would invalidate the comparison between different FOVs.

4.6 On frictional effects of the restraining system

The restraining system used for shear samples introduces a frictional force between the sample and the restraint. Two methods are used to quantify this friction contribution to the force measurement: primarily, there is a residual force that is constant after the sample breaks, providing a direct measure. Secondarily, the restraining system was tested with one end of a sample free, such that the only force detected by the load cell was due to the interaction between the sample and the restraint. Figure 4.25 shows a force-displacement plot wherein the post-fracture residual force is displayed. It is demonstrated that the residual force is a constant of 165 N ± 10 N over an additional 2 mm of displacement. It is proposed that this post-fracture variance is a demonstration of the worst-case performance as the fractured sample was able to deform such that interaction between the restraint and sample was maximised.

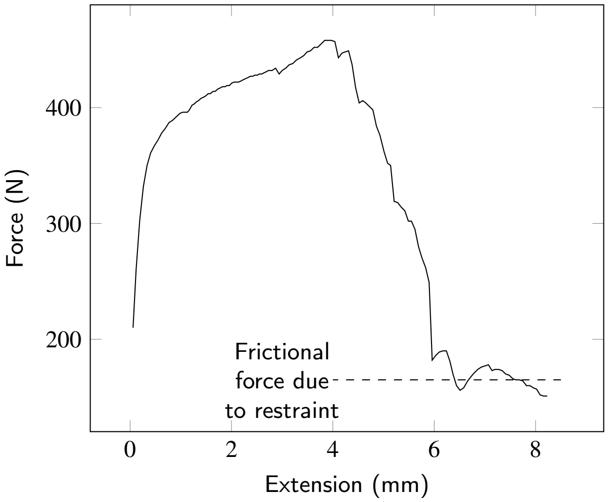

Figure 4.25: *Friction due to the restraint identified post fracture*

The calibration methodology for damage-onset strain was chosen as the ultimate tensile strength; however, this is not negatively effected by the introduction of a superimposed force if that force is constant. The damage softening coefficient calibration may be negatively effected if the force-displacement curve is used, and indeed, in both Figures 4.26 and 4.26 a stair-step effect is found. This is very likely due to the interaction of the burr present across the sample geometry against the restraining system and is not of major consequence unless this causes a non-uniform deformation in the region of interest. No evidence of non-uniform deformation is present; inspection of the strain field shows symmetric strain across the sample symmetry plane, indicating that any such effect (if present) is insignificant in comparison to the desired test forces. By using a calibration based on the strain in the ROI, the effect of the frictional interaction is reduced but not eliminated because only highly local deformation is considered. The stair-step effect in the reduction of the force is still present, but because the strain in the ROI is increasing rapidly in comparison to the overall sample, a smoother overall result is obtained. Improving the restraining system so that it is manufactured from a low-friction, high-hardness material is recommended. Samples may also be prepared with a fine abrasive paper to remove any burrs on the interacting surfaces. Additionally, because the restraint was closed using a total of 4 bolts, the potential for uneven clamping force is introduced unless a torque wrench is used. A revised method for clamping that more evenly distributes forces should be designed in the future.

4.6.1 Damage softening calibration

The damage softening coefficient, β, is used in the damage model to drive the damage softening between the two loci. This coefficient was calibrated using the shear sample geometry because all damage was highly contained in the small region of interest. The displacement or strain at peak force (i.e. the onset of damage as defined for this model) and at fracture were mapped to 0 and 1, respectively. The curve in Equation 5.22, restated below for clarity, was fit to this data. A full explanation is detailed in Section 5.2.1. This produces a plot with force on the Y axis and damage on the X axis, referred to as a force-damage curve. This representation is preferred as opposed to stress damage because the sample cross-sectional area is harder to measure with the shear geometry and would simply scale the Y axis with no effect on the calibration.

Figures 4.26 and 4.27 show a selection of representative force-damage curves, with the green portion indicating the section of the curve selected for fitting and red indicating the fitted curve. Appendix A contains graphs for every sample. In both cases, the exponential decay equation provides a good fit in most instances. A slightly lower coefficient with a lower standard deviation between samples was found for the strain-based calibration. The value of the coefficient was calculated for each repetition, and the mean average value was selected for use in the model.

$$F = F_{max} \frac{1 - \exp \beta \bar{D}}{1 - \exp \beta} \tag{5.22}$$

Measure	Displacement	Strain
Average	7.528949964	6.355451858
Std.Dev.	3.109705096	2.318971551

Table 4.8: *The average and standard deviations for the two measures*

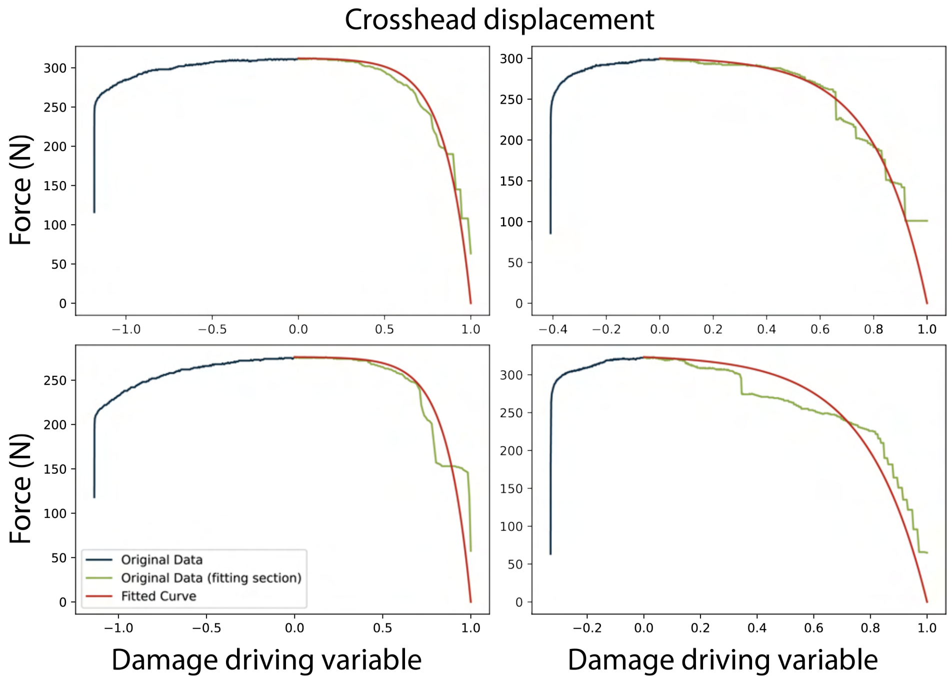

Figure 4.26: *Exponential damage softening coefficient calibration, using crosshead displacement as the base for the damage variable.*

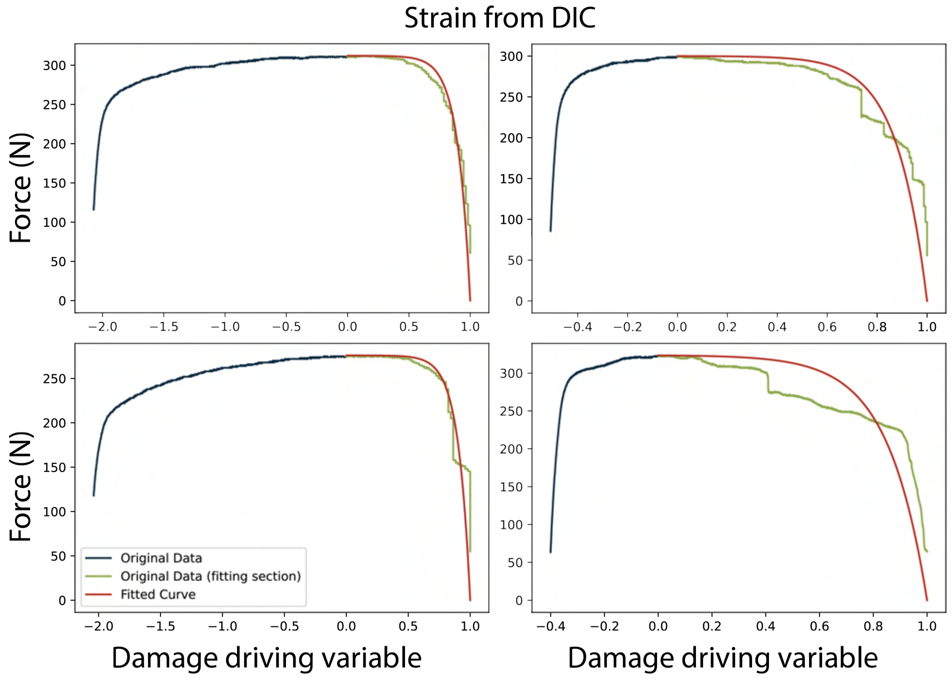

Figure 4.27: *Exponential damage softening coefficient calibration, using true strain in the shear region as calculated from DIC, averaged over a* $1\,\mathrm{mm}^2$ *area as the base for the damage variable.*

4.7 Fracture initiation locations

The location of fraction initiation is further investigated in this section to provide confidence that the edge failure displayed in previous sections is representative of the true fracture dynamics and not an effect of misalignment. Figures 4.28 to 4.32 show a time series of images for a selection of samples that were imaged using a high magnification telecentric lens and strong incident lighting. The size effect in these images is clearly visible, with grains freely deforming out of plane in all 0.2mm samples (known as the orange peel effect), a behaviour that is not visible with the 2mm sample and is clear by comparison of Figures 4.31 and 4.32. It is clear from visual inspection that the crack has a strong preference to propagate along the grain boundaries. This intergranular cleavage is also present in shear samples, and in many cases, a primary crack initiates outside of the shearing zone. Figure 4.30 shows a sample in which the mode of failure is dominated by crack initiation from the top and bottom of the sample, and the ROI intended to shear rotates as a result. Figure 4.31 shows the intended mode of deformation for this sample type. The propagation of cracks in the manner shown in Figure 4.30 could not be controlled. Interestingly, this same deformation occurs in some 2mm shear samples after high strain in the centre, indicating that the failure of the material is extremely sensitive to stress state intrinsically and not only due to the size effect. The proposed mechanism to explain the stochastic nature of the crack initiation is as follows: for the NO20 samples, the size effect is significant, and the grain distribution over the small ROI will promote crack initiation either at the top and bottom or allow shearing, depending on the orientation of the grains and location of grain boundaries. Prior to the crack initiation, no difference is seen in the strain distribution in DIC or the applied force because the effect is highly localised.

Through the utilisation of an X-ray microscope in conjunction with a specially devised tensile sample, the possibility of void formation and coalescence at sizes exceeding approximately 2.49 µm was eliminated. In all samples investigated in this manner, the apparent mechanism of fracture was intergranular cleavage facilitated by large shearing or plasticity in the nearby grains. A classic cup and cone fracture can be observed in Figure 4.33, which was initiated by the mechanism described. The sample for this experiment was produced by remote laser cutting, and a significant burr is visible at this scale. A graph of the force-displacement curve for this sample type can be found in Appendix C.

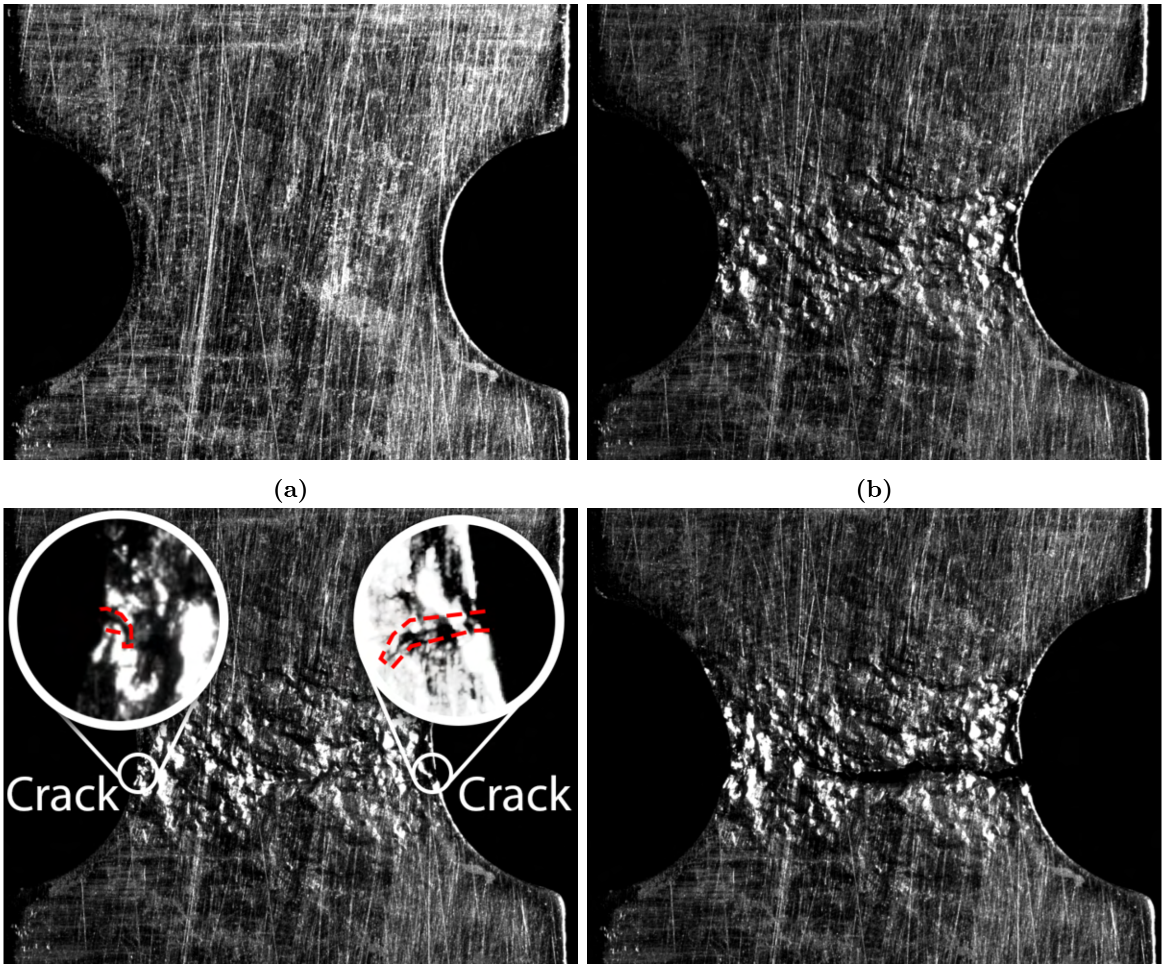

(a) **(b)**

(c) **(d)**

Figure 4.28: *Unpainted NO20 (0.2mm thickness) 4mm notch sample: (a) prior to deformation, (b) plastic deformation, (c) prior to fracture, cracks initiate at both sides, (d) right side crack propagates.*

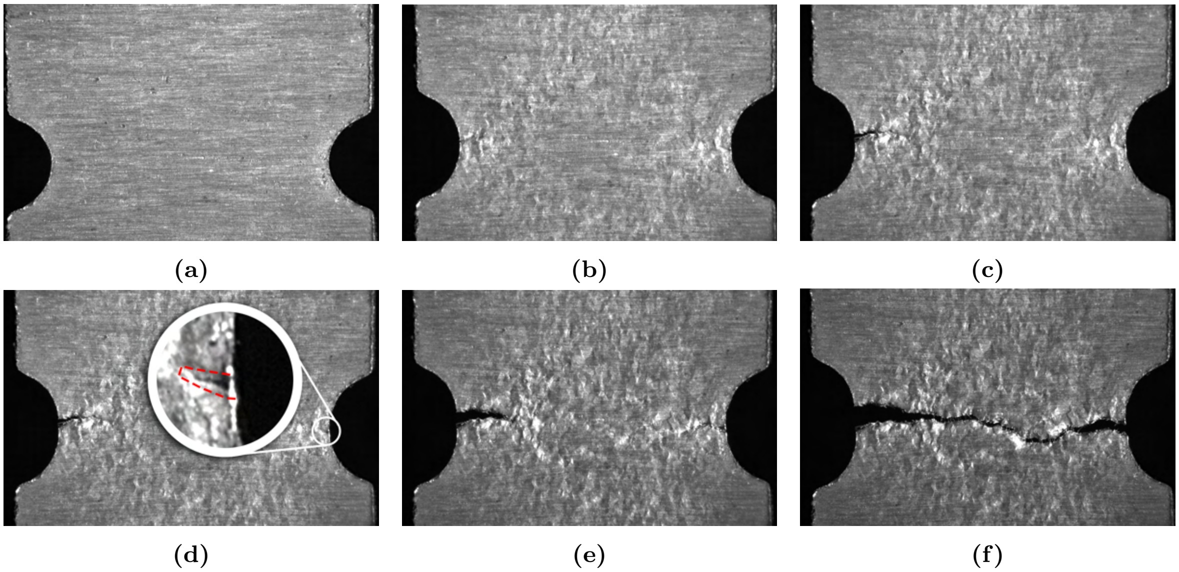

Figure 4.29: *Unpainted NO20 2mm notch sample with electrically insulating coating still present: (a) undeformed sample, (b) plastic deformation, an imperfection is immediately revealed left edge of ROI, (c) imperfection propagates a crack, (d) the same frame repeated showing a crack on the right, (e) the second crack propagates from the right, (f) cracks merge*

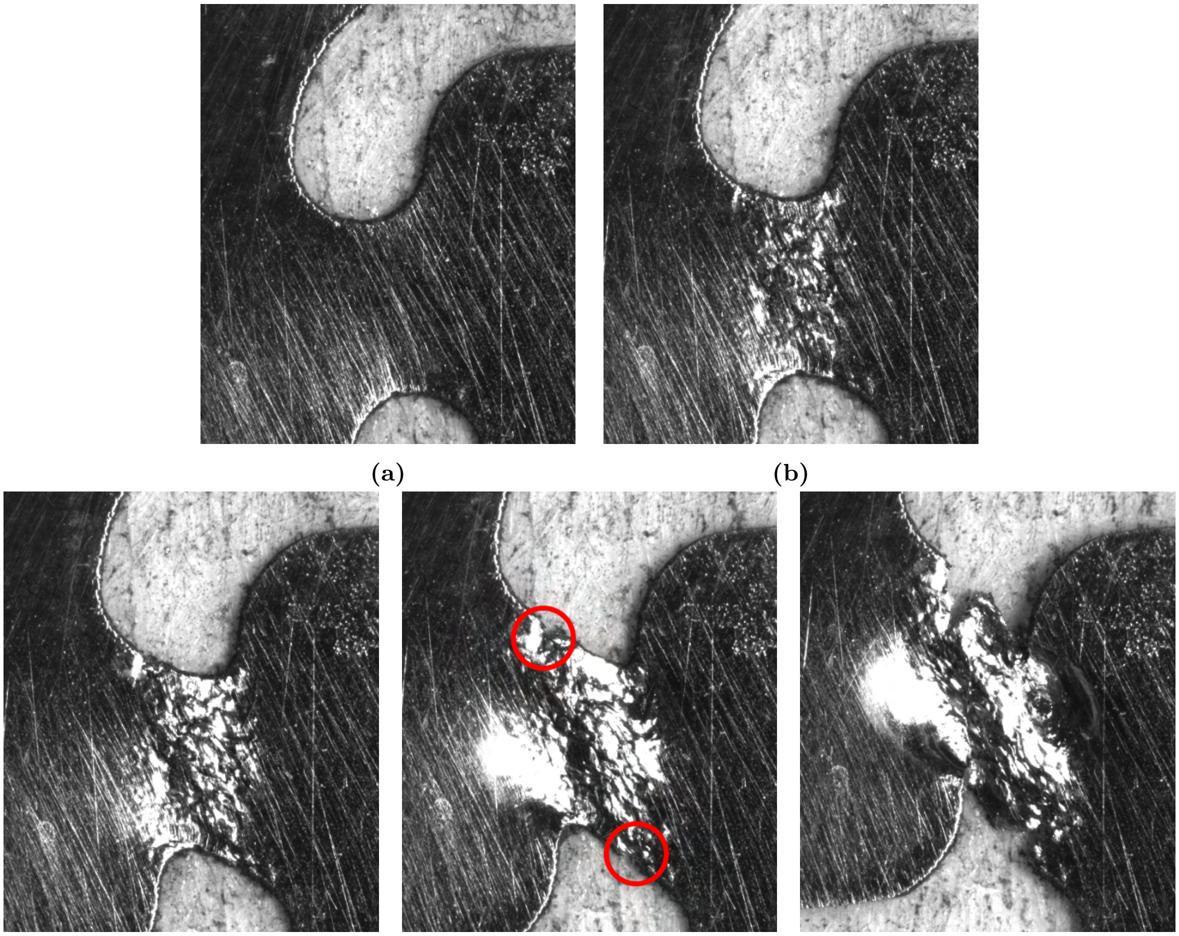

(a) **(b)**

(c) **(d)** **(e)**

Figure 4.30: *A constrained* 0.2 mm *thickness shear sample showing: (a) sample prior to deformation, (b) plastic deformation, (c) and (d) crack initiation is annotated, (e) central piece rotates as cracks progress.*

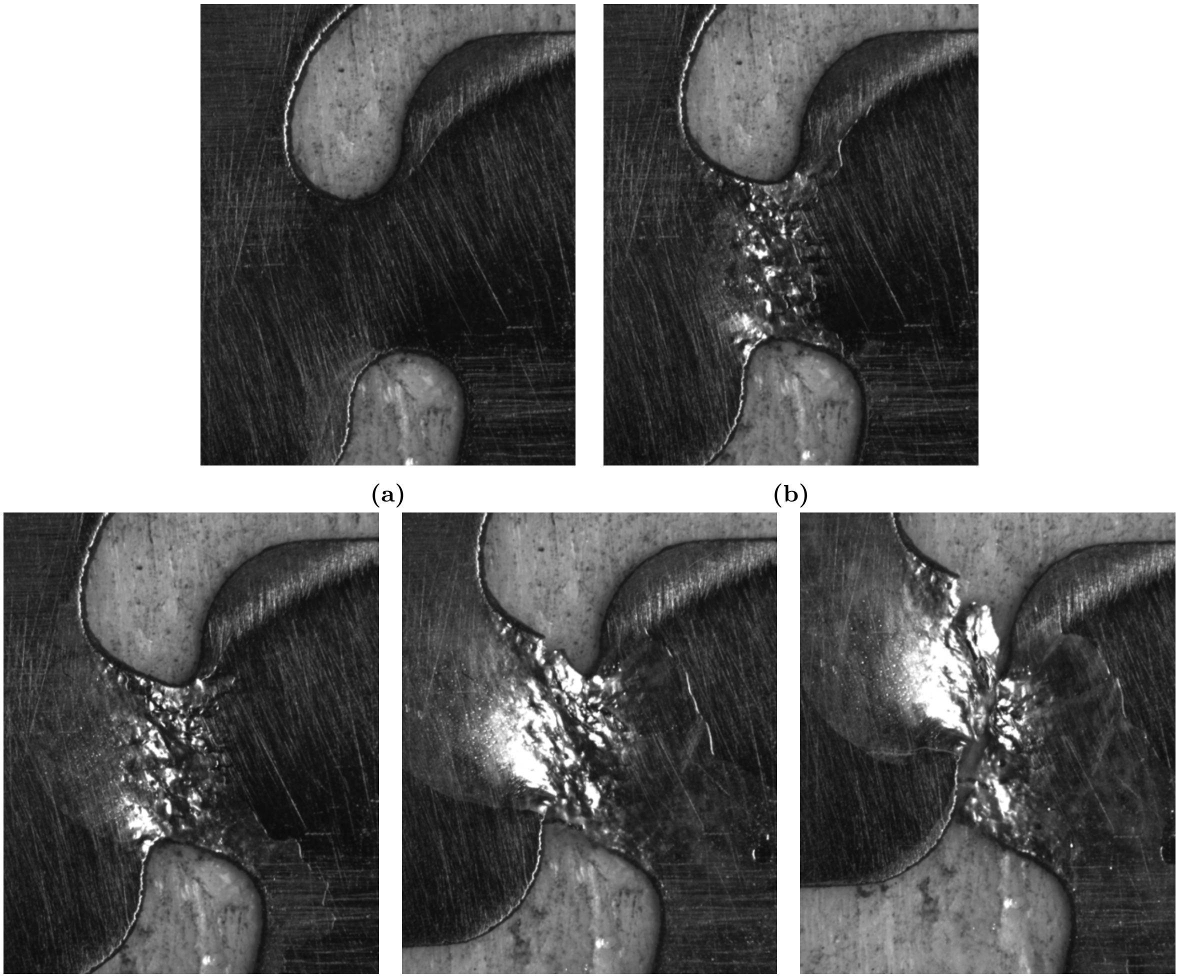

(a) **(b)**

(c) **(d)** **(e)**

Figure 4.31: *A constrained* 0.2 mm *thickness shear sample: (a) prior to deformation, (b) plastic deformation, (c) further deformation purely in shear, (d) a crack appears in the top left of ROI, (e) shear fracture away from initial crack. Oil was added to the surface in an attempt to reduce specular reflections which is visible in the last three frames.*

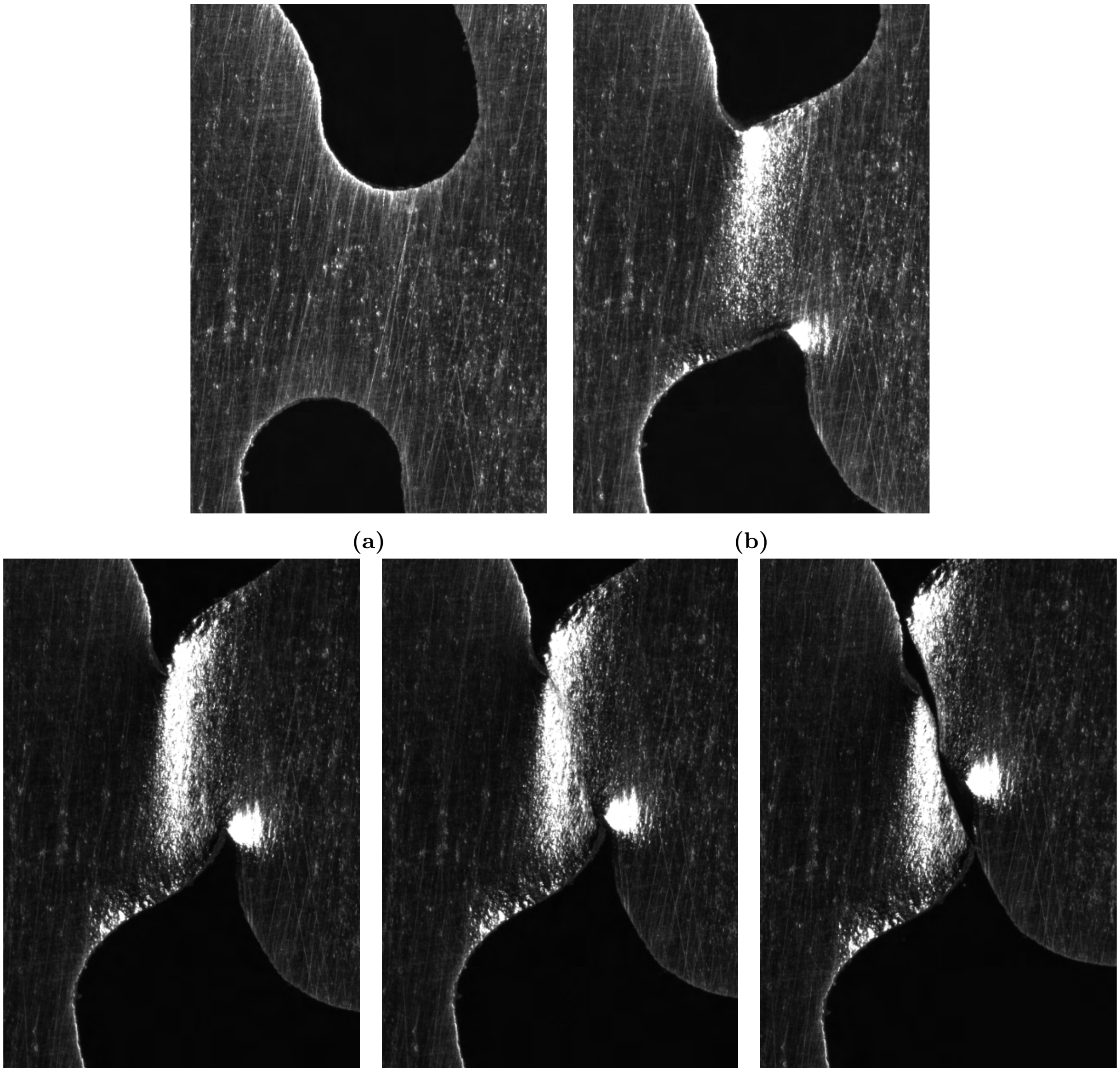

(a) **(b)**

(c) **(d)** **(e)**

Figure 4.32: *2mm thickness sample which displays different behaviour and requires no restraint, (a) undeformed sample, (b) plastic deformation, (c) prior to crack initiation, (d) crack initiates and shear band visible, (e) fracture.*

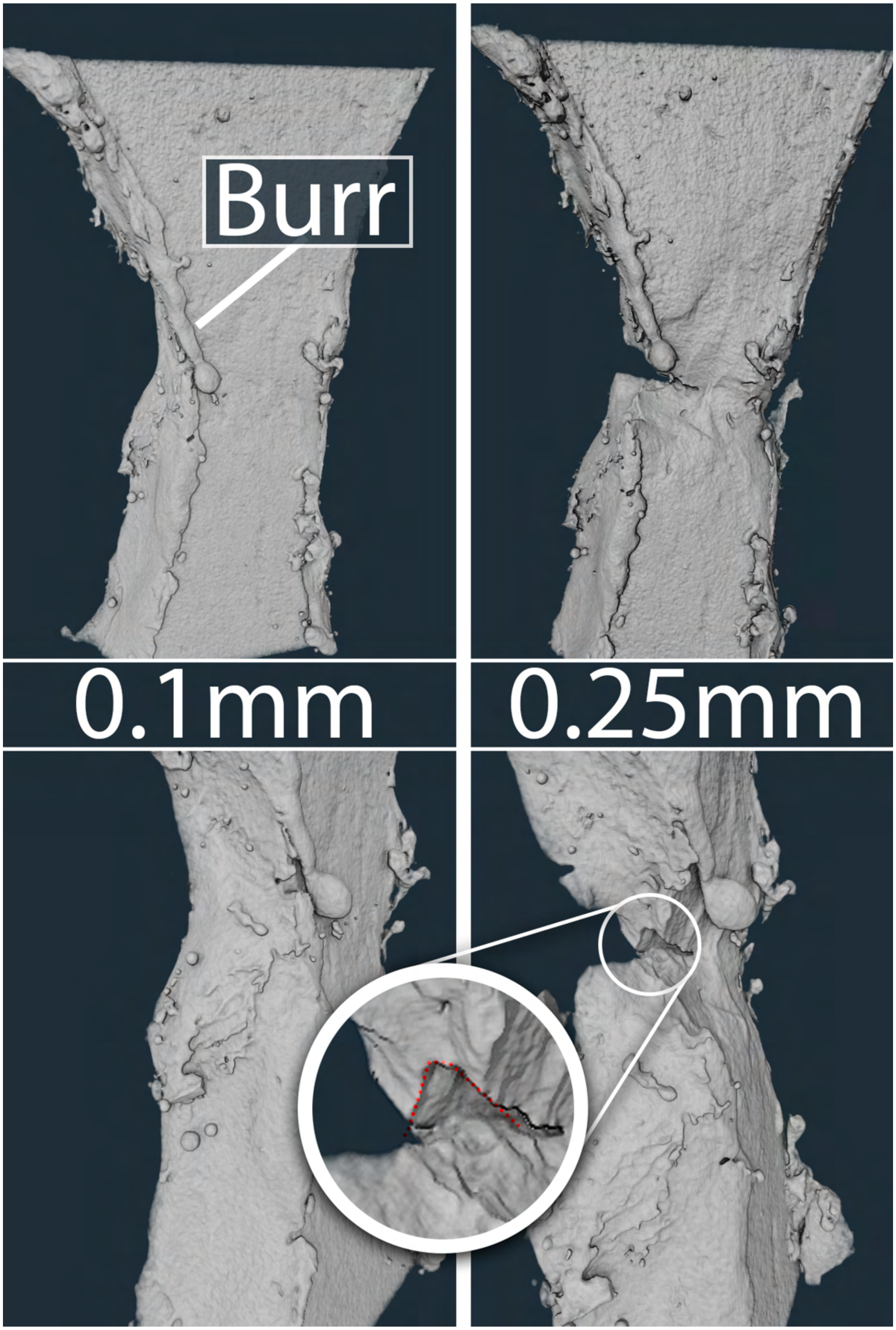

Figure 4.33: *X-ray microscope imagery of a sample while applying in situ tension. Left images are at* 0.1 mm *extension (same sample, different views), and images on the right are at* 0.25 mm *extension. The zoomed pop up shows the cup of the cup and cone fracture.*

4.8 Hall effect damage sensing

Thus far, the damage-onset strain has been defined as the strain at which the ultimate tensile strength is observed. This definition is sufficient to produce a calibration for the numerical modelling later presented, but it is desirable to link the mechanical and magnetic damage such that the model may be used to predict iron loss in blanked products. This section demonstrates a novel technique for in situ damage detection in thin ferromagnetic material.

The technique was trialled using two arrangements of hall effect sensors and two permanent magnet locations. The sensor data is normalised such that the maximum and minimum values captured for each hall sensor are mapped between zero and one. The figures presented in this section present the normalised sensor values with the force - displacement curves; in this way, a comparison is possible between the aforementioned damage onset strain and the results of the hall sensors. It is found that the normalised values show a clear trend of changing magnetic flux in response to the straining of the sample, although in many cases it is not clear how to interpret this in the context of damage. Figure 4.34 shows the results for a star arrangement of sensors with a central permanent magnet. In this arrangement, the first sensor detects an increasing magnetic flux density, which stagnates after the ultimate tensile strength. This may be explained by the movement of the magnet relative to the sample. An offset permanent magnet condition is shown in Figure 4.35; in this case, all sensors detect a decreasing field strength.

A linear arrangement of sensors with an offset sensor is used in Figure 4.36; this arrangement provides the best comparison between sensors. The initial reduction in the value of sensor 3 is explained by the relative movement of the sample, magnet, and sensors. This arrangement produces the best agreement with the decrease in force experienced prior to the sample fracture. Further discussion on this technique and the results in this section can be found in Section 6.5.

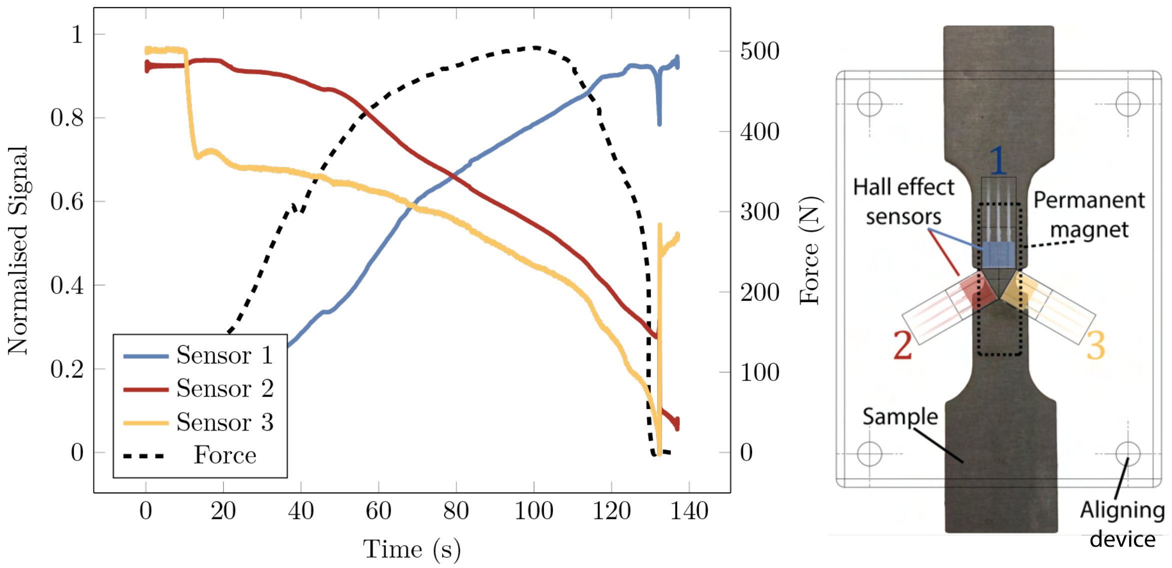

(a) (b)

Figure 4.34: *Hall effect sensor and force plotted for a star arrangement of sensors with a central permanent magnet.*

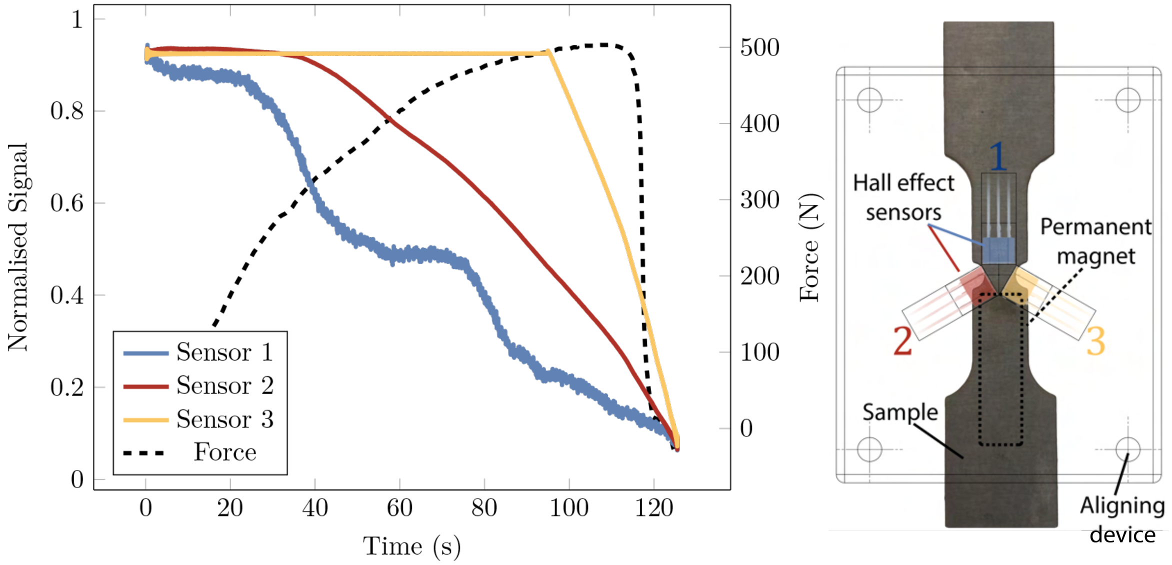

(a) (b)

Figure 4.35: *Hall effect sensor and force plotted for a star arrangement of sensors with an offset permanent magnet.*

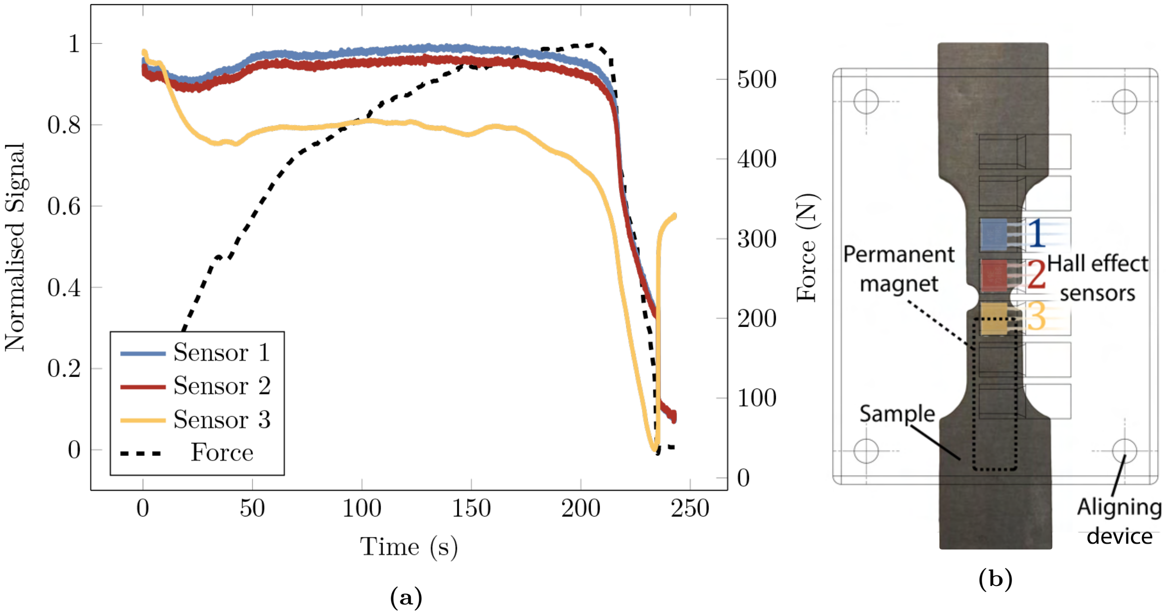

Figure 4.36: *Hall effect sensor and force plotted for a linear arrangement of sensors with an offset permanent magnet.*

Chapter 5

Modelling

A custom material model was implemented in the VUMAT subroutine for the commercial finite element software ABAQUS. The objective of improving the simulation of damage and fracture of materials required the implementation of a model for the elastic and plastic response of the material. As the material exhibited elastoviscoplastic behaviour, the Johnson-Cook model was identified as appropriate primarily for this reason; the implementation of any model is not trivial, and the ability to compare the implementation with the ABAQUS built-in version was a secondary benefit. The explicit solver was chosen for several reasons, primarily because the complex contact conditions required in the simulation of blanking mean that convergence with an implicit solver would be extremely difficult, if not impossible. Secondly, the blanking process is highly dynamic; explicit solvers work by transmitting stress and strain as waves through the material. This chapter explains the implementation of all parts of VUMAT, focusing on the novel, uncoupled, non-local, highly stress-state sensitive damage softening model. The calibration geometries are simulated, and the model is verified using a novel two-stage geometry and in blanking.

5.1 Elastoviscoplastic implementation

The model implements an isotropic linear elastic formulation below the yield stress and a radial return Johnson-Cook plasticity formulation, which is uncoupled from the damage portion. The strain increments are decomposed into volumetric and deviatoric portions (Equations 5.1 and 5.2, respectively), and a trial stress increment is calculated, which is added to the old stress. The Mises equivalent of the updated stress can then be compared to the yield stress as defined by the Johnson Cook model (Equation 2.16, restated below).

$$\Delta\varepsilon_{vol} = tr(\Delta\varepsilon) \qquad (5.1)$$

$$\Delta\varepsilon_{dev} = \Delta\varepsilon - \frac{1}{3}\varepsilon_{vol} \qquad (5.2)$$

$$\sigma_{trial} = \sigma_{old} + 2G\Delta\varepsilon_{dev} + 2k\Delta\varepsilon_{vol} \qquad (5.3)$$

Where k is the bulk modulus and G is the shear modulus, calculated from Equations 5.4 and 5.5 respectively.

$$k = \frac{E}{3(1-2v)} \qquad (5.4)$$

$$G = \frac{E}{2(1+v)} \qquad (5.5)$$

The deviatoric stress is

$$\boldsymbol{S} = \sigma_{trial} - \frac{1}{3} tr(\sigma_{trial})\boldsymbol{I} \tag{5.6}$$

where $\boldsymbol{I}$ is the identity tensor. The Mises uniaxial equivalent stress can now be calculated as:

$$\overline{\sigma} = \sqrt{\frac{3}{2}\boldsymbol{S} : \boldsymbol{S}} \tag{5.7}$$

which is compared to the yield stress as defined by the Johnson Cook criteria:

$$\sigma_y\left(\varepsilon_{\mathrm{p}}, \dot{\varepsilon}_{\mathrm{p}}, T\right) = \left[A + B\left(\varepsilon_{\mathrm{p}}\right)^n\right]\left[1 + C\ln\left(\dot{\varepsilon}_{\mathrm{p}}^*\right)\right]\left[1 - \left(T^*\right)^m\right] \tag{2.16}$$

If the material point is in the elastic region, the trial stress is accepted. If the material point has yielded, a radial return approach is used to scale the stress back to the yield surface.

$$\boldsymbol{S}_{new} = \frac{\sigma_y}{\sigma_{mises}}\boldsymbol{S} \tag{5.8}$$

The elastic strain increment can be found:

$$\Delta\varepsilon_{el} = \frac{\boldsymbol{S}_{new} - \boldsymbol{S}_{old}}{2G} \tag{5.9}$$

As such the plastic strain increments are:

$$\Delta\varepsilon_{pl} = \Delta\varepsilon - \Delta\varepsilon_{el} \tag{5.10}$$

The equivalent deviatoric plastic strain increment is obtained by:

$$\Delta\bar{\varepsilon}_{pl} = \sqrt{\frac{2}{3}\Delta\varepsilon_{dev}^{pl} : \Delta\varepsilon_{dev}^{pl}} \tag{5.11}$$

The new stress is then found and the plasticity calculations for the increment are complete

$$\sigma_{new} = \frac{2G}{1 + (3G\varepsilon_{pl}/\sigma_y^{new})} + \frac{1}{3} tr(\sigma_{trial})\boldsymbol{I} \tag{5.12}$$

Where σ_y^{new} is the new value for the yield surface based on the total deviatoric equivalent strain.

5.2 Progressive damage and failure

5.2.1 Extension to Bao-Wierzbicki fracture model

Implementation of loci

The loci representing the fracture and damage onset curves deviate from the Bao and Wierzbicki paper and many of its derivatives in that a piecewise cubic polynomial is used. This is justified because there are a limited number of stress states available to assess in geometries manufactured from sheet stock; therefore, fewer experimental points are obtainable. In this case, it is preferable to simply interpolate between known points as opposed to attempting to fit the original equations. Further justification is provided according to the Stone–Weierstrass theorem [177], that any continuous function may be uniformly approximated by a polynomial, as such using piecewise polynomials allows the surface to be reduced to that generated by the original equations. One caveat to this approach is that the asymptotic region cannot be reproduced by piecewise polynomials, and as such, the model uses the asymptotic function presented in [178] as described in Section 5.2.1.

The data from Section 4.5.4 was used to produce the calibration loci as shown in Figure 5.1. The constant fitting scripts are printed in Appendix E for convenience. Due to the extremely limited number of calibration points, there is some degree of numerical error associated with this approach; namely, it is possible to see that in the region where $\eta = 0.2$ to $\eta = 0.3$ the fracture curve has a lower value than the damage onset curve. This behaviour is evidently impossible, and the model overcomes such a problem by, in such a case, making the two values equal. There is evidence of this *damage window narrowing* in the points around the region; however, the minima around $\eta = 0.25$ is likely slightly above the calibrated value, and a new sample geometry to capture this would be required.

The justification for this approach is further developed by considering the two possible fracture modes found in the shear sample geometry. The intended shear mode fracture of the sample was hindered by an additional mode of fracture occurring beyond the designated region of interest. The utilisation of Digital Image Correlation (DIC) in the investigation revealed a fracture strain value of 30%. Furthermore, employing reverse analysis without considering the effects of damage indicated a stress state transition band wherein η transitions from 0.2 to 0.3 in the vicinity of the fracture. Figure 5.2 shows the transition in comparison to the DIC result. Although the location of the band and the fracture do not coincide perfectly in this simulation, this is easily explained because there was no damage enabled.

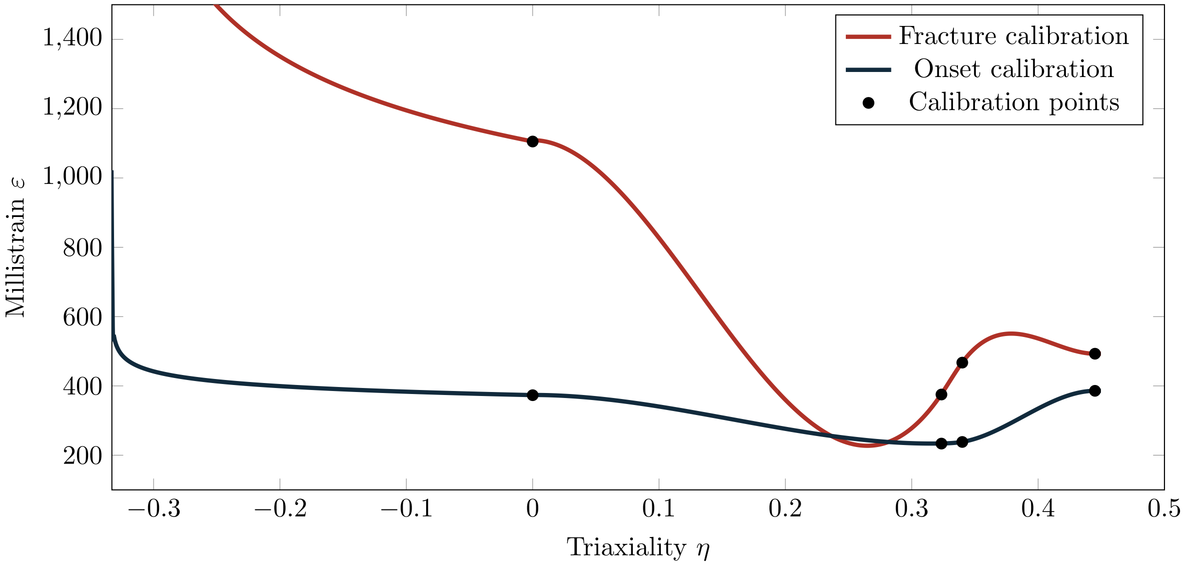

Figure 5.1: *The calibrated loci plotted with the experimental points.*

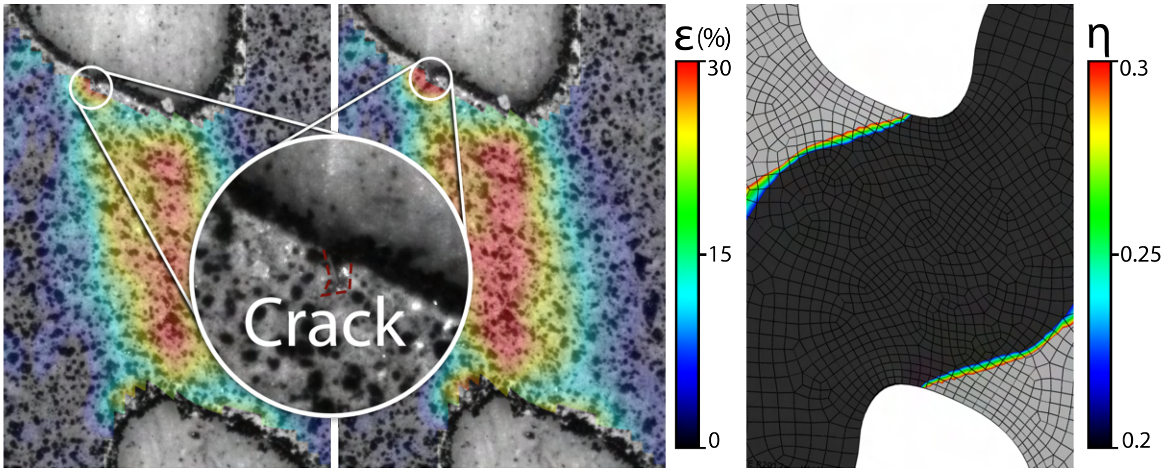

Figure 5.2: *Two frames from DIC (left) for a shear sample which fails outside the at $\varepsilon_f = 30\%$ near the region where η transitions from 0.2 to 0.3, indicated using ABAQUS results (right)*

Asymptotic calibration for negative stress triaxiality

In agreement with the literature, failure was not observed in the material at or below a triaxiality of -1/3; other models have included an asymptotic function to represent this. Depending on the calibration and the imposed connectivity conditions, it may or may not be possible to represent this via polynomial fitting as used in higher triaxiality regions. Additionally, the problem of acquiring data in this low triaxiality region is highlighted; buckling under compression in such thin samples is a common issue. Two strategies for the negative triaxiality (i.e. compressive) region of the stress-triaxialty space were developed. Firstly, assuming data in the negative stress stage could not be gathered, it is reasonable to assume that the function must be continuous and that the derivatives of the functions at the intersection should be equal. The asymptotic function used in Bao and Wierzbicki [131] (Equation 5.13) was used under these assumptions, and the constants were calibrated by the following procedure.

$$\varepsilon = A(\eta + \frac{1}{3})^{-B} \text{ for } -\frac{1}{3} \leq \eta \geq 0 \tag{5.13}$$

The problem is essentially a minimisation of error between the evaluation of the functions at the intersection, and of their gradients. An error function is defined such that

$$f(A, B) = E_{total} \tag{5.14}$$

where E_{total} is the total error. This total error is calculated as:

$$E_{total} = E_{intercept} + E_{gradient} \tag{5.15}$$

To obtain these errors, the value of the calibrated cubic section at the intersection where $\eta = 0$ is calculated:

$$
\begin{aligned}
\eta_0 &= c_1x^3 + c_2x^2 + x_3x + c_4 \\
\eta_0 &= c_10^3 + c_20^2 + c_30 + c_4 \\
\eta_0 &= c_4
\end{aligned}
\tag{5.16}
$$

where c_n is a calibration constant for the cubic section. The intercept is now defined, and the first error term, $E_{intercept}$ may be defined as:

$$
E_{intercept} = \left| \frac{A(\frac{1}{3})^{-B} - \eta_0}{\eta_0} \right| \tag{5.17}
$$

The fitting function is evaluated, and the difference between the fitting function value and target value is compared. This is then divided by the target value in order to get a relative measure of error. The importance of this division will be explained shortly. Next, the gradient of the fitting function, $\nabla\eta$, is compared in a similar manner:

$$
\nabla\eta = \frac{A(\frac{1}{3} + \delta)^{-B} - \eta_0}{\delta} \tag{5.18}
$$

where δ is a very small number, in order to perform numerical differentiation. The error can be calculated as:

$$
E_{gradient} = \left| \frac{\nabla\eta - \nabla\eta_0}{\nabla\eta_0} \right| \tag{5.19}
$$

Again, a relative measure is taken by the division of the difference between the target and fitted values by the division of the target value, $\nabla\eta_0$. This is important because the gradient may be large in comparison to the intercept, and without relative measures of error, the gradient term would dominate, and the fitting function may fail to converge quickly or at all. The initial guess for the constants is set at $A = \varepsilon_f$, $B = 1.0$ and the Nelder-Mead minimisation algorithm [179] is used to find the appropriate values via the SciPy Optimise package. The script used is found in Appendix E.

Such an approach is not suitable where the gradient from the negative to positive stress states is positive or where data from the negative triaxiality region is available. In the latter case, an additional cubic interpolation section may be added, and the same fitting functions modified so that the intercepts and gradients are calculated at the minimum bound of the cubic section.

If, however, the gradient is positive, enforcing the continuity of gradients is impossible. In this case, setting the boundary condition of the cubic section to be clamped or natural, iethe first or first and second derivatives, respectively, equal to zero, naturally produces a curve that approximates the asymptotic section. The assumptions made in the calibration of the asymptotic section are further justified because the condition of a lower compressive failure strain cannot arise in a physically consistent manner; the compressive failure should always equal or be higher than the shear.

Stress state averaging integral

The stress triaxiality of any specimen varies throughout the deformation history; therefore, using the instantaneous value would be incorrect, as the experimental calibration procedure depends not only on the instantaneous value but also on some averaged value. Bao and Wierzbicki [131] proposed an integral based on the stress state and strain increments. Such an approach is well justified in that the damage variable is controlled by essentially the same integral in the following equation:

$$\eta_{avg} = \frac{1}{\varepsilon_f} \int_0^{\varepsilon_f} \eta d\varepsilon \tag{5.20}$$

Strictly speaking, the calibration of the loci could be done on two sets of integrated stress states, with one integral limited by 0 and the damage onset strain, and the other by the damage onset and fracture strains. Such a complication was neglected in this study, with the integral limits being 0 and the fracture strain for both loci.

Another approach to the averaging procedure would be to implement a rolling average where the averaging window is controlled by a specific strain change. This may improve the responsiveness to changes in stress state at the cost of a more difficult calibration routine, wherein the aforementioned multi-part calibration procedure is required, using an arithmetic mean between limits instead of the integral. In addition, there is increased uncertainty in the calibration values because the stress state cannot be measured experimentally and must be simulated based on the elastoviscoplastic model with damage softening and fracture disabled, thus neglecting any damage softening that may significantly change the stress state.

A different calibration would be required in this case as the integral value and arithmetic mean value may differ significantly. For example, the arithmetic mean (and instantaneous) value of an ASTME8 sample is $\frac{1}{3}$, whereas the integrated value with limits at fracture is approximately 0.12.

A penalty term is introduced in order to reduce the impact of failing elements on the non-local stress state calculation; without this term, the non-local term may deviate significantly from the local term instead of acting as a spatial average. The penalty term is the inverse of the exponential used in the damage softening term.

Stress state penalty term

The model is designed to be highly sensitive to stress state in order to capture the behaviour of the material in the blanking process, which may undergo a significant change in stress state with small strain increments. This can, however, produce significant numerical instability in damaged elements and in practical simulations with high mass scaling due to stress wave propagation after fracture. As stress is degraded through damage softening, the triaxiality of that element may become unstable. In order to improve model stability, a penalty term is introduced to the non-local triaxiality increments. This choice to reduce the element sensitivity to the triaxiality effect is justifiable because the stress state calibration using the averaging integral does not consider damage softening. The triaxiality increment is defined as:

$$\Delta\eta = \eta_{inc} \frac{1 - e^{\beta\tilde{D}}}{1 - e^{\beta}} \tag{5.21}$$

where the change in stress state, $\Delta\eta$ is equal to the stress state increment η_{inc} multiplied by a softening term which is the same as that used in the damage softening equation.

Octree for spatial data

The subroutine used for returning the ID of the elements in the interaction radius requires sorting and accessing a large number of variables based on their spatial position. This is a computationally intensive task if a suitable data structure is not chosen. An octree is a hierarchical data structure that recursively subdivides space until each cube contains either one or no elements, making it easier to search for elements based on their spatial position. Figure 5.3 shows a diagram of an octree, displaying the recursive subdivision of space and its nodal representation. In this diagram, it is evident that physically close elements are located within the same parent node. The centroid locations of each element are precomputed and stored in the octree. The subroutine uses the ID of the current element to find its initial coordinates and then searches the octree for all elements that are within the interaction radius, R.

Traversing the octree is faster than sorting and searching through three columns of coordinates. This is because the tree is traversed upward rather than searching through all elements. This means that the algorithm can quickly find the elements that are within the interaction radius without having to sort or search through all elements. As a consequence of the precomputation, the non-local algorithm always acts on the same elements based on the initial centroid coordinates. Large straining will not remove elements from the interaction radius.

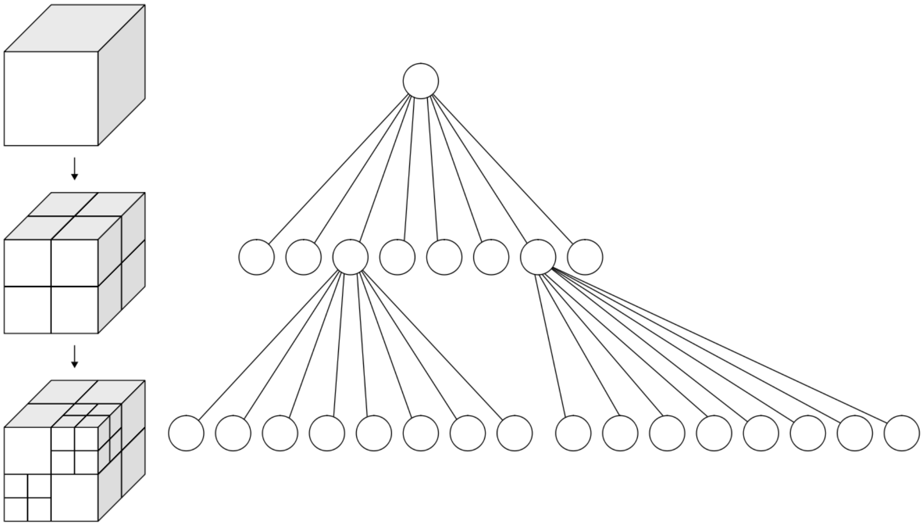

Figure 5.3: *A diagram representing the spatial partitioning strategy of the octree data structure. Reproduced from [180] under CC BY-SA 3.0*

Damage softening parameter

The stress in the region of interest of the shear samples is difficult to determine due to the complex and changing geometry; as such, the softening parameter is calibrated on a force true-log strain curve. This is justifiable because all damage is occurring in the region of interest, and as such, any decrease is purely the effect of damage in said region. The damage is calculated as the relative position between two loci; consequently, the true strain between the peak force and fracture can be directly used in the calibration, remapped between 0 and 1. The calibration can therefore be achieved by finding the value of β which fits:

$$F = F_{max} \frac{1 - \exp \beta \bar{D}}{1 - \exp \beta} \tag{5.22}$$

where F is the current force; F_{max} is the peak force, which defines the damage onset strain (i.e. the strain at the ultimate tensile strength); and D is the position of the remapped strain, i.e. the relative position between the two loci. Figure 5.4 shows this procedure graphically.

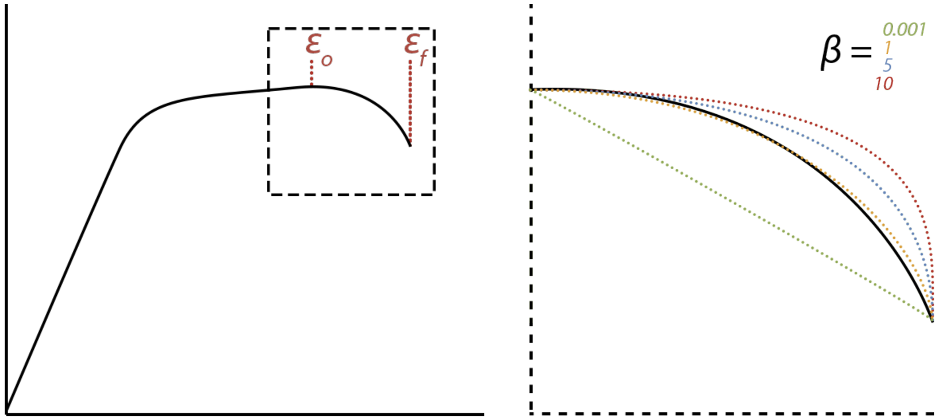

Figure 5.4: *A graphic depicting the influence of the damage softening coefficient β and the its calibration in in terms of the position between two points which form the damage loci.*

The results of this fitting procedure are displayed in Section 4.6.1. The model implements the softening as:

$$\sigma_{new} = (1 - D)\sigma \tag{5.23}$$

where σ_{new} is the stress tensor, σ is the undamaged stress tensor, and D is the damage variable. The damage variable is calculated by

$$D = \frac{1 - \exp \beta \bar{D}}{1 - \exp \beta} \tag{5.24}$$

Where $\bar{D}$ is the damage as a percentage between the damage onset and fracture loci, and β is the damage softening coefficient.

Algorithm

In this section, the details of the implementation of the damage softening part of the VUMAT are explained. The VUMAT interfaces with another subroutine, VEXTERNALDB, which runs prior to the execution of the material model and is responsible for loading a precomputed list of element centroid positions into shared memory and generating the octree data structure required for the non-local portions of the model. The discussion of the damage model continues from the end of the plasticity calculation, as described in Section 5.1. The damage model is uncoupled; therefore, the undamaged stress, $\boldsymbol{\sigma}$, would be the value accepted at the end of the increment, assuming no damage is present in the element.

On the first increment, the weights of the non-local interactions for all elements within the interaction radius are calculated and cached. The source element is the actual element under consideration, i.e. the final damaged stress will apply to this element. The target element is a neighbouring element within the interaction radius, the state of which is defined to influence the source element. The distance from the source element x, is calculated according to:

$$x = ||\boldsymbol{x_i} - \boldsymbol{x_0}|| \tag{5.25}$$

where the location of the target element is $\boldsymbol{x_i}$, and the location of the source element is $\boldsymbol{x_0}$. The bold symbol represents in this case the vector of coordinates in three dimensional space. For each element a multiplier is calculated based upon this distance:

$$\alpha = \frac{1 - x}{R} \tag{5.26}$$

A set of multipliers is now generated where elements located closer to the source element are weighted more heavily than elements far from the source element. Because there are fewer elements in the interaction radius for elements on the boundary of a simulation in comparison to the centre, this weighting will produce artificial hardening of sample edges. To clarify, this is because the total non-local strain would be lower due to a lower number of elements being integrated. In order to correct this flaw, the multipliers are normalised by collecting the sum of all multipliers, α^{Σ}:

$$\alpha^{\Sigma} = \sum_{i=1}^{N} \alpha_i \tag{5.27}$$

where N is the total number of elements in the interaction radius and α_i is the multiplier for some neighbouring element. Dividing each multiplier by the total of the multipliers provides the normalised value, $\bar{\alpha_i}$:

$$\bar{\alpha_i} = \frac{\alpha_i}{\alpha^{\Sigma}} \tag{5.28}$$

As already explained, this calculation occurs only once on the first increment; after this, the normalised multiplier $\bar{\alpha_i}$ for the interaction is recalled from a cache array.

The state variables provided at the start of the increment are the strain increment $\boldsymbol{\varepsilon}$, undamaged stress $\boldsymbol{\sigma}$, the total of stress state increments η^{Σ}, and the total of strain increments $\boldsymbol{\varepsilon}^{\Sigma}$.

For clarity in later steps, disambiguation between terms associated with damage is addressed now. The relative position between the strain loci is the damage driving variable, D. This value is used in the damage softening variable $\bar{D}$, and the softened strain is calculated as $\boldsymbol{\sigma}^D = \boldsymbol{\sigma}(1 - \bar{D})$. The exact definition will be explained later in this section; for now, the reader must only be aware that there is a difference between the terms.

The first step is to calculate the new stress state. In accordance with the equation used in the calibration (see Section 5.2.1), the model integrates the stress state by the strain increment. Such that:

$$\eta_{avg} = \int_0^{\bar{\varepsilon}} -\frac{\sigma_{hyd}}{\bar{\sigma}} \, d\bar{\varepsilon}_{inc} \tag{5.29}$$

where $\bar{\varepsilon}$ is the equivalent strain, σ_{hyd} is the hydrostatic stress, and $\bar{\sigma}$ is the Von Mises equivalent stress. In order to prevent numerical errors in this step arising and to provide increased stability the following conditions must be met for this calculation to occur:

1. The equivalent incremental strain $\bar{\varepsilon}_{inc}$ must be greater than zero

   AND

2. There must be no damage in the element $D = 0$

   OR

3. The damaged stress $\bar{\sigma}^D$ must be greater than the damaged yield surface $\sigma_y(1 - \bar{D})$

More formally:

$$\bar{\varepsilon}_{inc} > 0 \wedge (D = 0 \vee \bar{\sigma}^D > \sigma_y(1 - \bar{D})) \tag{5.30}$$

The damaged equivalent stress $\bar{\sigma}^D$ is calculated in the same manner as the equivalent stress, but uses the tensor components multiplied by $(1 - \bar{D})$. Further numerical stability is provided by a penalty term Γ:

$$\Gamma = 1 - \frac{1 - \exp \beta D}{1 - \exp \beta} \tag{5.31}$$

This penalty is multiplied by the increment of stress state, such that the averaged stress state term is finally fully defined as:

$$\eta_{avg} = \frac{1}{\bar{\varepsilon}} \int_0^{\bar{\varepsilon}} -\frac{\sigma_{hyd}}{\bar{\sigma}} \Gamma \, d\bar{\varepsilon}_{inc} \tag{5.32}$$

If the condition in Equation 5.30 is not met, the values from the previous increment are simply taken as the current values.

The second step is to deal with the non-local variables of the model. The maximum normal strain ϵ_1 and averaged stress state η_{avg} are non-local. Each element places its local value of ϵ_1 and η_{avg} in a shared array which is globally accessible. When a non-local calculation is required the element retrieves the IDs of all elements in its interaction radius, and indexes the shared array by neighbouring ID to retrieve the non-local data. For every element in the interaction radius the non-local value is multiplied by the weighting calculated once at the start of the simulation. The non-local strain contribution ϵ_i^α per element is calculated by:

$$\epsilon_i^\alpha = \epsilon_i \alpha_i \tag{5.33}$$

where ϵ_i is the maximum principal strain of the target element and α_i is the pre-calculated normalised weighting for the target element. In a similar manner the non-local strain is calculated as:

$$\eta_i^\alpha = \eta_i \alpha_i \tag{5.34}$$

The sum of these values over the N elements in the interaction radius provides the final non-local variable:

$$\varepsilon_{NL} = \sum_{0}^{N} \varepsilon_i^{\alpha} \tag{5.35}$$

$$\eta_{NL} = \sum_{0}^{N} \eta_i^{\alpha} \tag{5.36}$$

These two values provide the location in stress-state strain space, the same space in which the damage onset and fracture loci are plotted in Figure 5.1. If $\eta_{NL} \leq -\frac{1}{3}$ no fracture is possible and no damage can be accumulated, so the model skips to Equation 5.39, otherwise the model calculates the damage driving variable D as the relative location between the two loci in this space with the following equation:

$$D = \frac{\varepsilon_{NL} - \varepsilon_i}{\varepsilon_f - \varepsilon_i} \tag{5.37}$$

where ε_i and ε_f are the values of the damage initiation locus and fracture locus, respectively, evaluated at η_{NL}. The damage driving variable is defined to be monotonically increasing; as such, if $D_{new} < D_{old}$, the new value is discarded. The degradation of stress is then modelled exponentially using the following formula:

$$\bar{D} = \frac{1 - \exp \beta D}{1 - \exp \beta} \tag{5.38}$$

$$\boldsymbol{\sigma}^D = \boldsymbol{\sigma}(1 - \bar{D}) \tag{5.39}$$

where β is a model coefficient termed the *exponential softening coefficient.* The new stress at the end of the increment is set equal to $\boldsymbol{\sigma}^D$, and the undamaged stress $\boldsymbol{\sigma}$ is saved as a state variable and used for the plasticity calculations in the next increment. In this manner, the damage model remains completely uncoupled from the plasticity model and provides the expected hardening behaviour.

A flowchart of the overall operation of the model is shown in Figure 5.5.

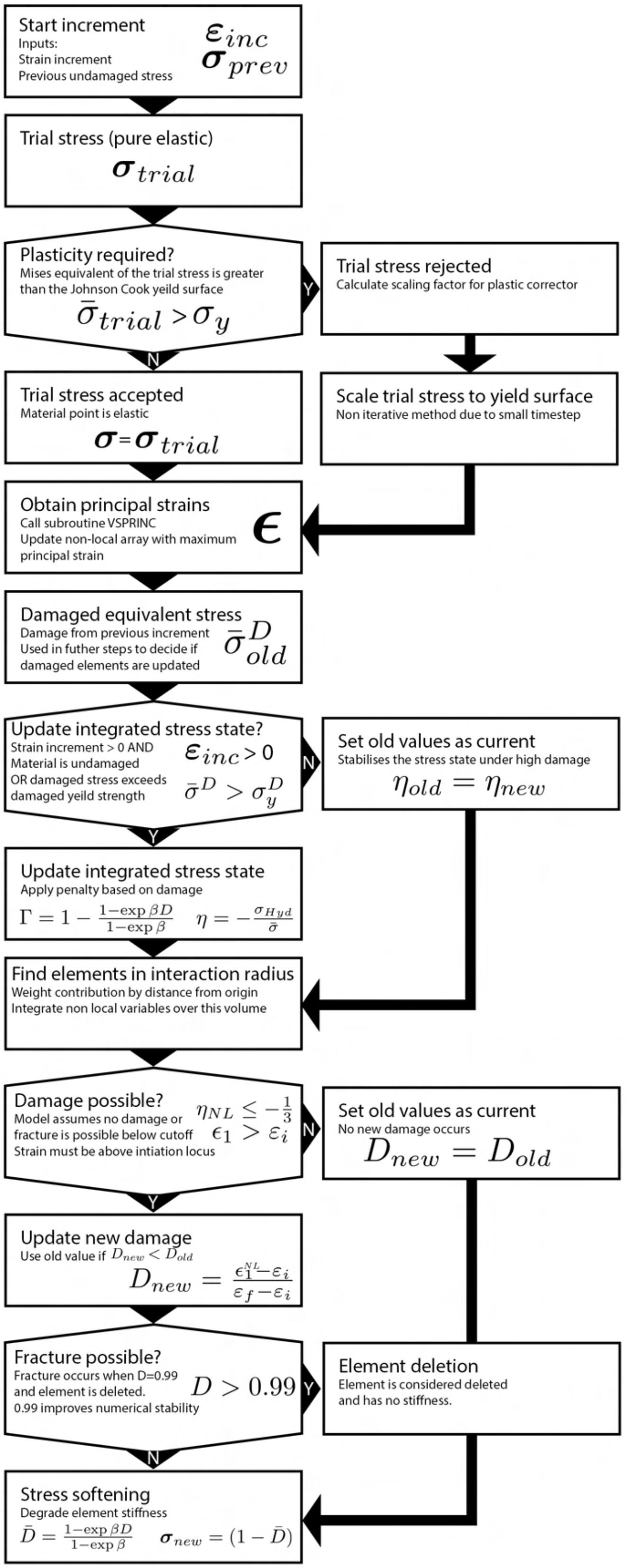

Figure 5.5: *A flowchart for the model operation*

5.3 Multithreading implementation

Multithreading is a technique in computer science that enables parallel processing of tasks. In the context of numerical simulation software like ABAQUS, multithreading can significantly improve runtime performance. This is because it allows the simulation to make use of multiple processor cores simultaneously by decomposing the model into several domains, upon which each core can independently work.

ABAQUS supports multithreading using either MPI (Message Passing Interface) or threads. MPI is a standardised communication interface for parallel computing that enables processes to communicate and exchange information, whereas threads are lightweight processes within a single process that can run in parallel on different cores of the same CPU.

Common blocks are shared memory locations in FORTRAN that can be accessed by multiple threads. However, this is now considered deprecated the recommended way is via the use of modules. Modules are units of code and memory that can be shared by multiple threads, and they allow for memory sharing between threads. However, it is important to note that the shared memory should not be written to by the threads, as this could cause unpredictable behaviour. In the case of the presented VUMAT, it is safe to write to the shared memory without additional checks or multithreading techniques such as semaphores, as each thread only writes to its own *nblock* (number of elements passed to the subroutine) of unique element addresses. This way, each thread operates independently and does not interfere with the memory of other threads. Without additional checks the performance overhead of the multithreading implementation is significantly reduced, however this limits the use to thread mode only.

5.4 Mesh Sensitivity

A key aspect of non-local models is their resilience to mesh sensitivity; the non-local interaction radius, which provides an integrated value that is physically relevant, prevents the pathological mesh sensitivity found in local implementations of strain softening damage models.

To test the mesh sensitivity of the damage model, a simple test geometry consisting of a 10 by 1 mm part was generated with mesh sizes ranging from 0.25 mm to 0.02 mm. This geometry was used because it is easy to generate a structured mesh and allows different element aspect ratios to be tested in a controlled manner. The top edge of the specimen was fixed with an encastre boundary condition, and a velocity boundary condition was applied to the bottom edge along the vertical axis. The damage softening coefficient, β, was set to 0.1 to approximate linear softening; this is the worst-case scenario and exacerbates the potential sensitivity as significantly more stress is degraded in low-damage regions.

Figure 5.6 shows the result of the study; in each case, the frame taken prior to fracture is shown, which was consistent across every trial. The left grouping shows the magnitude of displacement; it is noted that this value was equal within 0.01 mm at the bottom edge of the sample between all samples. The right grouping shows the damage driving variable, which again is consistent in magnitude and distribution across each sample type.

The exact location of the necking varies for each specimen, but this is to be expected as there is no preferred location for damage initiation due to the rectangular geometry, and this location is essentially randomly determined by the accuracy limitations inherent in the floating-point representation of real numbers and the propagation of stress waves in the solver. The examples labelled (c) and (d) are generated with a bias in the mesh; with finer elements at the ends in (c) and in the centre in (d), there is no bias in the necking at the location of the smaller elements, which would indicate mesh sensitivity. In fact, the necking occurs outside the region of the finest mesh in (d).

In each case, the morphology of the damaged specimen is equivalent, and the distribution of damage occupies the same physical space. This again provides confidence that mesh sensitivity is eliminated, as the damaged region would be smaller in a mesh-sensitive model because more stress is degraded at the initial damage site, leading to more severe necking in those elements.

Figure 5.7 shows the stress strain curve for the element with the highest damage in each sample. Convergence is found for meshes (b), (c), and (d). The stress dissipation is more severe in the (a) mesh because it is extremely coarse, meaning there is an error in the normalising procedure for the non-local variables. Some difference is found in the force at the damage onset for the (d) mesh, which is again a result of the low total number of elements in the interaction radius, showing the biased elements have still generated a bias in the stress dissipation for this sample with a low number of elements. When the damaged volume becomes large enough to encompass the smallest elements of the mesh, the stress once again converges. This result proves the mesh insensitivity but shows the ongoing requirement for a sufficiently refined mesh.

In conclusion, this section has shown that the model is insensitive to the mesh used, given sufficient refinement. Three key metrics have been used: the total displacement to failure, the distribution of the magnitude of the damage driving variable, and the stress-strain curve at the most damaged element.

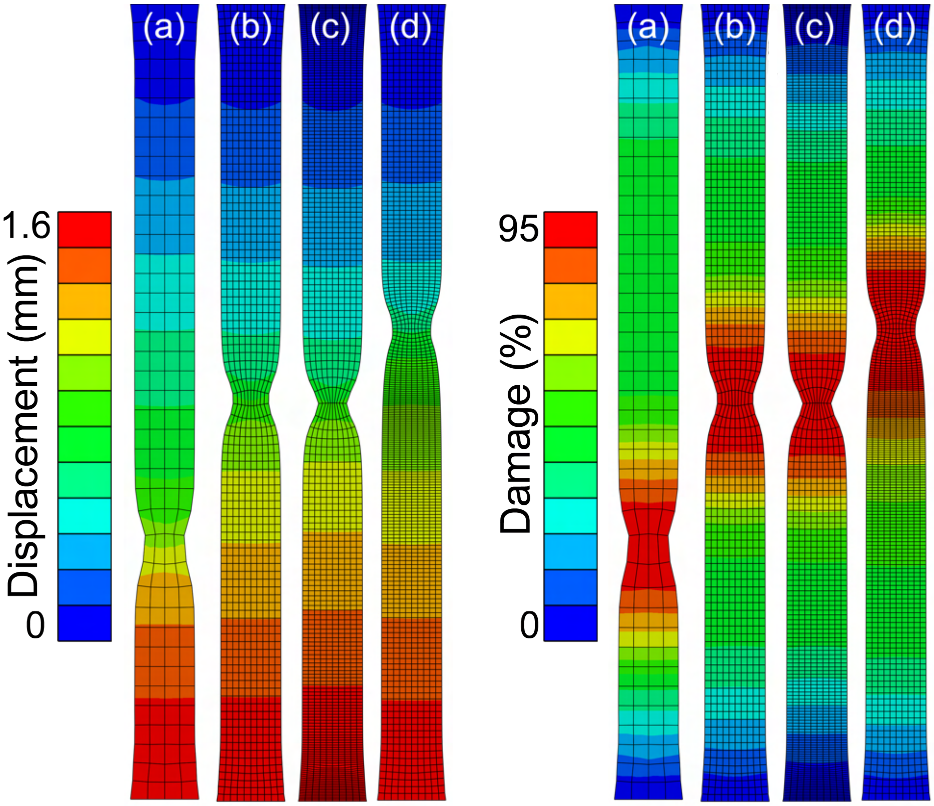

Figure 5.6: *Several test cases to used to study mesh sensitivity in the damage model. Four samples are shown at the same time just prior to fracture initiation, left grouping shows displacement, right grouping shows the damage driving variable.*

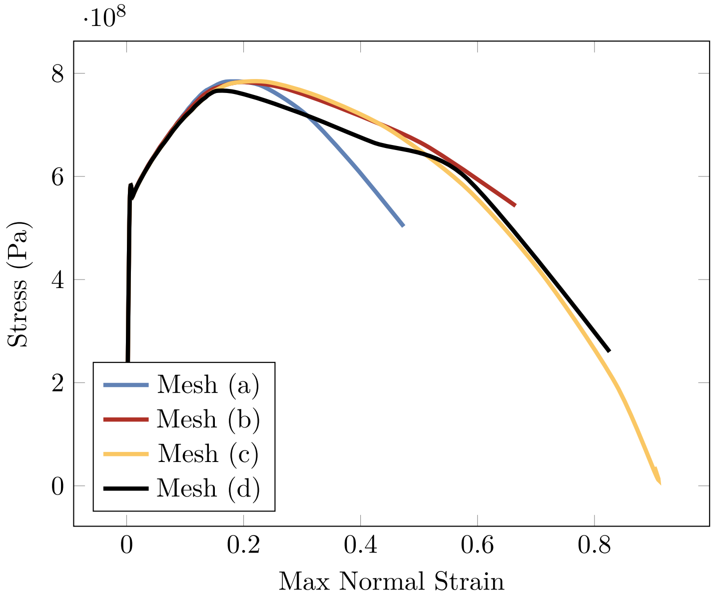

Figure 5.7: *Stress strain curves for the element with the highest damage in each sample.*

5.5 Simulation of calibration samples

In the following sections a variety of parameters must be calibrated or confirmed, and to do so the calibration samples were simulated. This section explains and justifies the simulation settings and setup for each of the test coupons.

The quasi-static calibration test coupons were simulated to form the first part of the verification and to provide a value for the interaction radius via reverse analysis. The explicit solver is conditionally stable and very small time steps must be taken to maintain model stability. The size of the smallest element and the density of the material (and hence the wave propagation velocity) are the factors that affect the stable time step. ABAQUS uses the following equation to estimate the minimum time step required:

$$c_d = \sqrt{\frac{E}{\rho}} \tag{5.40}$$

where E is the Young's modulus and ρ is the mass density. The small size of the elements required to accurately simulate the high gradients in the test coupons, combined with the high mass density of the material, means that very small time increments are required, on the order of 10^{-9} or 10^{-10} seconds. The quasi-static tests were run over a period of several minutes, so the computational effort required to simulate this would not be feasible without some degree of scaling. Two strategies are employed: one is to scale the mass for the smallest elements; this significantly increases the time step because, due to meshing difficulties from complex geometry, some elements are generated that are significantly smaller than the bulk element size just outside the region of interest. Another strategy is to scale the time in which the deformation occurs. By setting all time-dependent variables to 0, i.e., removing the viscoplastic term from the Johnson-Cook plasticity model, the rate of deformation can be significantly increased, thus reducing the total number of increments required for the same deformation. In both cases, care must be taken not to inadvertently introduce inertial effects. There are a number of ways to check this, including checking the energy balance and integrated reaction force at the boundary conditions. If inertial conditions are dominant, the integrated reaction force at the boundary will be unstable due to stress waves propagating through the model; under quasi-static conditions, such instability is not present. In addition, the ratio of the total kinetic energy in the model to the total internal energy can be compared; if the kinetic energy is high, i.e., greater than 10% of the internal energy, this indicates inertial dominance. Energy outputs can also be used to indicate the need for mesh refinement if, for example, the artificial strain energy is large compared to other energies.

5.5.1 Tensile geometry

To confirm correct behaviour at a positive stress triaxiality of $\eta = 1/3$ the tensile geometry was simulated. It was partitioned such that a structured mesh could be used in the central reduced section. An encastre (i.e. fully fixed) boundary condition was applied to the bottom face of the grip section, and a velocity boundary condition of $4\,\mathrm{mm\,s^{-1}}$ was applied to the top face. Figure 5.8 shows the geometry, applied boundary conditions, and an example mesh with a 0.1 mm element size. The boundary conditions are applied on the top and bottom faces, which were found to give identical results to other schemes, such as those applied to the front and back faces of the grip section or the grip section cells. The structured mesh in the reduced section can be observed, with a swept mesh in the grip section to allow for easy meshing around the curved sections. Hexahedral elements of type C3D8R (8 node linear brick, reduced integration, hourglass control) were used. A mass scaling scheme to a target time increment of $1 \times 10^{-7}\,\mathrm{s}$ which resulted in a in a scaled mass of $3.6 \times 10^{5}\%$ that of the original element.

Figures 5.9, 5.10, and 5.11 show the damage driving variable, non-local maximum principal strain, and non-local triaxiality, respectively, for the tensile geometry. The location of fracture initiation is incorrectly predicted as the centre of the sample, but the characteristic ‘flat’ fracture initiation perpendicular to the long axis of the sample, followed by fracture propagation at an approximate 40° angle, is successfully reproduced.

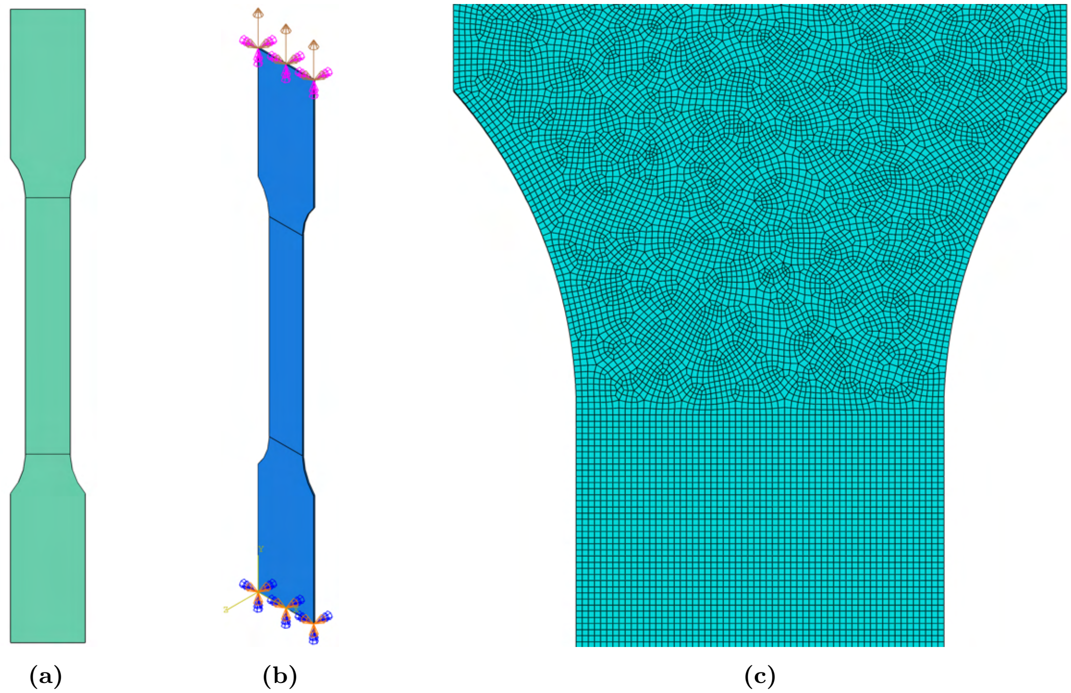

Figure 5.8: *Tensile geometry simulation setup. (a) sectioned geometry, (b) applied boundary conditions, (c) example of mesh at 0.1mm element size.*

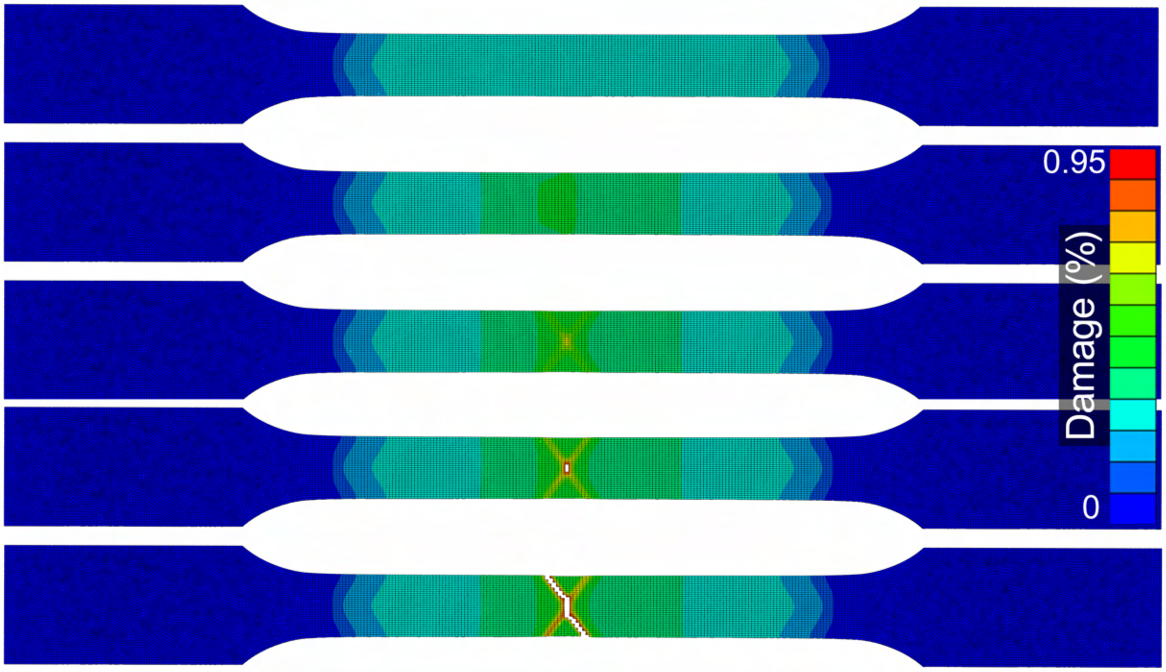

Figure 5.9: *Damage variable of the tensile sample prior to and post fracture*

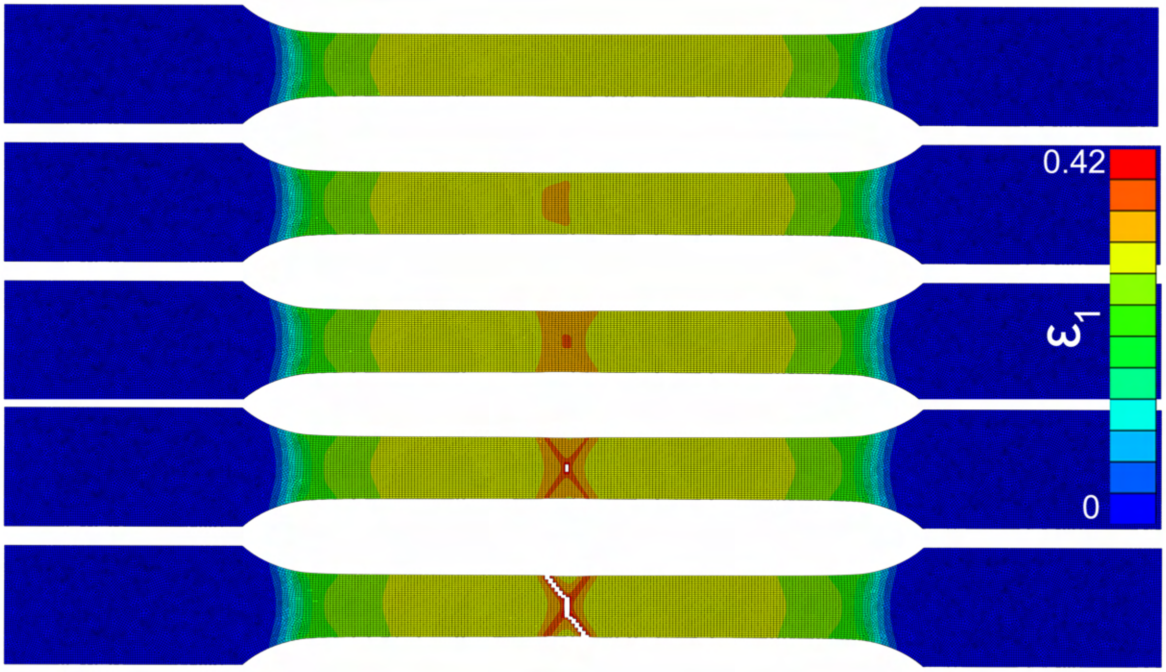

Figure 5.10: *Non-local maximum principal strain of the tensile sample prior to and post fracture*

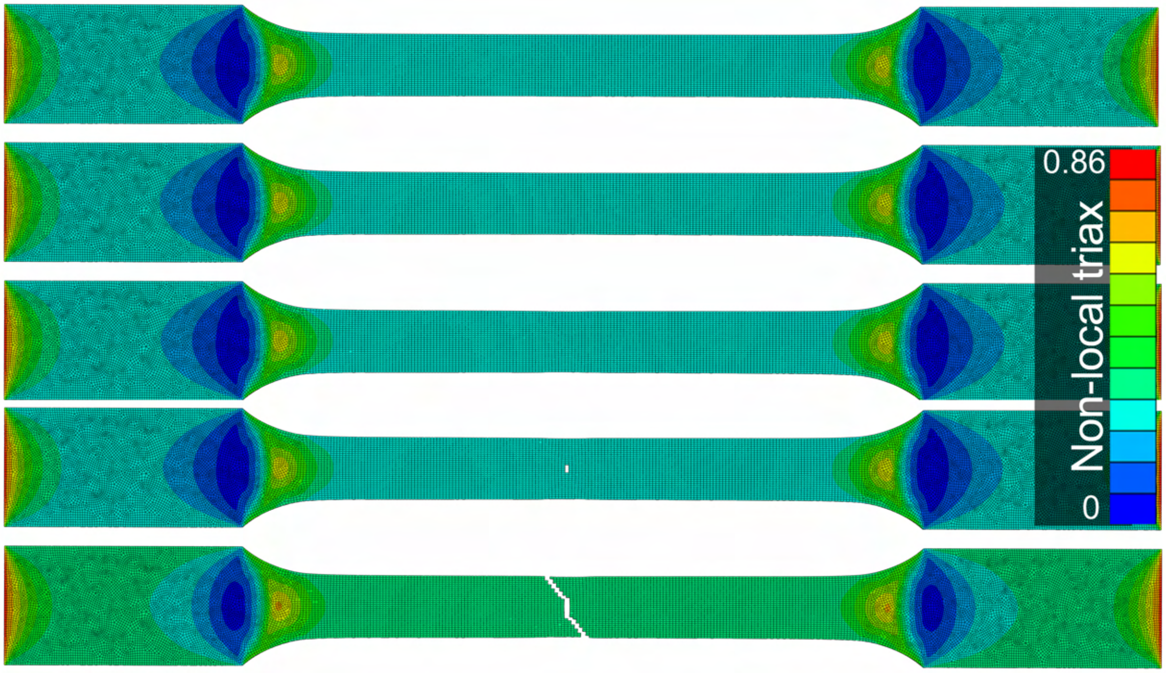

Figure 5.11: *Non-local triaxiality of the tensile sample prior to and post fracture*

5.5.2 Shear geometry

In a similar manner to the tensile geometry, the shear geometry was partitioned to allow for a structured mesh where possible. Due to the much more complex shape, this region required careful sectioning to achieve this goal, as demonstrated in Figure 5.12. In comparison to the tensile geometry, an additional boundary condition restricting out of plane movement was required to prevent buckling, enforced on the central front and back faces of the section as to recreate the experimental setup.

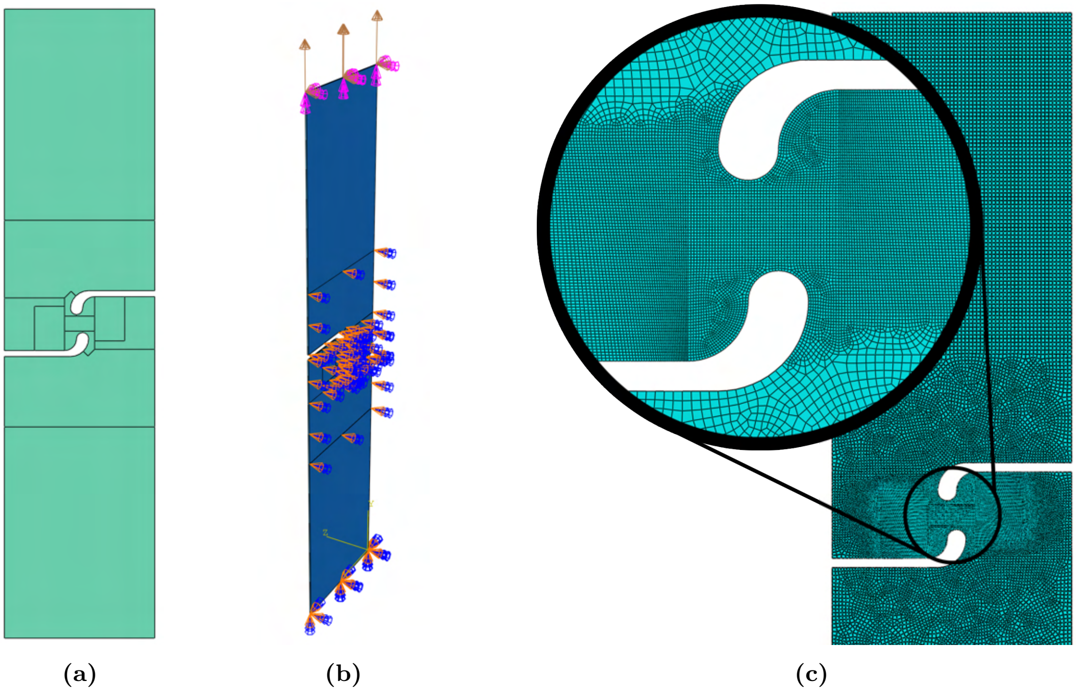

(a) **(b)** **(c)**

Figure 5.12: *Shear geometry simulation setup. (a) sectioned geometry, (b) applied boundary conditions, (c) example of mesh at 0.1mm element size.*

The results of the simulation are shown in Figures 5.14, 5.15, and 5.16. Figure 5.14 shows the damage driving variable evolution through five frames. It is notable that damage initiation is observed in the central shearing region (frame 1) of the sample, but that because of the low initial softening, a secondary damage site becomes active (frame 2) and dominates the evolution. Fracture initiation is observed from the bottom of the sample in frame 3, which quickly causes a compensatory secondary fracture in frame 4 due to the changing stress state. From this point, the central region of the sample rotates as the cracks propagate vertically on either side. Figure 5.15 shows the non-local triaxiality throughout this same simulation; the desired stability and responsiveness of this field are demonstrated between frames 3 and 5, wherein the stress state in the centre of the sample remains approximately equal to 0, but the value for elements near the crack path changes due to the larger strain increments. The crack propagates along the transition between shear and tensile mode deformation at the stress state 0.2-0.3. Figure 5.16 shows the non-local value of maximum principal strain and again shows stress-state-dominated damage and crack evolution. The first frame shows uniform shearing in the region of interest, which is continued into the second frame. Fracture

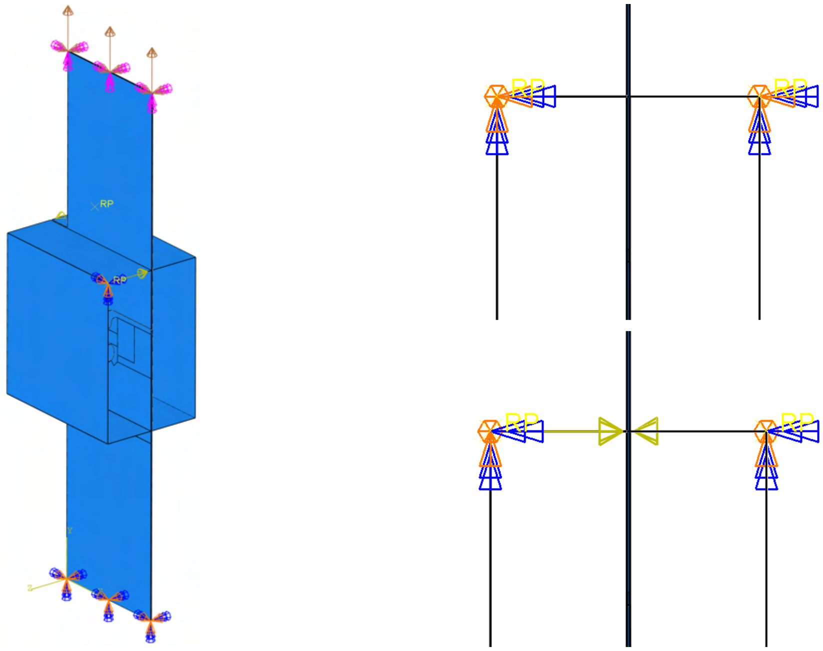

(a) **(b)**

Figure 5.13: *Alternative method for simulating the shear restraint using contact, (a) two analytical parts act as restraints, (b) the restraints may be fixed (top) or a force applied to act as a clamp (bottom).*

occurs outside of the region with the highest strain because of the stress state, and the crack actually propagates alongside the region with higher strain (frame 4). The final frame shows steady-state vertical crack propagation, wherein the bands of high strain are aligned with crack propagation.

This result agrees very well with experimentally observed sample behaviour in some cases, but a true shearing mode has also been observed in experiments. It was suspected that the requirement for mode to arise would be larger initial shearing due to damage, which would suppress the secondary damage onset phenomenon. To test this, the exponential softening coefficient, β, was set to 0.1 to produce an essentially linear softening response. The results of this change are displayed in Figure 5.17.

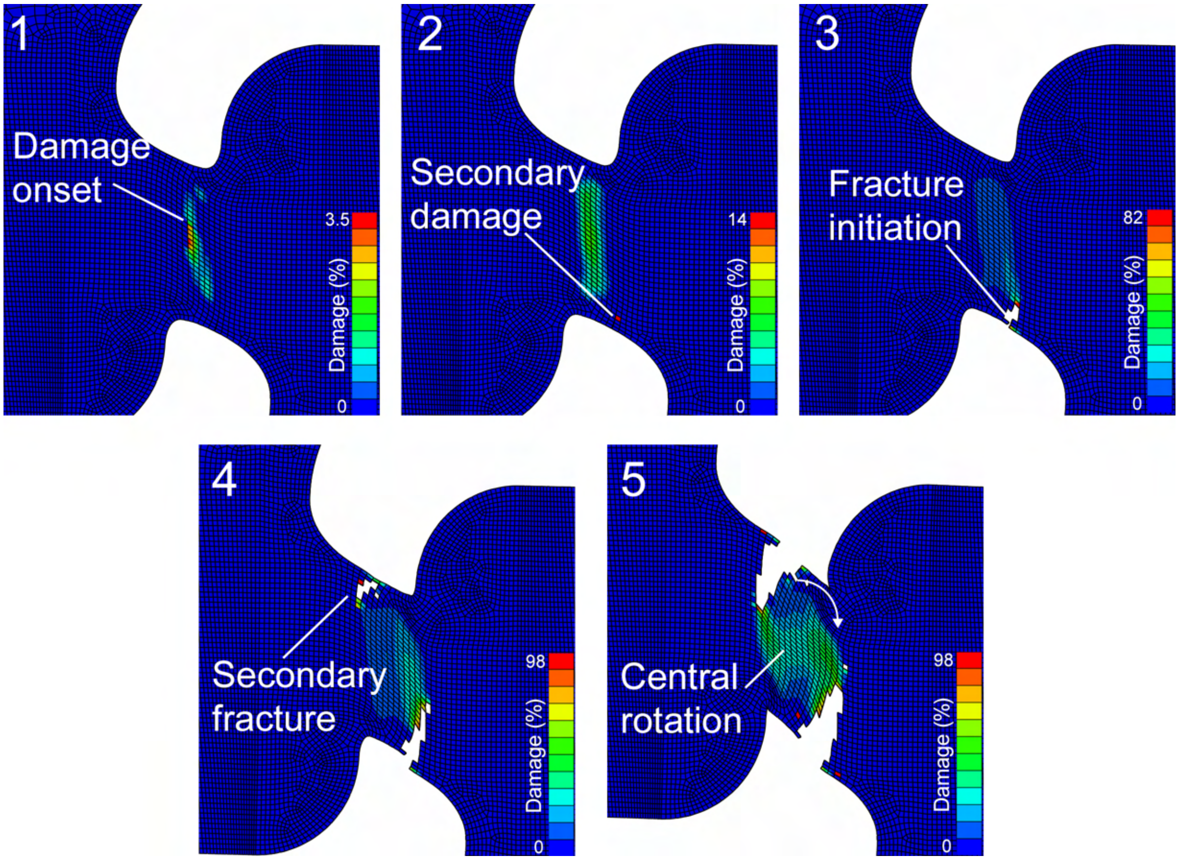

Figure 5.14: *Damage variable throughout deformation of the shear sample with the calibrated softening coefficient*

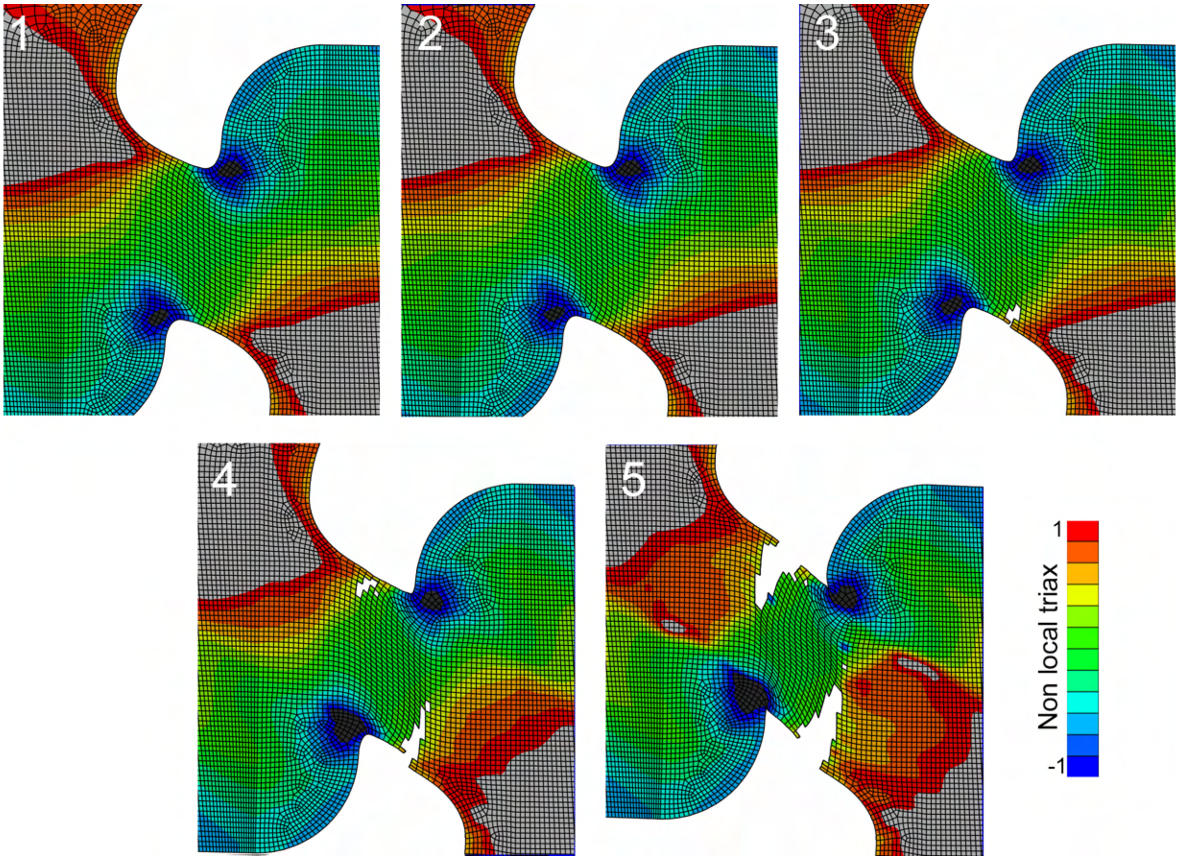

Figure 5.15: *Non-local stress triaxiality throughout deformation of the shear sample with the calibrated softening coefficient*

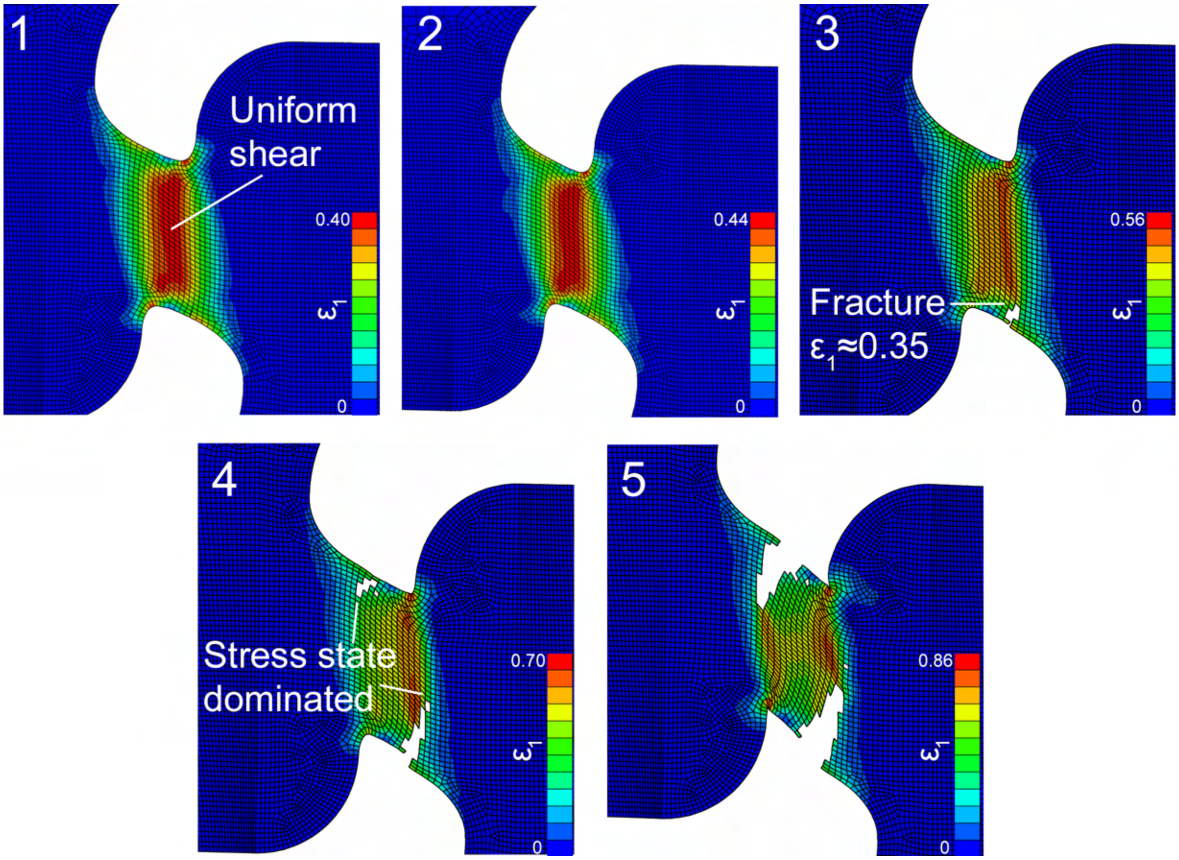

Figure 5.16: *Non-local maximum principal strain throughout deformation of the shear sample with the calibrated softening coefficient*

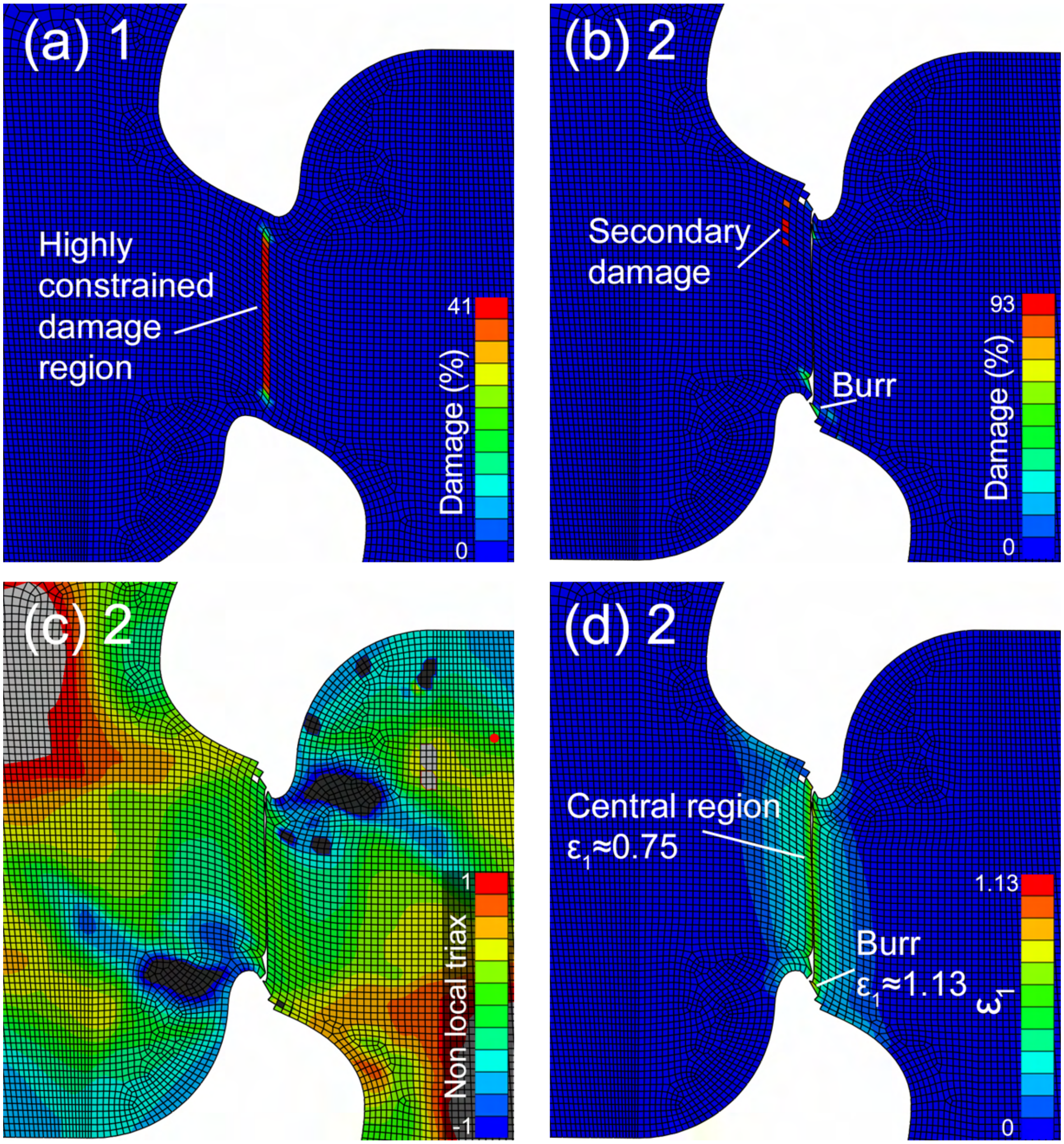

Figure 5.17: *The shear sample with a coefficient $\beta = 0.1$ which produces linear stress degradation.*

5.6 Simulation of blanking

5.6.1 Worn tool

A worn tool with a radius of 0.15 mm and a clearance of 10% was simulated for the blanking of 0.35 mm sheet. A velocity boundary condition was applied to the tool of 100 mm min^{-1}, and a concentrated force on the stripped plate of 200 N. The part was simulated in 3D with an extruded depth of 50 µm with plane strain boundary conditions applied on the edges in the extrusion direction. Figure 5.18 shows the damage driving variable at three stages of the punch penetration. It is shown that with the exponential damage softening term $\beta = 6.355$ the damage is highly localised and is almost nonexistent outside of the elements, which are eventually deleted. It is noted that in this case a number of large elements are deleted, leading to significant mass loss; this is not physically representative and is considered an error, as discussed later in this section. Figure 5.19 shows the non-local maximum principal strain. As seen in other test cases and the blanking experiment displayed in Section 4.4, the fracture initiates at the bottom edge of the sample outside the band of high strain. The fracture propagates vertically towards the top of the sheet, following the path of the fracture minima in the damage and fracture loci. Figure 5.20 shows the stress state in the material: a large region in the fracture zone is between 0.2 and 0.3, and high values outside the calibration range are found throughout the sample.

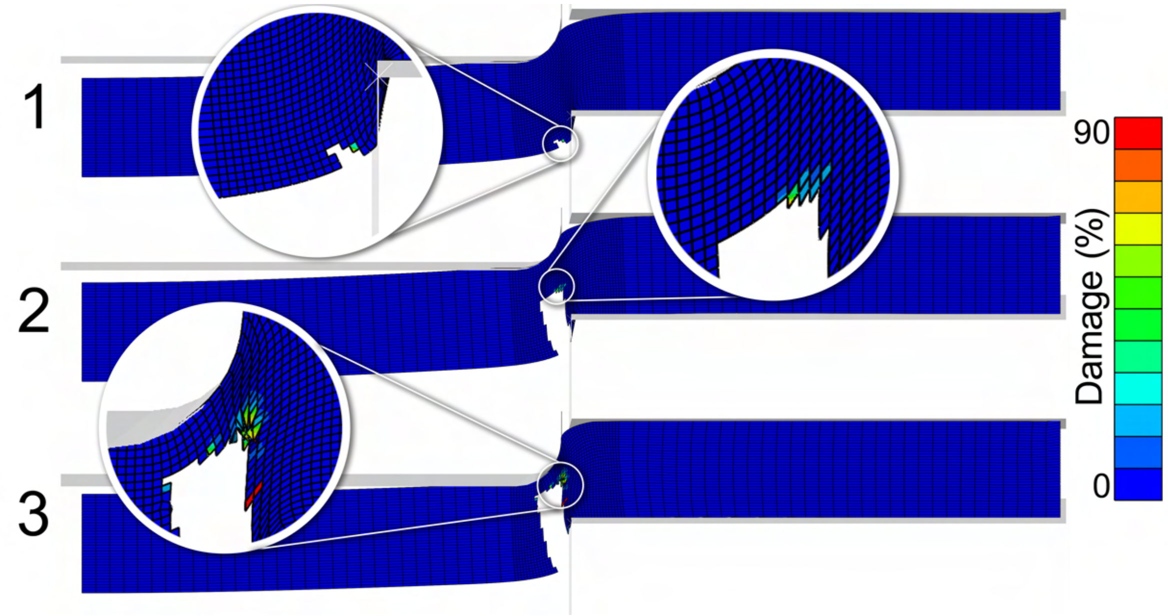

Figure 5.18: *Damage driving variable at three points through the stroke of the tool*

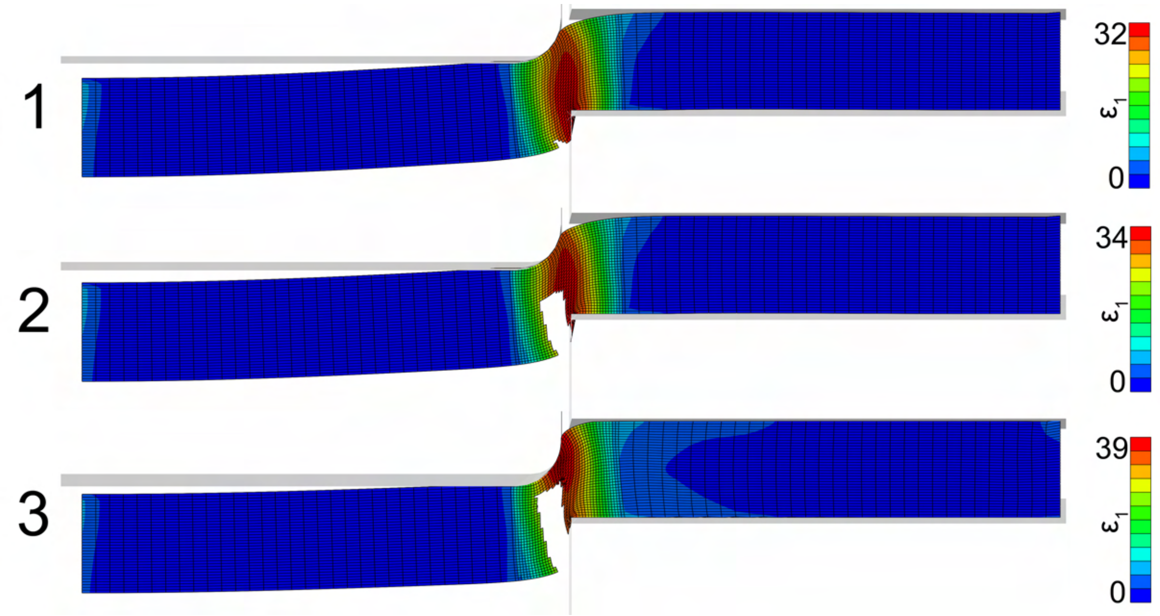

Figure 5.19: *Non-local maximum principal strain at three points through the stroke of the tool*

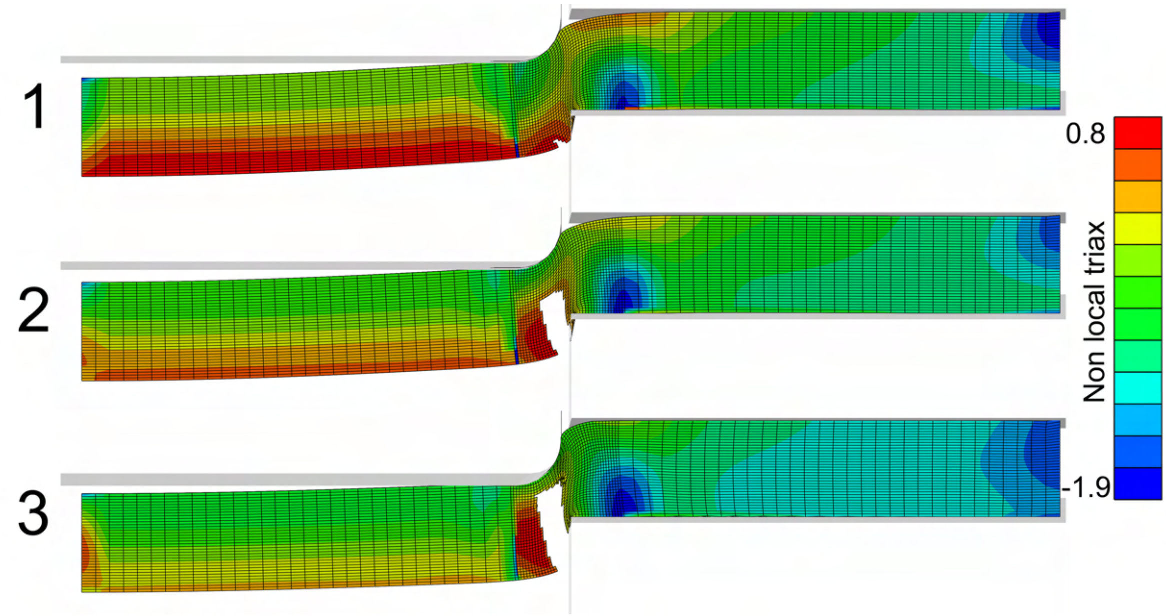

Figure 5.20: *Non-local stress state at three points through the stroke of the tool*

5.6.2 New tool

A new tool was simulated with a radius of 0.015 mm, this radius was chosen to ease contact over-penetration. The same parameters, boundary conditions, and loads were used as for the old tool. Figures 5.21,5.22, and 5.23 show the damage driving variable, non-local maximum principal strain, and non-local stress state at various stages throughout the punch travel. It is possible to see the burr on the blanked part is improved in this condition, and the fracture dynamics are quite different, with a more localised shearing producing a band of damage prior to fracture. Additionally, in this condition, fracture occurs from the top face of the sample first, with a secondary fracture occurring from the bottom and meeting the first some time later.

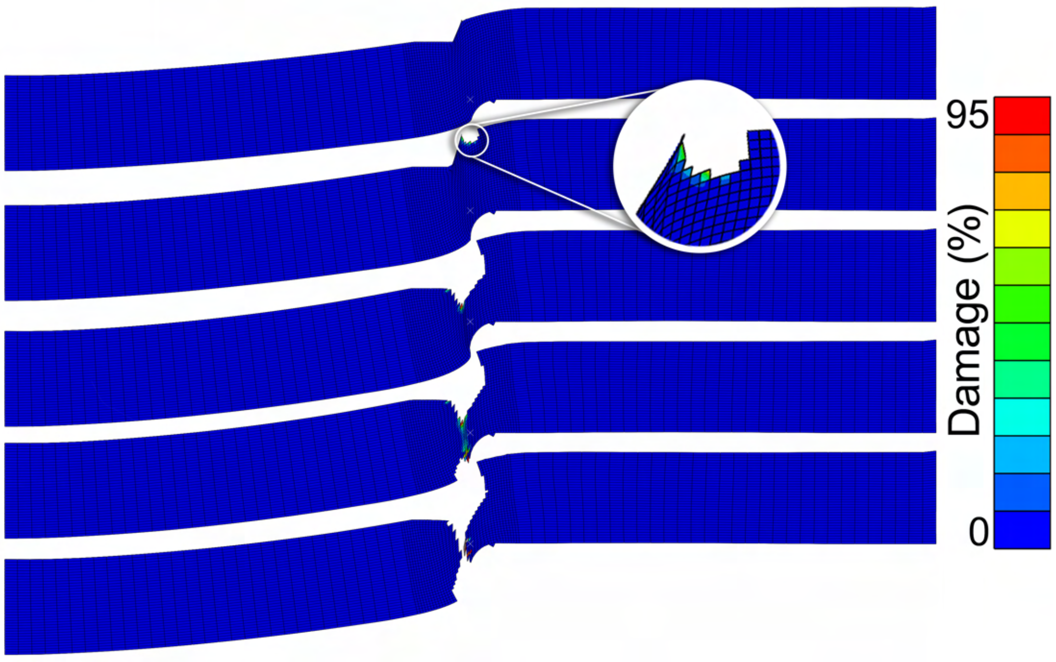

Figure 5.21: *Damage driving variable evolution for the new tool geometry.*

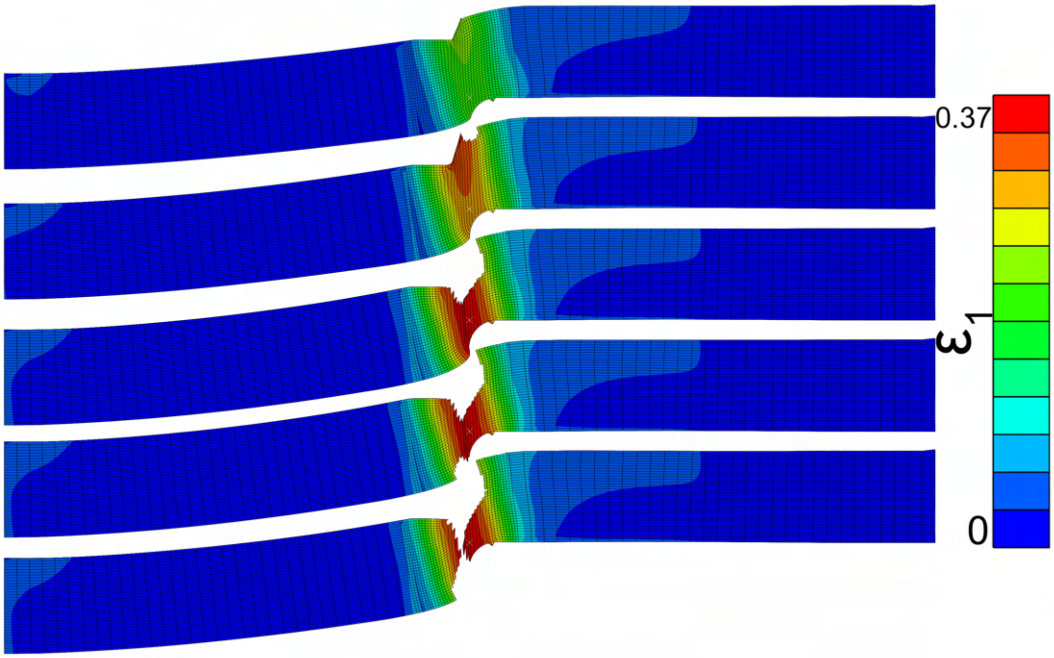

Figure 5.22: *Non-local maximum principal strain evolution for the new tool geometry.*

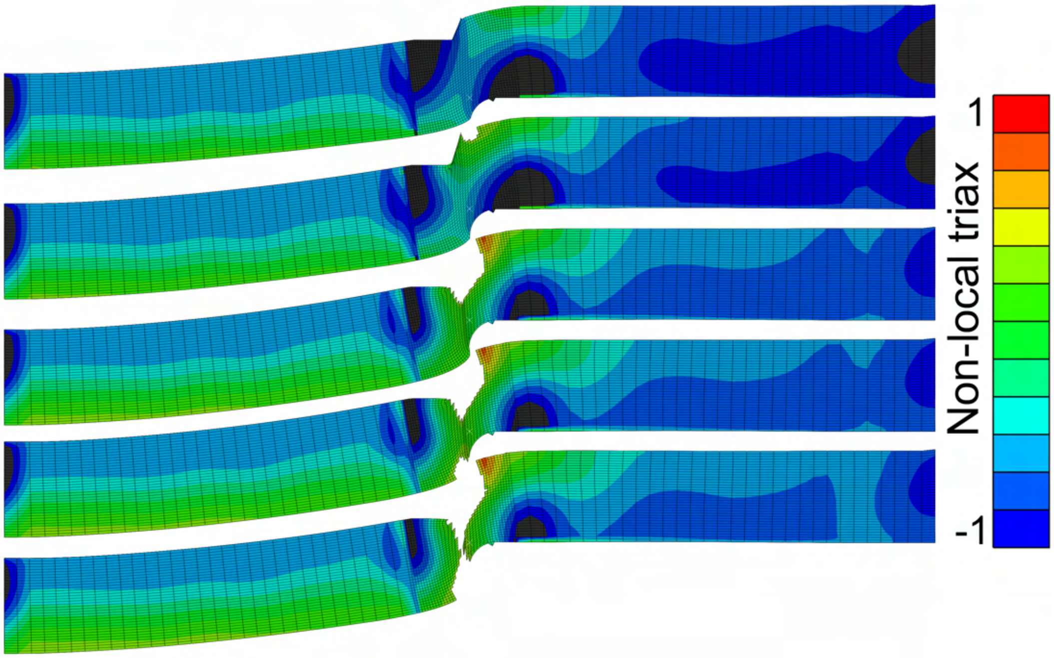

Figure 5.23: *Non-local stress state evolution for the new tool geometry.*

Chapter 6

Discussion

In this chapter, the results of the experimental work and different aspects of the numerical modelling approach are discussed. A critical analysis of the developed and applied methodology in the application of producing a calibration for the novel damage softening model is undertaken - exploring the assumptions made and the source of experimental errors. Various aspects of the damage softening model are assessed for suitability in the application of blanking, and an assessment of the consequences of the choice of a non-local model formulation is undertaken. The consequences of the development of the model are made clear and its strengths and weaknesses in comparison to alternative existing models in the literature are discussed. Other aspects of the finite element model are discussed, such as the suitability of the Johnson Cook plasticity model for the material, and why this model was chosen for implementation.

Previous work on this material has shown a critical influence of the microstructure on the properties of the cut edge in blanking due to the low number of grains taking part in the deformation [2]. A consequence of this is that grains that are aligned in a favourable manner (i.e. the slip planes are aligned with the direction of deformation) deform more easily, and can influence the required cutting force and cut edge quality. In accordance with these findings, the present work set out to develop a model that is suitable for calibration using the final sheet product as opposed to a bulk product because of the different properties observed due to the dominant effect of the grain size, and has demonstrated that the local fracture strain of the material is indeed independent of the sheet orientation because a 'weak point' generated by the grain boundaries is always available to initiate fracture. Any observed anisotropy is therefore a result of combined effects of the anisotropies present in the plasticity and damage response of the material. The model developed therefore treats the damage initiation and fracture as an isotropic process which provides simpler calibration. A number of steps towards a coupled model for the prediction of iron loss with edge damage and strain softening have been undertaken in the development of the model and the technique of using hall sensors to measure flux decrease through deformation. In this chapter, the reason for the sensitivity of the model, the consequences of this sensitivity, and the ability to produce an additional locus for the magnetic damage is assessed.

Severe plastic deformation in shear has been demonstrated and qualitatively characterised in comparison to other stress states and in this chapter the methodology of such measurements is critically analysed.

6.1 Elastic to plastic transition

The damage softening coefficient calibration was shown to vary in Section 4.6.1 depending on if the strain was calculated from DIC (i.e. the maximum normal strain scalar field averaged over the region of interest) or based on crosshead displacement. The stress-strain curves generated from both methods showed good agreement, particularly in the mid to high strain regions of the curves; however it is noted that at low strains, particularly at the elastic to the plastic transition some variance between the two is apparent. This variation can be explained by the non-uniform transition which is clearly visible in the DIC images. The sample shows uniform deformation in the elastic and plastic regions, but the transition period is non uniform. The elastic strain is small (1%) and uniform across the sample, but regions of up to 3% strain occur before the stress-strain curve exits the linear portion. This is a result of the large grain size in comparison to the sample thickness, where grains with slip planes that are favourably aligned with the deformation will transition to plasticity first preferentially.

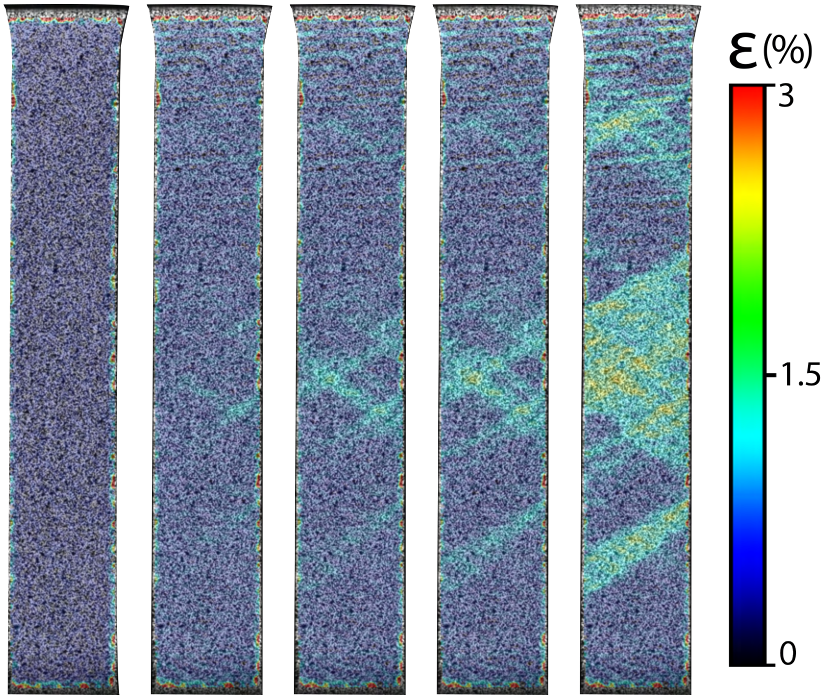

Figure 6.1: *DIC composite image of the elastic to plastic transition showing the maximum normal strain.*

It is noted that at higher temperatures, the sharp transition is not observed, and the DIC results indicate that such a non-uniform transition as seen in room temperature tests is not present; instead the deformation remains uniform and the second derivative of the stress with respect to strain is closer to zero. Figure 6.2 shows this reduced spatial strain gradient, the regions of higher strain are more smoothly distributed. This may be explained by the increased energy available to promote dislocation glide in all crystals, thus reducing the effect of a favourable orientation (i.e. where the direction of the force is aligned with the slip planes). Such an effect is discussed in Mukherjee et al. [181] in the context of creep, but applicable in this case also. The difference in this behaviour at higher temperatures results in difficulty fitting the Johnson Cook model temperature parameters, using data from 100 °C produces a value of $m = 3.18116e - 4$, causing under prediction of stress at 300 °C. The Reduced χ^2 value was used to compare various calibration values generated from trials at varying temperatures, a better fit across all data points was found using the 300 °C trials to calibrate m.

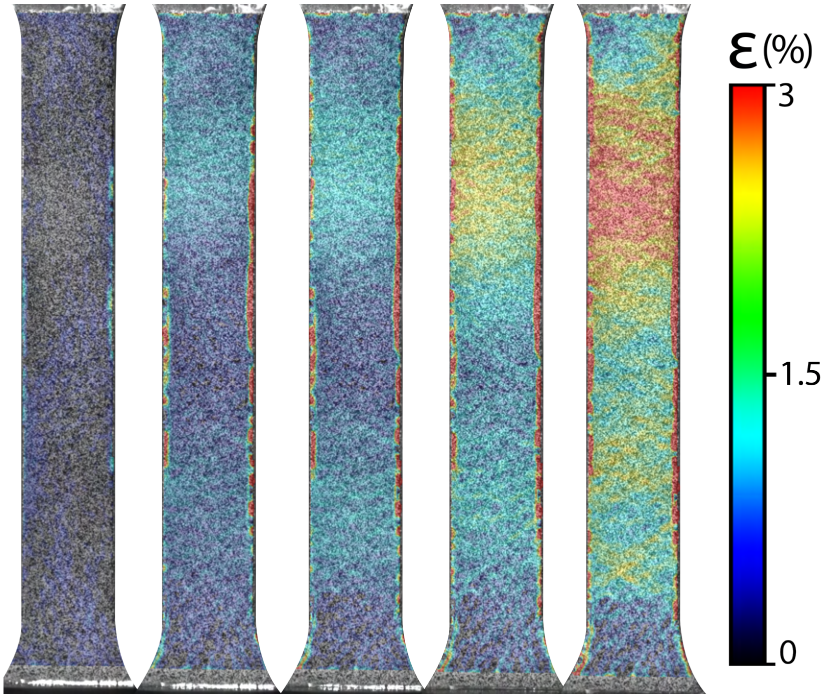

Figure 6.2: *DIC composite image of the elastic to plastic transition at* 200 °C, *showing the maximum normal strain.*

6.2 Speckle quality assessment for DIC

The quality of the speckle pattern generated for each sample was assessed using a variety of metrics established in the literature. This is important because the speckle pattern is a key factor in the spatial strain resolution achievable with DIC. Figure 6.3 shows a composite of representative speckle patterns used in this work. The subset size for each specimen type was chosen to be of equal physical size among all specimens used to calibrate the model. The minimum physical subset size was determined by the 'worst' pattern overall. For this reason, this section focuses on the DIC preparation and discusses the suitability of the cohort of sample geometries used.

Table 6.1 shows the Shannon entropy (1D) and the 2D entropic measure of speckle quality based on the principles outlined in [169]. It is clear that the speckle patterns used in this study are of high quality in terms of randomness, a key indicator of pattern quality [77, 75]. The 2D entropy measure presented here scores the 4th, 5th and 7th patterns in Figure 6.3 lower than the 1D counterpart because of the geometric information encoded in this measure, i.e. the patterns are not as well distributed, with patches on light and dark areas. In the application of speckle quality assessment, this geometric awareness is an excellent feature and provides an alternative to established quality measures [86, 87, 83]. Table 6.1 also includes a measurement for the unpainted edge of the in-situ blanking sample shown in Figure 4.16, in which case a weakness of the metric is identified because the entropy values are comparable to those of the 5th pattern in Figure 6.3. The entropy should not be considered in isolation, and other methods such as those presented in [167, 168] wherein the size and density on a subset level are considered are required. This is because high information density (i.e. randomness) is only one aspect to a successful correlation, the features must be highly distinguishable such that the correlation criteria can be minimised/maximised easily.

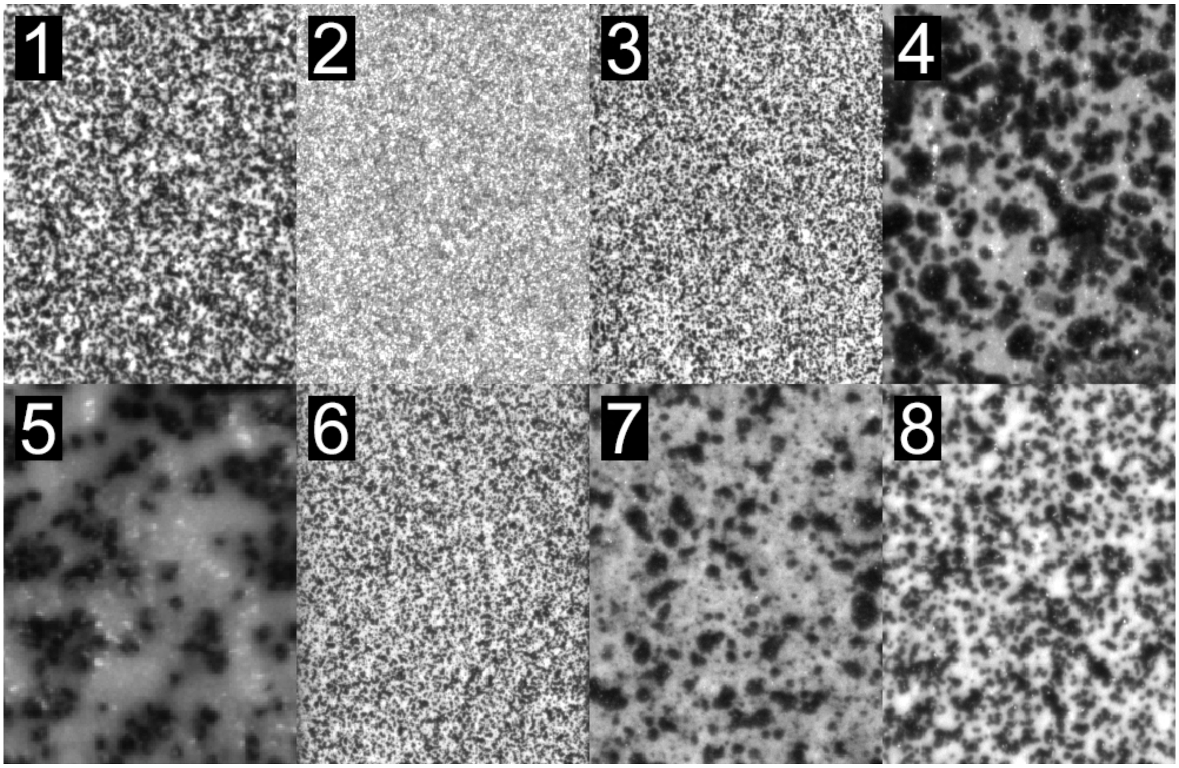

Figure 6.3: *A representative selection of speckle patterns used in this work*

Pattern	Entropy Value 1D	Entropy Value 2D
1	7.11	7.18
2	6.91	7.15
3	7.16	7.19
4	7.02	6.63
5	7.12	5.39
6	7.51	7.21
7	6.77	6.56
8	7.70	7.02
Unpainted	6.60	5.87

Table 6.1: *A qualitative comparison of pattern randomness for the samples in Figure 6.3*

6.3 Determination of fracture point

The determination of the frame that should be used as the instant prior to fracture can be ambiguous for some samples, which produce a slower ‘tearing’ style of fracture in comparison to those wherein the fracture propagates quickly. The accuracy of the model is strongly influenced by the value of localised strain which can change significantly (as much as 20%) in the last moments prior to fracture. DIC can measure only surface displacements, and to do so requires (for the most part) a painted layer to track, therefore introducing two barriers to precisely identifying the exact moment of fracture.

For these reasons, a robust and quantifiable method was required, because visual identification of the crack was not considered adequate. By identifying the second derivative of the strain field a consistent and reliable value of strain can be determined in comparison to optical identification. Figure 6.6 shows a series of frames with the maximum normal strain overlaid, in this case the sample has a well defined fracture that is easily identified optically, Figure 6.7 shows the averaged value of strain and its derivatives in a small area in the vicinity of the fracture, the dashed line indicating the identified frame prior to fracture. In both cases the same frame is chosen and therefore this methodology is proven to be valid. Figure 6.4 shows a tearing type failure wherein the optical method is highly subjective and inconsistent, Figure 6.5 identifies an appropriate frame in this case too.

The derivative threshold method cannot detect the best frame in some ‘sliding’ dominated fractures - that is where large strain localisation occurs and the rate of change of strain in these is small. A possible improvement to the method would be to look at the derivatives not only of the maximum normal strain but also another parameter such as the shear strain, and identify the frame by considering if either of those measures surpass the threshold.

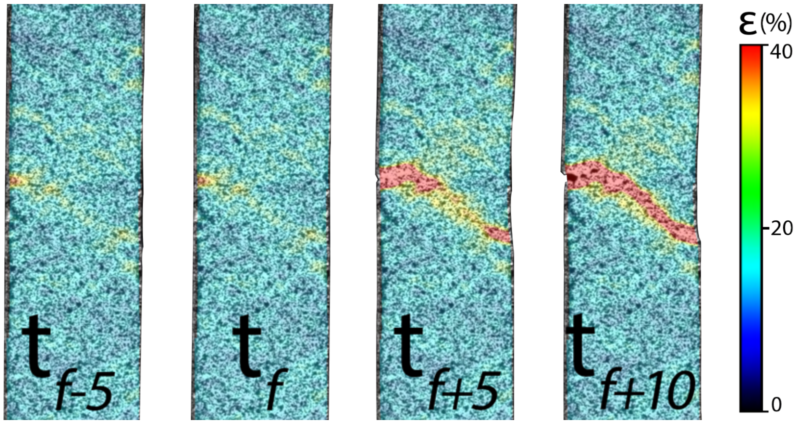

Figure 6.4: *A time series of frames from DIC with the maximum normal strain overlaid. The frame identified as the frame immediately prior to fracture is denoted f. In this sample it is difficult to optically identify the exact frame which should be used.*

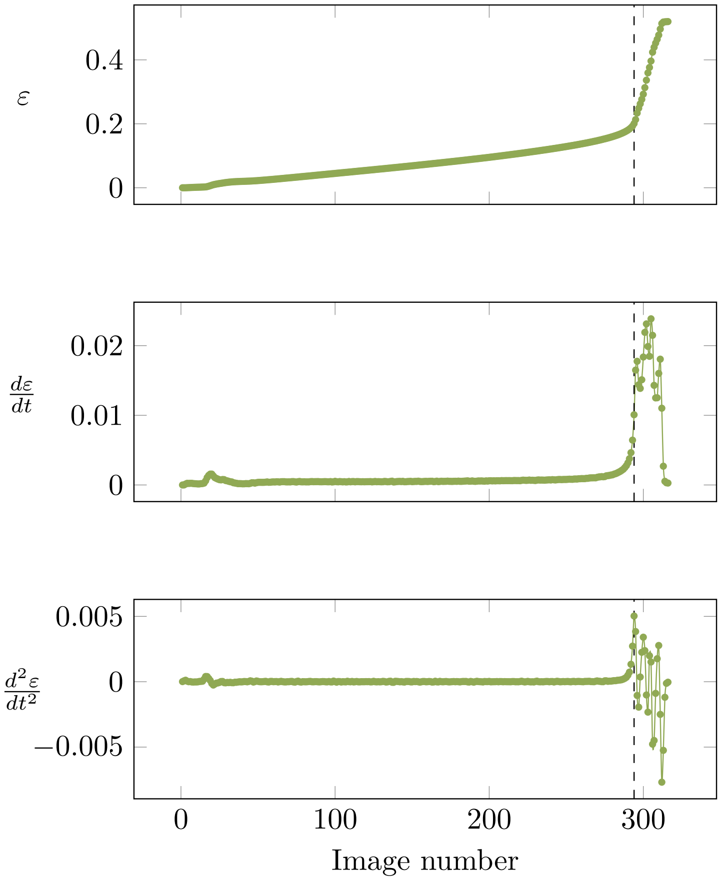

Figure 6.5: *The maximum normal strain plotted per frame, with its first and second derivatives, for the sample shown in Figure 6.4. A dashed line indicates the frame which is chosen to be representative of fracture.*

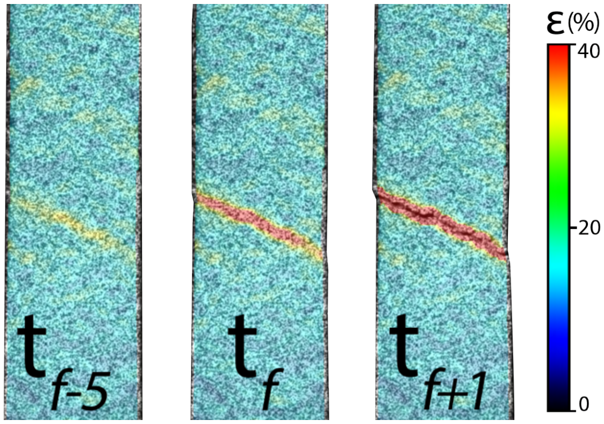

Figure 6.6: *A time series of frames from DIC with the maximum normal strain overlaid. The frame identified as the frame immediately prior to fracture is denoted f. The fracture is obvious for this sample using optical identification.*

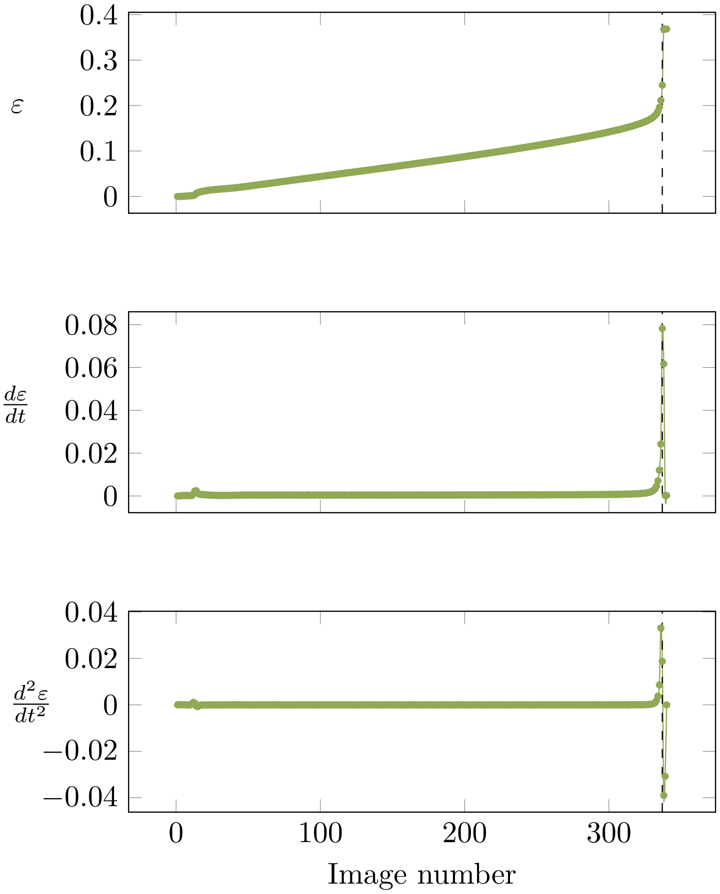

Figure 6.7: *The maximum normal strain plotted per frame, with its first and second derivatives, for the sample shown in Figure 6.6. A dashed line indicates the frame which is chosen to be representative of fracture. In this sample it is clear that this method produces meaningful fracture identifications.*

6.4 On the location of fracture initiation

It is typically expected that samples will have maximum damage in the central region due to this being the location of the highest stress state. This causes fracture initiation from the centre of the sample, as opposed to at or near to the edge as observed with the majority of samples in this study. In order to understand this edge based fracture initiation and exclude the possibility of experimental biases which could have produced this behaviour further investigation was undertaken. As displayed in Section 4.2 the preparation method was not significant in the location of fracture initiation - this indicates that both edge surface roughness and any heat effect due to the sample preparation method is insignificant. Another possible unintended cause of such a failure would be the misalignment of samples in the grips, such that the applied force was not uniform. To guard against this possibility the sample was aligned against a a square edge placed on the grip of the uniaxial tensile testing machine - this meant that the samples were consistently angled for each repeat, but no preference for the side of fracture initiation or largest crack growth was found - once again indicating a true material behaviour as opposed to an effect from experimental bias. Section 4.7 proves that in most cases the fracture actually initiates simultaneously on both sides, which again this strengthens the argument that the edge fracture is a material characteristic. It is also important to note that the thickness of the samples provides a plane stress state - this will suppress the aforementioned tendency to fail from the centre.

The consequence of this finding is that the effect of the stress state for this material when considered as a continuum cannot fully explain the fracture initiation. Microstructural properties due to the large grain size produce anisotropies on the macroscopic scale which dominate the fracture initiation.

The most likely requirement to fully reproduce the fracture dynamics would be to discard the continuum assumption, and an alternative approach would require, for example, crystal plasticity finite element analysis (CPFEM) which is significantly more computationally expensive with more challenging requirements for calibration. Alternatively, the introduction of Lode Angle could be considered to produce fracture and damage onset surfaces, as the effect of Lode Angle has been shown to be significant in the literature [182, 97, 183]. The Lode Angle was specifically neglected in the model due to the difficulty in producing samples with varying Lode Angle and stress states from the sheet stock. It is proposed that although introducing this parameter would improve the prediction, the introduction would not be significant in comparison to other factors such as the effect of the large grain size, as clear evidence of material non-homogeneity is found even in the elastic to plastic transition as discussed in Section 6.1.

Another supporting piece of evidence to strengthen this argument is that the behaviour of edge based fracture initiation was also observed in microscopic samples produced for the x-ray microscope investigation. These samples had a reduced section of width 0.5 mm, with a sample thickness of 0.2 mm. The width to thickness ratio was 2.5 and therefore would not be considered in the plane stress condition as found in the macroscopic samples. These samples also showed no voids in the central region (above 2.49 µm). Once again this emphasises that the microscale dynamics dominate the fracture in this material and thickness, and that the inter-granular crack precipitation and propagation visible as demonstrated by the figures of Section 4.7 is the dominant mechanism.

Simulations with varying pressure applied from the restraining system show that the friction effect of the restraining system did not contribute to the location of fracture initiation, in every case showing the same behaviour as shown in 5.5.2. Additional cases where a boundary condition preventing out of plane motion was used (but no contact simulated) also revealed the same mode of fracture.

6.5 Hall Effect damage sensing

Hall effect damage sensing is based on the reduction of the magnetic permeability of the sample relative to that of the surrounding medium (i.e. air) and this study demonstrated a system using a permanent magnet for in-situ measurement during tensile testing. The results presented in Section 4.8 show a clear and detectable change in the measured flux density, which in most cases correlates with the force-displacement curve.

The principle of operation is that the sample is made of a material with high magnetic permeability, so that flux lines preferentially flow through the sample rather than through the air. Hall effect sensors are placed around the region of interest to detect the residual flux that escapes the sample and this value is taken as the undamaged flux. As the sample is strained, the flux density outside the sample will increase as the relative permeability of the sample decreases due to plastic strain and damage. Upon fracture, a large amount of flux will still be contained by the sample, but the greatly increased 'external flux' can be set as the value at fracture. Normalising the collected data so that the maximum and minimum voltages returned by the sensor fall between 0 and 1 provides a plot in which magnetic degradation is coupled to deformation, however, information about the absolute flux density measured is lost. The permanent magnets used were magnetised through their thickness and the Hall sensors were placed on the opposite side of the sample. This was to ensure that the flux lines cut the sensors in their sensing axis.

A number of arrangements for the relative positioning of the sensors and the permanent magnet were tested and the results compared to find the most suitable arrangement for detecting damage in the samples used in this study.

Firstly, it should be noted that in Figure 4.34, where the sensors are arranged in a star pattern with the magnet in the centre, one sensor shows an increasing value while the other two show decreasing values. As the magnet was loosely held in the alignment fixture, it is likely that some relative movement occurred between the magnet, sample and sensor. The increasing value indicates an increasing flux density detected - which is not the expected behaviour of a decreasing flux density due to reduced permeability. This result shows a weakness in the proposed method because the sensitivity to the flux delta due to changing permeability is much lower than the sensitivity to the position of the magnet relative to the sensors. Rearranging the equipment so that the magnet was offset from the region of interest gave a more interpretable result, with all sensors showing a decrease in signal with increasing strain. Figure 4.35 shows that for sensors 2 and 3 offset by 120 degrees from the sample axis, a decrease in signal is detected which is well in line with the expected behaviour, although the two signals differ in the strain at which the flux begins to decrease. Again this is suggested to be due to alignment, as the sensors are just overlapping the sample their sensitivity is extremely high and misalignment can cause large differences between the signals. In this arrangement, the sensor aligned with the sample axis (sensor 1) plateaued between 40 and 65 seconds, and the reason for this is not clear.

Figure 4.36 shows a linear arrangement of the sensors, which provides the best interoperability of the results, with clear decreases in signal occurring just prior to the ultimate tensile strength. As all three sensors have been arranged in the same orientation, the signal for each is directly comparable, which is an advantage over the star arrangement. It should be noted that in this arrangement, because the sensors were further away from the flux source, a steeper gradient is measured near failure than in the other arrangements. Overall, the method presented shows promise for in situ damage measurement of highly permeable thin materials. A linear array of sensors is favoured, allowing direct comparison of all sensors, as results may be ambiguous with other arrangements. Contrary to initial expectations, placing the permanent magnet further away from the region of interest and the sensors gave better results and interpretability of the measurement as the change in detected flux was clear. The Hall effect sensors used are extremely sensitive, so the signal to noise ratio is still sufficiently low with this change.

In comparison to the methodology presented by Silva et al. [158], this work produces a continuous measurement which may be more suitable for the detection of damage just prior to fracture because of the small strains required to make large changes to the stress state at this stage.

6.6 Interaction radius

The non-local model requires a physical size over which to average the element based strain values, in doing so virtually eliminating the pathological mesh sensitivity found in local models. This size, the Interaction Radius, R, should be physically relevant in the ideal case, but should not be so large that a very high number of elements are contained within it because this will be less computationally efficient.

6.6.1 On the choice of interaction radius

In the literature, the interaction radius is typically related to so-called *major heterogeneities* in the material microstructure [184], although in other studies no such physically meaningful connection is made [185]. Major heterogeneities are more typical in concrete damage problems where the size of the aggregates may provide a sensible measure; however, two primary choices for the interaction radius are available in the present work. Firstly, the physical size of the DIC subset may be used the calibrate the model. The subset size used constrains the calibration by the fact that all strain gradients in the subset are averaged to provide a single value for that material point. In combination with the step size. the minimum resolvable spatial strain gradient is on the order of the physical size of these parameters, therefore the interaction radius may be controlled by this value. Secondly, the grain size of the material is on average 150 µm, and the grain boundaries may provide a suitable major heterogeneity in arresting or deflecting stress and strain localisation caused by damage on the micro level. This strategy was used in the simulations presented in the modelling chapter, and a radius of 200 µm was used to ensure the radius encompassed and ‘averaged’ the effect of more than one grain.

6.6.2 Computational cost with large radii

It is noted that the size of the interaction radius in comparison with the average element size can have a considerable influence on the computational cost of the model if the choice of element size is significantly smaller than the interaction radius [186]. This is because the model must average the non-local variables for every element within the interaction radius. In some cases where the interaction radius is based upon the physical size of the subset used in the DIC measurements it may be beneficial to recalibrate the strain loci and interaction radius of model to adjust the interaction radius such that it is more suitable for extremely fine meshes. This requirement highlights a fundamental weakness of this integral type non-local formulation wherein computational practicalities must be taken into account. It is important to note that such a weakness is still preferable to the local model alternative of calibration for a specific mesh size - which can still suffer from various mesh sensitivities arising form for example element aspect ratios not equal to one.

The requirement to keep the subset size consistent assumes that the fracture strain does not converge for all sample types in the calibration procedure by DIC, meaning that one value of subset size is required to be chosen which is achievable across all sample types and representative of the high degree of localisation found at the site of fracture initiation. 'Achievable' in this sense refers to the ability to have a self consistent physical subset size between each sample, and is dependent on the resolution of the cameras used and size disparity between sample geometries (as well as numerous parameters such as the distance between sample and camera, the optical length of the lenses used, speckle quality, etc.). Assuming the fracture strain converges for every sample tested, one can choose the interaction radius to be computationally convenient, or rather choose an alternative physical basis such as the grain size. The DIC good practices guide [77] notes that if the maximum strain amplitude doesn't converge, one may only report the strain is a minimum bound, and repeated testing with a smaller field of view is required for convergence. Acquiring convergence is sometimes not practical, for example in the case of an ASTM-E8 sample there is a large area over which fracture may occur.

6.7 Calibration of Johnson Cook parameters

It has been shown that the yield stress is highly dependent on the strain rate. As shown in Figure 4.19 the true stress at $\varepsilon_{pl} = 0$ is above 5 MPa with a strain rate just over 20 times that of the reference strain rate, whereas in Figure 4.18 at the reference strain rate the yield stress is 395.7 MPa. A number of methods for calibration of the Johnson Cook model exist [170], and the strategy employed in this work was the Equivalent Plastic Strain (EPS) method. Gambirasio and Rizzi [170] showed that this method can be among the most accurate, however the non homogeneous nature of the elastic to plastic region at higher temperatures causes significant additional error for high temperature tests. The Johnson Cook model assumes the material response is isotropic, which may not be valid in this material because of the large grain sizes. Previous work has used Voronoi cell based division modify material properties of plasticity models based on grain orientation [110], and it is proposed that a similar methodology would produce better plasticity results. Because the downstream damage model is informed by the plasticity model the accuracy in this step is critical for good damage model results. The literature also shows that the yield strength and ultimate tensile strength is lower in this material for the 0.2mm thickness [2] due to this size effect. This again weakens the justification for the use of the Johnson Cook model, and it is noted that poor results at the plasticity stage will lead to poor results in the damage and fracture stages.

6.8 Non-local model considerations

This section discusses some considerations with the implementation of the non-local damage model. Two aspects are discussed principally, the computational effort required to implement such a model, and the choice of the non-local variable. Two approaches were trialled for the implementation of the routine which finds elements within the interaction radius, but only one was feasible, the reason for this is explained and the potential advantages of such an implementation considered. The choice non-local variable is then discussed, not only considering which values to track non-locally, but the choice of which scalar strain value to use.

6.8.1 Time complexity

As discussed briefly in Section 5.2.1 an octree was chosen as the data structure to represent the spatial information (i.e. the element centroid coordinates) required for the non-local calculations. The time complexity of searching such a data structure is O($log_2(N)$). An alternative method of providing information on neighbouring elements was explored, wherein a pre-cached list of first order neighbours is found, which is then used to produce arbitrary n order neighbours. By calculating neighbouring elements in this manner, large interaction radii can be used with extremely fine geometry, without a nonphysical contribution to damage in non-connected elements. Figure 6.8 shows how such an error arises graphically. Unfortunately the time complexity of this algorithm is O(n^3), which becomes completely infeasible for models of even a modest number of elements (50,000). Despite this time complexity it is thought that the main performance penalty is a result of CPU cache misses. Using the octree approach allows the CPU to predicatively load data into its cache with high accuracy, whereas no such prediction can be made in the case of the failed approach - causing cache misses requiring RAM access which is approximately 100 times slower to access [187].

By combining the two strategies, it would be possible to gain the benefits of the failed method. A possible implementation is proposed wherein the damage variable is considered non-local. Each element calculates and updates damage locally while comparing the damage of its first order neighbours. If the local damage of the neighbour is lower than the origin element, the neighbour's damage is updated by addition of a contribution from the origin element in combination with the centroid distances. In this case the time complexity is no longer O(n^3) because only first order neighbours are required.

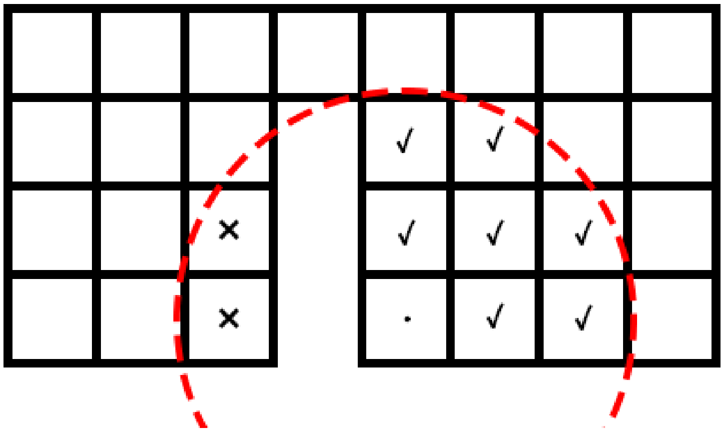

Figure 6.8: *A diagram showing that a large interaction radius (represented by a red dashed circle) may include non connected elements, represented via crossed squares.*

6.8.2 Damage driving variable choice

As discussed in Section 2.4.3 the non-local variable may be chosen arbitrarily, and in the presented model the maximum normal strain was chosen to drive damage and fracture. This choice is based upon the desire to eliminate the requirement for force based measures (and consequently energy based damage driving formulations) due to the high variability in fracture observed using such metrics in Section 4.2.3. Displacement to failure local models are a widely available alternative, however the pathological mesh sensitivity exhibited by these can only partially be rectified using a characteristic element length which additionally adds the constraint that all elements in the damage zone should be the same size and of aspect ratio as close to 1.0 as possible [113]. The presented non-local extension to the Bao-Wierzbicki fracture model allows the traversal of strain-stress state space in such a manner that large differences in material response may be represented. There are many possibilities however for the choice of strain variable to use for calibration for example the strain tensor used in the DIC calculations, and strain scalar measure. The tensor choice is the more simple of the aforementioned considerations - because the ABAQUS explicit solver passes strain increments in tensor form, and the logarithmic output is available by default and appropriate for metal plasticity, an obvious choice for the calibration is to also use the logarithmic strain tensor. More explicitly, the strain increments are obtained by integration of the rate of deformation $\boldsymbol{D}$ across some time increment dt:

$$\Delta\varepsilon = \int_{t_n}^{t_{n+1}} \boldsymbol{D} dt \tag{6.1}$$

which is equivalent to the logarithmic strain tensor, $ln(\sqrt{\boldsymbol{F} \cdot \boldsymbol{F}^T}) = ln(\lambda)$ if the principal directions of strain co-rotate with the material axes [113].

The scalar strain value chosen as the damage driving variable does not have such an obvious appropriate choice, although the choices are limited to ensure applicability to all sample types test, for example axial strain ε_{yy} may be a fine choice for an ASTM-E8 dog bone type sample but becomes meaningless for capturing total strain in a shear sample because the majority of strain is not aligned Y direction (instead being shear strain). The maximum normal strain is (almost exactly) equivalent to axial strain in such dog bone samples, and has an established use in sheet forming fracture mechanics models in the form of forming limit diagrams wherein the ratio of major to minor strain is used. As such the maximum normal strain is an attractive scalar value for use, however two reasonable alternatives exist in the form of the von Mises equivalent strain ε_{VM} and the Tresca equivalent strain ε_T. Both of these scalar equivalent strains are easily obtained from the tensorial values calculated from DIC analysis. Of these options, ε_{VM} is again highly established in metal plasticity and used in the determination of yield in the Johnson Cook plasticity model. Using ε_{VM} increases the difference between tension and shear dominated for both damage onset and fracture strain.

Figure 6.9 shows a comparison between the average of the maximum normal strains versus von Mises equivalent for selected sample types and orientations, the error bars indicate the standard error of the mean. The von Mises scalar value is smaller for tensile dominated samples and larger for shear dominated samples in comparison to the maximum principal strain. The Y axis is logarithmic as the shear sample geometry fractures at large strains. The difference can be accounted for by the additional terms considered by the von Mises as shown in Equation 6.2:

$$\overline{\varepsilon} = \frac{3}{2}\sqrt{\frac{2}{3}(e_{xx}^2 + e_{yy}^2 + e_{zz}^2) + \frac{3}{4}(\gamma_{xy}^2 + \gamma_{yz}^2 + \gamma_{zx}^2)} \tag{6.2}$$

where the terms e_{ab} are defined as:

$$\begin{aligned} e_{xx} &= +\frac{2}{3}\varepsilon_{xx} - \frac{1}{3}\varepsilon_{yy} - \frac{1}{3}\varepsilon_{zz} \\ e_{yy} &= -\frac{1}{3}\varepsilon_{xx} + \frac{2}{3}\varepsilon_{yy} - \frac{1}{3}\varepsilon_{zz} \\ e_{zz} &= -\frac{1}{3}\varepsilon_{xx} - \frac{1}{3}\varepsilon_{yy} + \frac{2}{3}\varepsilon_{zz} \end{aligned} \tag{6.3}$$

It could be argued that this provides a more ‘holistic’ scalar interpretation of the strain state at the material point but it must be considered that this value must still be calibrated using surface strain, as such an assumption in the calibration must be made. In this case the assumption was chosen such that the plane stress condition was present. Given the 0.2 mm thickness this assumption is very likely valid, however it is noted that the restraining system was used on the shear samples which likely introduced a small compressive stress through the sample thickness, possibly invalidating it. For this reason the model was chosen to be calibrated based on the maximum normal strain, which requires no such assumption and can be directly acquired from DIC.

The model also includes the stress state as a non-local variable, in this manner the damage driving space is fully non-local. Strictly, such an additional non-local variable is not required, however due to the highly dynamic manner in which the stress state may change in the region of fracture the inclusion of stress state as a non-local variable produces a more stable stress state integral, which in combination with the penalty term as described in Section 5.2.1 stabilises the model response under highly damaged and non-proportional loading. Without such mechanisms for stress state integral stabilisation the elements in the region of fracture may fail in a non-physical way. Figure 6.10 shows the effect of the non-local averaging and

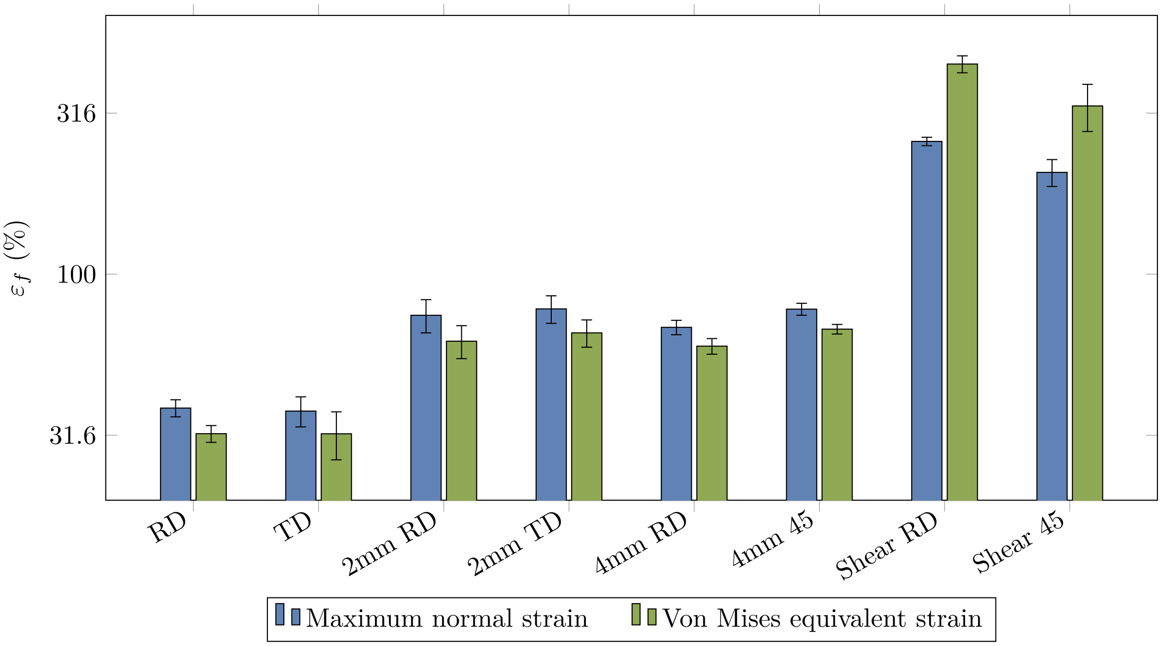

Figure 6.9: *A bar chart showing the difference in fracture strain, ε_f, as reported by the scalar values ε_{Max} and ε_{VM} for a selection of sample types.*

penalty term on the stress state of an element in comparison to a non smoothed element, demonstrating that the smoothed value under monotonic loading remains almost constant. In doing this the numerical stability of the model is significantly improved.

Importantly, this penalised value is still justifiable because it is an internal variable that drives the non-local variable of integrated stress state for the undamaged material response. The calibration point's position on the stress state axis is determined by the integrated value of the triaxiality of an undamaged sample (found via FEA). This introduces a small error, but because the damage portion of the total integral is so small it is considered acceptable. As such the model should attempt to mitigate any large influence from the damage portion of the response under monotonic loading, but still be responsive under non monotonic loading. The penalty term allows such behaviour by suppressing the influence of highly damaged elements on the non-local value.

6.8.3 Numerical stability

Section 5.2.1 describes enhancement to numerical stability provided by only updating the damage variable if the damaged equivalent stress is greater than the damaged yield strength. Figure 6.11 shows the numerical instability caused if such a check is not made. The reason for this behaviour is sudden unloading in some cases causes the propagation of stress waves of significant magnitude. These stress waves cause minute changes in the equivalent strain, which is used as the divisor when averaging the non-local triaxiality. This causes incorrect stress state changes tending toward zero, and because the and the material point traverses triaxiality-strain space as a result spurious damage is accumulated. The mitigation strategy functions well, and stabilises the model such that this behaviour is no longer observed.

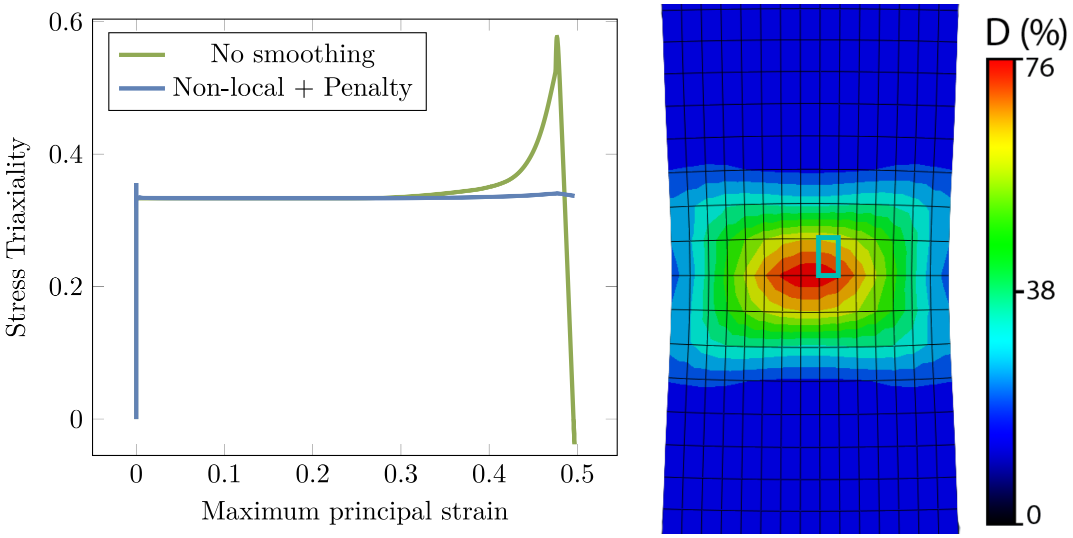

Figure 6.10: *Left: A comparison of the stress state in the region of fracture with no smoothing and smoothing by non-locality and penalty combined. Right: The element for which the triaxiality is calculated is highlighted in blue.*

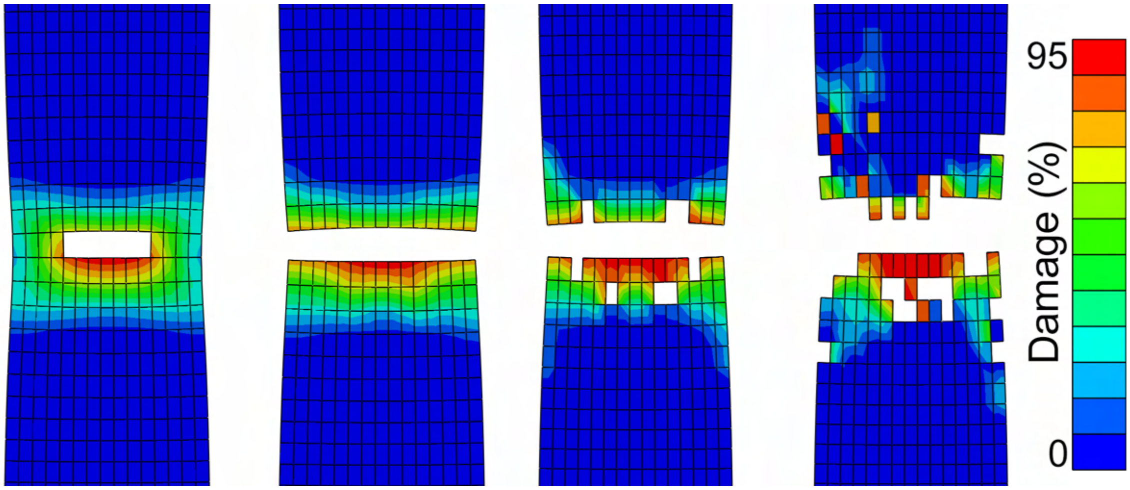

Figure 6.11: *Numerical instability is demonstrated post fracture due to propagating stress waves.*

6.9 Validation of the numerical model

6.9.1 Blanking using in-situ DIC

A direct comparison between macro-scale samples and the in situ blanking cannot be made because of the vastly different scales. The methodology of controlling the physical subset size to be equal among sample geometries used a 0.33 mm subset size whereas the in-situ blanking samples were imaged on the sample edge which was of total thickness 0.2 mm to 0.35 mm. As shown in Figure 4.16 (b) a shear band forms prior to fracture, but the fracture does not occur along this band. This formation was not clear in the samples painted for use with DIC, probably due to the paint and sample not adhering well under such extreme conditions - i.e. the painted surface was a poor strain witness. Under such conditions an improved approach may be to produce a micro-grid by electron beam lithography as shown in [188].

With this limitation considered, it is possible to achieve a correlation on the unpainted sample, albeit a poor one across most of the sample, and this is demonstrated in Figure 6.12. The results of the correlation contain a significant amount of error due to the poor imaging conditions, it is paramount that the other scalar fields displayed in Figure 6.12 (b-e) are used in conjunction to allow a quantitative identification of areas affected by biases in the correlation. The unpainted sample was processed with a subset size of 9 pixels, the minimum possible, but no convergence of the strain value was obtained (in comparison with larger subset sizes), as such the maximum strain of approximately 50% in the shear band is a minimum and should not be considered the true strain. Sub-figures 6.12 (c-e) display a variety of scalar fields which are used in determining the validity of the results in the shear bad and left hand side of the sample. Firstly, it is shown in Subfigure 6.12 (b) that the shear strain outside of the shear band is extremely small, so the maximum shear angle should be essentially random outside of this area, and essentially uniform inside the shear band, this test is passed across the sample providing the first indication that the shear band provides true values. Secondly, the divergence of the vector field should uniform. A positive divergence indicates the material point is ‘expanding’, and likewise a negative divergence indicates ‘shrinking’. In this context due to the conservation of volume expected from a solid any non zero divergence is indicative of bias, however the right hand side of the sample and bottom edge of the shear band display an increase and noise in this field demonstrating that these points should be discarded from analysis. A small positive divergence is which is uniform across the sample (excluding noise), which may be a result of the Poisson effect. Finally, the confidence region is displayed in Subfigure 6.12 (e) for the correlation, the smaller the value the better the confidence in the DIC match. It is found that the majority of the left hand side of the sample has a much lower value, indicating good high confidence in the result.

The result of this analysis indicates that the shear band measurement can be trusted as a minimum value, and that, excluding the bottom edge, a value of 46.37% is accepted. This is a high value in comparison to the 5% maximum normal strain value away from the shear band. Further analysis is not possible due to the poor image quality, however this increased shear strain corroborates with the results found for macroscopic samples wherein significantly higher shear strains are tolerated before fracture in comparison to tensile stress states and other studies using in plane torsion testing have found much higher fracture strain for highly localised shear for various Al and steel alloys [189]. In a similar manner blanking was investigated using optical flow in two materials, showing very high equivalent strain in a narrow region indicating shear band formation [79]. For BCC materials, as also observed in this work, a smooth development of the shear band is observed in that the deformation is highly localised to the shear band. Despite this localisation and once again likely due to the microstructural size effect the fracture did not initiate from this area, unlike the fracture observed by Hartmann et al. [79]. Other work using a non-local damage formulation has shown that the use of re-meshing is possible and results in adequate localisation in blanking [190]

The validation case presented in Section 5.6 have been shown to correctly predict the location of fracture initiation, peak blanking forces, and to produce the typical geometric features associated with blanking, such as a burr and rollover zone. However, it is clear that a number of aspects are problematic, most notably the mass loss seen at the cut edge and the over-prediction of the size of the rollover. A number of influences may explain these problems, three main issues being: mesh refinement, calibration sensitivity and the assumption of homogeneity.

The mesh refinement is likely to be insufficient in this case, due to time constraints a full mesh sensitivity study could not be undertaken for this simulation and a coarse mesh of only 4 elements was used across the clearance between punch and die. Such a coarse mesh is likely to be problematic as the high spatial strain gradients cannot be adequately resolved. It is arguable that the element formulation was also sub-optimal, with reduced integration elements susceptible to zero energy mode bending and requiring hourglass control. Hourglass mitigation was enabled and the artificial strain energy reached a maximum of 0.2×10^{-3} J, the ratio of strain energy to artificial strain energy was less than $\frac{1}{1000}$, indicating that hourglassing was not a significant factor.

The calibration shown in Section 5.2.1 shows the error associated with the limited number of calibration stress states where the fracture locus falls below the damage initiation locus. This is negated in the model by using the higher of the two values as the fracture locus and having a region where instantaneous fracture occurs without damage accumulation. For better predictions in blanking, the exact value of the fracture locus needs to be calibrated at this point - although as shown in Figure 5.2 the true value is likely to be well approximated.

Finally, the assumption of homogeneity in plasticity and damage and fracture is considered. It is known that the large grain size (see Section 4.1) means that on average only 1-3 grains are present through the thickness of the sheet. This means that there may be significant anisotropy in the plasticity, moreover the fracture dynamics illustrated in Section 4.7 show that the crack path is often deflected along the grain boundaries. Such effects were not considered in this simulation. As shown in Section 5.5.2, suppression of the fracture minima or more severe strain softening results in significantly different fracture dynamics.

As the simulated region was a reduced section with a thickness of 50 µm the force values were scaled such that the total path length of the cut edge in the simulation matched that experimental condition. The resulting force-time graph is plotted in Figure 6.13. It is found that the predicted force shows a decrease at 0.05 s, and this is associated with slipping between the stripper plate and work causing a small displacement toward the tool. The peak force of 21.5 kN compares vary favourably with the values reported in literature of 20-21 kN for this punch speed and sample thickness [2].

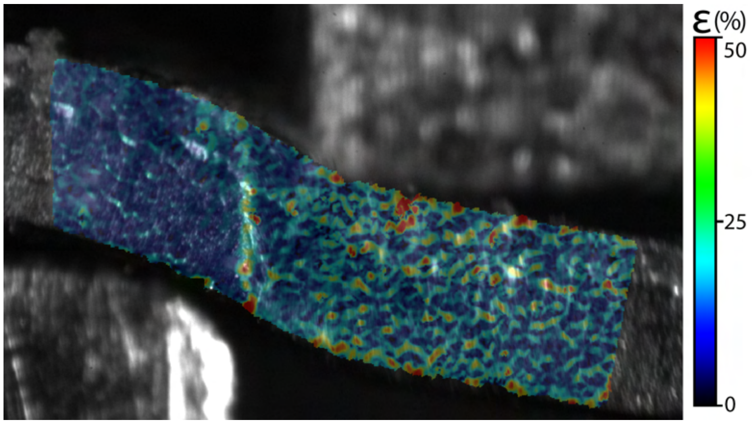

(a) *Max Normal Strain (%)*

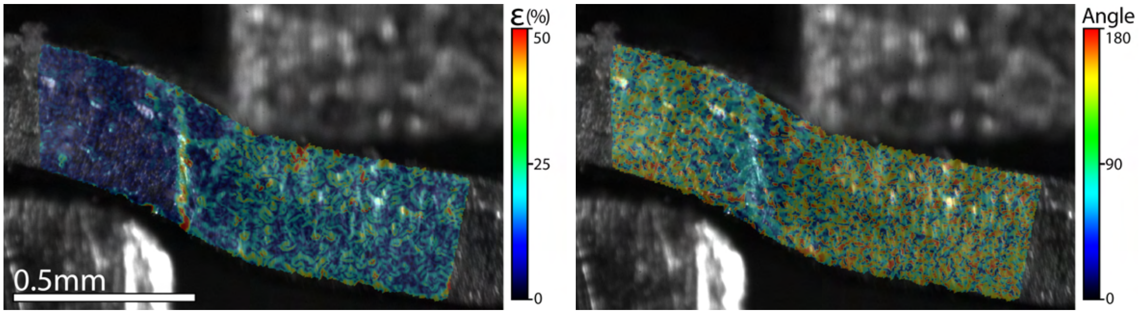

(b) *Max Shear Strain (%)* **(c)** *Max Shear Angle (rad)*

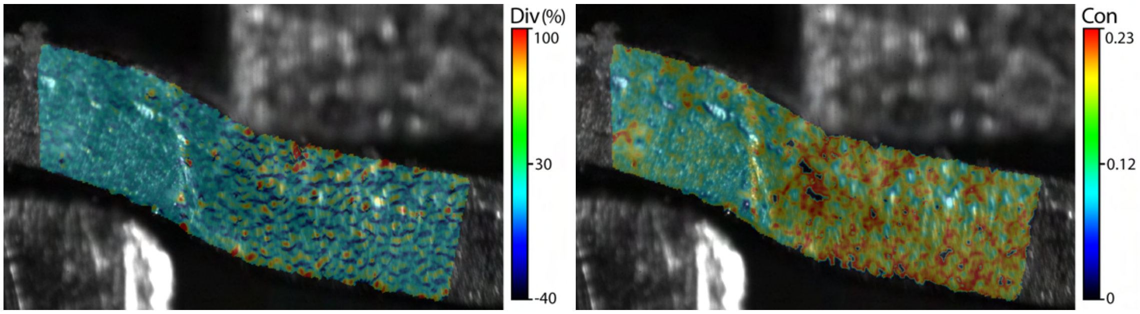

(d) *Divergence (%)* **(e)** *Confidence Region (pixel)*

Figure 6.12: *DIC analysis scalar fields are shown for the unpainted in situ sample displayed in Figure 4.16.*

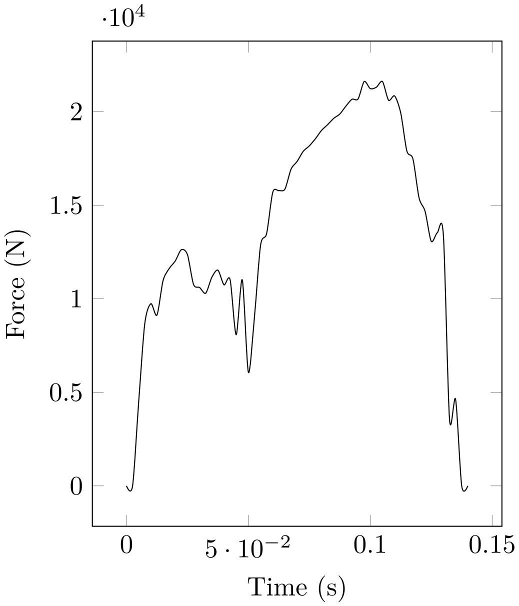

Figure 6.13: *Predicted forces on the punch due in blanking for the new tool.*

6.9.2 Novel two stage geometry

The novel two stage geometry presented in Section 3.7 was developed to verify that path dependence of the damage and fracture response in the material was indeed present, and that the model could successfully predict such an effect. Other two stage geometries have been presented in the literature, such as the two step tensile test wherein a specimen is strained, interrupted and notched, and then strained again to failure [132]. This methodology was excluded from consideration for the present study for the following reasons: a larger change of stress state which traverses the shear region of stress state is desired; the additional processing step could cause edge damage effects which are significant for thin samples; and the thickness of the material means clamping the sample for the notching step could cause out of plane deformation. Inspiration for the new sample is evident based on the well established bi-axial cruciform and the ASTM-E8 sample geometries. A notch was added at the interface to promote damage accumulation in a predictable region during tensile loading.

Figure 6.14 shows the evolution of the damage variable with the non-local triaxiality and maximum principal strain for the two stage geometry loaded first in shear, then in tensile modes. The transition occurs at simulation time 0.45 seconds, and a sharp increase in the damage variable is shown almost immediately afterwards. This proves the path dependence of the model and the same behaviour is compared in the DIC results displayed in Figure 6.15 where the sample is first loaded in shear to 80% maximum normal strain, and almost instantaneous fracture occurs when loaded in tension after this.

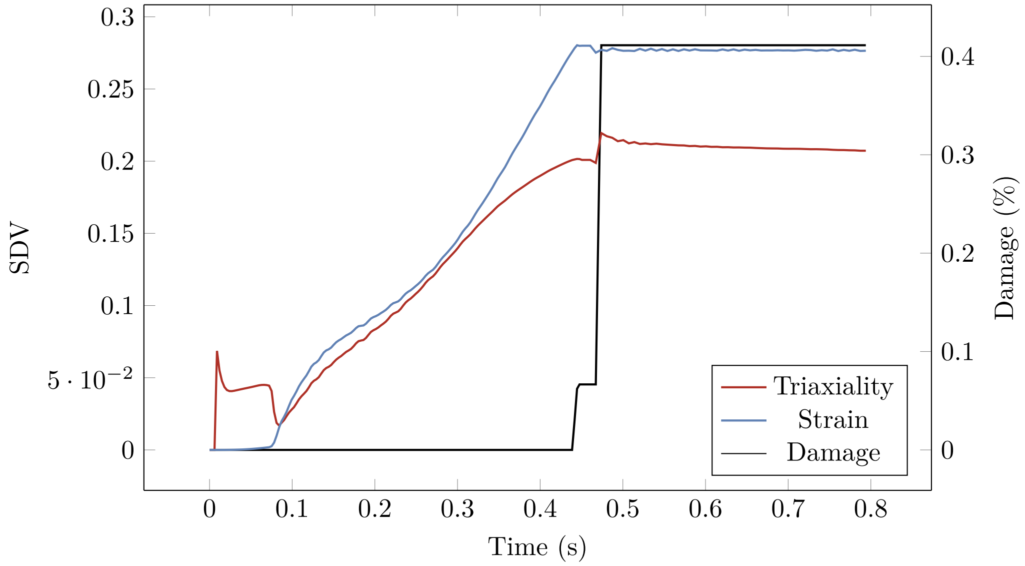

Figure 6.14: *Evolution of state variables in the two stage sample simulation.*

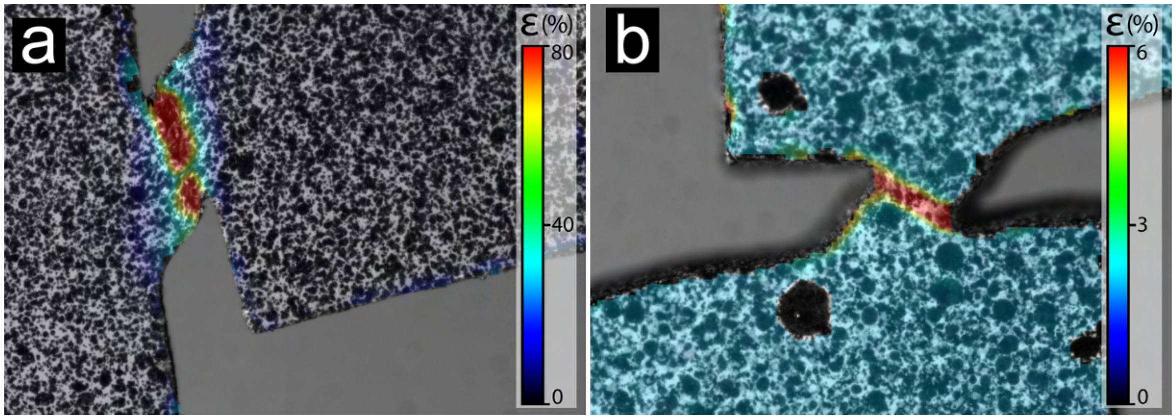

Figure 6.15: *DIC results for the two stage sample, (a) shear loading, (b) prior to fracture in tension.*

6.10 Sources of error in calibration

6.10.1 Averaged stress state

Integrated value for triaxiality is dependent on fracture strain. The value is found by reverse analysis of an undamaged sample, which by definition is slightly different from the actual damaged sample (although the model does use the undamaged stress). If the fracture strain occurs at the edge, the triaxiality is different from the centre, this means the location of the fracture matters when doing this calibration.

6.10.2 Compressive stress states calibration

Data on fracture under compressive (negative) triaxialities could not be obtained in this work. A specimen producing a stress state approximately equal to $-\frac{1}{3}$ was used, but as expected, no fracture occurred before buckling. Bao and Wierzbicki [131] produced cylindrical specimens for this purpose, which is not possible with the rolled material. The use of stacked discs has been demonstrated in the literature [191] as a viable alternative to obtaining data in the compression regime with sheet material. Notwithstanding this shortcoming, it was possible to produce a calibration for the asymptotic region with some meaningful justification. The cubic interpolation between calibration points used to represent the loci was chosen specifically because the piecewise Bezier curves it produces are differentiable - and enforcing differentiability between the curve ending at a triaxiality of 0 and the asymptotic section means that the parameters for the asymptotic section can be uniquely defined. Asymptotic calibration using this method is influenced by the boundary condition used to calibrate the rest of the loci. In this paper the 'natural' boundary condition is used, where it is assumed that the second derivative at the boundary is zero and calibration is only possible if the first derivative of the curve is negative. If this were not the case, it would not be possible to match the derivatives of the asymptotic section and the piecewise curve. Fortunately for this material and those tested in [131] this is the case.

Chapter 7

Conclusions and Future Work

7.1 Conclusions

In this study, a novel non-local damage model has been developed based upon an extension to the Bao-Wierzbicki fracture model. The model may be calibrated exclusively with uniaxial tests on various sample geometries manufactured from the silicon steel product of interest with thickness 0.2 mm. The material has been characterised using a highly local strain measurement, which has been shown to be required to overcome variance in the fracture mechanics at such reduced thicknesses, which is a result of the large size of the grains in comparison to the sample thickness. The identification of fracture under imperfect imaging techniques has also been demonstrated, using derivatives in combination with the affirmations localised strain measurement. This is a very important factor due to the rapidly increasing strain near fracture and DIC requiring the speckle pattern to act as a strain witness - which may not be the case at or post-fracture. A restraining system to ensure thin shear samples fail in a shearing mode as opposed to buckling was developed, allowing far greater calibration range than previously possible, this system had minimal effect on the stress state at the region of interest.

The model has been demonstrated to reproduce experimentally observed damage and fracture mechanics. The model has provided insight into the importance of the damage softening mechanism by showing different fracture dynamics produced by different softening coefficients.

Various experimental techniques have been used alongside the calibration methodology to further justify and validate the calibration strategy. Using an x-ray microscope on microscale tensile samples proved that no voids larger than 2.5 µm were detectable in the material at any point in the fracture, and verified the fracture initiation from the edge of the sample is a result of the material properties as opposed to experimental bias. The methodology and sample geometry for the testing of such a small cross-sectional sample may be applied in other materials for similar testing and validation.

The use of nanoindentation and EBSD was trialled to couple the hardness and crystallographic orientation for further modelling, but no correlation could be found. This result indicates that such a methodology is likely unsuitable for purpose and should not be pursued further for modelling purposes, although some indication of hardness changes at grain boundaries may warrant further investigation into the microscale fracture mechanics of silicon steel.

A technique for identifying damage onset and fracture with respect to the change in magnetic flux passing through the sample was presented, and several arrangements were trialled to find the optimal experimental setup for this purpose. It was found that an offset field with several sensors arranged in a linear manner was the best for the detection of damage.

A worn tool and larger than ideal clearances were used in a lab scale blanking demonstration to validate the macroscopic findings of the calibration sample, and high-strength shear bands were observed, which ultimately did not fracture. It can be stated that these dynamics are due to the damage and fracture properties of the material where a significant minima is observed at stress triaxialities between 0.2 and 0.3. Improvements to prior work in this field by use of a technique to produce finer speckles for DIC allowed higher spatial resolution to be obtained. The use of several quality metrics on the DIC results also allowed limited data to be gathered from unpainted samples.

7.2 Recommendations for future work

The work presented in this thesis provides a number of potential further avenues of research, particularly in the extension of the developed model. The model was shown to provide good predictions using a relatively low number of calibration samples; however, no sample with a stress state between $-\frac{1}{3}$ and 0 was tested. Further work in developing and testing a sample which can provide data in this region is of critical importance for better predictions in compression-dominated loading conditions. The model is also formulated to be easily extensible, such that an additional locus of points which represent the strain at which magnetic properties are degraded may be easily added - this ‘magnetic damage locus’ would require interrupted tests of the various geometries presented in this work coupled with a measure of the degradation of magnetic properties. Such degradation may be measured with the hall effect method presented in this thesis or via an alternative more established method such as a small scale single sheet tester. Upon coupling of the magnetic loss to the damage verification work could be undertaken to investigate novel blanking methods to produce minimum magnetic degradation.

The model currently is formulated for the use in 3D with reduced integration elements only, and does not support re-meshing via arbitrary Lagrangian-Eulerian methods. Both of these shortcomings could be addressed with fairly little extra work and would provide great additional utility. The use of fully integrated elements is required in some problems where bending is a dominant mode; two dimension simulations are highly preferred where possible for the reduced computational cost; and ALE adaptive re-meshing may also save significant computational cost by refining the mesh only where required. The VUMAT is called at every integration point per element, so this would simply require an averaging to provide the non-local values. For ALE compatibility the centroid coordinates of the elements should be recalculated during the simulation if a re-meshing step has occurred.

Further investigation into the combined influence of blanking speed and clearance is required, promoting highly localised shear and retarding the development of tensile dominated stress states is critical for good edge quality. This may be achieved by producing very high strain rates, with punch velocities up to $8\,\mathrm{m\,s^{-1}}$ in specially designed adiabatic punches. Although in this study no effect of temperature on the fracture strain was found using an environmental heating chamber this should be validated by other means.

The attempted coupling of crystallographic orientation and nanohardness could be retried by use of lower indentation forces and a finer grid of indents. The difficulty in preparing samples for this test was noted because the material is extremely sensitive to the preparation method. In particular in the final stages of polishing with colloidal silica the prepared surface readily oxidises in seconds under normal conditions. The removal of the colloidal silica quickly after the final step is critical to prevent crystallisation of the colloidal silica on the sample surface, however using isopropyl alcohol for this method is relatively ineffective and water often causes immediate oxidation.

Bibliography

[1] Oleksandr Hoshtanar. *Dynamic Domain Observation In Grain-Oriented Electrical Steel Using Magneto-Optical Techniques.* PhD thesis, 2006.

[2] H. Ghadbeigi, A. Al-Rubaye, F. C.J. Robinson, D. Hawezy, S. Birosca, and K. Atallah. Blanking induced damage in thin 3.2% silicon steel sheets. *Production Engineering*, 14 (1):53–64, 2 2020. ISSN 18637353. doi: 10.1007/s11740-019-00931-1.

[3] Y. Demir, O. Ocak, Y. Ulu, and M. Aydin. Impact of lamination processing methods on performance of permanent magnet synchronous motors. In *Proceedings - 2014 International Conference on Electrical Machines, ICEM 2014*, pages 1218–1223. Institute of Electrical and Electronics Engineers Inc., 11 2014. ISBN 9781479943890. doi: 10.1109/ICELMACH.2014.6960337.

[4] Hannes Alois Weiss, Philipp Trober, Roland Golle, Simon Steentjes, Nora Leuning, Silas Elfgen, Kay Hameyer, and Wolfram Volk. Impact of Punching Parameter Variations on Magnetic Properties of Nongrain-Oriented Electrical Steel. In *IEEE Transactions on Industry Applications*, volume 54, pages 5869–5878. Institute of Electrical and Electronics Engineers Inc., 11 2018. doi: 10.1109/TIA.2018.2853133.

[5] Yu Qian Wang, Xiao Ming Zhang, Zhen He, Guo Qing Zu, Guang Fa Ji, Jun Yang Duan, and R. D.K. Misra. Effect of copper precipitates on mechanical and magnetic properties of Cu-bearing non-oriented electrical steel processed by twin-roll strip casting. *Materials Science and Engineering A*, 703:340–347, 8 2017. ISSN 09215093. doi: 10.1016/j.msea.2017.07.075.

[6] Ivan Petryshynets, František Kováč, Branislav Petrov, Ladislav Falat, and Viktor Puchý. Improving the magnetic properties of non-oriented electrical steels by secondary recrystallization using dynamic heating conditions. *Materials*, 12(12), 6 2019. ISSN 19961944. doi: 10.3390/ma12121914.

[7] P Shcherbakov, I Bogdanov, S Kozub, L Tkachenko, E Fischer, F Klos, G Moritz, and C Muehle. Magnetic Properties Of Silicon Electrical Steels
}And Its Application In Fast Cycling Superconducting Magnets
}At Low Temperatures. Technical report, 2004.

[8] H. Shokrollahi and K. Janghorban. Soft magnetic composite materials (SMCs), 7 2007. ISSN 09240136.

[9] Minghu Peng, Yunbo Zhong, Tianxiang Zheng, Lijun Fan, Junfeng Zhou, Weili Ren, and Zhongming Ren. 6.5 wt% Si high silicon steel sheets prepared by composite electrodeposition in magnetic field. *Journal of Materials Science and Technology*, 34(12): 2492–2497, 12 2018. ISSN 10050302. doi: 10.1016/j.jmst.2018.06.004.

[10] Yoshihiko Oda, Masaaki Kohno, and Atsuhito Honda. Recent development of non-oriented electrical steel sheet for automobile electrical devices. *Journal of Magnetism and Magnetic Materials*, 320(20):2430–2435, 10 2008. ISSN 03048853. doi: 10.1016/j.jmmm.2008.03.054.

[11] Philip Beckley. *Electrical Steels for Rotating Machines*. Institution of Engineering and Technology, 1 2002. ISBN 9780852969809. doi: 10.1049/PBPO037E. URL `https://digital-library.theiet.org/content/books/po/pbpo037e`.

[12] Tanya Ros-Yanez, Daniel Ruiz, José Barros, Yvan Houbaert, and Rafael Colás. Study of deformation and aging behaviour of iron-silicon alloys. *Materials Science and Engineering A*, 447(1-2):27–34, 2 2007. ISSN 09215093. doi: 10.1016/j.msea.2006.10.075.

[13] A J Moses. Development of alternative magnetic core materials and incentives for their use. Technical report, 1992.

[14] F. González and Y. Houbaert. A review of ordering phenomena in iron-silicon alloys. *Revista de Metalurgia*, 49(3):178–199, 6 2013. ISSN 1988-4222. doi: 10.3989/revmetalm.1223.

[15] David E Laughlin, Kazuhiro Hono, David Laughlin, and Kazuhiro Hono. *Physical Metallurgy*. Elsevier, Oxford, NETHERLANDS, THE, 2014. ISBN 9780444537713.

[16] T. J. Yang, Venkatraman Gopalan, P. J. Swart, and U. Mohideen. Direct observation of pinning and bowing of a single ferroelectric domain wall. *Physical Review Letters*, 82(20):4106–4109, 1999. ISSN 10797114. doi: 10.1103/PhysRevLett.82.4106.

[17] Yoshihiko Oda, Yasushi Tanaka, Atsushi Chino, and Katsumi Yamada. The effects of sulfur on magnetic properties of non-oriented electrical steel sheets. Technical report, 2003.

[18] Feng Fang, Shangfeng Che, Diwen Hou, Yuanxiang Zhang, Yang Wang, Weina Zhang, Guo Yuan, Xiaoming Zhang, R. D.K. Misra, and Guodong Wang. Thin-gauge non-oriented silicon steel with balanced magnetic and mechanical properties processed by strip casting. *Materials Science and Engineering A*, 831, 1 2022. ISSN 09215093. doi: 10.1016/j.msea.2021.142284.

[19] P. Rubin, R. Larker, E. Navara, and M. L. Antti. Graphite Formation and Dissolution in Ductile Irons and Steels Having High Silicon Contents: Solid-State Transformations. *Metallography, Microstructure, and Analysis*, 7(5):587–595, 10 2018. ISSN 21929270. doi: 10.1007/s13632-018-0478-6.

[20] Hong Yu Song, Hai Tao Liu, Yin Ping Wang, and Guo Dong Wang. Secondary recrystallization behavior in a twin-roll cast grain-oriented electrical steel. *Journal*

of Magnetism and Magnetic Materials, 428:325–332, 4 2017. ISSN 03048853. doi: 10.1016/j.jmmm.2016.12.109.

[21] Hong Yu Song, Hai Tao Liu, Yin Ping Wang, and Guo Dong Wang. Microstructure and texture evolution of ultra-thin grain-oriented silicon steel sheet fabricated using strip casting and three-stage cold rolling method. *Journal of Magnetism and Magnetic Materials*, 426:32–39, 3 2017. ISSN 03048853. doi: 10.1016/j.jmmm.2016.11.038.

[22] Yin Ping Wang, Hai Tao Liu, Hong Yu Song, Jia Xin Liu, Hui Ying Shen, Yang Jin, and Guo Dong Wang. Ultra-thin grain-oriented silicon steel sheet fabricated by a novel way: Twin-roll strip casting and two-stage cold rolling. *Journal of Magnetism and Magnetic Materials*, 452:288–296, 4 2018. ISSN 03048853. doi: 10.1016/j.jmmm.2017.12.064.

[23] Yang Wang, Yuan Xiang Zhang, Xiang Lu, Feng Fang, Yun Bo Xu, Guang Ming Cao, Cheng Gang Li, R. D.K. Misra, and Guo Dong Wang. A novel ultra-low carbon grain oriented silicon steel produced by twin-roll strip casting. *Journal of Magnetism and Magnetic Materials*, 419:225–232, 12 2016. ISSN 03048853. doi: 10.1016/j.jmmm.2016.06.036.

[24] Willian Roberts. *Cold Rolling of Steel*. 1 edition, 1978. ISBN 9780824767808.

[25] Hadi Pirgazi, Roumen H. Petrov, and Leo Kestens. Modeling the Magnetic Properties of Non-Oriented Electrical Steels Based on Microstructural Parameters. *Materials Science Forum*, 702-703:734–737, 12 2011. doi: 10.4028/www.scientific.net/msf.702-703.734.

[26] Grigory Lyudkovsky, P. K. Rastogi, and M. Bala. Nonoriented Electrical Steels. *JOM*, 38(1):18–26, 1 1986. ISSN 1047-4838. doi: 10.1007/BF03257950.

[27] A. Chaudhury, R. Khatirkar, N. N. Viswanathan, V. Singal, A. Ingle, S. Joshi, and I. Samajdar. Low silicon non-grain-oriented electrical steel: Linking magnetic properties with metallurgical factors. *Journal of Magnetism and Magnetic Materials*, 313(1):21–28, 6 2007. ISSN 03048853. doi: 10.1016/j.jmmm.2006.11.217.

[28] Pampa Ghosh, Richard R. Chromik, Babak Vashegi, and Andrew M. Knight. Effect of crystallographic texture on the bulk magnetic properties of non-oriented electrical steels. *Journal of Magnetism and Magnetic Materials*, 2014. ISSN 03048853. doi: 10.1016/j.jmmm.2014.04.051.

[29] B. D. Cullity and C. D. Graham. *Introduction to Magnetic Materials*. John Wiley & Sons, Inc., Hoboken, NJ, USA, 11 2008. ISBN 9780470386323. doi: 10.1002/9780470386323. URL `http://doi.wiley.com/10.1002/9780470386323`.

[30] R. M. Bozorth and L. W. McKeehan. An Explanation for Directions of Easy Magnetization in Ferromagnetic Cubic Crystals. *Physical Review*, 51(3):216–216, 2 1937. ISSN 0031-899X. doi: 10.1103/PhysRev.51.216. URL `https://link.aps.org/doi/10.1103/PhysRev.51.216`.

[31] Felix Kling. Miller indices illustration, 11 2010. URL `en.wikipedia.org/wiki/File:Miller_Indices_Felix_Kling.svg`.

[32] Dan Wei. *Micromagnetics and Recording Materials*. Springer Berlin Heidelberg, Berlin, Heidelberg, 2012. ISBN 978-3-642-28576-9. doi: 10.1007/978-3-642-28577-6.

[33] J E L Bishop and E W Lee. The Behaviour of Ferromagnetic Sheets in Alternating Electric and Magnetic Fields. I. A Domain Theory of the Skin-Effect Impedance and Complex Permeability. Technical Report 1364, 1963. URL `https://www.jstor.org/stable/2414471`.

[34] K. M. Podurets and S. S. Shilstein. Measurement of the domain wall thickness in silicon iron using the adiabatic spin-flip effect on neutron refraction. In *Physica B: Condensed Matter*, volume 297, pages 263–267, 3 2001. doi: 10.1016/S0921-4526(00)00850-4.

[35] Tadao Nozawa, Masato Mizogami, Hisasi Mogi, and Yukio Matsuo. Domain structures and magnetic properties of advanced grain-oriented silicon steel. *Journal of Magnetism and Magnetic Materials*, 133(1-3):115–122, 5 1994. ISSN 03048853. doi: 10.1016/0304-8853(94)90504-5. URL `https://linkinghub.elsevier.com/retrieve/pii/0304885394905045`.

[36] Ekta Bhatia, Zoe H. Barber, Ilari J. Maasilta, and Kartik Senapati. Domain wall induced modulation of low field H-T phase diagram in patterned superconductor-ferromagnet stripes. *AIP Advances*, 9(4), 4 2019. ISSN 21583226. doi: 10.1063/1.5087925.

[37] A.J. Moses. Electrical steels: past, present and future developments. *IEE Proceedings A (Physical Science, Measurement and Instrumentation, Management and Education)*, 137(5):233–245, 9 1990. ISSN 2053-7905. doi: 10.1049/ip-a-2.1990.0039.

[38] N. Leuning, S. Steentjes, M. Schulte, W. Bleck, and K. Hameyer. Effect of elastic and plastic tensile mechanical loading on the magnetic properties of NGO electrical steel. *Journal of Magnetism and Magnetic Materials*, 417:42–48, 11 2016. ISSN 03048853. doi: 10.1016/j.jmmm.2016.05.049.

[39] K. Matsumura and B. Fukuda. Recent developments of non-oriented electrical steel sheets. *IEEE Transactions on Magnetics*, 20(5):1533–1538, 9 1984. ISSN 0018-9464. doi: 10.1109/TMAG.1984.1063223.

[40] E. Stephenson and A. Marder. The effects of grain size on the core loss and permeability of motor lamination steel. *IEEE Transactions on Magnetics*, 22(2):101–106, 3 1986. ISSN 0018-9464. doi: 10.1109/TMAG.1986.1064281.

[41] N. Leuning, S. Steentjes, and K. Hameyer. Effect of grain size and magnetic texture on iron-loss components in NO electrical steel at different frequencies. *Journal of Magnetism and Magnetic Materials*, 2019. ISSN 03048853. doi: 10.1016/j.jmmm.2018.07.073.

[42] Fausto Fiorillo. *Characterization and Measurement of Magnetic Materials*. Elsevier, 2004. ISBN 9780122572517. doi: 10.1016/B978-0-12-257251-7.X5000-X.

[43] G. Bertotti. General properties of power losses in soft ferromagnetic materials. *IEEE Transactions on Magnetics*, 24(1):621–630, 1 1988. ISSN 0018-9464. doi: 10.1109/20.43994.

[44] Xuefei Wei, Alexander Krämer, Gerhard Hirt, Anett Stöcker, Rudolf Kawalla, Martin Heller, Sandra Korte-Kerzel, Lucas Böhm, Wolfram Volk, Nora Leuning, Kay Hameyer, and Johannes Lohmar. Influence of process parameters on grain size and texture evolution of fe-3.2 wt.-% si non-oriented electrical steels. *Materials*, 14(22), 11 2021. ISSN 19961944. doi: 10.3390/ma14226822.

[45] Yuanke Mo, Zhihao Zhang, Hongjiang Pan, and Jianxin Xie. Improved Plasticity and Cold-rolling Workability of Fe-6.5wt%Si Alloy by Warm-rolling with Gradually Decreasing Temperature. *Journal of Materials Science and Technology*, 2016. ISSN 10050302. doi: 10.1016/j.jmst.2016.01.017.

[46] Chaoyu Han, Junpin Lin, Shibo Wen, Feng Ye, Yongfeng Liang, and Bao Zhang. Flow Behavior Characteristics and Processing Map of Fe-6.5wt. %Si Alloys during Hot Compression. *Metals*, 2018. doi: 10.3390/met8030186.

[47] Helmi A. Youssef, Hassan A. El-Hofy, and Mahmoud H. Ahmed. *Manufacturing Technology*. CRC Press, 8 2011. ISBN 9781439897089. doi: 10.1201/b11792. URL `https://www.taylorfrancis.com/books/9781439897089`.

[48] *Metal Forming Handbook*. Springer Berlin Heidelberg, Berlin, Heidelberg, 1998. ISBN 978-3-642-63763-6. doi: 10.1007/978-3-642-58857-0. URL `http://link.springer.com/10.1007/978-3-642-58857-0`.

[49] Hongzhi Cao, Linpo Hao, Jingwen Yi, Xianglin Zhang, Zhonghan Luo, Shenglin Chen, and Rongfeng Li. The influence of punching process on residual stress and magnetic domain structure of non-oriented silicon steel. *Journal of Magnetism and Magnetic Materials*, 406:42–47, 5 2016. ISSN 0304-8853. doi: 10.1016/J.JMMM.2015.12.098.

[50] Soumya Subramonian, Taylan Altan, Bogdan Ciocirlan, and Craig Campbell. Optimum selection of variable punch-die clearance to improve tool life in blanking non-symmetric shapes. *International Journal of Machine Tools and Manufacture*, 75:63–71, 2013. ISSN 08906955. doi: 10.1016/j.ijmachtools.2013.09.004.

[51] R Hambli. Design of Experiment Based Analysis for Sheet Metal Blanking Processes Optimisation. Technical report, 2002.

[52] Soumya Subramonian, Taylan Altan, Craig Campbell, and Bogdan Ciocirlan. Determination of forces in high speed blanking using FEM and experiments. *Journal of Materials Processing Technology*, 213(12):2184–2190, 2013. ISSN 09240136. doi: 10.1016/j.jmatprotec.2013.06.014.

[53] H. A. Weiss, P. Trober, R. Golle, S. Steentjes, N. Leuning, K. Hameyer, and W. Volk. Loss reduction due to blanking parameter optimization for different non-grain oriented electrical steel grades. In *2017 IEEE International Electric Machines and Drives Conference, IEMDC 2017*. Institute of Electrical and Electronics Engineers Inc., 8 2017. ISBN 9781509042814. doi: 10.1109/IEMDC.2017.8002188.

[54] Wei Wu, Hongzhi Cao, Hao Ou, Zhichao Chen, Xianglin Zhang, Zhonghan Luo, Shenlin Chen, and Rongfeng Li. Effects of punching process on crystal orientations, magnetic and mechanical properties in non-oriented silicon steel. *Journal of Magnetism and Magnetic Materials*, 444:211–217, 12 2017. ISSN 03048853. doi: 10.1016/j.jmmm.2017.07.003.

[55] Changgeng Zhang, Lan Yang, and Yongjian Li. Punching effects on local magnetic properties near the edge of nonoriented electrical steels. *COMPEL - The International Journal for Computation and Mathematics in Electrical and Electronic Engineering*, 2022. ISSN 03321649. doi: 10.1108/COMPEL-01-2022-0064.

[56] Bohdal, R. Patyk, K. Tandecka, S. Gontarz, and D. Jackiewicz. Influence of shear-slitting parameters on workpiece formation, cut edge quality and selected magnetic properties for grain-oriented silicon steel. *Journal of Manufacturing Processes*, 56:1007–1026, 8 2020. ISSN 15266125. doi: 10.1016/j.jmapro.2020.05.049.

[57] Didin Zakariya and Muslim Mahardika. Influence of Clearance and Punch Velocity on the Quality of Pure Thin Copper Sheets Blanked Parts. In *IOP Conference Series: Materials Science and Engineering*, volume 157. Institute of Physics Publishing, 11 2016. doi: 10.1088/1757-899X/157/1/012012.

[58] Yani Kurniawan, Muslim Mahardika, and Suyitno. Effect of punch velocity on punch force and burnish height of punched holes in punching procces of pure titanium sheet. In *Journal of Physics: Conference Series*, volume 1430. Institute of Physics Publishing, 1 2020. doi: 10.1088/1742-6596/1430/1/012053.

[59] Adrianus Maria Goijaerts. *Prediction of ductile fracture in metal blanking.* Technische Universiteit Eindhoven, 1999. ISBN 9038627513. doi: 10.6100/IR527727.

[60] Peter Demmel, Hartmut Hoffmann, Roland Golle, Carsten Intra, and Wolfram Volk. Interaction of heat generation and material behaviour in sheet metal blanking. *CIRP Annals - Manufacturing Technology*, 64(1):249–252, 2015. ISSN 17260604. doi: 10.1016/j.cirp.2015.04.091.

[61] I. T. Gürbüz, F. Martin, U. Aydin, A. B. Asaf Ali, M. Chamosa, P. Rasilo, and A. Belahcen. Experimental characterization of the effect of uniaxial stress on magnetization and iron losses of electrical steel sheets cut by punching process. *Journal of Magnetism and Magnetic Materials*, 549, 5 2022. ISSN 03048853. doi: 10.1016/j.jmmm.2021.168983.

[62] Daisuke Miyagi, Kohei Miki, Masanori Nakano, and Norio Takahashi. Influence of compressive stress on magnetic properties of laminated electrical steel sheets. *IEEE Transactions on Magnetics*, 46(2):318–321, 2010. ISSN 00189464. doi: 10.1109/TMAG.2009.2033550.

[63] N. Leuning, S. Steentjes, M. Schulte, W. Bleck, and K. Hameyer. Effect of elastic and plastic tensile mechanical loading on the magnetic properties of NGO electrical steel. *Journal of Magnetism and Magnetic Materials*, 417:42–48, 11 2016. ISSN 03048853. doi: 10.1016/j.jmmm.2016.05.049.

[64] K. Mori, Y. Abe, Y. Kidoma, and P. Kadarno. Slight clearance punching of ultra-high strength steel sheets using punch having small round edge. *International Journal of Machine Tools and Manufacture*, 65:41–46, 2013. ISSN 08906955. doi: 10.1016/j.ijmachtools.2012.09.005.

[65] Maximilian Lorenz, Matthias Menzl, Christian Donhauser, Michael Layh, and Bernd R. Pinzer. Optical inline monitoring of the burnish surface in the punching process. *International Journal of Advanced Manufacturing Technology*, 118(11-12):3585–3600, 2 2022. ISSN 14333015. doi: 10.1007/s00170-021-07922-6.

[66] Christian Kubik, Sebastian Michael Knauer, and Peter Groche. Smart sheet metal forming: importance of data acquisition, preprocessing and transformation on the performance of a multiclass support vector machine for predicting wear states during blanking. *Journal of Intelligent Manufacturing*, 33(1):259–282, 1 2022. ISSN 15728145. doi: 10.1007/s10845-021-01789-w.

[67] Xiang Fang, Wei Wang, François Brisset, Anne Laure Helberg, and Thierry Baudin. Microstructure and texture evolution of nonoriented silicon steel during the punching process. *International Journal of Minerals, Metallurgy and Materials*, 29(11):2064–2071, 11 2022. ISSN 1869103X. doi: 10.1007/s12613-021-2404-1.

[68] Ma Teng, Yang Junfeng, Yu Zuyuan, Li Guodong, and Natsu Wataru. Influence of the punch with concave cutting-edge on the blanking force in micro punching process. *Procedia CIRP*, 113:166–171, 2022. ISSN 22128271. doi: 10.1016/j.procir.2022.09.126. URL `https://linkinghub.elsevier.com/retrieve/pii/S2212827122013257`.

[69] U. Aravind, Uday Chakkingal, and P. Venugopal. A Review of Fine Blanking: Influence of Die Design and Process Parameters on Edge Quality, 1 2021. ISSN 15441024.

[70] Yanxiong Liu, Tao Cheng, Lin Hua, and Huajie Mao. Research on the effect of ultrasonic vibration on the roll-over during the fine blanking process. *Journal of Mechanical Science and Technology*, 31(2):835–843, 2 2017. ISSN 1738494X. doi: 10.1007/s12206-017-0135-z.

[71] Yang Liu, Chunju Wang, Haibo Han, Debin Shan, and Bin Guo. Investigation on effect of ultrasonic vibration on micro-blanking process of copper foil. *International Journal of Advanced Manufacturing Technology*, 93(5-8):2243–2249, 11 2017. ISSN 14333015. doi: 10.1007/s00170-017-0684-4.

[72] Bing Pan, Zixing Lu, and Huimin Xie. Mean intensity gradient: An effective global parameter for quality assessment of the speckle patterns used in digital image correlation. *Optics and Lasers in Engineering*, 48(4):469–477, 4 2010. ISSN 01438166. doi: 10.1016/j.optlaseng.2009.08.010.

[73] J. Blaber, B. Adair, and A. Antoniou. Ncorr: Open-Source 2D Digital Image Correlation Matlab Software. *Experimental Mechanics*, 55(6):1105–1122, 7 2015. ISSN 17412765. doi: 10.1007/s11340-015-0009-1.

[74] Bing Pan, Anand Asundi, Huimin Xie, and Jianxin Gao. Digital image correlation using iterative least squares and pointwise least squares for displacement field and strain field measurements. *Optics and Lasers in Engineering*, 47(7-8):865–874, 7 2009. ISSN 01438166. doi: 10.1016/j.optlaseng.2008.10.014.

[75] Hubert Schreier, Jean-José Orteu, and Michael A. Sutton. *Image Correlation for Shape, Motion and Deformation Measurements*. Springer US, Boston, MA, 2009. ISBN 978-0-387-78746-6. doi: 10.1007/978-0-387-78747-3.

[76] Sun Yaofeng and John H.L. Pang. Study of optimal subset size in digital image correlation of speckle pattern images. *Optics and Lasers in Engineering*, 45(9):967–974, 9 2007. ISSN 01438166. doi: 10.1016/j.optlaseng.2007.01.012.

[77] Rory Bigger, Benoît Blaysat, Christofer Boo, Manuel Grewer, Jun Hu, Amanda Jones, Markus Klein, Kavesary Raghavan, Phillip Reu, Timothy Schmidt, Thorsten Siebert, Micah Simenson, Daniel Turner, Alessandro Vieira, and Thorsten Weikert. A Good Practices Guide for Digital Image Correlation. Technical report, International Digital Image Correlation Society, 10 2018. URL `http://idics.org/guide/`.

[78] Bing Pan, Liping Yu, Dafang Wu, and Liqun Tang. Systematic errors in two-dimensional digital image correlation due to lens distortion. *Optics and Lasers in Engineering*, 51(2):140–147, 2013. ISSN 01438166. doi: 10.1016/j.optlaseng.2012.08.012.

[79] Christoph Hartmann, Philipp Lechner, and Wolfram Volk. In-situ measurement of higher-order strain derivatives for advanced analysis of forming processes using spatio-temporal optical flow. *CIRP Annals*, 70(1):251–254, 1 2021. ISSN 17260604. doi: 10.1016/j.cirp.2021.04.033.

[80] S. Boukhtache, K. Abdelouahab, F. Berry, B. Blaysat, M. Grédiac, and F. Sur. When Deep Learning Meets Digital Image Correlation. *Optics and Lasers in Engineering*, 136, 1 2021. ISSN 01438166. doi: 10.1016/j.optlaseng.2020.106308.

[81] Ru Yang, Yang Li, Danielle Zeng, and Ping Guo. Deep DIC: Deep learning-based digital image correlation for end-to-end displacement and strain measurement. *Journal of Materials Processing Technology*, 302, 4 2022. ISSN 09240136. doi: 10.1016/j.jmatprotec.2021.117474.

[82] D. Lecompte, A. Smits, Sven Bossuyt, H. Sol, J. Vantomme, D. Van Hemelrijck, and A. M. Habraken. Quality assessment of speckle patterns for digital image correlation. *Optics and Lasers in Engineering*, 44(11):1132–1145, 11 2006. ISSN 01438166. doi: 10.1016/j.optlaseng.2005.10.004.

[83] Sun Yaofeng and John H.L. Pang. Study of optimal subset size in digital image correlation of speckle pattern images. *Optics and Lasers in Engineering*, 45(9):967–974, 9 2007. ISSN 01438166. doi: 10.1016/j.optlaseng.2007.01.012.

[84] Yong Su, Qingchuan Zhang, Xiaohai Xu, and Zeren Gao. Quality assessment of speckle patterns for DIC by consideration of both systematic errors and random errors. *Optics and Lasers in Engineering*, 86:132–142, 11 2016. ISSN 01438166. doi: 10.1016/j.optlaseng.2016.05.019.

[85] Bing Pan, Huimin Xie, Zhaoyang Wang, Kemao Qian, and Zhiyong Wang. Study on subset size selection in digital image correlation for speckle patterns. *Optics Express*, 16(10):7037, 5 2008. ISSN 1094-4087. doi: 10.1364/OE.16.007037. URL `https://opg.optica.org/oe/abstract.cfm?uri=oe-16-10-7037`.

[86] Tao Hua, Huimin Xie, Simon Wang, Zhenxing Hu, Pengwan Chen, and Qingming Zhang. Evaluation of the quality of a speckle pattern in the digital image correlation method by mean subset fluctuation. *Optics and Laser Technology*, 43(1):9–13, 2 2011. ISSN 00303992. doi: 10.1016/j.optlastec.2010.04.010.

[87] G. Crammond, S. W. Boyd, and J. M. Dulieu-Barton. Speckle pattern quality assessment for digital image correlation. *Optics and Lasers in Engineering*, 51(12):1368–1378, 12 2013. ISSN 01438166. doi: 10.1016/j.optlaseng.2013.03.014.

[88] Lawrence E Malvern. INTRODUCTION TO THE MECHANICS OF A CONTINUOUS MEDIUM. Technical report, 1977.

[89] T. Coppola, L. Cortese, and P. Folgarait. The effect of stress invariants on ductile fracture limit in steels. *Engineering Fracture Mechanics*, 76(9):1288–1302, 6 2009. ISSN 00137944. doi: 10.1016/j.engfracmech.2009.02.006.

[90] Lu Ming, Olivier Pantalé, and Olivier Pantalé An. Efficient and robust VUMAT implementation of elastoplastic constitutive laws in Abaqus/Explicit finite element code. Mechanics & Industry. *EDP Sciences*, 19(3):10, 2018. doi: 10.1051/meca/2018021{\"{i}}. URL `https://hal.archives-ouvertes.fr/hal-01905414`.

[91] WILLIAM K. RULE and S.E. Jones. A REVISED FORM FOR THE JOHNSON–COOK STRENGTH MODEL. *International Journal of Impact Engineering*, 21 (8):609–624, 9 1998. ISSN 0734743X. doi: 10.1016/S0734-743X(97)00081-X. URL `https://linkinghub.elsevier.com/retrieve/pii/S0734743X9700081X`.

[92] M. Nioi, C. Pinna, S. Celotto, E. Swart, D. Farrugia, Z. Husain, and H. Ghadbeigi. Finite element modelling of surface defect evolution during hot rolling of Silicon steel. *Journal of Materials Processing Technology*, 268:181–191, 6 2019. ISSN 09240136. doi: 10.1016/j.jmatprotec.2019.01.014.

[93] Stuart B Brown and Kwon H Kn. AN INTERNAL VARIABLE CONSTITUTIVE MODEL FOR HOT WORKING OF METALS. Technical report, 1989.

[94] A.R. Shahani, S. Setayeshi, S.A. Nodamaie, M.A. Asadi, and S. Rezaie. Prediction of influence parameters on the hot rolling process using finite element method and neural network. *Journal of Materials Processing Technology*, 209(4):1920–1935, 2 2009. ISSN 09240136. doi: 10.1016/j.jmatprotec.2008.04.055.

[95] Djordje Perić and D. R. J. Owen. A Model for Large Deformations of Elasto-Viscoplastic Solids at Finite Strain: Computational Issues. In Dieter Besdo and Erwin Stein, editors, *Finite Inelastic Deformations — Theory and Applications*, pages 299–312. Springer Berlin Heidelberg, Berlin, Heidelberg, 1992. doi: 10.1007/978-3-642-84833-9{_}27. URL `http://link.springer.com/10.1007/978-3-642-84833-9_27`.

[96] Yuanli Bai and Tomasz Wierzbicki. A new model of metal plasticity and fracture with pressure and Lode dependence. *International Journal of Plasticity*, 24(6):1071–1096, 6 2008. ISSN 07496419. doi: 10.1016/j.ijplas.2007.09.004.

[97] Yang Dong and Liang-Jiu Jia. Plasticity Model for Structural Steel with Lode Angle Dependence. *Journal of Bridge Engineering*, 26(12), 12 2021. ISSN 1084-0702. doi: 10.1061/(asce)be.1943-5592.0001784.

[98] Nousha Kheradmand, Bjørn Rune Rogne, Stéphane Dumoulin, Yun Deng, Roy Johnsen, and Afrooz Barnoush. Small scale testing approach to reveal specific features of slip behavior in BCC metals. *Acta Materialia*, 174:142–152, 8 2019. ISSN 13596454. doi: 10.1016/j.actamat.2019.05.031.

[99] James S.K.L. Gibson, Risheng Pei, Martin Heller, Setareh Medghalchi, Wei Luo, and Sandra Korte-Kerzel. Finding and characterising active slip systems: A short review and tutorial with automation tools. *Materials*, 14(2):1–17, 1 2021. ISSN 19961944. doi: 10.3390/ma14020407.

[100] R. Hill and J. W. Hutchinson. Differential Hardening in Sheet Metal Under Biaxial Loading: A Theoretical Framework. *Journal of Applied Mechanics*, 59(2S):S1–S9, 6 1992. ISSN 0021-8936. doi: 10.1115/1.2899489.

[101] Philip Eyckens, Hans Mulder, Jerzy Gawad, Henk Vegter, Dirk Roose, Ton van den Boogaard, Albert Van Bael, and Paul Van Houtte. The prediction of differential hardening behaviour of steels by multi-scale crystal plasticity modelling. *International Journal of Plasticity*, 73:119–141, 10 2015. ISSN 07496419. doi: 10.1016/j.ijplas.2014.12.004.

[102] S Takajo, S C Vogel, and C N Tomé. Viscoplastic self-consistent polycrystal modeling of texture evolution of ultra-low carbon steel during cold rolling. *Modelling and Simulation in Materials Science and Engineering*, 27(4):045003, 6 2019. ISSN 0965-0393. doi: 10.1088/1361-651X/ab0b92.

[103] Xiangyang Dong and Yung C. Shin. Predictive modeling of microstructure evolution within multi-phase steels during rolling processes. *International Journal of Mechanical Sciences*, 150:576–583, 1 2019. ISSN 00207403. doi: 10.1016/j.ijmecsci.2018.10.061.

[104] Ken Ichi Arai and Kazushi Ishiyama. Rolled texture and magnetic properties of 3% silicon steel. *Journal of Applied Physics*, 64(10):5352–5354, 11 1988. ISSN 0021-8979. doi: 10.1063/1.342369.

[105] F. Roters, P. Eisenlohr, L. Hantcherli, D. D. Tjahjanto, T. R. Bieler, and D. Raabe. Overview of constitutive laws, kinematics, homogenization and multiscale methods in crystal plasticity finite-element modeling: Theory, experiments, applications. *Acta Materialia*, 58(4):1152–1211, 2 2010. ISSN 13596454. doi: 10.1016/j.actamat.2009.10.058.

[106] M. Unterberg, P. Niemietz, D. Trauth, K. Wehrle, and T. Bergs. In-situ material classification in sheet-metal blanking using deep convolutional neural networks. *Production Engineering*, 13(6):743–749, 12 2019. ISSN 18637353. doi: 10.1007/s11740-019-00928-w.

[107] Zhengyi Jiang, Jingwei Zhao, and Haibo Xie. Simulation Models in Microforming. In *Microforming Technology*, pages 111–130. Elsevier, 2017. ISBN 9780128112120. doi: 10.1016/B978-0-12-811212-0.00006-6. URL `https://linkinghub.elsevier.com/retrieve/pii/B9780128112120000066`.

[108] Jie Xu, Bin Guo, Chunju Wang, and Debin Shan. Blanking clearance and grain size effects on micro deformation behavior and fracture in micro-blanking of brass foil. *International Journal of Machine Tools and Manufacture*, 60:27–34, 9 2012. ISSN 08906955. doi: 10.1016/j.ijmachtools.2012.04.001.

[109] Fengwei Sun, Edward D. Meade, and Noel P. O'Dowd. Strain gradient crystal plasticity modelling of size effects in a hierarchical martensitic steel using the Voronoi tessellation method. *International Journal of Plasticity*, 119:215–229, 2019. ISSN 07496419. doi: 10.1016/j.ijplas.2019.03.009.

[110] Juanjuan Han, Wei Zheng, Shubo Xu, and Guanghan Dang. The regionalized modelling and simulation of the micro-tensile process based on 3D Voronoi model. *Materials Today Communications*, 31, 6 2022. ISSN 23524928. doi: 10.1016/j.mtcomm.2022.103614.

[111] K. S. Zhang, Wu MS, and R. Feng. Simulation of microplasticity-induced deformation in uniaxially strained ceramics by 3-D Voronoi polycrystal modeling. *International Journal of Plasticity*, 21(4):801–834, 4 2005. ISSN 07496419. doi: 10.1016/j.ijplas.2004.05.010.

[112] Wenhai Gai, Rui Zhang, and Ran Guo. Two-scale Modeling of Composites damage with Voronoi cell finite element method for microscale computation. *Composite Structures*, 291, 7 2022. ISSN 02638223. doi: 10.1016/j.compstruct.2022.115659.

[113] Dassault Systemes. ABAQUS theory manual, 2017.

[114] H Hooputra, H Gese, H Dell, and H Werner. A comprehensive failure model for crashworthiness simulation of aluminium extrusions. *International Journal of Crashworthiness*, 9(5):449–464, 9 2004. ISSN 1358-8265. doi: 10.1533/ijcr.2004.0289.

[115] Shakir Gatea, Hengan Ou, Bin Lu, and Graham McCartney. Modelling of ductile fracture in single point incremental forming using a modified GTN model. *Engineering Fracture Mechanics*, 186:59–79, 12 2017. ISSN 00137944. doi: 10.1016/j.engfracmech.2017.09.021.

[116] V Tvergaard and A Needleman. ANALYSIS OF THE CUP-CONE FRACTURE IN A ROUND TENSILE BAR. Technical Report I, 1984.

[117] Yuxi Yan, Quan Sun, Jianjun Chen, and Hongliang Pan. The initiation and propagation of edge cracks of silicon steel during tandem cold rolling process based on the Gurson-Tvergaard-Needleman damage model. *Journal of Materials Processing Technology*, 2013. ISSN 09240136. doi: 10.1016/j.jmatprotec.2012.11.006.

[118] Zao He, Hao Zhu, and Yumei Hu. An improved shear modified GTN model for ductile fracture of aluminium alloys under different stress states and its parameters identification. *International Journal of Mechanical Sciences*, 192, 2 2021. ISSN 00207403. doi: 10.1016/j.ijmecsci.2020.106081.

[119] Z.L Zhang, C Thaulow, and J Ødegård. A complete Gurson model approach for ductile fracture. *Engineering Fracture Mechanics*, 67(2):155–168, 9 2000. ISSN 00137944. doi: 10.1016/S0013-7944(00)00055-2. URL `https://linkinghub.elsevier.com/retrieve/pii/S0013794400000552`.

[120] Rahul Chhibber, N. Arora, S. R. Gupta, and B. K. Dutta. Estimation of Gurson material parameters in bimetallic weldments for the nuclear reactor heat transport piping system. *Proceedings of the Institution of Mechanical Engineers, Part C: Journal of Mechanical Engineering Science*, 222(12):2331–2349, 12 2008. ISSN 09544062. doi: 10.1243/09544062JMES1001.

[121] Jian Peng, Ying Wang, Qiao Dai, Xuedong Liu, Lin Liu, and Zhihong Zhang. Effect of stress triaxiality on plastic damage evolution and failure mode for 316L notched specimen. *Metals*, 9(10), 10 2019. ISSN 20754701. doi: 10.3390/met9101067.

[122] W. T. Li, Z. Y. Cai, H. Li, L. F. Peng, X. M. Lai, and M. W. Fu. The modified GTN-Thomason criterion for modelling of ductile fracture considering shear factor and size effect in micro-scaled plastic deformation. *International Journal of Mechanical Sciences*, 204, 8 2021. ISSN 00207403. doi: 10.1016/j.ijmecsci.2021.106540.

[123] Abdolvahed Kami, Bijan Mollaei Dariani, Ali Sadough Vanini, Dan Sorin Comsa, and Dorel Banabic. Numerical determination of the forming limit curves of anisotropic sheet metals using GTN damage model. *Journal of Materials Processing Technology*, 216:472–483, 2 2015. ISSN 09240136. doi: 10.1016/j.jmatprotec.2014.10.017.

[124] Jean Lemaitre. A Continuous Damage Mechanics Model for Ductile Fracture. *Journal of Engineering Materials and Technology*, 107(1):83–89, 1 1985. ISSN 0094-4289. doi: 10.1115/1.3225775.

[125] Ashwani Verma and Ravindra K. Saxena. Determination of Lemaitre damage parameters for DP590 steel using Teacher-Learner based optimization. In *Journal of Physics: Conference Series*, volume 1240. Institute of Physics Publishing, 8 2019. doi: 10.1088/1742-6596/1240/1/012101.

[126] Ali Mkaddem, Ridha Hambli, and Alain Potiron. Comparison between Gurson and Lemaitre damage models in wiping die bending processes. *International Journal of Advanced Manufacturing Technology*, 23(5-6):451–461, 2004. ISSN 02683768. doi: 10.1007/s00170-003-1701-3.

[127] Ridha Hambli. Comparison between Lemaitre and Gurson damage models in crack growth simulation during blanking process. Technical report, 2001.

[128] Pavan Kumar and Puneet Tandon. Investigating the capability of the Lemaitre damage model to establish the incremental sheet forming process. *Archives of Civil and Mechanical Engineering*, 22(2), 5 2022. ISSN 16449665. doi: 10.1007/s43452-022-00391-y.

[129] Junhe Lian, Yuan Feng, and Sebastian Münstermann. A Modified Lemaitre Damage Model Phenomenologically Accounting for the Lode Angle Effect on Ductile Fracture. *Procedia Materials Science*, 3:1841–1847, 2014. ISSN 22118128. doi: 10.1016/j.mspro.2014.06.297.

[130] J. Lian, M. Sharaf, F. Archie, and S. Münstermann. A hybrid approach for modelling of plasticity and failure behaviour of advanced high-strength steel sheets. *International Journal of Damage Mechanics*, 22(2):188–218, 3 2013. ISSN 10567895. doi: 10.1177/1056789512439319.

[131] Yingbin Bao and Tomasz Wierzbicki. On the cut-off value of negative triaxiality for fracture. *Engineering Fracture Mechanics*, 2005. ISSN 00137944. doi: 10.1016/j.engfracmech.2004.07.011.

[132] B. Wu, X. Li, Y. Di, V. Brinnel, J. Lian, and S. Münstermann. Extension of the modified Bai-Wierzbicki model for predicting ductile fracture under complex loading conditions. *Fatigue and Fracture of Engineering Materials and Structures*, 40(12):2152–2168, 12 2017. ISSN 14602695. doi: 10.1111/ffe.12645.

[133] Bo Wu, Stefan Buchkremer, Sebastian Münstermann, Junhe Lian, Drazen Veselovac, Wolfgang Bleck, and Fritz Klocke. Modeling of Chip Breakage in Machining of AISI 1045 Steel by Using an Improved Damage Mechanics Model. *Steel Research International*, 88(7), 7 2017. ISSN 16113683. doi: 10.1002/srin.201600338.

[134] V. Keim, A. Nonn, and S. Münstermann. Application of the modified Bai-Wierzbicki model for the prediction of ductile fracture in pipelines. *International Journal of Pressure Vessels and Piping*, 171:104–116, 3 2019. ISSN 03080161. doi: 10.1016/j.ijpvp.2019.02.010.

[135] T. W.J. de Geus, R. H.J. Peerlings, and M. G.D. Geers. Competing damage mechanisms in a two-phase microstructure: How microstructure and loading conditions determine the onset of fracture. *International Journal of Solids and Structures*, 97_98:687–698, 10 2016. ISSN 00207683. doi: 10.1016/j.ijsolstr.2016.03.029.

[136] Jun Min Seo, Hune Tae Kim, Yun Jae Kim, Hiroyuki Yamada, Tomohisa Kumagai, Hayato Tokunaga, and Naoki Miura. Effect of strain rate and stress triaxiality on fracture strain of 304 stainless steels for canister impact simulation. *Nuclear Engineering and Technology*, 54(7):2386–2394, 7 2022. ISSN 2234358X. doi: 10.1016/j.net.2022.02.002.

[137] Milan Jirásek. Nonlocal damage mechanics. Technical report.

[138] S. Felder, N. Kopic-Osmanovic, H. Holthusen, T. Brepols, and S. Reese. Thermo-mechanically coupled gradient-extended damage-plasticity modeling of metallic materials at finite strains. *International Journal of Plasticity*, 148, 1 2022. ISSN 07496419. doi: 10.1016/j.ijplas.2021.103142.

[139] Fadi Aldakheel, Peter Wriggers, and Christian Miehe. A modified Gurson-type plasticity model at finite strains: formulation, numerical analysis and phase-field coupling. *Computational Mechanics*, 62(4):815–833, 10 2018. ISSN 01787675. doi: 10.1007/s00466-017-1530-0.

[140] Homer H Chen and Thomas S Huang. A survey of construction and manipulation of octrees. *Computer Vision, Graphics, and Image Processing*, 43(3):409–431, 9 1988.

ISSN 0734189X. doi: 10.1016/0734-189X(88)90092-8. URL `https://linkinghub.elsevier.com/retrieve/pii/0734189X88900928`.

[141] Ankit Ankit, Chongmin Song, Sascha Eisenträger, Sen Zhang, and Ehab Hamed. Dynamic non-local damage analysis using an octree pattern-based massively parallel explicit solver. *Computer Methods in Applied Mechanics and Engineering*, 400:115598, 10 2022. ISSN 00457825. doi: 10.1016/j.cma.2022.115598.

[142] C. C. Tasan, J. P.M. Hoefnagels, and M. G.D. Geers. Identification of the continuum damage parameter: An experimental challenge in modeling damage evolution. *Acta Materialia*, 60(8):3581–3589, 5 2012. ISSN 13596454. doi: 10.1016/j.actamat.2012.03.017.

[143] C. C. Tasan, J. P.M. Hoefnagels, and M. G.D. Geers. A critical assessment of indentation-based ductile damage quantification. *Acta Materialia*, 57(17):4957–4966, 10 2009. ISSN 13596454. doi: 10.1016/j.actamat.2009.06.057.

[144] C. C. Tasan, J. P.M. Hoefnagels, and M. G.D. Geers. Indentation-based damage quantification revisited. *Scripta Materialia*, 63(3):316–319, 8 2010. ISSN 13596462. doi: 10.1016/j.scriptamat.2010.04.018.

[145] L. Vecchiato, A. Campagnolo, and G. Meneghetti. Numerical calibration and experimental validation of the direct current potential drop (DCPD) method for fracture mechanics fatigue testing of single-edge-crack round bars. *International Journal of Fatigue*, 150, 9 2021. ISSN 01421123. doi: 10.1016/j.ijfatigue.2021.106316.

[146] Victoria Brinnel, Benedikt Döbereiner, and Sebastian Münstermann. Characterizing Ductile Damage and Failure: Application of the Direct Current Potential Drop Method to Uncracked Tensile Specimens. *Procedia Materials Science*, 3:1161–1166, 2014. ISSN 22118128. doi: 10.1016/j.mspro.2014.06.189.

[147] Richi Kumar, Jacques Besson, Andrew King, Anna Dahl, and Thilo F. Morgeneyer. X-ray microtomography investigation of damage fields ahead of cracks in CT and SENT C-Mn steel samples. *International Journal of Fracture*, 2022. ISSN 15732673. doi: 10.1007/s10704-022-00674-8.

[148] H. Scott, J. D. Boyd, and A. K. Pilkey. Micro-computed tomographic imaging of void damage in a hot-rolled complex phase sheet steel. *Materials Science and Engineering A*, 682:139–146, 1 2017. ISSN 09215093. doi: 10.1016/j.msea.2016.11.020.

[149] Pierre Thibault, Martin Dierolf, Andreas Menzel, Oliver Bunk, Christian David, and Franz Pfeiffer. High-resolution scanning X-ray diffraction microscopy. *Science*, 321 (5887):379–382, 7 2008. ISSN 00368075. doi: 10.1126/science.1158573.

[150] Michael Herbig, Andrew King, Péter Reischig, Henry Proudhon, Erik M. Lauridsen, James Marrow, Jean Yves Buffire, and Wolfgang Ludwig. 3-D growth of a short fatigue crack within a polycrystalline microstructure studied using combined diffraction and phase-contrast X-ray tomography. *Acta Materialia*, 59(2):590–601, 2011. ISSN 13596454. doi: 10.1016/j.actamat.2010.09.063.

[151] A. King, W. Ludwig, M. Herbig, J. Y. Buffire, A. A. Khan, N. Stevens, and T. J. Marrow. Three-dimensional in situ observations of short fatigue crack growth in magnesium. *Acta Materialia*, 59(17):6761–6771, 2011. ISSN 13596454. doi: 10.1016/j.actamat.2011.07.034.

[152] S. Takajo, C. C. Merriman, S. C. Vogel, and D. P. Field. In-situ EBSD study on the cube texture evolution in 3 wt % Si steel complemented by ex-situ EBSD experiment — From nucleation to grain growth. *Acta Materialia*, 166:100–112, 3 2019. ISSN 13596454. doi: 10.1016/j.actamat.2018.11.054.

[153] Yong Keun Ahn, Yong Kwon Jeong, Tae Young Kim, Ji Ung Cho, and Nong Moon Hwang. Texture evolution of non-oriented electrical steel analyzed by EBSD and in-situ XRD during the phase transformation from γ to α. *Materials Today Communications*, 25, 12 2020. ISSN 23524928. doi: 10.1016/j.mtcomm.2020.101307.

[154] M. Mehdi, Youliang He, Erik J. Hilinski, Narayan C. Kar, and Afsaneh Edrisy. Non-oriented electrical steel with core losses comparable to grain-oriented electrical steel. *Journal of Magnetism and Magnetic Materials*, 491, 12 2019. ISSN 03048853. doi: 10.1016/j.jmmm.2019.165597.

[155] Claire Schayes, Jérémie Bouquerel, Jean Bernard Vogt, Frédéric Palleschi, and Stefan Zaefferer. A comparison of EBSD based strain indicators for the study of Fe-3Si steel subjected to cyclic loading. *Materials Characterization*, 115:61–70, 5 2016. ISSN 10445803. doi: 10.1016/j.matchar.2016.03.020.

[156] F. Klocke, D. Lung, and S. Buchkremer. Inverse identification of the constitutive equation of inconel 718 and AISI 1045 from FE machining simulations. In *Procedia CIRP*, volume 8, pages 212–217. Elsevier B.V., 2013. doi: 10.1016/j.procir.2013.06.091.

[157] Sheng Cai and Lin Chen. Parameter identification and blanking simulations of DP1000 and Al6082-T6 using Lemaitre damage model. *Advances in Manufacturing*, 9(3):457–472, 9 2021. ISSN 21953597. doi: 10.1007/s40436-021-00350-5.

[158] David D.S. Silva, Rafael A. Raimundo, Daniel N.L. Alves, Micael R. Andrade, Ramon A. Torquato, Rodinei M. Gomes, Marco A. Morales, and Danniel F. Oliveira. Evaluation of mechanical ductile damage in sheet metal based on low-field magnetic analysis. *Journal of Magnetism and Magnetic Materials*, 539, 12 2021. ISSN 03048853. doi: 10.1016/j.jmmm.2021.168403.

[159] Seunghee Park, Ju Won Kim, Changgil Lee, and Jong Jae Lee. Magnetic flux leakage sensing-based steel cable NDE technique. *Shock and Vibration*, 2014, 2014. ISSN 10709622. doi: 10.1155/2014/929341.

[160] Jie Tian, Wei Wang, Hongyao Wang, Qiang Bai, Zeyang Zhou, and Pengbo Li. Enhancing Wire-Rope Damage Signals Based on a Radial Magnetic Concentrator Bridge Circuit. *Sensors*, 22(10), 5 2022. ISSN 14248220. doi: 10.3390/s22103654.

[161] Xiang Kong, Lukas Helfen, Mathias Hurst, Daniel Hänschke, Djamel Missoum-Benziane, Jacques Besson, Tilo Baumbach, and Thilo F. Morgeneyer. 3D in situ study

of damage during a 'shear to tension' load path change in an aluminium alloy. *Acta Materialia*, 231:117842, 6 2022. ISSN 13596454. doi: 10.1016/j.actamat.2022.117842.

[162] N. Habibi, F. Pütz, M. Könemann, V. Brinnel, S. Münstermann, M. Feistle, and W. Volk. Numerical quantification of damage accumulation resulting from blanking in multi-phase steel. In *IOP Conference Series: Materials Science and Engineering*, volume 418. Institute of Physics Publishing, 9 2018. doi: 10.1088/1757-899X/418/1/012058.

[163] Michael Brünig, Daniel Brenner, and Steffen Gerke. Stress state dependence of ductile damage and fracture behavior: Experiments and numerical simulations. *Engineering Fracture Mechanics*, 141:152–169, 6 2015. ISSN 00137944. doi: 10.1016/j.engfracmech.2015.05.022.

[164] C.H. Pham, F. Adzima, J. Coër, and P.Y. Manach. Anti-Buckling Device for Ultra-Thin Metallic Sheets Under Large and Reversed Shear Strain Paths. *Experimental Mechanics*, 57(4):593–602, 4 2017. ISSN 0014-4851. doi: 10.1007/s11340-017-0256-4.

[165] Fabian Stiebert, Heinrich Traphöner, Rickmer Meya, and A. Erman Tekkaya. Characterization of Flow Curves for Ultra-Thin Steel Sheets With the In-Plane Torsion Test. *Journal of Manufacturing Science and Engineering*, 144(3), 3 2022. ISSN 1087-1357. doi: 10.1115/1.4051919.

[166] Moritz Zistl, Michael Brünig, and Steffen Gerke. Analysis of damage and fracture behavior in ductile metal sheets undergoing compression and shear preloading. *International Journal of Material Forming*, 15(4), 7 2022. ISSN 19606214. doi: 10.1007/s12289-022-01705-4.

[167] Phillip Reu. All about speckles: Speckle Size Measurement. Technical report, 2014.

[168] Phillip Reu. All about Speckles: Speckle Density. Technical report, 2015.

[169] Kieran G. Larkin. Reflections on Shannon Information: In search of a natural information-entropy for images. *arXiv preprint*, 2016.

[170] Luca Gambirasio and Egidio Rizzi. On the calibration strategies of the Johnson-Cook strength model: Discussion and applications to experimental data. *Materials Science and Engineering A*, 610:370–413, 7 2014. ISSN 09215093. doi: 10.1016/j.msea.2014.05.006.

[171] ASTM International. Test Methods for Tension Testing of Metallic Materials. Technical report, 2022. URL `https://www.astm.org/e0008_e0008m-22.html`.

[172] Ammar Dawood Ghali Al-Rubaye. Characterization of blanking induced magneto-mechanical cut edge defects in non-oriented electrical steel By. Technical report, 2019.

[173] A. Niazi, J. B. Pieri, E. Berger, and R. Jouty. Note on electromigration of grain boundaries in silicon iron. *Journal of Materials Science*, 10(2):361–362, 2 1975. ISSN 0022-2461. doi: 10.1007/BF00540359. URL `http://link.springer.com/10.1007/BF00540359`.

[174] J. Peirs, P. Verleysen, W. Van Paepegem, and J. Degrieck. Novel pure-shear sheet specimen geometry for dynamic material characterisation. pages 35–41. EDP Sciences, 2009. doi: 10.1051/dymat/2009005.

[175] B. Wu, X. Li, Y. Di, V. Brinnel, J. Lian, and S. Münstermann. Extension of the modified Bai-Wierzbicki model for predicting ductile fracture under complex loading conditions. *Fatigue and Fracture of Engineering Materials and Structures*, 40(12):2152–2168, 12 2017. ISSN 14602695. doi: 10.1111/ffe.12645.

[176] A. Niazi, J. B. Pieri, E. Berger, and R. Jouty. Note on electromigration of grain boundaries in silicon iron. *Journal of Materials Science*, 10(2):361–362, 2 1975. ISSN 0022-2461. doi: 10.1007/BF00540359. URL `http://link.springer.com/10.1007/BF00540359`.

[177] M. H. Stone. The Generalized Weierstrass Approximation Theorem. *Mathematics Magazine*, 21(4):167, 3 1948. ISSN 0025570X. doi: 10.2307/3029750.

[178] Yingbin Bao and Tomasz Wierzbicki. On fracture locus in the equivalent strain and stress triaxiality space. *International Journal of Mechanical Sciences*, 2004. ISSN 00207403. doi: 10.1016/j.ijmecsci.2004.02.006.

[179] Fuchang Gao and Lixing Han. Implementing the Nelder-Mead simplex algorithm with adaptive parameters. *Computational Optimization and Applications*, 51(1):259–277, 1 2012. ISSN 0926-6003. doi: 10.1007/s10589-010-9329-3.

[180] Octree diagram, 2010. URL `https://commons.wikimedia.org/wiki/File:Octree2.svg`.

[181] Azaiya K Mukherjee, James E Bird, John E Dorn, and Escholarship Org. Lawrence Berkeley National Laboratory Recent Work Title EXPERIMENTAL CORRELATIONS FOR HIGH-TEMPERATURE CREEP Publication Date. Technical report, 1968. URL `https://escholarship.org/uc/item/31p4z5v2`.

[182] Liang Xue and Tomasz Wierzbicki. Ductile fracture initiation and propagation modeling using damage plasticity theory. *Engineering Fracture Mechanics*, 75(11):3276–3293, 7 2008. ISSN 00137944. doi: 10.1016/j.engfracmech.2007.08.012.

[183] Jian Peng, Peishuang Zhou, Ying Wang, Qiao Dai, David Knowles, and Mahmoud Mostafavi. Stress triaxiality and lode angle parameter characterization of flat metal specimen with inclined notch. *Metals*, 11(10), 10 2021. ISSN 20754701. doi: 10.3390/met11101627.

[184] Milan Jirásek and Rodrigue Desmorat. Localization analysis of nonlocal models with damage-dependent nonlocal interaction. *International Journal of Solids and Structures*, 174-175:1–17, 11 2019. ISSN 00207683. doi: 10.1016/j.ijsolstr.2019.06.011.

[185] Viggo Tvergaard and Alan Needleman. Effects of nonlocal damage in porous plastic solids. *International Journal of Solids and Structures*, 32(8-9):1063–1077, 4 1995. ISSN 00207683. doi: 10.1016/0020-7683(94)00185-Y.

[186] Zdeně P Baž ant and Milan Jirá sek. Nonlocal Integral Formulations of Plasticity and Damage: Survey of Progress. doi: 10.1061/ASCE0733-93992002128:111119.

[187] D. Patterson, T. Anderson, N. Cardwell, R. Fromm, K. Keeton, C. Kozyrakis, R. Thomas, and K. Yelick. A case for intelligent RAM. *IEEE Micro*, 17(2):34–44, 1997. ISSN 02721732. doi: 10.1109/40.592312. URL `http://ieeexplore.ieee.org/document/592312/`.

[188] H. Ghadbeigi, S.R. Bradbury, C. Pinna, and J.R. Yates. Determination of micro-scale plastic strain caused by orthogonal cutting. *International Journal of Machine Tools and Manufacture*, 48(2):228–235, 2 2008. ISSN 08906955. doi: 10.1016/j.ijmachtools.2007.08.017.

[189] Heinrich Traphöner, Till Clausmeyer, and A. Erman Tekkaya. Material characterization for plane and curved sheets using the in-plane torsion test – An overview. *Journal of Materials Processing Technology*, 257:278–287, 7 2018. ISSN 09240136. doi: 10.1016/j.jmatprotec.2018.02.030.

[190] Khemais K Saanouni, E Diamantopoulou, C Labergère, and K Saanouni. Ductile damage prediction in a blanking process based on a nonlocal micromorphic model. Ductile damage prediction in a blanking process based on a nonlocal micromorphic model. Technical report. URL `https://www.researchgate.net/publication/326416680`.

[191] D. Steglich, X. Tian, J. Bohlen, and T. Kuwabara. Mechanical Testing of Thin Sheet Magnesium Alloys in Biaxial Tension and Uniaxial Compression. *Experimental Mechanics*, 54(7):1247–1258, 2014. ISSN 17412765. doi: 10.1007/s11340-014-9892-0.

[192] By C E Stromeyer, by Sir Benjamin Baker, and Hopkinson All. The determination of fatigue limits under alternating stress conditions. *Proceedings of the Royal Society of London. Series A, Containing Papers of a Mathematical and Physical Character*, 90 (620):411–425, 7 1914. ISSN 0950-1207. doi: 10.1098/rspa.1914.0066. URL `https://royalsocietypublishing.org/doi/10.1098/rspa.1914.0066`.

Appendices

Appendix A

Additional exponential softening coefficient plots

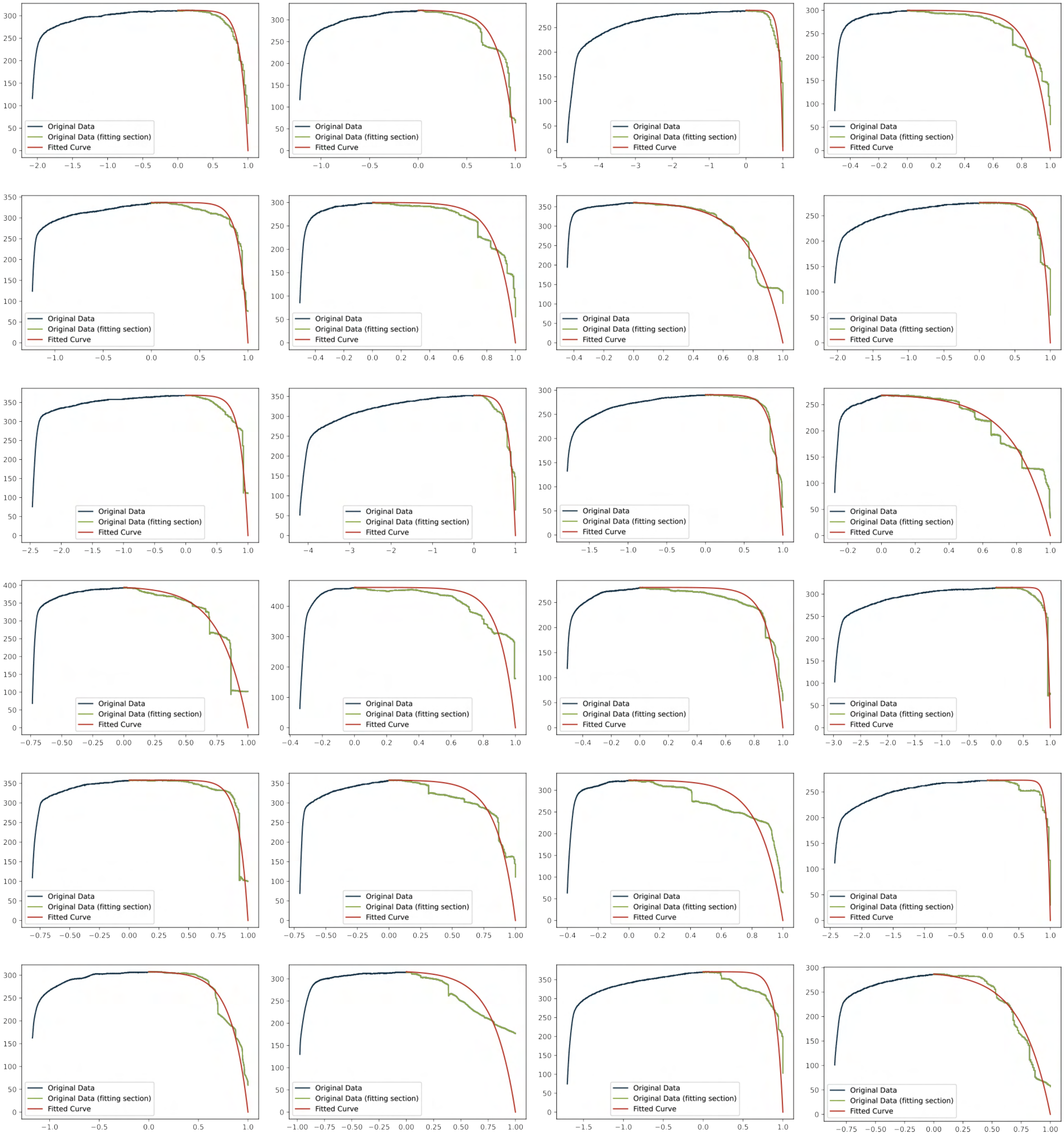

Figure A.1: *Exponential damage softening coefficient calibration, using crosshead displacement as the base for the damage variable. All plots are Y axis force (N), X-axis damage variable.*

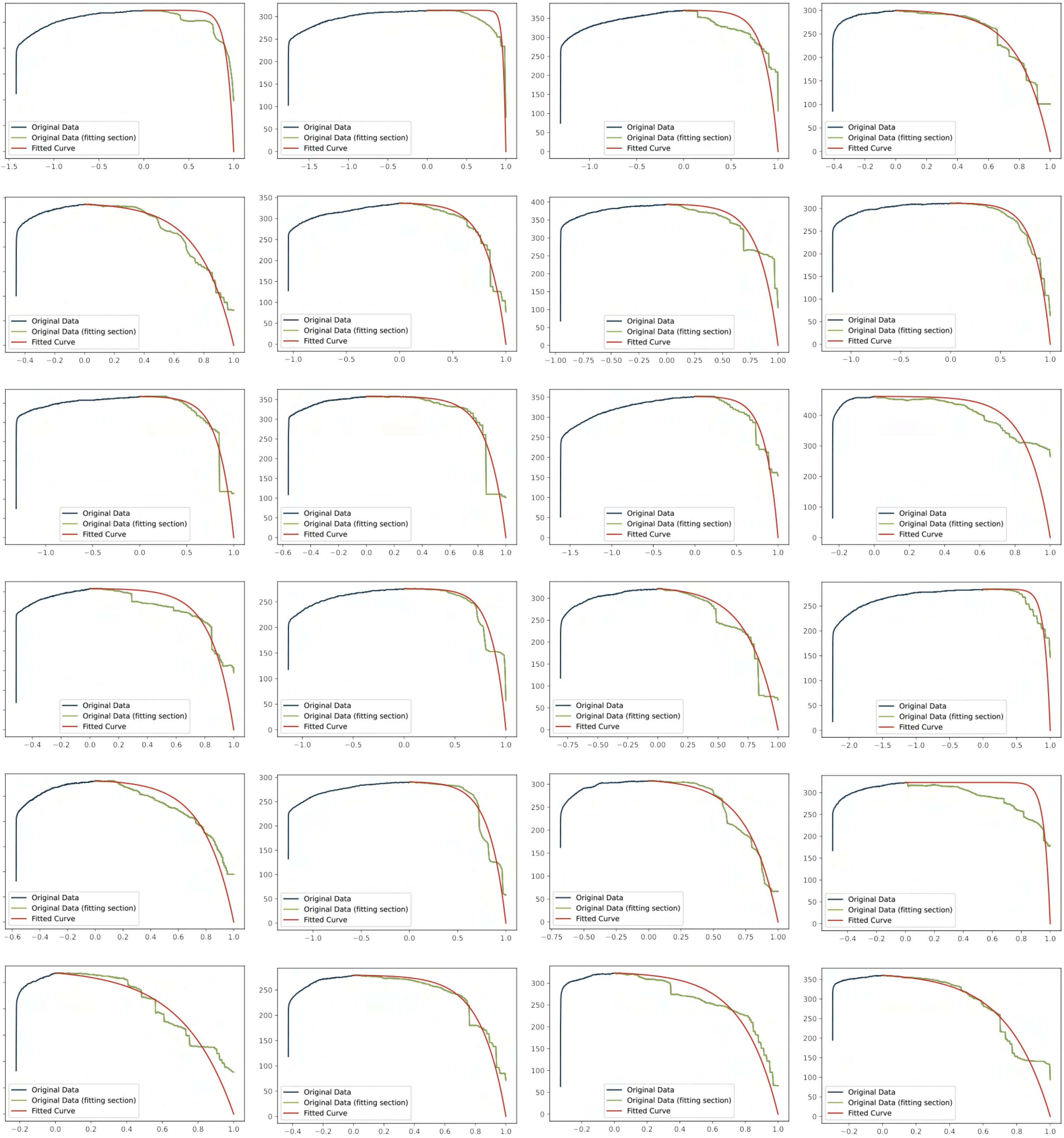

Figure A.2: *Exponential damage softening coefficient calibration, using true strain in the shear region as calculated from DIC, averaged over a* $1\,\mathrm{mm}^2$ *area as the base for the damage variable. All plots are Y axis force (N), X-axis damage variable.*

Appendix B

Additional Hall effect sensor data

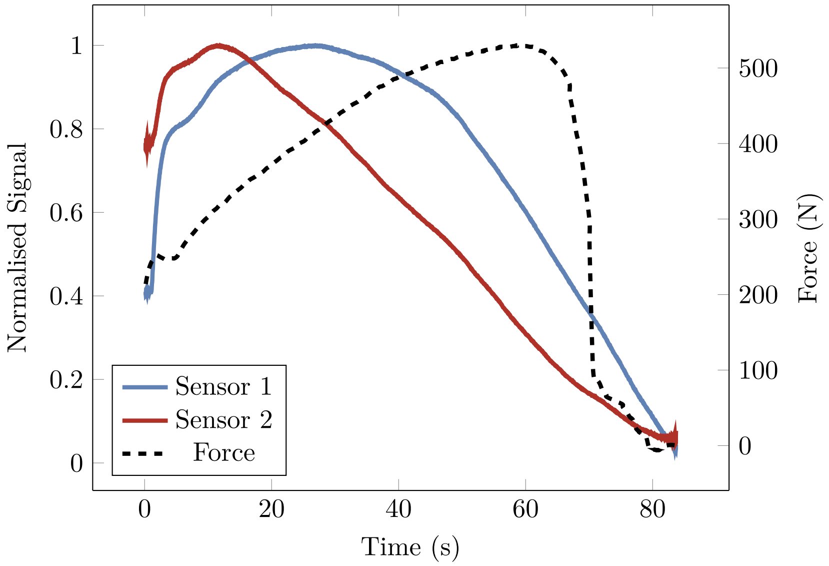

Figure B.1: *An additional plot of Hall effect sensing in the star configuration.*

Appendix C

Force - displacement for uCT samples

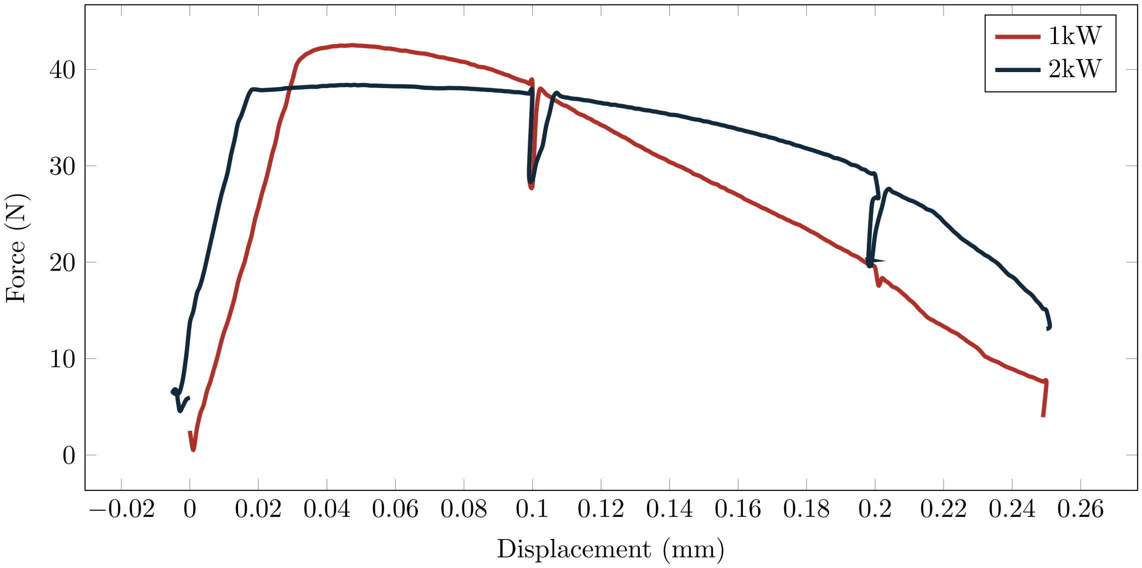

Figure C.1: *Force - displacement for the X-ray microscope sample type.*

Appendix D

Addition effects of laser cutting

The influence of the laser power during remote laser cutting was investigated, macroscopic effects such as the influence on fracture strain were of particular concern, however edge hardness and magnetic loss were also investigated as these as these are not yet available in literature for this technique.

D.1 Effect of laser cutting on mechanical properties

Figure D.1 shows the hardness measurement from the cut edge for a 2 kW laser power at $8\,\mathrm{m\,s^{-1}}$ for 4 rows of indents. A clear influence is displayed with material hardness increased toward the cut edge, this increased hardness zone extends for 800 µm with a sharp decrease over a region if approximately 40 µm. Figure D.2 takes the average of the 4 rows and plots the standard error as a shaded region, a comparison between a power of 250 W and 2000 W (as shown in Figure D.1) is made. Some degree of influence is still shown, however the zone of increased hardness in the low power setting is less than half that of the higher power setting. An increased variability is also shown for the higher power which may be indicative of applied internal stresses due to the heating. It is shown that the hardness of lower laser parameters is approximately equal to that produced by blanking [2], although the gradient is higher. High laser power displays a significantly increased hardness which extends much further into the bulk material in comparison to blanking.

The laser power level is shown to have some effect on the fatigue life of the material. Silicon steel displays extreme fatigue resistance under the yield strength. Samples tested with any stress ratio where the peak force was less than 490 N did not fail within one million cycles.

A number of samples were tests with a stress ratio of $r = 0$, Figure D.3 shows results for both laser power parameters and the Stromeyer model for fatigue [192] is plotted for $C = 13.77$, $\sigma_w = 395.8$ MPa. Below the yield stress of σ_y =395.8 MPa no fracture was observed in either sample type. The fit for this model achieved an R-Square value of 0.80

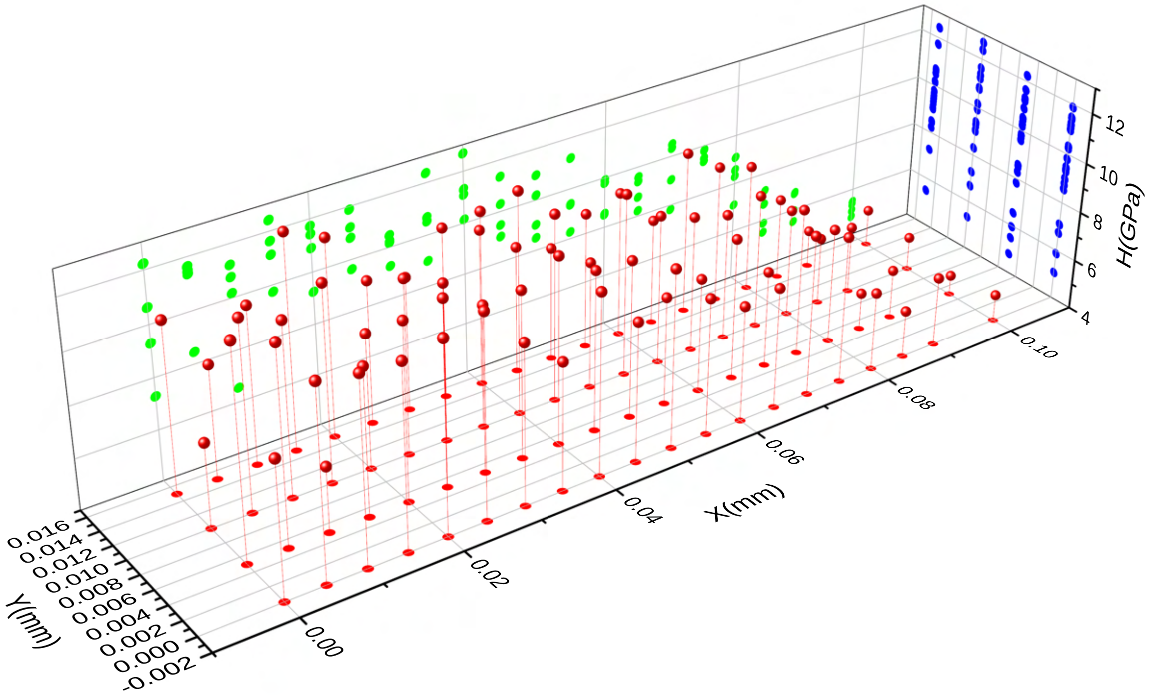

Figure D.1: *A plot of the hardness values from the cut edge for a sample cut using 2000*W *power laser parameter. The x axis displays the distance from the cut edge.*

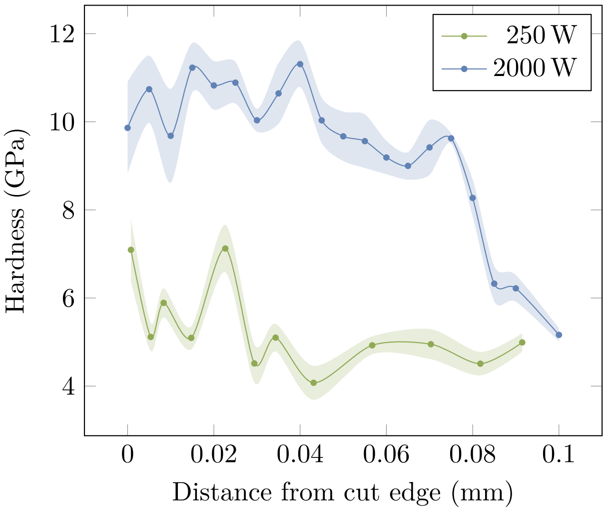

Figure D.2: *A comparison of the hardness at the cut edge, the solid line indicates the mean average hardness over the measurement area, and the shaded area shows the standard error. The bulk material hardness was measured as approximately* 4 GPa, *in agreement with other studies [2].*

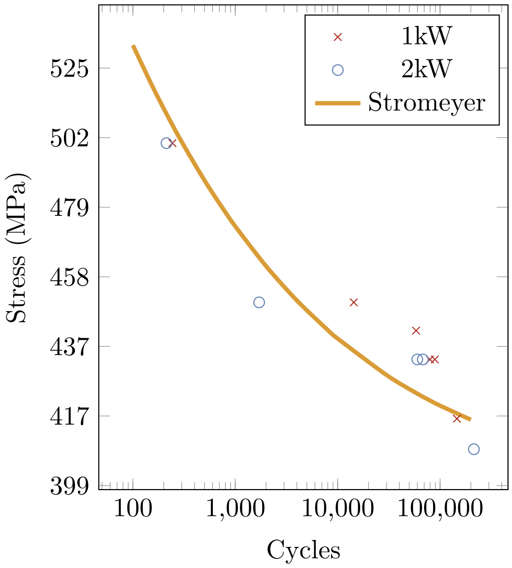

Figure D.3: *Fatigue life comparison between laser power levels.*

D.2 Magnetic property degradation due to edge damage

The specific loss was investigated for samples with an increasing number of slots cut by laser cutting at a power of 1 kW. Figure D.4 shows the loss at several frequencies and induced field strengths for samples in the RD and TD.

An approximately linear relationship is displayed between the number of slots and the specific loss. This relationship is displayed across all frequencies and induced magnetic field values. It is noted that for the 4 slot variant a slightly higher loss is observed for samples in the rolling direction, indicating that the HAZs may be combining. As the slots were spaced 6mm apart there is some doubt to such a hypothesis and further work is required for verification. Note that the difference between RD and TD samples is reduced in this case, and that TD samples do not display this non linear increase in loss. Saturated samples correlated less strongly with the linear relationship shown at other inductions, however this is likely a result of the ±0.05 T induction error at saturation arising from the maximum current draw in the induction coil of the single sheet tester.

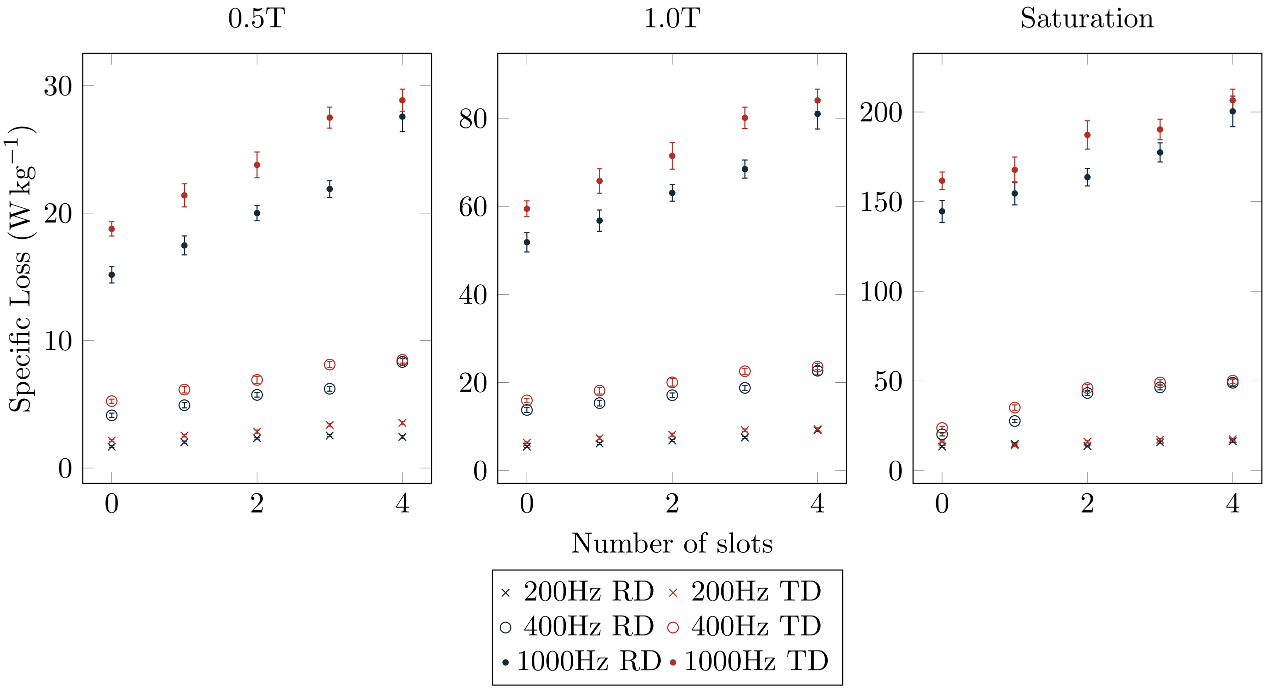

Figure D.4: *Specific loss as a function of the number of cuts in the material, presented at various field inductions and frequencies. A linear relationship is apparent in all cases.*

Appendix E

Scripts for model calibration

```python
from scipy.interpolate import CubicSpline
import numpy as np
import matplotlib.pyplot as plt

plt.style.use('seaborn-poster')
x = [0,0.3235, 0.34, 0.445 ] #integrated strain at failure
y = [373.8694118,233.963,238.5171429, 385.81] #onset
#y = [1109.041765,376.47, 467.8042857, 492.8783333] #fracture strain in millistrian
# use bc_type = 'natural' adds the constraints as we described above
f = CubicSpline(x, y, bc_type=((1, 0.0), (1, 0.0))) # ensure 1st derivative is 0 at ends (clamped)
#This means differentiability between sections, and outside of tested area is extrapolated as last known value instead of weird value due to
#cubic interpolation being way out of range.
x_new = np.linspace(-0.1, 0.45, 1000)
y_new = f(x_new)
plt.figure(figsize = (10,8))
plt.plot(x_new, y_new, 'b')
plt.plot(x, y, 'ro')
plt.title('Interpolated curve')
plt.xlabel('Stress state')
plt.ylabel('Millistrain')
plt.show()
f.c # Coefficients
f.x # Breakpoints
k,l=np.shape(f.c)

for i in range(l):
    print("Coefficients of first term between " + str(f.x[i]) +" and " + str(f.x[i+1]) +" :")
    print(str(f.c[0,i]) + " x^3 + "+str(f.c[1,i]) + " x^2 + "+str(f.c[2,i]) + " x + "+str(f.c[3,i]) +" \n")
    #print(str(f.c[0,i])+"(x-" + str(f.x[i]) +")^3"+str(f.c[1,i])+"(x-" + str(f.x[i]) +")^2"+str(f.c[2,i])+"(x-" + str(f.x[i]) +")"+str(f.c[3,i])+"(x-" + str(f.x[i]) +")^0 \n")
```

Listing E.1: Script to calibrate model using piecewise cubic interpolation

```python
INITIAL_GUESS_A = 1000
```

```
INITIAL_GUESS_B = 0.1
#The x^3 + x^2 + x + c for the portion of the calibration locus closest to zero

#FRACTURE:
#SHEAR_CUBIC = 94979.68828414206
#SHEAR_QUAD = -37725.98663598951
#SHEAR_LINEAR =0.0
#SHEAR_CONST =1109.041765

#ONSET:
SHEAR_CUBIC = 8942.01413083842
SHEAR_QUAD = -4229.611173269809
SHEAR_LINEAR =0.0
SHEAR_CONST =373.8694118

MIN_X = -0.01


def errorInConstants(constants):
    NUMERICAL_DIF_NUDGE = 0.000001
    A,B = constants
    #I could calculate the below values by putting in the calibrated values for shear portion here and evalutating at 0 and 0.00001
   # OBJECTIVE_VAL = 1.24 # Needs to be equal to the value of the cubic interpolation at 0 for the shear portion of the curve
   # OBJECTIVE_DIF = -0.55 # Needs to be equal to the value of the derivative of the cubic int
   # cubicEquationGradientAtZero = -SHEAR_CONST + (SHEAR_CUBIC*(NUMERICAL_DIF_NUDGE)**3+SHEAR_QUAD*(NUMERICAL_DIF_NUDGE)**2+SHEAR_LINEAR*(NUMERICAL_DIF_NUDGE)+SHEAR_CONST)
    #print(cubicEquationGradientAtZero)
    cubicEquationAtZero =(SHEAR_CUBIC*(0-MIN_X)**3+SHEAR_QUAD*(0-MIN_X)**2+SHEAR_LINEAR*(0-MIN_X)+SHEAR_CONST)
    cubicEquationAtNudge =(SHEAR_CUBIC*(NUMERICAL_DIF_NUDGE-MIN_X)**3+SHEAR_QUAD*(NUMERICAL_DIF_NUDGE-MIN_X)**2+SHEAR_LINEAR*(NUMERICAL_DIF_NUDGE-MIN_X)+SHEAR_CONST)
    OBJECTIVE_VAL = cubicEquationAtZero
    OBJECTIVE_DIF = (cubicEquationAtNudge-cubicEquationAtZero)/NUMERICAL_DIF_NUDGE
    newValue = A*(1/3)**-B
    difference1 = abs((newValue - OBJECTIVE_VAL)/OBJECTIVE_VAL) #divide by objective to get a "relative" measure of difference, this is required because the gradient may be a large number and drown out the other objective of matching y intercept
    print(difference1)
    newDiffVal = ((A*(NUMERICAL_DIF_NUDGE+1/3)**-B) - newValue)/NUMERICAL_DIF_NUDGE
    difference2 = abs((newDiffVal - OBJECTIVE_DIF)/OBJECTIVE_DIF) #divide by objective to get a "relative" measure of difference, this is required because the gradient may be a large number and drown out the other objective of matching y intercept
    totalError = difference1  + difference2

    return totalError

```

```
import scipy.optimize as spo

newA,newB = spo.minimize(errorInConstants,[INITIAL_GUESS_A,INITIAL_GUESS_B], method="Nelder-Mead",tol=0.00000000000001).x

print("New A value: ", newA, " New B value: ", newB)
```

Listing E.2: Script to calibrate model asympototic parameters

```
import Pkg; Pkg.add("ImageSegmentation")
Pkg.add("IndirectArrays")
using Images
using ImageSegmentation, TestImages
using IndirectArrays
using FileIO

# img = FileIO.load(raw"C:\Users\Luke\OneDrive\Desktop\testimage7.jpg")
img = FileIO.load(raw"C:\Users\Luke\OneDrive\Desktop\testimages\shear_2_0001_small.png")

img = Gray.(img)
bw = Gray.(img)# .> 0.5

(Gray.(bw))

#minimum(gray.(Gray.(img)))
grady,gradx= ImageFiltering.imgradients(img,KernelFactors.sobel, "reflect")
Gray.(gradx)
gradx
#maximum(gray.(Gray.(gradx)))
#any(gray.(Gray.(gradx)).<-1/256)
#sum = 0
#for element in gray.(gradx)
#    if element > 1/256
#        sum += 1
#    end
#end
#print("waco ", sum )
using StatsBase
h = fit(Histogram, (vec(gray.(gradx)),vec(gray.(grady))), (-0.5:1/256:0.5,-0.5:1/256:0.5) )
Gray.((h.weights)/256)
Gray.((((h.weights/256)./maximum(h.weights/256)).^0.1).*maximum(h.weights/256))
function entropy2D(array)
    sum = 0
    len = reduce(+,array)
    for element in array
        if element != 0
            sum += (element/len)*log2(element/len)
            #print("probability: ", element/len, "\n")
        end
    end
    return -0.5*sum
end

```

```
print("Traditional Entropy: ",Images.entropy(img),"\n2D Entropy:          ", entropy2D(h.weights))
#To match paper exactly
#deltaX(x,y) = [(x+1, y) - (x-1, y)] / 2
#deltaY(x,y) = [(x, y+1) - (x, y-1)] / 2

xkernel = centered([1 0 -1; 0 0 0;1 0 -1]);
ykernel = centered([1 0 1; 0 0 0;-1 0 -1]);
dx=imfilter(img, xkernel)
dy = imfilter(img, ykernel)
h2 = fit(Histogram, (vec(gray.(dx)),vec(gray.(dy))), (-0.5:1/256:0.5,-0.5:1/256:0.5) )
print("Traditional Entropy: ",Images.entropy(img),"\n2D Entropy:          ", entropy2D(h2.weights))
Gray.((h2.weights)/256)
Gray.((((h2.weights/256)./maximum(h2.weights/256)).^0.1).*maximum(h2.weights/256))
```

Listing E.3: Script to calculate 2d entropy of speckle pattern